Testing the Ariel Exoplanet Space Observatory

Robert Spry

Christ Church

University of Oxford

A thesis submitted for the degree of

Doctor of Philosophy

Michaelmas Term 2023

ABSTRACT

Ariel is an ESA mission that will use the transit spectroscopy method to observe the atmospheres' of ~1000 exoplanets. Ariel is a 1 m class cryogenic space telescope that will be placed in a halo orbit around the Earth-Sun L2 point. To detect atmospheric molecular absorption features, Ariel will produce medium-resolution spectra ($R \geqslant 15$) using three spectroscopic channels covering 1.1 – 7.9 µm as well as having photometric channels covering 0.5 – 1.1 µm. The technical driver for Ariel, though, is the photometric stability. This is to enable the detection of atmospheric spectral features that are a signal of tens of ppm relative to the host star. Ariel, therefore, aims to have tens of ppm stability over long (10 hr) timescales.

To achieve Ariel's science goals, the payload requires detailed calibration and performance verification. The testing of the integrated Ariel payload will be the subject of this work. The ground calibration of the Ariel payload will take place in 2026 in the 5m vacuum chamber at the Rutherford Appleton Laboratory's space instruments test facility. The payload will be enclosed in a Cryogenic Test Rig (CTR), to provide a space-like (35 K) thermal environment. During the cryogenic vacuum testing, the payload will be illuminated by the Optical Ground Support Equipment (OGSE). The OGSE used to calibrate the payload is being developed by a team led by Oxford University and the University of Lisbon.

The author joined the project just before mission adoption. The thesis was submitted just after the completion of the payload Preliminary Design Review (pPDR). The work completed in this thesis focused, therefore, on performance simulation, requirement derivation and design of the OGSE system. In this thesis, many of the key performance parameters will be derived. It will be shown how these parameters have shaped the OGSE system from an architectural level down to the detailed design.

To define the performance parameters of the OGSE, the calibration observation modes must be defined. Methods were, therefore, defined to show how the OGSE can be used to perform the payload-level calibration of Ariel. End-to-end radiometric simulations were also provided to simulate the focal plane signal when the payload is illuminated in the various calibration modes of the OGSE.

The photometric stability and dark current tests were identified as particular drivers for the OGSE design. The need for dark testing of the payload was used to derive the thermal requirements for the system. Finite Element Analysis (FEA) was then used to assess the thermal performance of the OGSE system, and thus enable low-background testing of the payload (<1 $e^{-}pix^{-1}s^{-1}$). The other performance driver identified was the photometric stability test. End-to-end time-domain simulations of this test were performed to derive the required performance of OGSE flux monitoring systems. OGSE monitoring detector candidates were then assessed to demonstrate these could be used to verify the stability of the payload.

Alignment during ground testing was discovered to be a critical technical risk to the OGSE system. It will be shown how monitoring alignment from ambient to cryogenic temperatures led to a major redesign of the OGSE architecture. Moreover, Ariel's tiny field of view (~30'') leads to extreme (arcsecond) alignment maintenance requirements. An alignment monitoring system will be presented, built and verified, to enable the closed-loop monitoring required to keep the OGSE spot within the payloads' spectrometer slits.

PREFACE

The work completed in this thesis was completed in the 2019-2023 time frame - encompassing the COVID-19 pandemic. This project underwent significant restructuring to account for this. Remote work mandated an increased emphasis towards modelling and analysis and a greatly reduced quantity of experimental work.

Significant portions of this work was developed as part of the various Ariel instrument and mission reviews. Occasionally, as appropriate, requirement identifiers (e.g. R-SCI-210) are used in this thesis. The full wording of selected requirements is given in Appendix C.

ACKNOWLEDGEMENTS

There are many people I would like to thank for the impact they had on this DPhil: My supervisor Neil Bowles and Keith Nowicki for their guidance and support throughout this project, the OGSE team (past and present) for numerous insightful discussions; this includes Rory Evans, Jake Hutchinson, Maisie Rashman, JP Walker, Waqas Mir, Bob Watkins, Simon Calcutt, and Matthias Texa. I would also like to thank the members of the wider Ariel mission consortium for their review and feedback on the OGSE development. In addition I am grateful to Subi Sarkar for allowing us to adapt ExoSim for ground test simulations and to Lorenzo Mugnai for providing ground-test specific simulations using Ariel-RAD.

On a personal note, I would like to thank my parents Sally Spry and Alasdair Spry for their endless support in my of my academic pursuits and my partner Connie Chen, who kept me sane when doing a PhD during the pandemic.

Finally I would like to thank STFC for their funding of this work.

TABLE OF CONTENTS

LIST OF ACHRYNOMIS

ADU	Aribetry Digital Units
AIRS	Ariel InfraRed Spectrometer
AIT	Assembly Integration and Test
Ariel	Atmospheric Remote-sensing Infrared Exoplanet Large-survey
BRDF	Bidirectional Reflectance Distribution Function
CDR	Critical Design Review
CDS	Correlated Double Sampling
CFRP	Carbon Fibre Reinforced plastic
CTR	Cryogenic Test Rig
EM	Engineering Model
F/#	F-number (focal ratio)
FEA	Finite Element Analysis
FGS	Fine Guidance Sensor
FOM	Figure Of Merit
FOV	Field Of View
MLI	Multi-Layer Insulation
NDR	Non-Destructive-Read
OAP	Off-Axis Parabolic (mirror)
OGSE	Optical Ground Support Equipment
PAC	Percentage Area Coverage
PDR	Preliminary Design Review
PFM	Proto-flight Model
PIP	Payload Interface Plate
PLM	Payload Module
PSF	Point Spread Function
QE	Quantum Efficiency
RAL	Rutherford Appleton Laboratory
SRR	System Requirement Review
STM	Structural Thermal Model
STOP	Structural-Thermal- Optical-Performance
TA	Telescope Assembly
TIS	Total Integrated Scatter

TOB	Telescope Optical Bench
T-VAC	Thermal Vacuum
WFE	Wave Front Error

1 THE ARIEL MISSION

Since the first detection of a planet around another star [1], the field of exoplanet science has seen rapid developments with the discovery of thousands of planets in the last decade [2]. Of these thousands, compositional information has been retrieved for tens of planets [3]. These planets provide a tantalizing glimpse into the vast parameter space to be explored by exoplanet observations.

An example of such an extreme world is the hot Jupiter WASP-43b which orbits its host star with a period of 19 h [4]. Retrievals of the temperature for this planet indicate that it has temperature gradients of ~ 1000 K between the day and night side of the planet [5]. Exoplanets can act as laboratories for conditions that cannot be observed within our solar system, providing a more general framework for understanding planetary processes.

Ariel aims to be the first mission to characterise ~1000 exoplanets, enabling exoplanet demographic studies for the first time.

In this section, we will describe the Ariel mission in the context of the range of methods of observing exoplanet atmospheres. It will then be discussed how the Ariel science goals have shaped the payload and the calibration measurements that must be made. The required calibration measurements, in turn, drive the design of the optical ground support equipment, the subject of this DPhil.

1.1 WHY IS ARIEL THE NECESSARY NEXT STEP FOR EXOPLANET SCIENCE?

To see why Ariel will be so critical for exoplanet science, we consider how the Ariel mission will sit in the context of other exoplanet observing methods.

1.1.1 Methods for observing exoplanets

Until recently, the main advances in exoplanet science were in detection. Various discovery methods have been developed and are summarised by [6]. Four of the most successful methods are direct imaging, microlensing, transits, and radial velocity. Each method probes a different region of the

mass/orbit parameter space (illustrated in Figure 1) and can retrieve different physical properties of the planet. As a result, these complementary methods provide a more complete picture of exoplanets than any method alone.

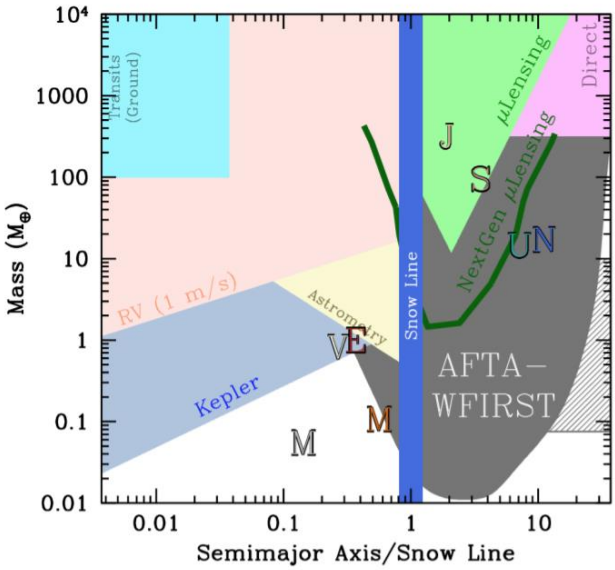

Figure 1: Relative sensitivity of different observational methods as a function of planet mas and orbital distance. Soler system planets are shown by their corresponding letters. The semi-major axis is scaled by the snow line distance $a_{snow} = 2.7 \text{ AU } (M_*/M_\odot)$. *Figure courtesy of B. Scott Gaudi and Matthew Penny published in [6].*

Primary transits (Figure 2) cause a drop in light when a planet passes in front of its host star. This drop in light depends on the relative size of the planet to the star hence this method provides a direct measurement of the planet's radius. Primary transits have proved the most numerous method of planet detection with 4000 planets [2] detected to date[1], thanks in part to the TESS, CHEOPS, Kepler, Gaia, and CoRoT missions. This number is expected to grow significantly by the time Ariel launches

[1] Correct as of 14/9/23

with new results from PLATO (PLAnetary Transits and Oscillation of stars)[7] as well as ground-based surveys.

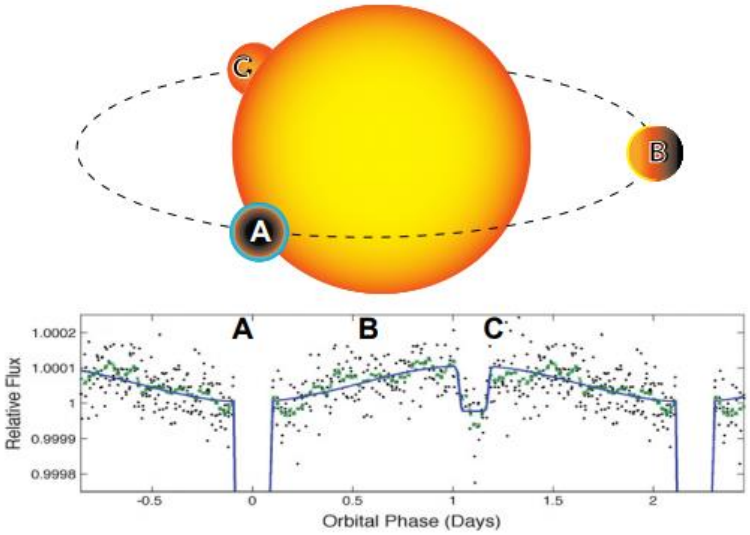

Figure 2: A sample transit photometry light curve. [8, 9]

The second crucial observational method is the radial velocity method. This method uses high-resolution ($R = 25{,}000 - 100{,}000$ [10]) ground-based spectroscopy to observe a star's Doppler shift, which is caused by an orbiting planet. Since it is due to the planet's gravitational influence, this method can be used to retrieve the planet's mass and its ephemeris. Both are useful parameters to constrain atmospheric retrievals. Knowledge and maintenance of exoplanet ephemerides is also critical for scheduling Ariel's observations.

1.1.2 Why do we need to observe exoplanets spectroscopically?

By combining the mass measured by radial velocity measurements with the planet's radius measured from transits, we can get an estimate of the bulk density of an exoplanet. This density can be used as a first guess for the composition of an exoplanet, but this method is highly degenerate. If spectroscopic measurements are made, this can provide additional constraints on the atmosphere's composition,

temperature, structure, and cloud/haze coverage. Therefore, the goal for understanding exoplanets is to spectroscopically resolve their atmospheres. This is the approach Ariel will use.

1.1.2.1 The transit spectroscopy method

An example exoplanet light curve is shown in Figure 2. There are three features labelled on this plot: The transit (A), the phase curve (B) and the eclipse (C). The transit is seen as a drop in light when the planet passes in front of the host star, partially blocking the star's light. In addition to the star's light, there is also a measurable signal from the planet. The planet's flux includes both thermal emission as well as reflected light from the host star. When the planet passes behind the host star, the contribution from the planet is no longer seen causing a drop in light - referred to as the eclipse.

The final feature in Figure 2 is the phase curve. This flux variation is caused by the planet's brightness not being uniform across the planet's surface. As the planet moves from transit to eclipse, more of the day side of the planet becomes visible causing an increase in flux. Measuring the phase curve, therefore, provides insights into the day-night thermal gradients.

To gain compositional insights, light curve measurements can be made at multiple wavelengths. By differencing the in-transit flux from the out-of-transit flux, the transit depth can be estimated. The transit depth can then be measured at multiple wavelengths to produce a spectrum such as the one shown in Figure 3 (and similarly for the eclipse).

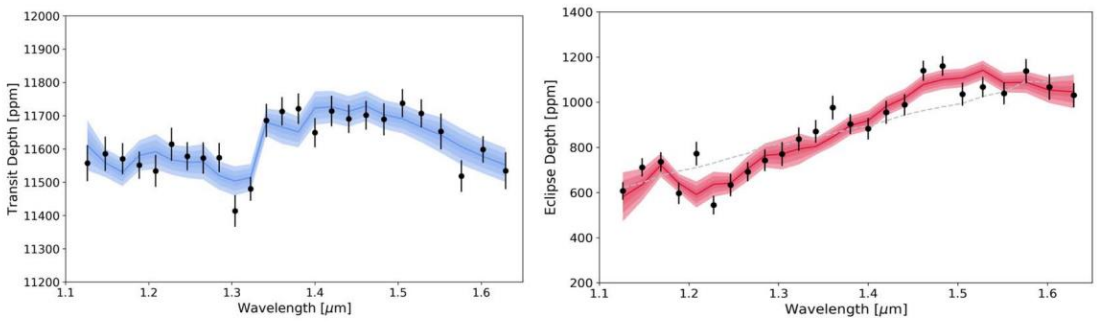

Figure 3: Example Hubble wide field camera 3 spectra of WASP-76 b [8, 11]. Left shows the transit spectra. Right shows the eclipse spectra.

1.1.2.2 Transit spectroscopy science goals

By measuring exoplanets spectroscopically, several additional questions can be addressed. Here we describe the specific questions that Ariel aims to address. A detailed description of these goals is given by Tinetti et al. [12] and can be summarised as:

- What are exoplanets made of?
- How do planets and planetary systems form?
- How do planets and their atmospheres evolve?

1.1.2.2.1 Composition

From transit/ eclipse spectra, retrieval tools such as TauREx [13] and NEMESIS [14] can be used to directly retrieve the abundances of certain molecular species. A sample of the molecular features that will be observable by Ariel is given in Figure 4. These species all have absorption features within the Ariel wavelength range. From the mixing ratios of the observable molecules (Figure 4), chemical models can be used to infer the presence of less visible molecules e.g. N_2.

With Ariel, bulk composition estimates will be carried out for a large sample (~ 1000) of exoplanets. Currently, the only method we have for populations greater than tens of planets is based on the bulk density. Even if the density of the planet could be exactly known, this does not uniquely constrain the composition of the interior; for example, a water world could have the same bulk density as a planet with a large iron core but an H/He atmosphere. With Ariel, it will be possible to break this degeneracy by observing during primary transits and retrieving the scale height of the atmosphere, hence the mean molecular weight. The scale height will be very different for a hydrogen versus a metal-rich atmosphere allowing these types of planets to be distinguished.

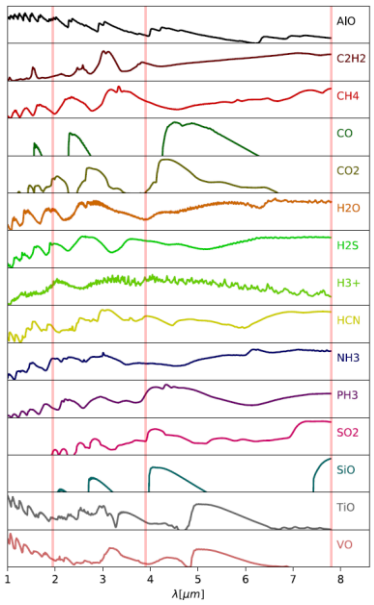

Figure 4: The spectrum of prominent atmospheric species plotted at constant spectral resolution (R=300).

Figure from [8]. (figure adapted to public domain version for ORA deposit)

Obtaining bulk compositions is something that still proves challenging even for the gas giants in our solar system [15]. Since transit spectroscopy only probes down to order unity optical depths, much of the atmosphere remains unseen. This is especially problematic for cool gas giants since certain molecular species will condense out at altitudes lower than we can see. This will cause the depletion of key molecular carriers of atomic species at the observed pressure levels. Therefore, these key carriers can remain undetected or their abundances underestimated. This means that for cool gas giants, converting from the observed abundance to the bulk abundance is very sensitive to the atmospheric chemical models used.

Ariel will get around this by observing large numbers of hot Jupiters (see [16]). These planets are expected to be sufficiently hot that these key atomic carriers will not have condensed out. Therefore, we expect the observed abundances to resemble the bulk composition more closely. Moreover, due to research in combustion engines, chemical models for the temperatures and pressures seen in hot Jupiters are more tightly constrained than for cooler planets, further making bulk composition estimates more reliable [12].

1.1.2.2.2 Formation

Composition information obtained from exoplanet spectra also has implications for understanding planetary formation. This includes understanding the distinction between super-Earths and sub-Neptunes [17], which are expected to form in different ways. Super-Earths are expected to reach their critical mass (the mass at which a planet's potential well is deep compared to the thermal energy of the gas in the disk) after the gas in the protoplanetary disk has dissipated whereas sub-Neptunes are expected to have reached their critical mass sufficiently early, so they were able to accrete a significant primary atmosphere. Each formation mechanism, therefore, produces a very different atmospheric composition, something that is directly observable by transit spectroscopy. Observing super-Earths and sub-Neptunes is key in deriving upper and lower radius limits of each formation pathway and constraining the importance of other formation methods, such as photoevaporation of sub-Neptunes becoming super-Earths[18].

Öberg et al. [19] was the first to point out another way composition could be used to understand planetary formation. They showed that core accretion in a protoplanetary disk with a thermal gradient would lead to chemical signatures in exoplanets' atmospheres. This is because species present in the gas phase versus the solid phase will vary as a function of temperature and hence, as a function of distance from the host star (Figure 5). The gas accreted during the formation of the planet's atmosphere will, therefore, reflect the disk's gas-phase composition at the formation location.

A popular metric for describing the atmospheric composition is the C/O ratio as this shows strong variation across the protoplanetary disk (Figure 5) [19]. The C/O ratio, therefore, provides insights into where the plant was formed. It will also test the core accretion model versus the gravitational instability model as the latter predicts that all planets should form with stellar C/O ratios.

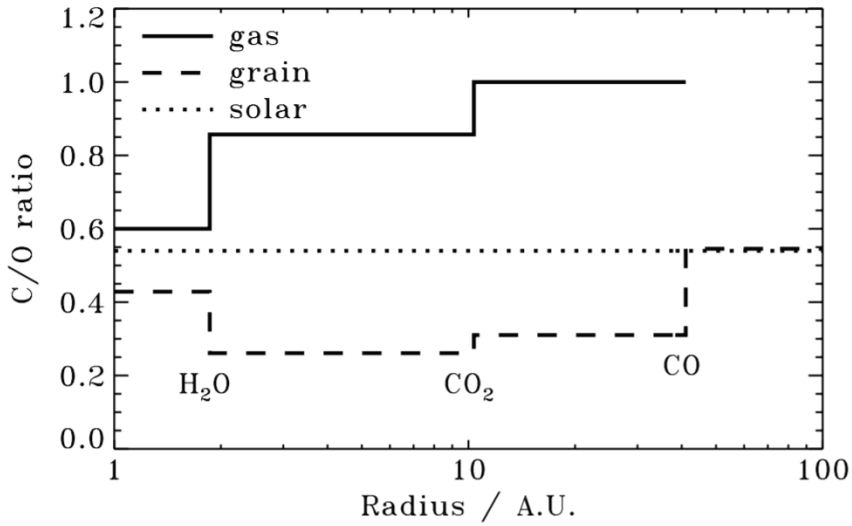

Figure 5: Carbon-to-oxygen ratios as a function of distance from the star [19]. The step-like features seen show the change in gas and grain composition in the protoplanetary disk as different species freeze out of the gas phase at their corresponding snow lines (H_2O, CO_2 and CO).

1.1.2.2.3 Evolution

The present-day atmospheric state is not only determined by the formation mechanism, the state also provides insights into the evolution processes. For sufficiently close-in exoplanets, a dominant evolution process is atmospheric escape. This process is known to depend strongly on (amongst other things) composition and the temperature profile of the atmosphere, both of which will be measured by Ariel. It will do this in multiple ways. Phase curve observations, alongside ingress/egress mapping during a secondary eclipse can be used to recover the 3D temperature structure of the exoplanet [20] which can constrain thermal transport models (e.g. molecular recombination timescales [21]).

A possible end state of atmospheric escape is the formation of a rocky core stripped of its atmosphere, such as LHS 3844b [22]. Using phase curve spectroscopy (see 1.1.2.1), the temperature distribution of this planet was observed. The large (1000 K) temperature gradients and the position of the hotspot relative to the substellar point were considered inconsistent with atmospheric circulation models which were used as strong evidence for a bare rocky core.

Along with phase curve observations, Ariel can also attempt to answer questions about atmospheric escape in a statistical sense. Transit spectroscopy can determine whether a planet has an atmosphere (or at least rule out a significant cloudless primary atmosphere). Due to Ariel's sample size, the presence or absence of atmospheres will be observed as a function of stellar type, semi-major axis, and planetary mass to observe photoevaporation limits.

As well as the statistical results, Ariel will be used to observe a small number of targets that are believed to currently be evaporating [23]. It is anticipated that we will be able to observe the Rayleigh/Mie scattering tail of the spectrum and hence, determine the size of the particles being lost from the evaporating planet.

1.1.3 Past and future spectroscopic missions

Transit/ eclipse spectroscopy, therefore, provides insights into a range of planetary science questions. Over the past decade, several telescopes have been used to spectroscopically observe exoplanets, however, none were specifically designed for this task. Here we describe some of the leading observatories and highlight the differences of Ariel.

The Hubble Space Telescope was the leading observational platform for exoplanet spectroscopic measurements providing coverage from $0.2 - 1.7\ \mu\mathrm{m}$ with the Wide Field Camera 3 (WFC3) (in two channels that cannot be viewed simultaneously) [24]. Until recently, Spitzer was also used for coverage in the IR [3] (Figure 6). A smaller number of successful characterisations have also been made from the ground including the detection of Titanium Oxide on WASP-19b using the low-resolution FOcal Reducer and low dispersion Spectrograph 2 (FORS2) on the VLT[25].

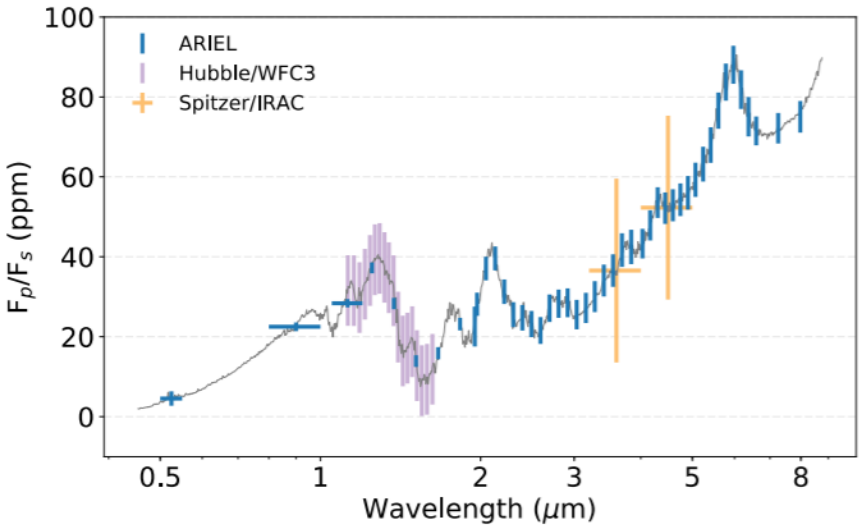

Figure 6: Comparison of the spectral range and expected noise performance of Ariel versus Hubble/Spitzer [23].

Current successes in atmospheric characterisation are dominated by JWST. JWST has a resolving power ~ 5.7 times that of Hubble and a collecting area 5.6 times that of Hubble. This means JWST provides much better spectral resolution whilst maintaining a similar S/N ratio [26]. JWST also provides a much broader spectral coverage from $0.6 - 28.8\ \mu\text{m}$ [26], allowing more molecular features to be observed. Predictions using retrievals of simulated spectra and instrumental noise models expect that JWST will be able to retrieve the metallicity to within a factor of 3 and the carbon-to-oxygen ratio within a factor of 1.6 within 2 transit events for favourable targets[27]. This marks a significant improvement over previously available data [28].

Further advancements will come with the launch of Ariel [12]. This mission has two key advantages over JWST. The first is the sample size of the mission. JWST is built around four broad science themes (early universe, stellar evolution, galactic evolution and exoplanets) [29], so observational time must be divided between them. Based on the level of community interest and mission overheads, Cowan et al. [30] estimated the observational time for exoplanet transits would be ~ 300 days. They further estimate the time required for different observations: approximately 2 days per giant planet, 12 days for phase curve mapping, and 100 days for a temperate terrestrial planet. Assuming some combination of these science goals are followed, then it is anticipated JWST will observe tens of

exoplanets. Ariel aims to probe the atmospheres of many more (~ 1000) atmospheres since it is a mission solely dedicated to exoplanets. This will provide unique statistical insights into exoplanet populations.

The second key advantage of Ariel is that it provides simultaneous spectral coverage from 0.5 to $7.8\ \mu\mathrm{m}$. For JWST to achieve this spectral range, it will require the use of multiple instruments typically needing observations of four transits [30]. Experience from Hubble has shown that instrumental systematics can provide significant problems when trying to combine data from different instruments, and this may limit retrieval precision. As well as the instrumental systematics, there is also stellar activity which provides a time-varying background that will be different for each observation. Barstow et al. [31] found in simulations that this effect dominates the uncertainty in JWST retrieved abundances for active stars.

Ariel is, therefore, well situated to revolutionise exoplanet science in the next decade. It will allow us to perform population studies on exoplanet atmospheres for the first time providing further insights into exoplanet composition, formation, and evolution.

1.2 HOW EXOPLANET SCIENCE DRIVES THE ARIEL DESIGN

1.2.1 Science requirements

The Ariel design is driven by its science goals (section 1.1.2). These goals motivate the science requirements of the payload, which in turn drives the payload design. A detailed description of the science requirements is given in the Ariel Science Requirement Document [32] and is summarised here. The key science requirements define the following:

- Spectral range
- Stellar targets
- Resolving power
- Photometric stability / Signal-to-noise

- Cadence

1.2.1.1 Spectral range

Ariel's primary goal is to observe the composition of a diverse range of exoplanets. The main molecules to be detected (H_2O, CO, CO_2, CH_4 and NH_3) have strong absorption features in the near and mid-infrared (Figure 4). For eclipse observations, the highest signal-to-noise retrievals will be possible when observing close to the black-body peak of the planet's spectrum. Conveniently, hot/warm Jupiters' black-body spectra peak in the same spectral window as these molecular features. It is for these reasons that Ariel will observe to $7.8\ \mu m$.

The NIR/visible part of the spectrum is dominated by Rayleigh/Mie scattering, so it can be used to detect the presence and nature of clouds and hazes. Star spots also show up more strongly in the visible spectrum, so star spots seen in the visible can be used to correct the IR spectra [33]. To enable these goals, the short-wave limit was set up to $0.5\ \mu m$ (Figure 7).

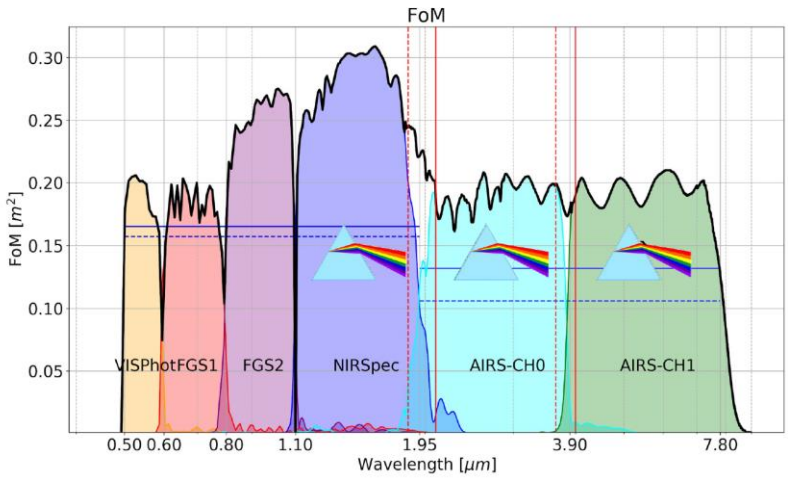

Figure 7: The spectral coverage of the different detectors, denoted by the figure of merit (FoM), which is defined to be the product of the collecting area, the optical throughput, and the detector quantum efficiency[8]. (This figure was switched to a public domain version for ORA use)

1.2.1.2 Photometric stability

In addition to the spectral range, the other key driver for Ariel is the photometric stability. Ariel uses the transit spectroscopy method to observe exoplanets (section 1.1.2.1). Because this is a time domain measurement, the uncertainty in the transit depth directly depends on the photometric stability/noise of the payload. Since the atmospheric signals of interest are on the order of tens of ppm (Figure 6), this implies the payload must be photometrically stable to tens of ppm over transit timescales (<10hrs; R-SCI-210).

Photon noise limits the photometric stability for the vast majority of Ariel's targets. The photon noise floor depends on both the brightness of the targets as well as the spectral resolution so must be considered together. To ensure a diverse population of exoplanets, Ariel has been designed to view targets between GJ 1214 and HD 219134 (K-magnitude of 8.8 to 3.25; R-SCI-260, R-SCI-270). This corresponds to a ~300 times dynamic range in the visible part of the spectrum. These targets must be observed with a resolution of R $\geqslant$ 15 between 1.10 and 1.95 µm, R $\geqslant$ 100 between 1.95 and 3.90 µm, and R $\geqslant$ 30 between 3.90 and 7.80 µm (R-SCI-100, R-SCI-105). Ariel will, therefore, be designed to meet the stringent SNR requirements, for the defined bright and faint targets, with a moderate spectral resolution.

1.2.2 Payload design

The payload design to meet the science requirements (section 1.2.1) is shown in Figure 8 & Figure 9. Ariel uses an off-axis Cassegrain telescope to collect stellar/planetary flux. The light then passes through a dichroic chain, which allows all focal planes to be illuminated simultaneously. The focal planes consist of 3 spectroscopic channels (labelled AIRS channel 0 and 1 and NIRspec) as well as the photometric channels in the FGS (fine guidance sensor), which will be used both for science and for source tracking.

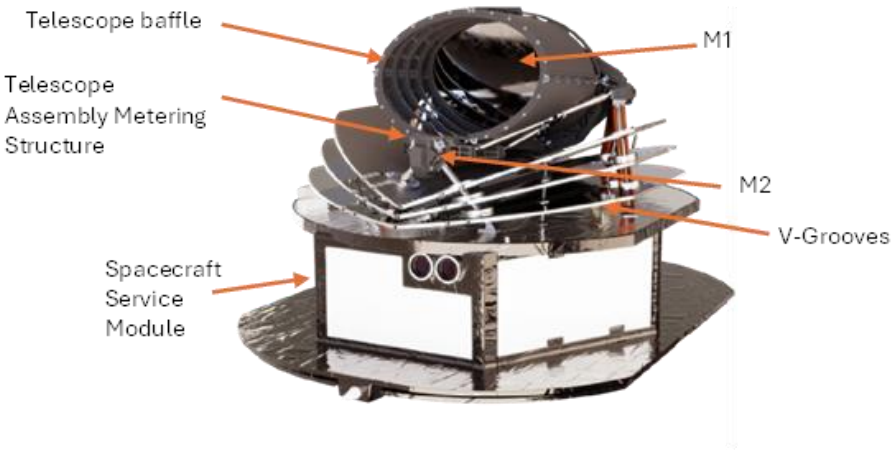

Figure 8: The Ariel payload + service module [34]. (This figure was switched to a public domain version for ORA use)

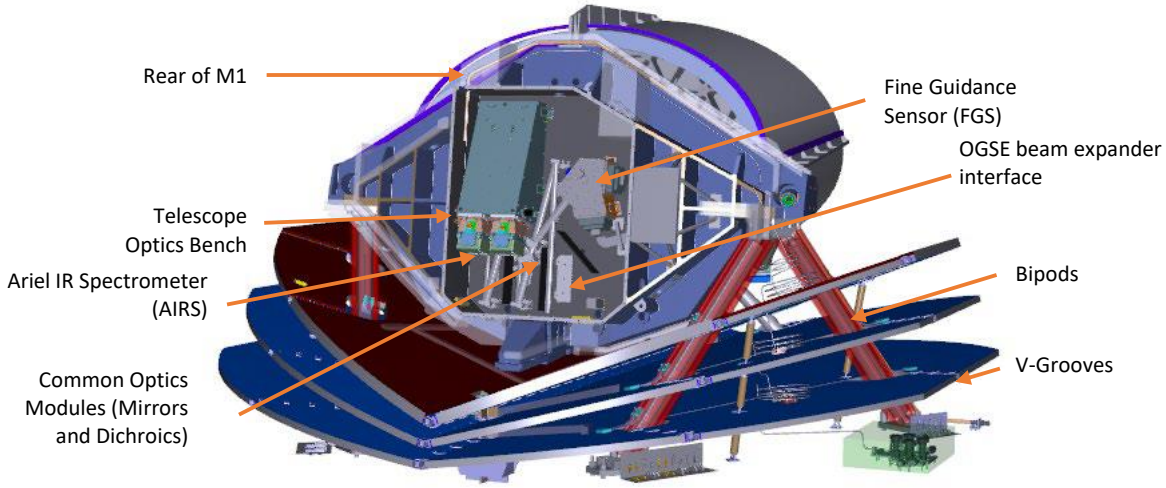

Figure 9: The telescope optical bench [34]. (This figure was switched to a public domain version for ORA use)

As discussed above (section 1.2.1.2), photometric stability is critical for Ariel. This has several design implications for the payload. For most targets, Ariel is photon noise limited. The noise floor, therefore, depends strongly on the size of the primary mirror and the throughput of the system. This drives the need for a 0.65 m^2 primary mirror (R-TEL-M1-0010; [35]).

To ensure, a photon-limited design, other noise sources must be minimised. The payload, therefore, uses low noise (<25 e^- per read; R-PRD-8812) MCT detectors. However, to reduce the dark current, the payload detectors need to be operated at cryogenic conditions, (e.g. AIRS Ch0 detector $T \leq 42$ K)

[36]. The dark current (along with thermal emission from optical elements) drives the thermal architecture shown in Figure 8. The payload uses low-conductivity Carbon Fibre Reinforced Plastic (CFRP) bipods and V-groves to isolate the ambient service module from the cryogenic optics (~50 K [37]).

In addition to needing cryogenic conditions, the payload also requires a thermally stable environment for the optics and detectors (<5 mK stability for the AIRS detectors [36]). This is to ensure a stable PSF and to avoid temperature-correlated gain drifts, as variability could cause photometric errors in the exoplanet transit signal. For Ariel, thermal stability is achieved by a combination of active control and operation at L2, with the service module always facing the sun.

1.2.3 Instrument design (AIRS +FGS)

The light from the telescope is split by wavelength using a series of dichroics to illuminate the different instruments (see Figure 9). The first dichroic (D1) cuts off at 1.95 microns, reflecting the short-wave component to the FGS. The long wave component is transmitted to AIRS.

AIRS [38] consists of two channels: CH1 and CH0, with CH0 covering 1.95 - 3.9 µm and CH1 covering 3.9 - 7.8 µm. A second dichroic (D2) splits the light between these two channels. Each channel functions as an independent instrument and both channels have the same optical architecture shown in Figure 10. At the input of each channel is a slit that sits at a focal plane. However, to avoid vignetting, the slit is oversized compared to the PSF making them essentially slitless[2]. After the slit, the light is

[2] The slitless nature of the spectrometers becomes important for multiple calibration measurements including the spectral resolution. Due to the lack of slit, the payload spectral resolution is determined by the payload PSF.

collimated using a lens and is dispersed using a prism. An imaging lens is then used to separate the angular (and thus wavelength) components on the focal plane.

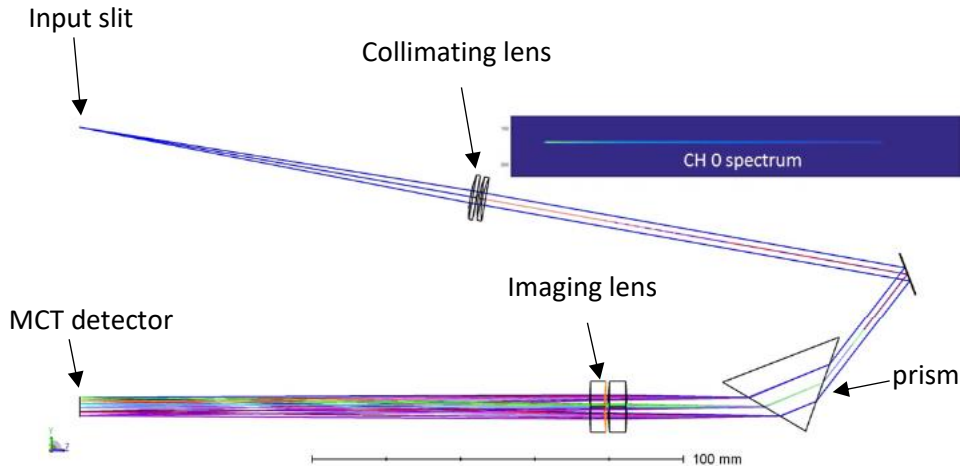

Figure 10: AIRS CH0 optical design [34, 38].

Light at wavelengths less than 1.95 microns is detected by FGS [39] using the design shown in Figure 11. Unlike AIRS, FGS takes a collimated input. The 13 by 20 mm elliptical input beam is further contracted by a Gregorian telescope within FGS. The light is then separated by a further three dichroics to pass signals to the four instrument channels - three photometric and one spectroscopic. The compact design uses two MCT detectors, to observe all four instrument channels.

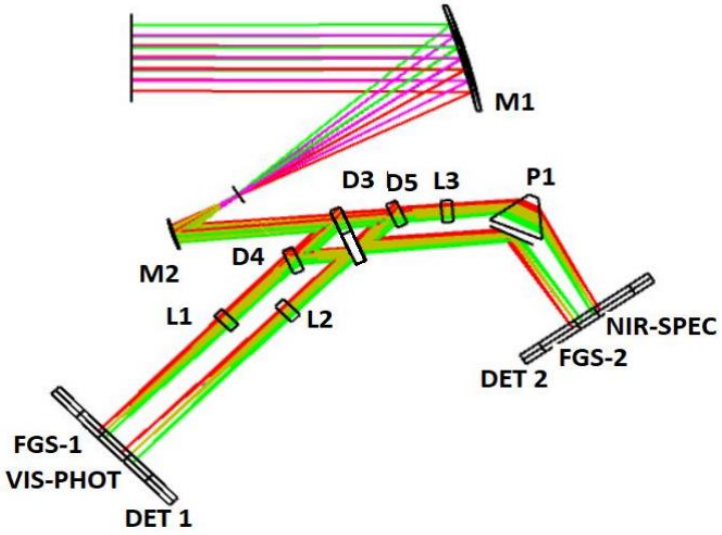

Figure 11: FGS optical design [39, 40] .

In this way, Ariel achieves simultaneous spectral coverage between 0.5 – 7.8 microns.

1.3 CALIBRATING ARIEL BEFORE LAUNCH

Achieving Ariel's ambitious science goals also requires detailed calibration before launch. Tests are performed at multiple levels: component (e.g. detector), unit (e.g. detector + full acquisition chain), system (e.g. AIRS) and eventually at payload level. Components are calibrated and the performance is verified at the lowest possible level and then verified at higher levels. The Payload level performance and calibration verification is the responsibility of the Optical Ground Support Equipment (OGSE).

1.3.1 Test campaigns of past missions

The Ariel test campaign has many similarities with previous large-scale space missions. Given Ariel's wide wavelength range, of particular interest are JWST, the Herschel space observatory and the Euclid mission.

1.3.1.1 JWST OGSE and ground calibration campaigns

A comprehensive description of the JWST Assembly Integration and Test (AIT) flow is provided in [41]. As with Ariel, it was planned that the science instruments (e.g. MIRI) would be fully calibrated and verified before integration into the Integrated Science Instrument Module (ISIM). Three T-VAC campaigns would then be used to verify the ISIM performance (Figure 12). The ISIM was then integrated into the telescope for a final telescope-level T-VAC campaign (Figure 13). The final integration phase incorporated the spacecraft and sunshield. The spacecraft level testing, was, however, only conducted in ambient conditions.

Whilst it was initially planned that all science instruments would be fully calibrated at the instrument level, ISIM level measurements proved critical for the full calibration flow. This was partly due to all the detectors in the three near-infrared instruments (NIRCam, NIRSpec, FGS/NIRISS) needing to be replaced due to a dark current issue. Moreover, in multiple cases, flight components were not ready

for instrument-level test campaigns. This meant significant amounts of de-risking and calibration were performed at the ISIM level for the first time. This highlighted the importance of calibration at later stages of integration.

Due to the telescope optical bench being an intrinsic part of the telescope structure, Ariel incorporated the functions telescope optical bench level campaign into the payload level campaign. Therefore, both the ISIM and payload-level OGSE designs for JWST are of interest.

At the ISIM level, JWST used the OGSE described in [42] (Figure 12). The telescope simulator is required to generate a beam with the correct pupil and focal surface locations as well as the correct f-number (F/#). The design to achieve this is based on a finite-conjugate reflective relay. The design uses a single-powered mirror to relay the image of source fibres to the instruments under test. A pupil wheel is used to place a series of masks in the beam. This wheel allows the JWST multi-segment pupil to be simulated. A diffuser is also present in the wheel for flat fielding. The system also features a complex set of modules for alignment monitoring internal to the telescope simulator as well as alignment to the science instruments.

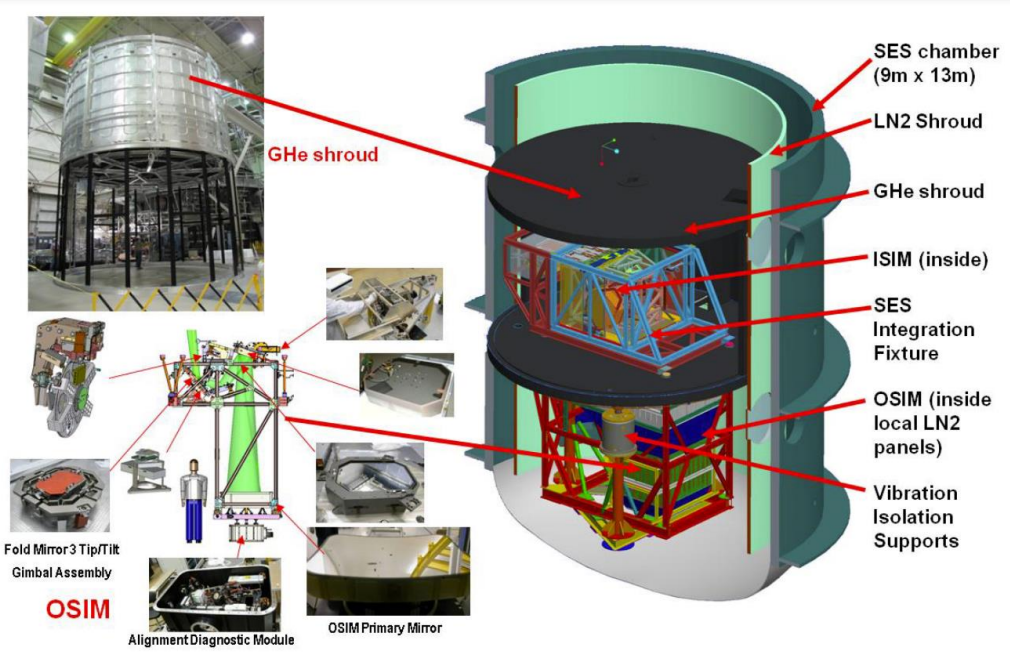

Figure 12: Configuration used to test the JWST Integrated Science Instrument Module (ISIM).

A separate OGSE was developed for payload-level testing and is described in [43], [44] and [45] (Figure 13). The design features a centre of curvature null interferometer for WFE mapping of the primary mirror, three sub-aperture flat mirrors above the payload for double pass testing, and a source module located close to the JWST Cassegrain focus. The source module has both up and down-facing sources. Those pointing towards the instrument modules enabled 'half-pass' testing. Other fibres pointed outward to the secondary mirror enabling 'pass-and-a-half' testing of the system. In addition, the design featured a videogrammetry system for course alignment of the telescope mirror segments. The combination of the videogrammetry, interferometry of the primary mirror, half-pass, and pass-and-a-half testing provided all the constraints required for verification of the cryogenic alignment of the telescope elements, and instruments. However, like Ariel, they note significant 1g aberrations are seen on-ground meaning performance verification is only possible by comparison to models.

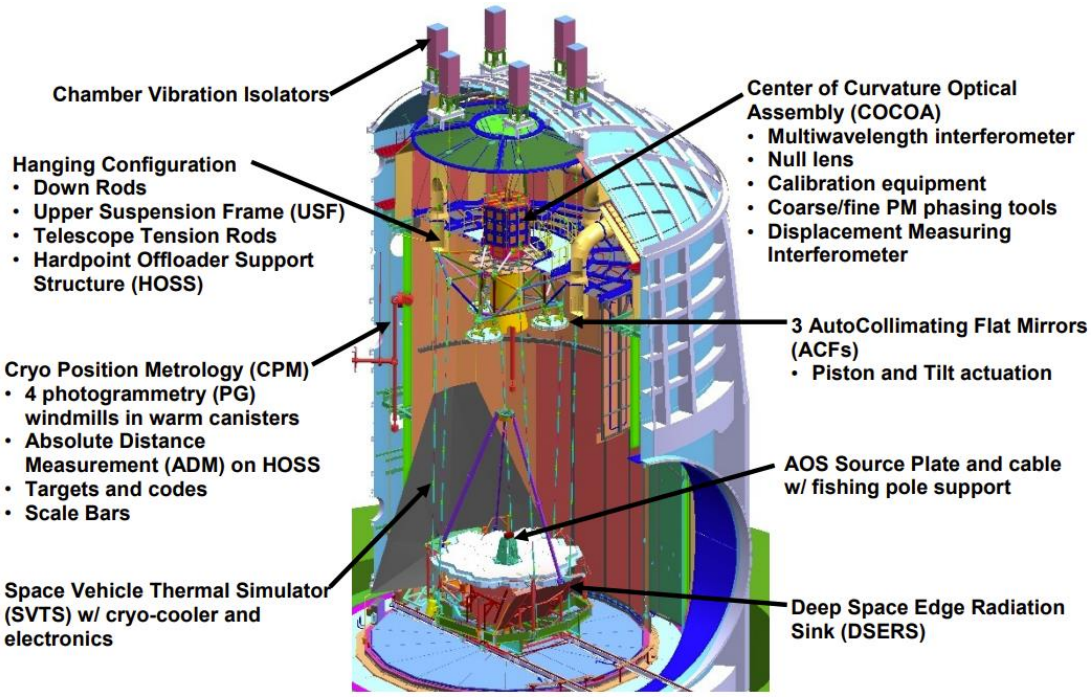

Figure 13: JWST payload-level test configuration [41]

1.3.1.2 Euclid testing

For Euclid, a different payload-level testing approach was adopted. A description of the test flow and results is reported in [46] & [47]. They performed telescope-level characterisation in ambient conditions. T-VAC testing was then done on the integrated telescope + instruments. A description of the OGSE used during the T-VAC campaign is provided in [48] (Figure 14). A 1.3 m collimator was used to fully illuminate the payload primary mirror. It consisted of an F/2 primary mirror, a hyperbolic secondary, and a fibre bundle at the focus. The source fibres were actuated in 3 axes so each fibre could be scanned across the payload FOV. However, to maintain alignment, the OGSE collimator was kept ambient whilst being subjected to an 80 K radiative environment.

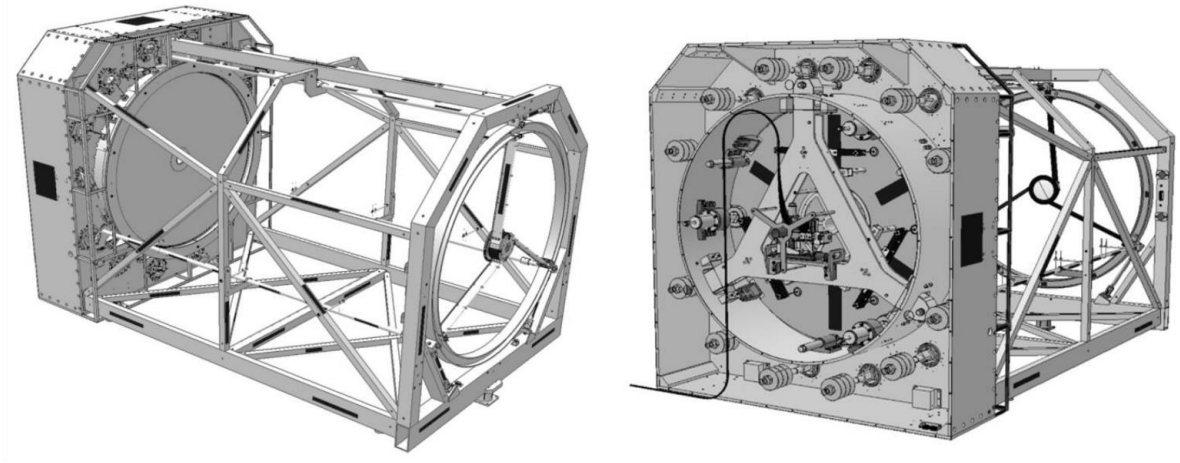

Figure 14: The collimator used during payload-level testing of Euclid [48].

1.3.1.3 Herschel testing

The Herschel space observatory on the other hand, operated in the far IR (55–672 μm) leading to a significantly more relaxed 6 micron WFE requirement. However, cryogenic optical characterisation remained critical for this mission as it had no refocusing mechanisms in either the telescope or instruments [49]. Rolo et al. [49] provides a review of the characterisation performed at the telescope level as well as at the integrated spacecraft level. During telescope-level testing, a double-pass Hartman filter design was used. This approach used a liquid flat mirror placed in front of the primary

mirror. This test was performed both at ambient as well as in T-VAC. Moreover, a theodolite and laser tracker were used to verify the M2 position during T-VAC. During payload-level testing, verification was primarily performed using a cryo-compatible photogrammetry system. An alignment camera system was also used to monitor tilts of selected reference surfaces (HACS).

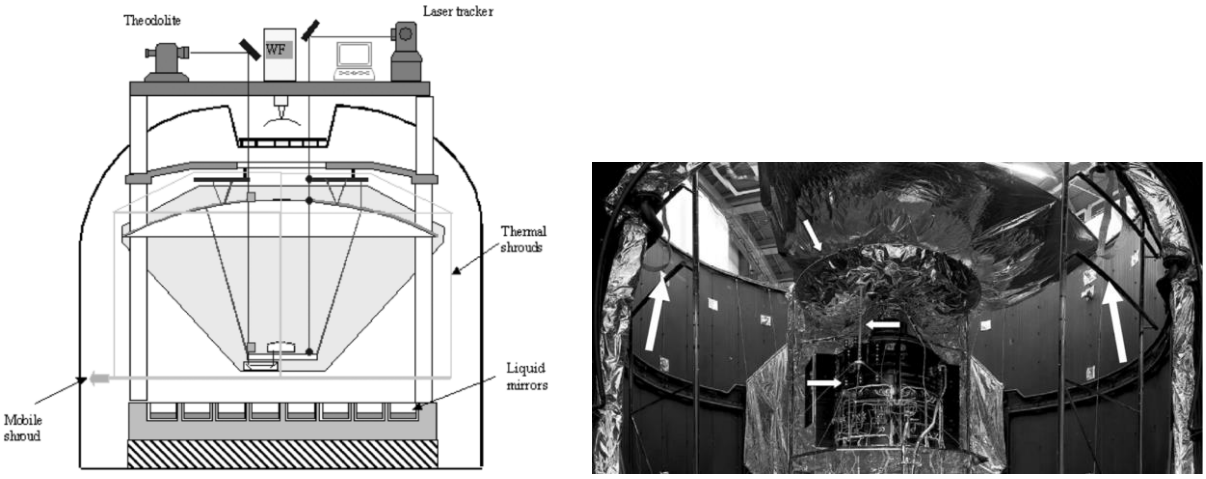

Figure 15: The left figure shows the double-pass Hartman configuration for telescope-level testing. The right figure shows the photogrammetry configuration used for payload testing. The white arrows indicate the retroreflective targets attached to the telescope's primary rim (top), the calibration bar (middle), and the cryostat vessel (bottom). On the left and right of the view are arrows showing the photogrammetry metrology system support structures [49].

1.4 THE ARIEL OGSE DESIGN

For Ariel, a somewhat different architecture for payload-level testing is required. Due to Ariel's extremely narrow FOV (~30'') and stringent WFE requirements (3 micron diffraction limit; R-PRD-0660), a Herschel-like photogrammetry-based design would not be sufficient (Figure 15 – right). A design that provides end-to-end testing is, therefore, required.

During phase A, a JWST-like double pass design was considered (Figure 13). However, the double sampling of the payload WFE would produce unacceptable aberrations at the focal planes. Moreover, the beamsplitter used to inject the OGSE beam was expected to cause significant ghosts. Because of this, a single-pass configuration sub-aperture design was adopted [50].

Unfortunately, due to the longer 8 micron wavelength cut-off of Ariel, an Euclid-like ambient OGSE (Figure 14) would lead to an unacceptable background in Airs CH1 (see 5.1.1.1). Because of this, Ariel requires a cryogenic (<70 K) OGSE (see Chapter 5 for further discussion). This introduces significant challenges for alignment maintenance. This led to the OGSE architecture shown in Figure 16 (See [51] for further details).

1.4.1 Architecture for payload-level testing of Ariel

Like many OGSE setups (section 1.3.1), the most critical functions are the following:

- Verify the cryogenic optical alignment of the payload
- Verify the functionality of all components
- Verify calibration products derived at sub-system and component level

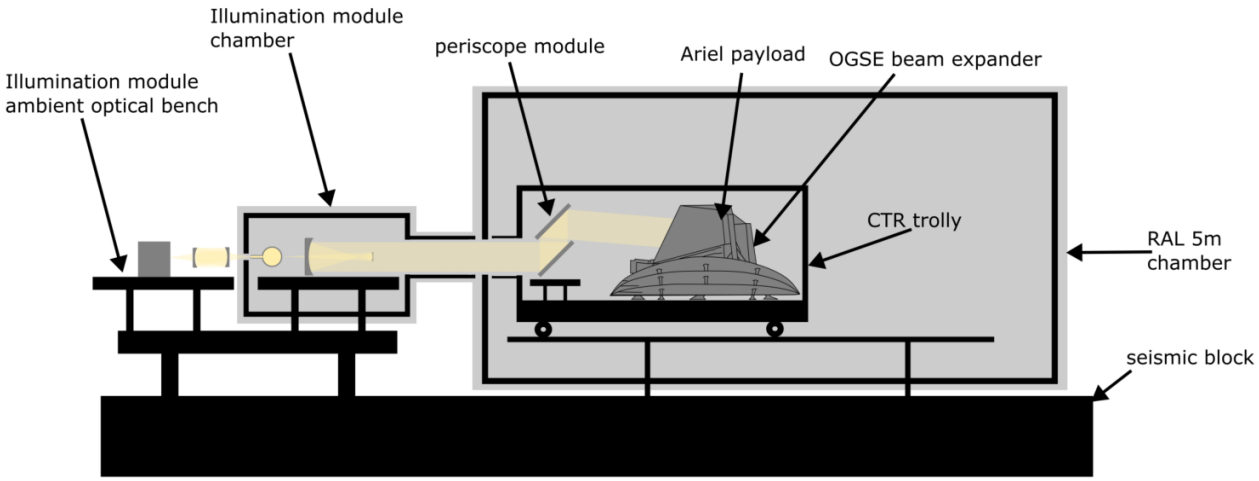

Figure 16: OGSE end-to-end architecture

To perform these tests, the Ariel payload will be tested in the 5 m diameter SCT 2 chamber at Ral Space. The test configuration is shown in Figure 16. A test beam is generated by the OGSE illumination module which sits outside the main chamber. To redirect the illumination module output to the payload line of sight, a periscope (Z-fold) is used. The illumination module output, is, however, ¼ the size of the payload primary mirror. To compensate for this, a four times beam expander is placed

within the payload on the telescope optical bench. This provides full aperture testing of the common optics and instruments.

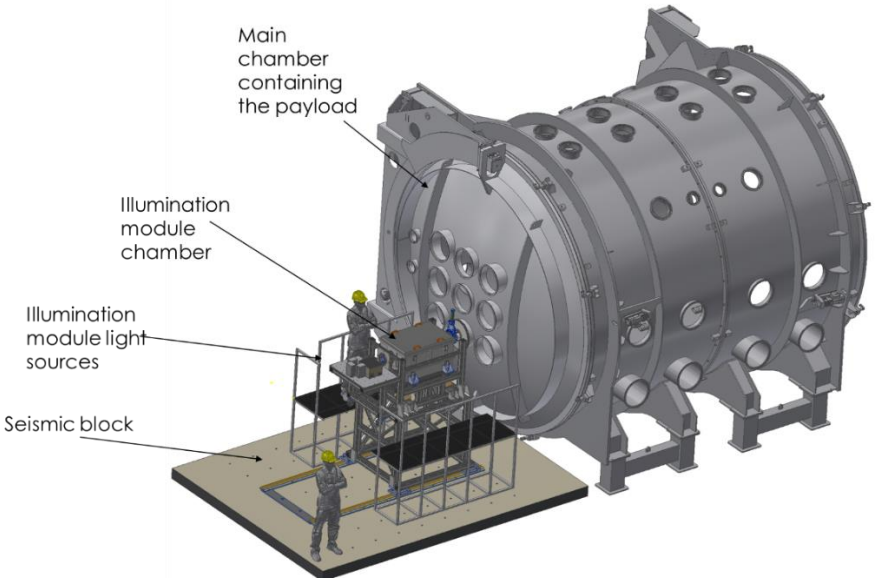

Figure 17: The OGSE illumination module integrated at the RAL space facility [51]

The Ariel OGSE, therefore, consists of three modules:

- The illumination module – contains the light sources, reference detectors, an integrating sphere and expansion optics. This generates a ¼ aperture collimated beam (~30 cm diameter).
- The periscope – a highly adjustable system capable of redirecting the illumination module output to the payload line of sight.
- The beam expander – sits within the payload and expands the beam by four times to produce a full-aperture beam in the payload common optics.

In addition to the OGSE modules, critical to the payload level testing is the cryogenic test rig (CTR) [52] provided by RAL space. The CTR consists of an ambient trolley and a cryogenic 35 K shroud (R-CTR-0430) [53]. This provides a flight-like radiative environment to enable thermal balance testing as well as enabling calibration in a representative thermal environment.

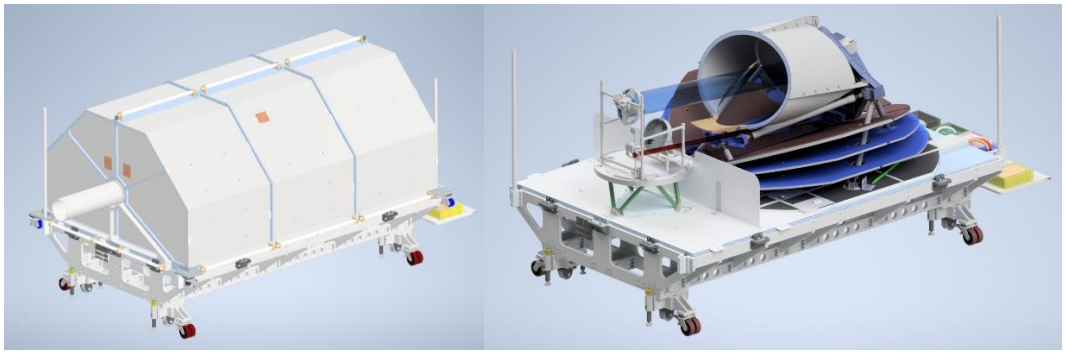

Figure 18: The cryogenic test rig (CTR) [54]. Shown with and without the shroud present.

1.4.2 OGSE driving requirements

The OGSE system design is driven by the calibration and performance verification functions it must perform for the Ariel payload. The calibration requirements document [55] and the payload test matrix [56] define the measurements that must be made with the OGSE. The required calibration products were then flowed to the performance requirements of the OGSE. Defining the test methods and flowing the calibration producers to performance requirements is the subject of Chapter 2.

Top-level Payload requirement	OGSE requirement	OGSE Design Implications
Measure molecular absorption features (e.g. H_2O) and detect clouds	Visible – IR operation (0.5-7.8 μm)	Cryogenic (65 K operation)
Single star viewing –> narrow payload FOV (30'')	4 arcsec pointing stability	- Challenging alignment - Micro vibrations and thermal drifts become challenging - Closed loop pointing control
Ability to view stars between GJ1214 and HD21913	300 times dynamic range in flux	Low f/# source relay optics.
Produce medium-resolution exoplanet spectra (R>15)	Wavelength calibration of the payload	Grating monochromator
Produce medium-resolution exoplanet spectra (R>15)	Verification of the payload spectral resolution/ optical quality[3]	- Point source sphere output - Stringent optical quality requirements ~100 nm RMS (with optics at ~65 K)
Detect atmospheric features that are tens of ppm compared to the star flux	Verify the payload's detectors are stable to tens of ppm	- Use of reference detectors to monitor source variability - mK thermal stability of our reference detectors.
Detect atmospheric features that are tens of ppm compared to the star flux	Verification of the flat field to enable to correction of pointing jitter-induced photometric errors.	Use of an integrating sphere to produce an extended, flat, output

Table 1: Summary of driving OGSE requirements (1)R-SCI-050, R-SCI-060 (2) R-PERF-180 (3) R-SCI-260, R-SCI-270 (4) R-SCI-105, R-SCI-100.

The flow down of selected requirements is summarised above in Table 1. These are the requirements that most stringently influenced the OGSE design. These requirements imply the OGSE must be

[3] For Ariel, the spectral resolution and the optical quality are closely related as Ariel uses wide slit spectrometers. This means the PSF size limits the spectral resolution of the instrument channels.

capable of generating a low WFE (<<200 nm RMS) image of the point source (50 μm pinhole). The flux passing through this small pinhole must be sufficiently large to match the payload's bright stellar target. Moreover, the low WFE condition must be met after the OGSE optics have cooled from ambient to ~65 K.

The OGSE output beam then must be aligned to the payload's tiny (~30'') FOV and remain stable to within arcseconds on many-hour timescales. This makes the OGSE extremely susceptible to thermoelastic drifts as well as micro vibrations e.g. from the cold heads.

To enable testing of the payload's photometric stability, the OGSE has also been designed to monitor and correct source flux changes to tens of ppm. To achieve this, a series of cryogenic broad-band reference detectors monitor the OGSE output flux. To reach tens of ppm stability the detectors are maintained to mK thermal stability.

The OGSE has extremely stringent performance requirements. This thesis will motivate the vast majority of the OGSE performance requirements as well as provide design solutions to meet these demanding requirements.

1.4.3 Illumination module

The OGSE architecture that meets these requirements consists of three modules. The illumination module, the periscope and the beam expander. The illumination module (see Figure 17, Figure 19) generates the test beam used for the calibration and performance verification of the Ariel payload. To provide adequate flux over the full 0.5-7.8 μm spectral band, the OGSE uses two broad-band light sources. A Rokide coated button heater that operates at 800 K and a Quartz-Halogen bulb that runs at 3360 K.

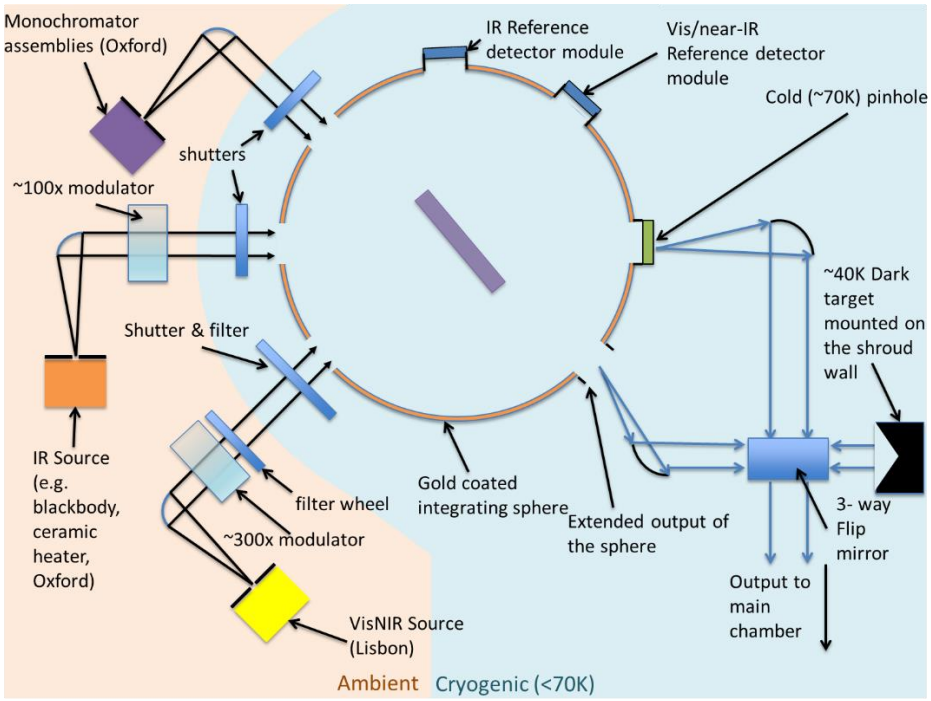

Figure 19: OGSE illumination module block diagram

For measurement such as the wavelength calibration monochromatic illumination is required. This is provided by a triple grating Czerny-Turner monochromator. At the monochromator's input, there are an additional three light sources: A SiN IR source, a Quartz-Halogen bulb and a mercury calibration lamp for spectral calibration.

Light from the monochromator as well as the two broad-band sources is relayed into an integrating sphere. The sphere combines the light from the various sources and allows one of two sphere outputs to be viewed: A 50 μm pinhole or an open port. The open port provides the uniform illumination required for flat fielding the payload. The integrating sphere also includes reference detectors that monitor changes in source flux. The sphere output is selected by a flip mirror. Also viewable by this flip mirror is a cryogenic (~40 K) dark target used for dark testing.

The optical relay after the sphere is shown in Figure 20. The sphere is imaged by an F/24[4] parabolic mirror. There is then a fold mirror that acts as the fine steering mirror. This mirror will be tilted to provide closed-loop pointing control. There is then an aperture plate that defines the pupil of the system. The position of this plate ensures that a pupil image lands on M1 (the surface that defines the pupil in flight).

After the pupil plate, there is a pair of parabolic mirrors that expand the beam from 35.8 mm to 275 mm. At the intermediate focus, there is a wheel mechanism that allows a series of masks to be placed in the beam e.g. a grid of pinholes that can be used to simulate a dense star field. The design of the illumination module optics will be discussed further in section 6.2.

[4] Elliptical aperture, F/24 is the geometric average of the major and minor directions.

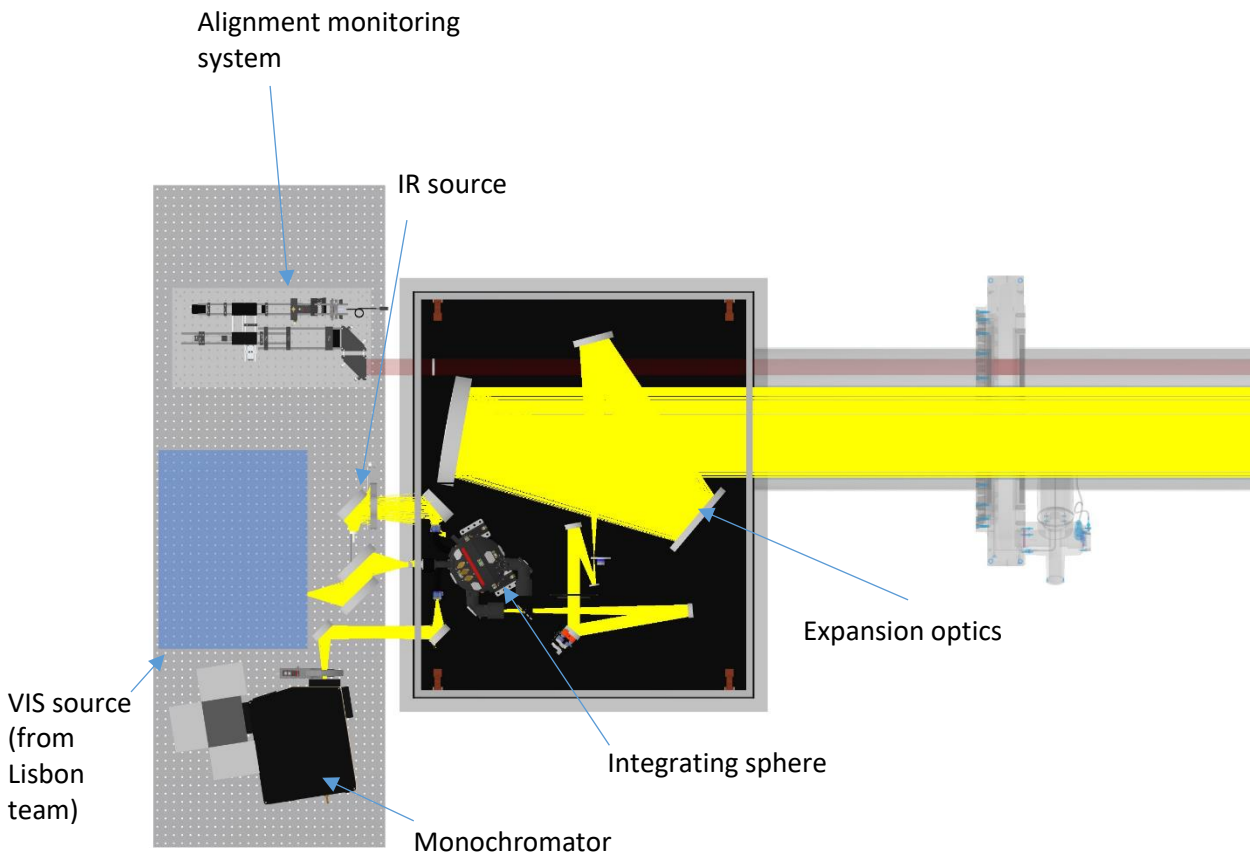

Figure 20: Illumination module design

Finally, the illumination module features an alignment monitoring system. This is an autocollimator-based system that simultaneously views two alignment targets. One in the illumination module, and the other on the payload. Using two detector channels, this alignment monitoring system is capable of simultaneously tracking changes in decentre and changes in tip/tilt. The design and test of the alignment monitoring system is detailed in section 6.3.

1.4.4 Periscope module

The output of the illumination module is then injected into the main 5 m test chamber. Unfortunately, the PLM line of sight does not point towards one of the chamber ports. This is primarily an artefact of old design but means that an additional OGSE module is required to redirect the incoming beam onto the payload primary mirror. The periscope also uses smaller (~ 2 inch) mirrors to redirect the alignment beam onto the payload alignment cube.

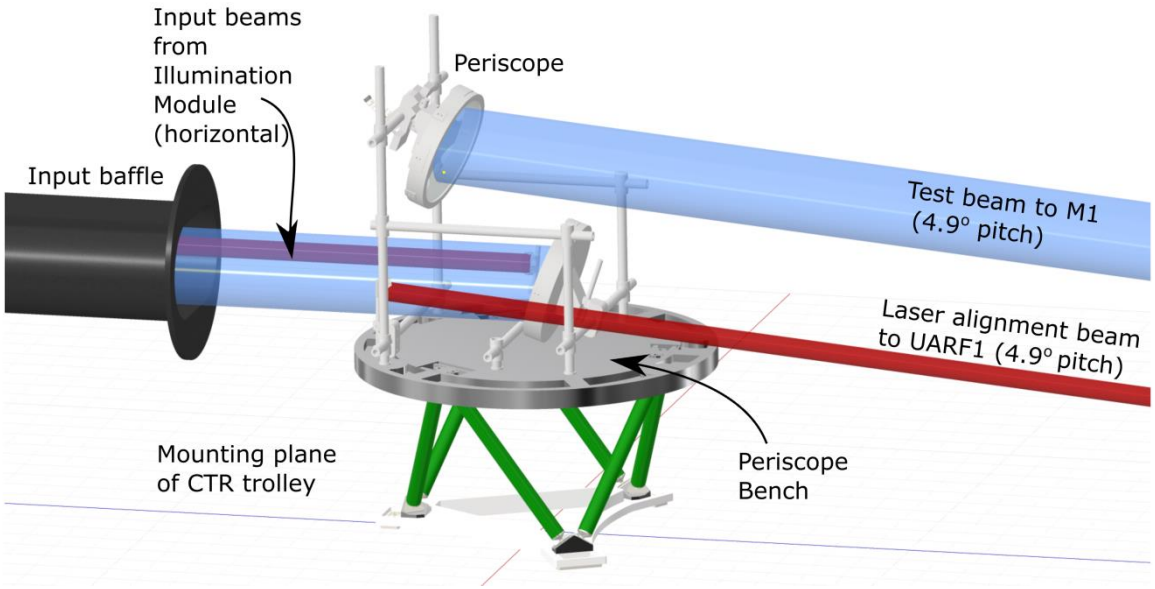

Figure 21: Pericope design [57].

1.4.4.1 The predecessor to the periscope – the target projector

The periscope uses ~30 cm flat mirrors to redirect the test beam. A previous iteration of the periscope, known as the target projector, expanded a smaller 22 mm illumination module output beam to produce a 275 mm (1/4 aperture) output. This used a pair of off-axis parabolic mirrors and many (~11) actuators to align the system and maintain focus during cooldown. The decision to move away from the target projector concept was primarily due to considerations of the alignment monitoring system. To constrain all of the degrees of freedom in the design, the alignment monitoring system was prohibitively complex (see section 6.1).

By modifying the illumination module such that it produces a 275 mm output, the target projector could be simplified to just become two flat mirrors with no cryogenic actuation. The periscope, therefore, became the baseline between PDR and CDR.

1.4.5 The beam expander

The OGSE beam expander [58] is the final module in the OGSE design. It sits within the PLM common optics during ground testing (Figure 9) and uses a pair of parabolic mirrors to expand the beam from ¼ sub-aperture to full aperture. This ensures the OGSE produces the correct diffraction-limited spot size at the focal plane. The need for the beam expander was primarily for programmatic reasons. During phase A/ B1, there was a need to reduce costs. Because of this, the decision was made to use a sub-aperture illumination of the payload [50]. Later it was discovered that the payload primary mirror deformation under 1g was so significant that a full aperture illumination concept would lead to an unusable spot on the focal plane [59]. Because of this sub-aperture illumination is desirable for most calibration products.

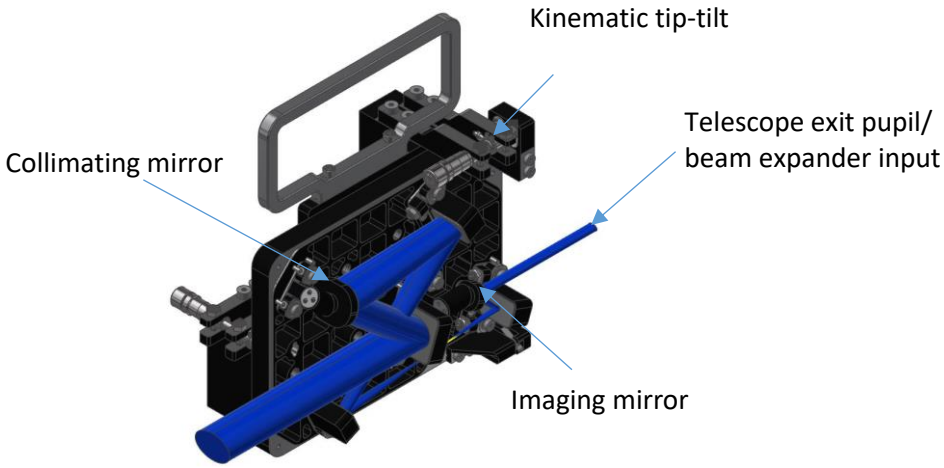

Figure 22: The OGSE beam expander [58].

The Illumination module, periscope, and beam expander, therefore, provide the full set of optical equipment required for the payload-level calibration of Ariel.

1.5 THESIS OVERVIEW

Ariel will lead to significant advances in the field of exoplanet science and is the driver of the Ariel design. However, to enable Ariel's ambitious scientific goals, detailed calibration is also required. The payload-level calibration of the Ariel is the subject of this thesis. The author has been majorly involved

in the development of the equipment to achieve this calibration, from the high-level system architecture down to the detailed design.

In Chapter 2, the payload ground calibration plan will be presented. This was created to define the methods the OGSE will use to calibrate the payload. These methods, in turn, drove design decisions within the OGSE system.

In Chapter 3, radiometric modelling work is presented to demonstrate the OGSE is consistent with simulating the range of stellar targets Ariel plans to view (GJ 1214 to HD 219134). Source designs will be presented to meet the bright target flux (HD 219134). However, for the monochromator, achieving an output flux brighter than the faint target proved challenging. This informed several improvements to optical relays including a reduction in the sphere size.

In Chapter 4, we assess the feasibility of one of the most challenging calibration measurements, the payload photometric stability test. End-to-end time-domain simulations of this measurement were produced to assess how various sources of uncertainty will contribute to this measurement. In particular, constraints were placed on the OGSE reference detector performance. Literature data was then used to assess the feasibility of detector candidates, as well as determine the thermal sensitivity of the detectors. A thermal control model will be presented to assess the achievable level of thermal stability.

In Chapter 5, we consider the OGSE thermal design. End-to-end simulations will be presented to assess how cold OGSE optics must get to test the payload dark current. FEA models will then be presented to assess the compliance of the illumination module thermal design. In addition to thermal emission, thermal stray light may also cause issues for testing the payload dark current. A model will be presented to assess the impact of thermal stray light from various surfaces within the test facility.

In Chapter 6 we consider the OGSE optical architecture. In particular, we consider, the feasibility of maintaining alignment of the PDR design over the vast (~210 K) range of operating temperatures. A trade-off study will be presented to simplify the alignment monitoring systems. This led to a major re-

design in the illumination module and target projector designs. The optical design for the new illumination module will be presented, as well as an analysis to demonstrate the design is capable of the various calibration functions.

In Chapter 6.3, the alignment maintenance system will be presented. This system monitors a pair of reference surfaces to ensure alignment between the illumination module and the payload. This work includes the full system development from requirement development, design, through to to build and test.

2 THE PAYLOAD GROUND TEST PLAN

To enable the Ariel science goals of characterising 500+ exoplanet atmosphere atmospheres, Ariel's performance must be verified on the ground. Moreover, calibration products must be developed to interpret and detrend Ariel's observation data. The role of the OGSE is to facilitate the payload level verification of Ariel's calibration and performance. The OGSE design is therefore driven by the calibration measurements it must make. In this section, we define the methods planned to be used to calibrate the payload. These methods are used to justify the design through the remainder of this document.

The tests planned at payload level are flowed down from the calibration requirements and the payload test matrix [55, 60, 61]. The payload calibration team specified the tests that are required to be conducted at different levels. It was the responsibility of the author to define how payload level calibration measurements would be made using the OGSE. In this chapter, an overview of the planned methods will be presented. It will also be highlighted where problems intrinsic to payload level testing prevent full verification. Full details on the payload test plan, created by the author, can be found in [62].

A few measurements are uniquely testable at payload level. These include optical ghosts, co-alignment, and out-of-band stray light[5]. There are many tests to verify calibration products derived at instrument level. These include measurements such as the noise performance, flat field, and non-linearity. The final class of measurements are those that are only available at payload level but are so compromised by the test conditions that either no verification is possible or only a qualitative sanity

[5] Out of band stray light is caused by spectral leaks, leading to light other than the design wavelength arriving at the detector.

check can be made. These include the payload point spread function, stray light and telescope to focal plane alignment verification.

2.1.1 Observation modes

The calibration methods discussed in this chapter are enabled by several observing modes and design features of the OGSE (Figure 20). These OGSE modes are listed in Table 2 along with a non-exhaustive list of calibration measurements the mode will be used for. The optical/mechanical design to achieve these modes is outlined in Figure 19 and described in detail in Chapter 6. Further details on the use of each of these modes will be provided in this chapter for each test.

The modes listed in Table 2 are not mutually exclusive and are, in many cases, used in combination with other modes listed.

Mode	Design feature	Example applicable test (not exhaustive)
Point source	50 µm pinhole	Point spread function (2.2.15)
Extended source	Open sphere port	Flat field (2.2.11)
Broad band mode	QTH and button heater broad-band sources	Photometric stability (2.2.5)
Monochromatic source	Grating monochromator	Wavelength calibration (2.2.14)
Rapid shuttering	Voice coil actuated, cryogenic, beam dump	Persistence (2.2.10), dark current (2.2.8)
Raster scanning	Fine steering mirror	Flat field (2.2.11)/ alignment
Source monitoring	Reference detectors mounted on the integrating sphere	Photometric stability (2.2.5) radiometric calibration (2.2.1)
Source modulation	Modulators at the source/ sphere input to allow testing across the full flux range of the payload.	Cross talk (photon noise limited frames required) (2.2.16)
FGS tracking mode	Short pass filter of the VIS source to illuminate FGS while the monochromator scans	Wavelength calibration (2.2.14)
Closed loop alignment maintenance	Closed loop pointing control using the fine steering mirror	All
Focal/ pupil masking[6]	Filter wheel at the pupil/ intermediate focus	Alignment

Table 2: OGSE calibration modes

In addition to the OGSE calibration modes, the payload readout modes also affect the calibration measurements that can be made at payload level. The payload uses quantum-well detectors that accumulate charge with time (Figure 23). The pixel charge is monitored at a fixed cadence through a series of Non-Distrutive Reads (NDR) (see [63]). After a defined exposure time, the detector is reset and the process repeats to create a series of star+planet exposures. To reduce the data volume, the payload decimates the NDRs (the decimation occurs in the Detector Control Unit (DCU)). One possible

[6] The requirement to have this is still to be confirmed

decimation method is Correlated Double Sampling (CDS) where the first and last NDR of each exposure are differenced to predict the slope of the ramp.

The decimated exposures are referred to as Science Frames (SFs) which are sent to the Instrument Control Unit for compression and storage. This then is converted to telemetry (TLM) for transmission to Earth. During ground testing, the payload data goes through the same decimation process, which has implications for certain calibration measurements and will be discussed later.

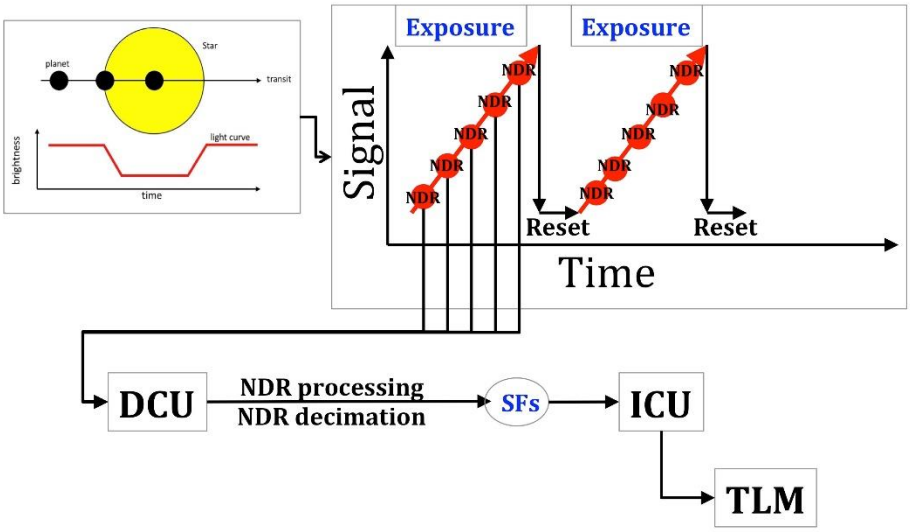

Figure 23: Schematic representation of the Ariel readout and data flow [63, 64]

2.2 PLANNED PAYLOAD-LEVEL TESTS

To motivate the OGSE design, the calibration functions must be defined. Here we will describe the various calibration measurements the OGSE will make and describe why those calibration measurements are necessary for exoplanet transit spectroscopy.

2.2.1 Radiometric calibration

The radiometric calibration provides the wavelength-dependent proportionality constant that relates the signal measured by the detectors (in digital units) to the spectral power incident on the Ariel primary mirror in units of e.g. $\mathrm{W\mu m^{-1}}$.

The radiometric calibration is primarily useful in eclipse retrievals. The measured eclipse flux ratio, ϕ, is given by: (see [65])

$$\phi = \left(\frac{R_P}{R_*}\right)^2 \left(\frac{F_p}{F_*}\right) \tag{2.1}$$

The radiometric calibration of Ariel gives a direct measurement of the stellar flux F_* enabling the planetary flux, F_p, and radius to be R_P retrieved from eclipse spectra.

The radiometric calibration also allows verification of the photometric channel band passes cut-on/ cut-offs.

2.2.1.1 Relative radiometric calibration

The Ariel radiometric calibration will be measured by injecting a known power and measuring the focal plane response. This is then repeated over the full wavelength range of the payload. To enable this, the point monochromatic source will be used (see Table 2, Figure 19). In this mode, we see a spot (as opposed to a spectrum) on all focal planes. By integrating across the focal plane, the total flux arriving at a focal plane can then be compared to the known power injected into Ariel to give the radiometric calibration.

The challenging part is knowing the spectral power injected into the payload with an uncertainty better than 5% (R-CAL-130). Effects such as changes in source temperature and humidity variations could cause the spectral power injected by the OGSE to not be repeatable to this level. For this reason, the radiometric calibration is planned to be traced back to calibrated reference detectors within the

integrating sphere. These reference detectors then measure the monochromator power at the same time we illuminate the payload.

The reference detectors within the sphere must also then be calibrated. It is planned this will be done during end-to-end testing of the illumination module (Figure 19). The output of the illumination module plus periscope will be re-imaged onto a thermal detector with a known spectral response (as verified by reflectance spectroscopy see [66]). The thermal detector measures the OGSE output power P_{out} in e.g. volts. The reference detector measures the sphere radiance S_{sphere}, also in e.g. volts. By taking the ratio of the OGSE output power to the sphere detector signal, the sphere detectors can be calibrated to predict the point source output power for a given measured signal $C_{point} \equiv P_{out}/S_{sphere}$. This calibration has arbitrary units and thus only provides the relative calibration with wavelength.

The reflectance spectra of a thermal reference detector act as the ground truth [66]. The sphere detectors are calibrated relative to the thermal detector and act as secondary calibration standards. The monochromator is then used to transfer the sphere detector calibration to the payload.

2.2.1.1.1 Beam expander throughput

The reference detection calibration C_{point} allows prediction of the OGSE output power, however, the beam expander within the payload will also impact the radiometric calibration measurement. A separate test setup (Figure 24) will be required to characterise the spectral throughput of the beam expander $\eta_{exp}(\lambda_0)$. By imaging the output of the monochromator onto a thermopile, the output power of the monochromator can be characterised (Figure 24). The beam expander can then be

inserted into the optical path[7]. The signal can then be re-measured by the thermopile. The ratio of signal with and without the beam expander present gives a direct measurement of the spectral throughput. The beam expander spectral throughput along with the OGSE output power provides all the information required to radiometrically calibrate the payload.

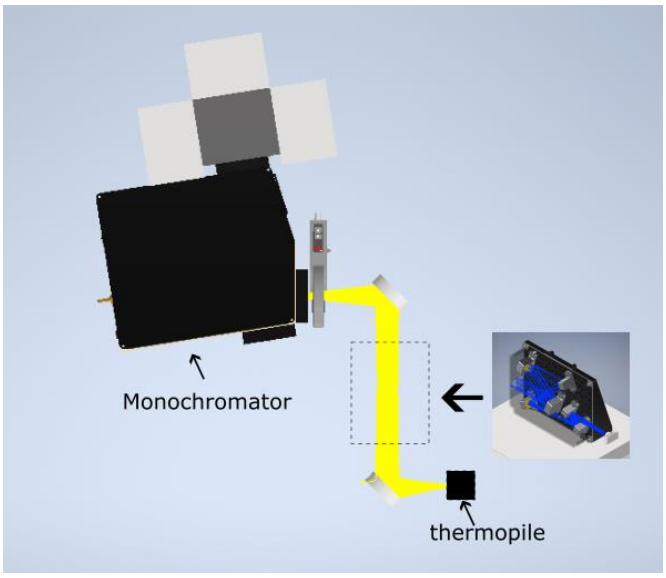

Figure 24: Beam expander spectral transmittance characterisation

The spatially integrated (in both x and y) Ariel focal plane signal, E, can be expressed as:

[7] Assuming the second mirror in the relay is sufficiently oversized to account for the beam expander magnification.

$$E(\lambda_0) = C_{point}(\lambda_0)S_{sphere}(\lambda_0) \times \eta_{exp}(\lambda_0) \times \eta_{ARIEL}(\lambda_0)\frac{\lambda_0}{hc}\, QE(\lambda_0)G(\lambda_0) \tag{2.2}$$

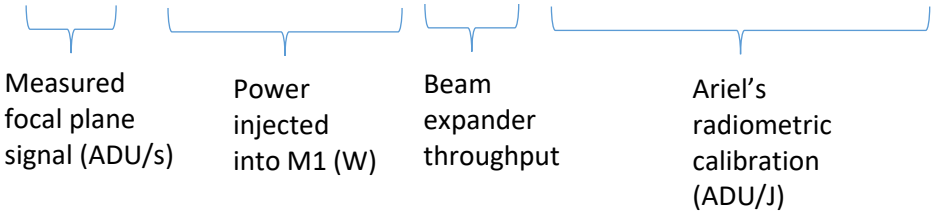

Where $S_{sphere}(\lambda_0)$ is the monochromator power as measured by the sphere reference detector at the monochromator wavelength λ_0 . C_{point} is the reference detector calibration η_{exp} is the throughput of the beam expander, η_{ARIEL} is the throughput of Ariel to a given focal plane, QE is the payload detector quantum efficiency, G is the gain of an Ariel detector. $R \equiv \eta_{ARIEL}(\lambda_0)\frac{\lambda_0}{hc}\, QE(\lambda_0)G(\lambda_0)$ is the wavelength-dependent proportionality constant between the input power and the measured signal. This defines the radiometric calibration. The radiometric calibration (in Arbitrary Digital Units per Joule [ADU/J]), R, is then tested using the following expression:

$$R(\lambda_0) = \frac{E(\lambda_0)}{C_{point}(\lambda_0)S_{sphere}(\lambda_0) \times \eta_{exp}(\lambda_0)} \tag{2.3}$$

For the relative flux calibration, we only require knowledge of the spectral dependence of R with no constraint on the absolute normalisation.

2.2.1.2 Absolute calibration

The absolute flux calibration is as described in section 2.2.1.1, except we now also care about the absolute normalisation of R. To get the absolute normalisation of R, we require absolute knowledge of the OGSE output power (in $\mathrm{W\mu m^{-1}}$).

To calibrate the absolute output power of the OGSE, the output of the OGSE can be imaged onto a small, calibrated sphere. Spheres are typically used for absolute power measurements as the power

measured by directly imaging onto a detector can be highly sensitive to the alignment of the output beam onto the detector. Spheres are also commercially available with traceable absolute radiometric calibrations[8]. No commercial calibrated sphere is known to cover the full Ariel wavelength, therefore, the OGSE output power will be measured at a small number of wavelengths in the visible and extended to other wavelengths using the relative calibration described in section 2.2.1.1. In this way, the absolute OGSE output power can be characterised over the full Ariel wavelength range.

2.2.2 System Figure of Merrit (FoM) (Throughput times QE)

For most of Ariel's targets, Ariel is designed to be a photon noise limited instrument. The noise floor is therefore set by the M1 collecting area, the throughput of the optics and the detector QE. Verification of the FoM (Throughput times QE) is therefore a partial verification of the payload noise floor. The FoM maps are also useful for detecting and removing dead pixels which can contribute excessive noise to science frames.

In many ways, FoM map generation is the same as the radiometric calibration described in section 2.2.1. Both rely on injecting a known power and measuring the focal plane response. However, for FoM map generation, the goal is to assess the responsivity of each pixel. During the radiometric calibration the point source is used, creating a spot on the instruments' (FGS, AIRS) focal planes. Each pixel, therefore, sees a different signal. To generate the FoM maps uniform illumination of the focal planes is required. To enable this, a flip mirror will be used to view an extended output of the integrating sphere (Figure 19). The monochromator will be used to provide the spectral information of the FOM.

[8] e.g. 7N6320A from Newport

Since the extended source is used, the OGSE absolute power calibration described in 2.2.1.2 is no longer valid and needs to be adapted slightly for FoM calibration. As before (in 2.2.1.2), to calibrate the output radiance, the OGSE output is imaged onto a calibration sphere. The calibration sphere directly measures the output power (W). The geometry of the imaging beam then needs to be known to convert the measured power to a measured radiance. The geometry can be precisely known using precision[9] focal and pupil stops. In this way, the OGSE output radiance can be known.

In the limit where the OGSE line width is narrow compared to the Ariel spectral resolution, the focal plane signal in each pixel, E_{pix}, (in ADU/s) can be evaluated using:

$$E_{pix}(\lambda_0) = C_{ext}(\lambda_0)S_{sphere}(\lambda_0)\eta_{exp}(\lambda_0)\eta_{ARIEL}(\lambda_0)A_{pix}\Omega_{fp}\frac{\lambda_0}{hc}\,QE(\lambda_0)G(\lambda_0) \qquad (2.4)$$

The focal plane signal in each pixel, E_{pix}, (in $\mathrm{ADUs^{-1}}$) is the measured quantity. $C_{ext}S_{sphere}$ is the output radiance of the OGSE ($\mathrm{Wm^{-2}sr^{-1}}$), λ_0 is the wavelength the monochromator is tuned to, A_{pix} is the effective collecting area of a focal plane pixel, Ω_{fp} is the solid angle subtended by the imaging collimator at the focal plane, η_{exp} is the throughput of the beam expander, η_{ARIEL} is the throughput of Ariel to a given focal plane, QE is the quantum efficiency of the payload detectors, G is the gain of an Ariel detector.

In this way, given knowledge of the payload pixel area and imaging F/#, the payload figure of merit $QE(x, y, \lambda_0)\eta(\lambda_0)$can be evaluated (Also required is knowledge of the detector gain $G(\lambda_0)$, this will be discussed in section 2.2.17). The FoM map then allows the photon noise floor to be quantified.

[9] <<10% error in area (G-CAL-130)

The pixel operability condition is defined in terms of the FoM map (as well as dark current and read noise criteria), by seeing if pixels fall below a FoM threshold, these pixels can be flagged and discarded from science operations.

2.2.3 Spectral stray light

Data from FoM/ radiometric testing can also be used to check for any spectral leaks in the payload. The payload uses a series of dichroics to spectrally separate the light from the telescope to the different focal planes. The prisms in Airs and FGS are also designed to illuminate each pixel with a narrow spectral band. Un-expected out-of-band transmission of dichroics can cause wavelengths other than the design wavelength to reach a detector.

When the payload is illuminated with the pinhole (Figure 19) and the OGSE monochromator, a signal is expected to be seen in a single spectral bin of the payload. If a signal is seen on other pixels/ detectors this can be attributed to spectral leaks or ghosts in the dichroic design. This is also a check for capacitive coupling between detector channels. If there is capacitive coupling between detector wiring, spurious signals can be seen at focal planes other than the one illuminated.

Testing the payload's out-of-band response does, however, place constraints on the spectral purity of the OGSE monochromator signal. OS filters will be used to attenuate higher-order ghosts. A FTIR will then be used to characterise the output of the monochromator to detect artifices in the monochromator output line shape. Artifacts could be e.g. due to higher diffraction orders, continuum scattering off the grating as well as the continuum thermal background. Dark frame subtraction will be necessary to correct for ambient thermal emission during this test (see section 3.5). The monochromator features a shutter at the input to enable this.

2.2.4 Spatial stray light

As well as spectral stray light there are spatial stray light effects that require characterisation. There are three classes of spatial stray light: (1) diffused light from the target under observation (2) scattered light from an off-axis star and (3) ghosts caused by partial reflections off payload optical elements.

The payload has required sizes for the focal plane spot sizes [67]. By integrating the flux outside this region, the diffused light can be compared to requirements constraining the diffused stay light. This is also a partial verification of the mirror surface roughness and particular contamination.

Scattered light verification is only a 'best effort' sanity check at payload level. The sub-aperture + beam expander configuration will likely change the stray light rejection properties of the payload. Because of this, it is only planned to verify near-field stray light sources ($\pm$ 140'). The OGSE beam is also only incident on the payload primary mirror. There is, therefore, no assessment of scattering off structural members such as the payload baffle.

Ghosts, on the other hand, can be fully validated at the payload level. Payload level is also the first time ghosts can be measured since they depend on partial reflections between the common optics dichroics and the instruments (see 1.2.2).

2.2.5 Gain drift variation

Ariel's driving science requirement is to detect atmospheric signals that are tens of ppm relative to the flux of the host star. Since transit depth measurements are relative measurements $\Phi(t_1) - \Phi(t_2)$, variations in the measured stellar signal directly correspond to uncertainty in the measured transit depth. Transits also occur on ~10 hr timescales. This means Ariel must not introduce variations in the stellar signal at the level of tens of ppm over long ~10 hr timescales (post-detrending).

Variations in the measured stellar signal can be caused by due to additive effects (e.g. dark current, read noise…), or variability can multiply the stellar signal (e.g. variations in the detector gain,

vignetting…). Meeting tens of ppm stability is a driving requirement for the payload and verifying this on ground was assumed to be a driving requirement for the OGSE design.

One class of variability that should be verified is the gain stability of the payload. In this context, gain drifts are defined to be any drifts that multiplies the signal. The challenge with verifying the gain stability is that gain variations are, by definition, degenerate with source flux variations. On ground, it is not possible to produce a source that is stable to the level of tens of ppm (~0.5% is typical). Therefore, variations in source flux must be monitored and corrected.

The method for verifying the payload gain stability is to perform a long (~10 hr) observation with the OGSE broad-band sources. The reference detectors on the sphere can then be used to correct for OGSE source variability. After correcting for source variability, any residual variability can be attributed to gain/ additive noise variations of the payload. Monitoring and correcting source variability to the level of tens of ppm over 10 hrs is expected to be extremely challenging. The feasibility of performing this correction is discussed in Chapter 4.

2.2.6 Additive drifts

In addition to multiplicative effects (gain/vignetting drifts), there are also noise sources that add to the stellar signal. These include detector read noise, dark current shot noise, thermal background shot noise etc. These effects must also be verified at payload level.

In all cases additive effects will be verified with the OGSE shuttered, with the payload line of sight pointed at a cryogenic beam dump. Due to Ariel's long wavelength (<7.8 μm) spectrometers, verifying payload additive noise sources implies the OGSE must be cooled to less than 70 K. It is the verification of the additive noise sources that drives the OGSE thermal requirements. In Chapter 5 end-to-end simulations will be presented to derive the OGSE thermal requirements, as well as analysis to show the OGSE will get sufficiently cold to test the payload dark current.

There are three classes of additive noise that can be distinguished at payload level:

(1) Noise that scales with integration time e.g. dark current shot noise, thermal emission shot noise etc.

(2) Noise that is independent of integration time and is spatially correlated across the detector array. E.g. from bias drifts.

(3) Noise that is independent of the integration time and is spatially uncorrelated across the detector array e.g. read noise.

The scaling of the above noise sources follows the representations in the Ariel noise model [68]:

$$Var\,(S) = N_{pix}\left[I_D \epsilon T + \left(\sigma_{rd}^2 + \sigma_L^2 + N_{pix}\sigma_b^2\right)N_{read}\right] \tag{2.5}$$

Where S is the measured signal in e^-, N_{pix} is the number of pixels integrated over, I_D is the dark current. Here I_D is interpreted as a generalised dark current that includes thermally liberated electrons within the detector as well as dark current caused by thermal emission from both the test environment and the instrument cavity. ϵ is an observational efficiency that accounts for dead time during resets. T is the observation time. $\sigma_{rd}^2$is the read noise variance, σ_L^2 is a generalised additive noise variance (assumed spatially uncorrelated), σ_b^2 is the bias noise variance. σ_b^2, σ_{rd}^2 & σ_L^2 are defined per pixel, per CDS read (see 2.1.1). The noise scaling defined by equation 2.5 will be used to distinguish different noise sources.

For CDS noise, it is required to produce noise maps with 5% accuracy (R-CAL-120). The CDS noise is measured from the standard deviation (σ) in a series of dark CDS reads. If N reads are measured, the uncertainty in the standard deviation is given by:

$$SE = \frac{\sigma}{\sqrt{2N-2}} \tag{2.6}$$

Therefore, if we want to measure the CDS read noise with an uncertainty of 5%, we require 401 reads. The CDS noise will likely also exhibit 1/f properties, with excess noise at long integration times (e.g. [69]). It is, therefore, desirable to verify the noise over the full range of saturation times between the bright to the faint target (up to ~1000 s). Due to time constraints, it is likely not possible to make 401

reads at the longest integration times (~1000 s). Therefore, it is planned to achieve the required 5% read noise uncertainty at the shortest integration time (10 Hz) and make lower fidelity maps at longer integration times. It is planned to use logarithmically fewer samples at longer time scales (Table 30). The resulting uncertainty in the measured read noise is shown in Figure 25. The predicted noise is shown with 20 $e^{-}pix^{-1}$ CDS noise (R-PRD-8812), 6 $e^{-}pix^{-1}$ additive noise (R-PRD-8811) and the shot noise that results from 0.1 $e^{-}pix^{-1}es^{-1}$ dark current (R-PRD-8813)[10]. Noise is assumed to be uncorrelated in time.

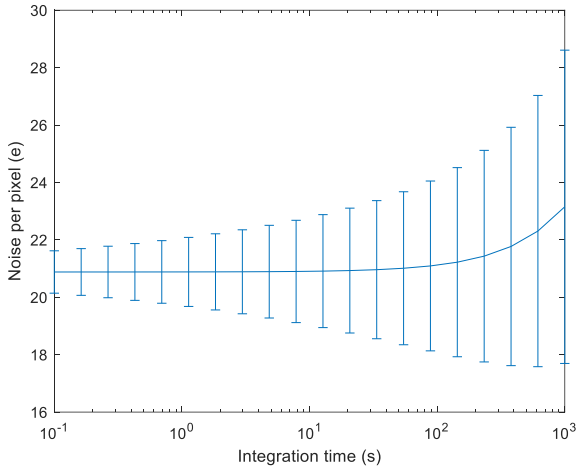

Figure 25: Measured noise vs integration time assuming white noise sources. Also shown is the uncertainty in measuring the detector noise when using the sampling shown in Table 30.

2.2.7 Bias drifts

It is useful to distinguish between spatially correlated (e.g. bias drifts) and un-correlated noise (e.g. read noise) since correlated noise can be corrected with reference pixels and non-illuminated pixels.

[10] Note these requirements are somewhat more relaxed for AIRS CH1.

This test allows quantification of the pre-correction bias drifts as well as an assessment of how effectively correlated drifts can be corrected using off-science/ reference pixels.

To assess the spatial correlation of the noise, the scaling of the noise with the number of pixels can be investigated. This follows the method planned for detector-level testing. A pair of dark CDS reads will be subtracted to generate a noise image[11]. A region of the detector will then be selected and the noise in this region of the detector will be summed. The analysis can then be repeated for different-sized regions on the detector to find the scaling of the noise with the number of pixels.

$$\sigma_{add}^2(N) = \sigma_{bias}^2 N^2 + \sigma_{read}^2 N \tag{2.7}$$

From this, one can estimate the relative contributions of bias noise and read noise to the dark timeline. To assess how well bias drifts can be corrected, payload pipeline steps [70]can be applied to the data (e.g. using off-science pixels, reference pixels, or temperature housekeeping data).

2.2.8 Pixel dark current

The dark current can also be verified from the dark sampling described in Figure 19. The required CDS, additive noise and dark current (R-PRD-8812, R-PRD-8811, R-PRD-8813) imply a noise of <23 $e^- pix^{-1}$ for a 1000 s integration. The dark current is required to be measured with an uncertainty less than the

[11] This measurement should be made at a sufficiently fast readout rate such that the read noise dominates over the dark current shot noise else this would manifest as an additional spatially uncorrelated term.

window mean dark current (100 $e^{-}pix^{-1}$)[12]. Therefore, the dark current verification comes for free when performing the long (1000 s) ramps during the CDS measurement.

It is, however, still to be seen how dark the test facility will be. In section 5.3 thermal stray light analysis will be presented to quantify this effect.

2.2.9 Random telegraph signal

Another contribution to the payload noise budget is the Random Telegraph Signal (RTS). RTS causes stochastic variations in signal between discrete levels. Such discrete jumps would manifest as photometric errors in the star/planet signal if not corrected. RTS can be seen as discrete jumps in the dark time series (see Figure 26). To identify which pixels experience RTS, a detection algorithm must be created. A Gaussian fitting method (Figure 27) such as the one presented in [71] is preferred as this allows the different signal levels to be immediately extracted from the fit.

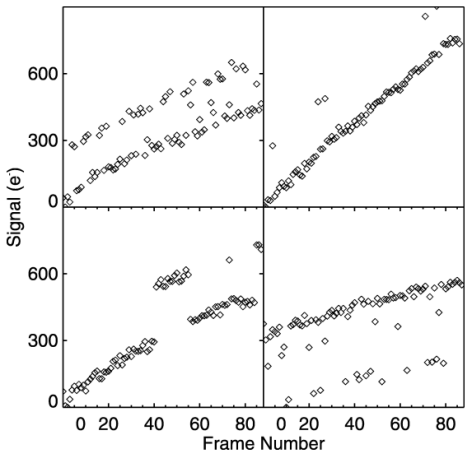

Figure 26: Examples of different types of RTS found in ROICs (from [72]).

[12]Except for Airs CH1 where the mean dark current is 1000 $e^{-}pix^{-1}$, with a measurement uncertainty of 41 $e^{-}pix^{-1}$

At the time of writing it is not clear if up-the-ramp data will be accessible during payload level testing. In flight, up-the-ramp data is decimated to produce CDS science frames. It is to be confirmed whether or not the un-decimated up-the-ramp detector will be accessible during calibration. This test is likely to be the most strongly impacted if only the decimated CDS frames are available. It will strongly impact our ability to detect stable-stable transitions such as the one shown in the bottom left quadrant of Figure 26. If this were decimated, we would only see a spike when the ROIC transitions from the lower to the upper state and a downward spike when the ROIC transitions back to the lower state. Only being able to see the spikes will also make extracting the time constants of the traps significantly more challenging.

Moreover, for a two-level system, CDS decimated data will produce 3 superimposed Gaussians compared to two when the detector is read up the ramp. One Gaussian will be associated with the reads where no transition occurs (lower – lower or upper - upper), one Gaussian will be associated with transitions to the upper state, and one Gaussian will result from de-excitations from the upper to the lower state. Qualitatitifuly, a two-level system such as the upper left plot in Figure 26 will look like the three-level system shown in Figure 27. This has two consequences: (1) symmetric 3-level systems may be hard to distinguish from 2-level systems. (2) The fit developed in [71] will need to be adapted such that we are fitting pairs of symmetric Gaussians.

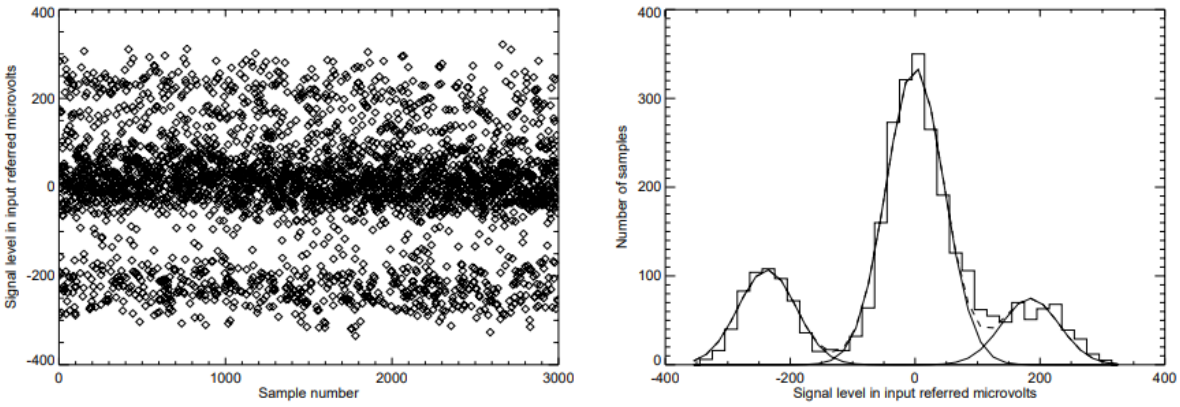

Figure 27: Example of the RTN detection using Gaussian fitting from [71]. This is shown for an RTN signal with 3 energy states.

2.2.10 Persistence

Another effect that can cause photometric drifts is persistence. This is of particular concern if Ariel performs a long (e.g. 10 hr) observation of a bright target followed by a faint target. Charge traps could de-excite during the faint target observation causing a spurious photometric drift.

Persistence is known to depend strongly on both the fluence, but also the soak time (the time before the detector is reset after being illuminated) [73]. It is therefore important that any persistence measurement is representative of not only the fluence but also the stare time on a target.

To ensure the measurement is sensitive to all charge traps with time constants within the Ariel frequency range (R-PRD-0470), each persistence measurement will need to have a stare of ~10hr followed by an extended dark[13]. The time needed to make persistence measurements is therefore not insignificant. It is for this reason that it is proposed to use the OGSE broad-band light sources to illuminate all channels simultaneously. This means that during the payload level persistence check, the fluence will not be the same for all pixels. However, the broad-band illumination will enable the full illumination of the focal plane arrays.

The worst-case persistence measurement, to represent a change in stellar target, would be to illuminate the pixels for ~10 hrs in the OGSE bright modes whilst the detectors are read out in the CDS mode (as they would be during science operations) followed by a dark observation. This would resemble the MCT persistence measurements made by Tulloch et al [73] shown in Figure 28 below.

[13] Until the persistence signal reached below 1% of the faint target

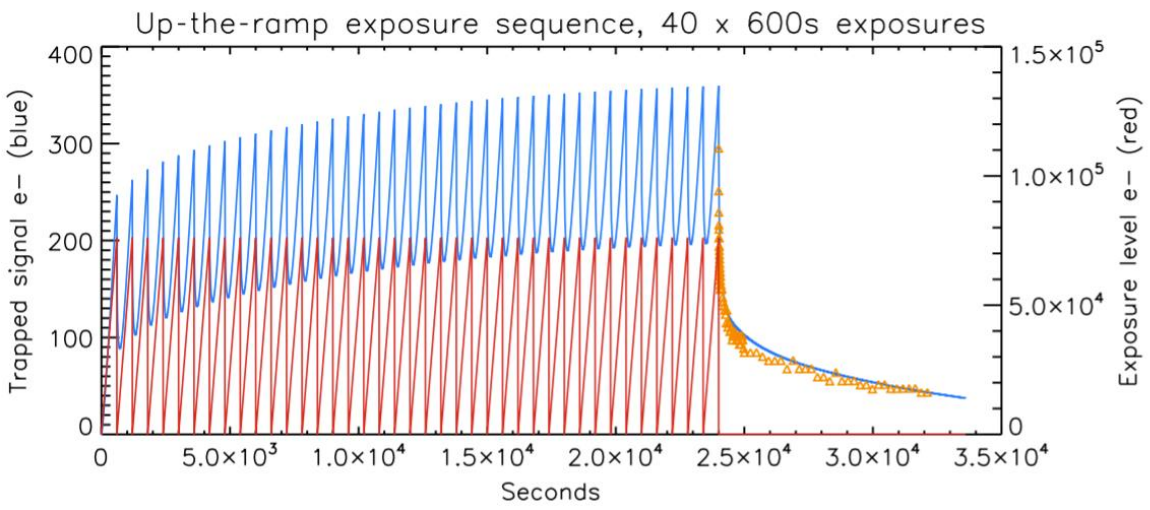

Figure 28 Comparison of the persistence model with an actual series of 40 up-the-ramp exposures of 600 s to a level of 75 ke⁻. Data taken with ERIS 5.3-µm detector. This test probed the model behaviour in a regime where very long-time constant traps contained significant charge. Figure from [73].

After shuttering the sources, the persistence drift will be observed. The correction, CAL_PERSIST (derived at lower-level testing), can be applied to the data. The residual variability can then be compared to 1% of the faint target. This checks that the CAL_PERSIST derived at lower levels can correct persistence to the required level.

For the OGSE, the key implication of the persistence measurement is the need to shutter the output on a timescale short compared to the focal plane integration time. This is challenging with the piezo actuators typically used at cryogenic conditions. To achieve this, a cryogenic voice coil actuator-based shutter mechanism was developed and is discussed in section 6.2.4.1.

2.2.11 Jitter susceptibility / Flat field

Jitter susceptibility is the final part of the noise budget to be verified at payload level. For Ariel, the primary reason for flat fielding is to reduce the impact of pointing jitter. The flat field and jitter susceptibility calibrations are, therefore, grouped. Pointing jitter is of concern if it leads to photometric variability in stellar signal at the level of tens of ppm. Pointing jitter does not, by itself, cause photometric variations. However, photometric variations can be introduced if the pointing jitter

causes vignetting or causes the spot to move onto pixels that are more or less sensitive. The role of the flat field is therefore to remove pointing correlated photometric variations. Two methods are planned for this (1) rastering a spot over the focal plane to directly measure pointing dependent flux variations and (2) uniformly illuminating the focal plane to measure the flat field response of the payload.

2.2.11.1 Intensity as a function of pointing

The baseline method for doing the flat field is to measure the focal plane intensity as a function of pointing. This method of extracting the underlying flat field from the intensity as a function of pointing is expected to closely resemble the methods for flat fielding done in-flight, further details of which can be found in [74] and references therein.

2.2.11.2 Extended source

The OGSE also plans to produce flat illumination of the focal planes. This follows the flat field method typically done at detector level [75]. Producing flat illumination at payload level is, however, complicated by the payload prisms. If the OGSE illuminated the payload with a broad-band source a spectrum would be seen at the focal plane – not a flat illumination. To produce flat illumination, the monochromator can be used. When the monochromator and the extended source are used a top-hat intensity distribution can be generated at the focal plane (simulations of this are presented in 3.4.3.2).

The top hat is centred on the nominal wavelength solution of the monochromator output wavelength. A flat field over this illuminated region can then be extracted. The top-hat extent is, however, limited by the size of the spectrometer slit and does not allow the full focal plane to be flat fielded at once. Therefore, only local flat fields can be generated using this method. By scanning the monochromator, the top hat can be shifted along the spectral direction to allow other parts of the detector to be flat-fielded (see Figure 44).

2.2.12 Pixel linearity correction and saturation

Ariel will use MCT detectors at its focal planes. These do, however, exhibit a non-linear flux dependence. This means that the rate of increase of the measured signal depends on the number of electrons that have been released since the last reset. The cause of this non-linearity is that the capacitance between the p-n junctions of the detector is dependent on the bias voltage (which increases during an integration). Further details on the theory behind this effect can be found in [76].

The consequence for science is to introduce a flux-dependent systematic, leading to uncertainty in the measured transit depth. However, [77] demonstrated that non-linearities will have a negligible effect on the spectra if non-linearities are corrected to a few per cent. For this reason, the OGSE is required to verify the payload non-linearity to better than 1% (R-CAL-040).

To sample the full pixel well depth without saturating any part of the detector it will be necessary to do this measurement using the OGSE monochromatic source. When the monochromator is operated with the extended sphere output a top-hat intensity distribution is seen at the focal planes (Figure 44). If this were done with the OGSE broad-band light source, pixels close to the OGSE source black body peak would saturate before others reached close (~ factor of 2) of their full well depth.

The typical method for measuring non-linearity is to observe it directly in the detector ramps (e.g. [78]). However, at the time of writing it is not clear if up the ramp data will be available due to decimation in the DCU. If available, up-the-ramp voltages can be used to directly observe non-linearity. Any curvature in the ramp can be used to derive a non-linearity correction. Source flux variation could also impact this measurement, however, at the level of 1% (R-CAL-040), this should not be an issue. If required, the OGSE reference detectors can be used to correct source changes.

If up the ramp data is not available plane integration times can be varied (e.g. [79]). By plotting the measured signal vs integration time and applying a polynomial fit a non-linearity correction curve can be derived.

The saturation thresholds are then immediately obtained from the non-linearity curves. For Ariel, saturation is defined as the signal (in ADU) where a pixel's linearity deviates by more than 5%. The saturation thresholds allow verification of the pixels' full well depth. Saturation data will also be used in the pipeline to flag saturated pixels.

2.2.13 Relative Pointing offset

To verify the co-alignment of the instrument channels, spot centroids will be measured. R-CAL-110 requires the OGSE to verify the co-alignment of instrument channels to 1/10th pix. To centroid in the spectral direction to 0.1 pix, it will be useful to produce a spot as opposed to a spectrum on all focal planes as the centroid of a spectrum will depend on the SED shape, knowledge of which may limit the precision of the measurement. The use of the monochromatic source to produce spots that can be centroided is therefore preferred.

Pointing stability is, however, a significant concern for the co-alignment measurements. In VISPhot (the focal plane with the largest f#), 1/10th pix corresponds to 40 mas at M1. A method that involved illuminating one channel, measuring the centroid, followed by another channel would require the OGSE test beam to remain stable to ~40 mas. This would imply sub-micron positional stability across the different modules – likely impossible. Therefore, a method that provides a spot on each channel simultaneously is likely critical to achieve this level of co-alignment.

The method of achieving simultaneous, pairwise, illumination of focal planes (and hence the coalignment) is different for the spectroscopic and the photometric planes:

- To measure the coalignment of the spectroscopic channels, we intend to use the spectral overlap between the spectroscopic channels defined in R-PRD-0400. This guarantees spectral overlap between 1.75 to 2.10 µm between the NIRSspec and AIRS CH0 and overlap from 3.65 to 4.00 µm between AIRS CH0 and AIRS CH1 (see [80]).

- To measure the coalignment of the photometric channels the broad-band VIS source can be used to produce spots on all the photometers.
- To measure the coalignment between the photometric channels and the spectroscopic channels, the VIS source can be short-pass filtered to produce a spot on VISPhot whilst the monochromator produces a spot on AIRS CH0.

By enabling simultaneous illumination, the pointing stability concern is mitigated by design.

For all focal planes, the centre of the field of view must be defined. This can either be defined by a central pixel index, or by rastering the OGSE source until it vignettes at the edge of the FOV (e.g. on the spectrometer slits). Once the OGSE spot is centred with respect to one channel, the simultaneous illumination methods described above can be used to generate a spot on a second focal plane. The centroid of the spots can then be measured to determine the alignment offset between channels.

It is also planned to verify the co-alignment as a function of temperature. This will be tested by ramping the PIP simulator temperature between the warm and cold interface temperature limits (243-293K; R-CTR-0360 [81]).

2.2.14 Wavelength calibration

During science operations, the observable quantity is the flux landing on each focal plane pixel. To enable comparison of the measured spectra to compositional spectral libraries, a mapping must be created that defines the wavelength solution of each pixel.

To perform the wavelength calibration the OGSE monochromator will be used (Figure 19). The monochromator takes 3 sources as an input. A mercury lamp to initially calibrate the monochromator and two broad-band sources that will provide continuous coverage over the full Ariel wavelength range. The mercury lamp provides spectral emission lines at known wavelengths. However, these lines only extend out to 600 nm, to calibrate beyond this in the IR, higher diffraction orders can be used.

These emission lines will be used to calibrate the turret angle as a function of output wavelength. Once the turret is calibrated, the broad-band inputs will be used to illuminate Ariel.

The wavelength calibration of the payload is made by measuring the position of the spot when the payload is illuminated by a source of known wavelength. The spot position can be measured to sub-pixel accuracy by centroiding the PSF.

As with the co-alignment, pointing drifts pose a challenge when measuring a series of spot centroids. Ariel uses spectrometer slits that are large compared to the PSF of the star. This means the wavelength solution depends on the pointing of the payload. Achieving sub-arcsecond pointing stability during the wavelength calibration is expected to be extremely challenging and likely is not possible. To help detrend any pointing variations during the wavelength calibration, the OGSE VIS broad-band source can be run with a short pass filter (~1 µm cut-off) that enables VISphot to monitor pointing variations simultaneously to the monochromator spectral scanning operation. The mechanism to achieve this filtering is described in section 6.2.4.3.

The OGSE can also be raster scanned to verify any spatial dependence of the wavelength solution (smile/keystone characterisation).

2.2.15 Spectral Resolutions/point spread function

To enable the detection of molecular features in exoplanets atmospheres, the payload is required to have a spectral resolution between R>15 to R>100 across the spectroscopic channels (PRD-0425, PRD-0421). The payload uses spectrometer slits that are large compared to the PSF of the star meaning the spectrometers are essentially slitless. Because of this, the spectral resolution of the detectors is limited

by the PSF size. By illuminating the payload with the point monochromatic source the spot size can be measured. In the spectral direction, the spot size is a direct measurement of the spectral resolution[14].

This test is, however, significantly impacted by the payload level test configuration. This test is likely only useful as a qualitative verification with the sub-aperture OGSE. This is for four reasons:

1) The sub-aperture OGSE will under-sample the Ariel WFE so will provide a non-conservative assessment of the PSF/ spectral resolution.
2) During payload level testing the payload line of sight is almost horizontal. Under these conditions, the 1g-induced aberrations on the payload primary mirror dominate the PSF.
3) Every effort will be made to verify the OGSE spot size in cryogenic conditions. This is, however, an extremely challenging verification. The achievable precision is still to be confirmed. In the event a non-compliant PSF is seen, it may not be clear if this is a payload or OGSE effect.
4) The sub-aperture/ beam expander means any vignetting-induced aberrations may not be seen.

2.2.15.1 FGS centroiding

Payload level teasing would also be the ideal time to verify the FGS centroiding performance. In particular, verifying the centroiding performance on the Ariel PSF. However, as noted, the PSF will be significantly different on ground vs in flight. Therefore, to validate the FGS centroiding algorithm, a series of masks could be placed at the OGSE pupil/ intermediate focus to change the spot shape. The centroiding consistency between the FGS channels will then be assessed for each PSFs.

[14] The OGSE source will have a spectral resolution >2x the payload spectral resolution to minimise spectral broadening caused by the non-zero OGSE spectral width.

2.2.16 Crosstalk

In addition to optical aberrations, crosstalk can also cause broadening of the observed spot. The method presented here follows that presented in [82]. The method requires faint, photon noise limited, illumination of the focal planes. The plan is to look for spatial correlations in the photon noise. In the absence of any cross-talk, any photon noise should be spatially un-correlated, when cross-talk is present the capacitive coupling between pixels causes a spatial smoothing of the photon noise. This spatial smoothing can be seen by measuring the autocorrelation of the detector when illuminated using a diffuse source in the photon noise-limited regime.

$$h[x,y] = \mathcal{F}^{-1}\left\{\left[\frac{\mathcal{F}\{R_D[x,y]\}}{2\sigma_N^2}\right]^{\frac{1}{2}}\right\} \tag{2.8}$$

h is the cross-talk response function, R_D is the autocorrelation of the photon noise frame D. The photon noise frame, D is the difference between two focal plane images. σ_N^2 is the variance of the photon noise which should be calculated using:

$$\sigma_N = \frac{1}{2}\sum_{i,j} R_D[i,j] \tag{2.9}$$

As an additional check, hot pixels can be used to verify cross-talk. Crosstalk would cause signal in hot pixels to couple to neighbouring pixels. This can be directly measured with payload dark frames.

When the extended source is used, the focal plane flux is greatly increased (~100x see 3.4.3.1). However, this test requires faint, photon noise-limited frames. The OGSE source is expected to be stable to ~0.5%. We therefore must ensure that the photon noise floor is larger ~0.5%. The fluence, therefore, needs to be less than ~4×10^4 electrons per read. The implications of this are discussed in 3.4.3.1.

2.2.17 Pixel gain

The method planned to derive the cross-talk maps also immediately provides the detector gain. The detector gain will likely not form a part of the payload data retrieval pipeline. It is however a useful parameter in determining spectra error bars since it allows the photon noise floor to be predicted from the measured signal. The gain allows the measured signal (in ADU) to be related to the number of photons detected by the MCT. The number of detected photons allows quantification of the photon noise. Therefore, the detector gain allows the measured signal to be related to the measurement noise floor.

The method described in 2.2.16 allows the photon noise, σ_N, to be directly calculated. Since photon detection is a Poissonian process, the number of detected photons can be calculated from the noise variance. The ratio of the measured signal (in ADU) to the number of detected photons gives the amplification gain in ADU/e^-.

Using the method described in 2.2.16 to evaluate the detector gain avoids a common source of error. [82] highlights the impact of crosstalk on gain measurements. Capacitive cross-talk leads to a spatial smoothing of the photon noise, leading to a reduction in the measured photon noise. This leads to an overestimate of the gain. An e.g. 1% crosstalk would lead to a 4% noise attenuation and result in an 8% overestimate in the gain per pixel.

2.3 CONCLUSIONS

In this chapter, the plan for payload-level calibration was defined. These calibration tests act as the top-level performance requirements of the OGSE. In the vast majority of cases, complete verification of instrument-level calibration produces can be derived. In some cases, quantities only measurable at payload level are obtained such as the end-to-end radiometric calibration, instrument co-alignment and ghost verification. In other cases, limitations of the payload level test setup limits meaningful verification. This includes the telescope to focal plane alignment, PSF and out-of-field stray light.

Testing of these quantities would only be feasible with a vertically orientated payload, a full aperture OGSE and no beam expander. Programmatic constraints prevent such a design.

The tests and methods described here have many design implications for the OGSE. The implications of the calibration measurements and methods will be explored in subsequent chapters. In Chapter 3 end-to-end radiometric simulations will be presented to simulate illumination conditions during calibration measurements. In Chapter 4 the implications for the gain stability test will be discussed. In Chapter 5, the requirement to verify the payload dark current will be used to determine the OGSE thermal requirements and design. Chapter 6 presents the optical design necessary to perform these measurements.

3 MEETING THE PAYLOAD FLUX REQUIRMENTS

Ariel is designed to view all stellar targets with fluxes between HD 219134 and GJ 1214. The Ariel OGSE must be able to test the instrument across this flux range. Achieving these bright fluxes through a 50 µm pinhole[15] has many consequences for the illumination module design which will be explored here.

In this chapter, I will show how fluxes for the Ariel stellar targets were flown down requirements on the source relays. Designs of these relays will be presented. To assess the performance of these designs, a monochromator radiometric model was created. This model includes effects such as out-of-band radiation. The output of the OGSE model was then combined with the payload end-to-end simulator to predict the focal plane signals during ground calibration.

It will be shown that the monochromator flux was non-compliant compared to Ariel's faintest target (GJ 1214). Because of this, it is desirable to reduce the sphere size from 30 cm to 15 cm. However, this has implications for the flat fielding performance of the OGSE. A tradeoff will be presented that balances the output flux against the output uniformity.

The work presented in the chapter summaries work created for multiple documents. The requirement derivation and optical design is reported in the OGSE design description and OGSE requirements document ([51, 83]). The sphere radius tradeoff is reported in [84]. The monochromator radiometric model is in preparation and will be reported in [85].

[15] A 50µm pinhole is required to ensure the image of the pinhole is small compared to the telescope point spread function.

3.1 THE BRIGHT AND FAINT STELLAR TARGETS

The goal of this analysis is to determine the OGSE source power required to test the payload. To determine the required OGSE source power, the stellar targets must be flowed to a requirement on the OGSE optics. It is not practical to generate a spectral flux that matches that of a star on ground. A QTH bulb, for example, produces a colour temperature close to HD 219134 in the visible, however, the silica glass bulb is opaque in the IR. Therefore, it is necessary to use two light sources: One in the visible and a second source in the IR. Each source will produce the correct band-averaged flux but will not match the spectral shape of the star (see Figure 29). To cover the full wavelength range of the payload the IR source is designed to cover 1.95 µm-7.8-µm. The VIS source is designed to cover 1.95-0.5 µm. These match the Airs and FGS bands respectively.

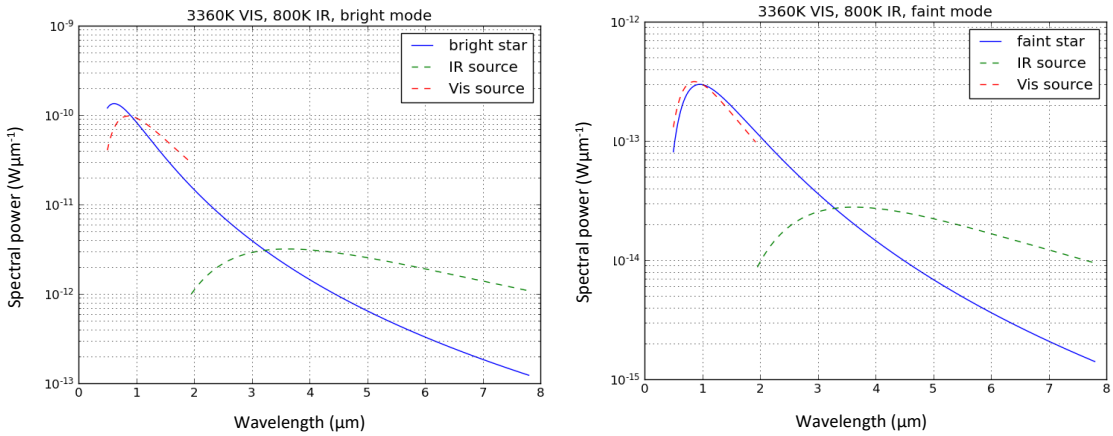

Figure 29: OGSE spectral power in the bright (left) and faint (right) observing modes.

The flux requirements are most stringent for the pinhole point source (Figure 19), so the point source will be focused on here. The flux from the extended source is described in section 3.4.3. Light leaving the sphere through the 50 µm pinhole is collimated by a parabolic mirror with an elliptical aperture. The mirror has an F/# of 19.57 and 29.43 in the major and minor directions respectively. We require the power collected by this mirror to match the power collected by Ariel when viewing a target star. Quantitatively, this can be written as (also accounting for the throughput of the OGSE):

$$A_{pin}\Omega_{col}\int_{\lambda_1}^{\lambda_2}\eta_{spr}L_{sphere}d\lambda = A_{M1}\Omega_{star}\int_{\lambda_1}^{\lambda_2}B(T_{Star},\lambda)d\lambda \quad (3.1)$$

A_{pin}, is the area of the pinhole at the output of the integrating sphere, Ω_{col} is the corresponding solid angle of the collimator that views the sphere output, η_{spr} is the optical efficiency of the sphere to Ariel relay optics (plus the beam expander), L_{sphere} is the sphere radiance, $B(T_{Star},\lambda)$ is the black body radiance of a star of temperature T_{star}. The right-hand side is the stellar flux (W).

Given knowledge of the sphere reflectivity, ρ, port fraction, f and the sphere surface area, the required sphere radiance can be used to determine the required injected source power Φ_i (see [86]).

$$L_{sphere} = \frac{\Phi_i}{\pi A_{sphere}}\frac{\rho}{1-\rho(1-f)} \quad (3.2)$$

Equation 3.1 determines the required sphere radiance for a given stellar target. In turn, 3.2 determines the sphere input power required to meet that sphere radiance. The final step is to define the input power in terms of the fundamental properties of the source:

$$\Phi_i = \eta_{sor}\varepsilon_{source}B(T_{source},\lambda)\,A_s\Omega_s \quad (3.3)$$

Where A_s is the source emitting area and Ω_s is the corresponding solid angle at the source, ε_{source} is the emissivity of the source. The factor of η_{sor} accounts for any optical losses between the source and the sphere.

Combining equations 3.1, 3.2 & 3.3 yields the following expression:

$$A_{pin}\Omega_{col}\int_{\lambda_1}^{\lambda_2}\eta_{spr}\frac{\eta_{sor}\varepsilon_{source}B(T_{source},\lambda)\,A_s\Omega_s}{\pi A_{sphere}}\frac{\rho}{1-\rho(1-f)}d\lambda = A_{M1}\Omega_{star}\int_{\lambda_1}^{\lambda_2}BB(T_{Star},\lambda)d\lambda \quad (3.4)$$

If we make the simplifying assumption that the source emissivity, the mirror throughput, and the sphere reflectivity are independent of the wavelength over the spectral band of interest (0.5-7.8 μm), then the following figure of merit (FOM_{source}) can be defined for the sources:

$$FOM_{source} \equiv \eta_{sor}\varepsilon_{source}A_s\Omega_s = \frac{\pi A_{sphere}A_{M1}\Omega_{star}\int_{\lambda_1}^{\lambda_2}B(T_{Star},\lambda)d\lambda}{A_{pin}\Omega_{col}\eta_{spr}\int_{\lambda_1}^{\lambda_2}B(T_{source},\lambda)d\lambda}\frac{1-\rho(1-f)}{\rho} \quad (3.5)$$

Using equation 3.5, the source figure of merit FOM_{source} can be calculated. This, however, depends on the source temperature. The VIS source is being delivered by the Lisbon team. They plan to use a QTH bulb with a colour temperature of 3360 K. For the IR source, it is planned to use a blackbody heater (see section 3.1.1). The temperature of which is free to tune. To minimise the dynamic range across the focal planes, 800 K was nominally selected as the source temperature as it delivers the maximally flat spectrum across the AIRS wavelength range (Figure 29).

All remaining parameters on the right side of equation 3.5 are constrained by other considerations. A_{sphere} is constrained by output uniformity considerations. The product $A_{pin}\Omega_{col}$ is constrained by image radius requirements. In this way, the requirement on the source figure of merit was defined (Table 3).

Three things are apparent from Table 3: (1) the large (10^{-5}) etendue requirement implies low F/# optics will be required to meet the bright target case (especially for the IR source) and (2) a large dynamic range of fluxes are required to modulate down to the faint target case (114 times for the IR source and 311 times for the VIS source). Finally, the bright VIS mode produces a significant thermal load on the sphere/ optical bench (~2.4 W). At the time of SRR, it was planned that the optical bench would be radiatively cooled. This was to minimise the micro vibrational coupling between the cold head and the optical bench. However, to dissipate the load from the VIS source alone, the radiator would have to be >3 m^2. The thermal design of the illumination module is discussed further in section 5.2.

Observing mode	Integrated sphere radiance ($Wm^{-2}sr^{-1}$)	Figure of merit (Source relay etendue times throughput times source emissivity) (m^2sr)	Thermal loading on the sphere (W)
Faint IR	0.0847	3.89×10^{-7}	0.0029
Faint VIS	0.230	3.39×10^{-9}	0.0078
Bright IR	9.69	4.47×10^{-5}	0.33
Bright VIS	71.5	1.05×10^{-6}	2.42

Table 3: Sphere radiance integrated across the source spectral band (7.8-1.95µm or 1.95-0.5µm), source figure of merit and source thermal load.

3.1.1 IR source design

The IR source is based around an Al_2O_3 button heater. This uses heritage from the HIRLDS calibration facility[87]. The button heater is a 1-inch diameter thermal emitter with a surface temperature of up to 1200 degrees. The design presented in this chapter is the evolution of the original preliminary design prepared by Rory Evans [51]. The design at PDR had the button heater in the vacuum chamber and a single ellipsoidal mirror that relays the button heater light directly to a light pipe at the entrance of the sphere (Figure 30– left). At CDR the button heater was moved outside the chamber and a pair of parabolic mirrors were used to relay the button heater light into the light pipe (Figure 30– right). The main reason for the design update was to simplify the design. The PDR concept required multiple temperature zones in the vacuum chamber (ambient and 70 K optical benches), liquid cooling of the source as well as a custom vacuum-compatible aperture/shutter mechanism. Moving the source outside the chamber greatly simplifies the thermal design as well as enabling off-the-shelf optics & mechanisms to be used.

The original reason for having an IR source close to the sphere is the need for a high etendue relay. The goal of the re-design is therefore to provide a simplified design that delivers comparable throughput.

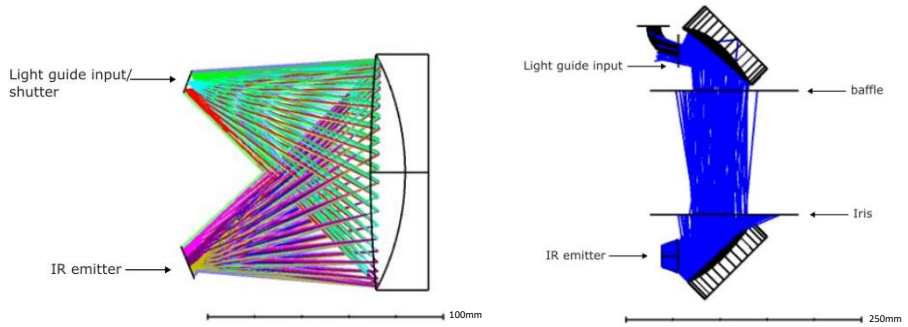

Figure 30: IR source design. Left shows the design proposed at PDR (light pipe not shown) [51]. Right shows the design prepared in advance of CDR.

A non-sequential model was created using the Zemax™ optical design and modelling software to assess the geometric throughput of this updated design (Figure 30 – right). The simulation used 10^7 photons which were isotropically emitted from the surface of the IR button heater over the full π sr hemisphere and across the full 1 inch aperture. Six percent of these photons arrive at the output of the light guide. This gives an effective etendue of the source of 9×10^{-5} $\mathrm{m}^2\mathrm{sr}$.

The old design (Figure 30- left) stopped the source down to 10 mm and transmitted light within an F/1 cone with negligible vignetting. Giving a source etendue of $5.34 \times 10^{-5}\mathrm{m}^2\mathrm{sr}$. The updated design, at first glance, produces a approximately two times increase in throughput. The throughput increase is largely due to the 1.5 times magnification factor introduced by the two parabolic mirrors. This enables the full 1-inch source to be mapped onto the 15 mm light guide. A factor of two margin was held with the old design in the form of the stop size. The stop in the old design could be increased from 10 mm to a maximum of 15 mm to deliver similar throughput to the new design. Therefore, the updated design produces a very similar throughput to the old ellipsoidal design enabling the same performance with considerable simplification.

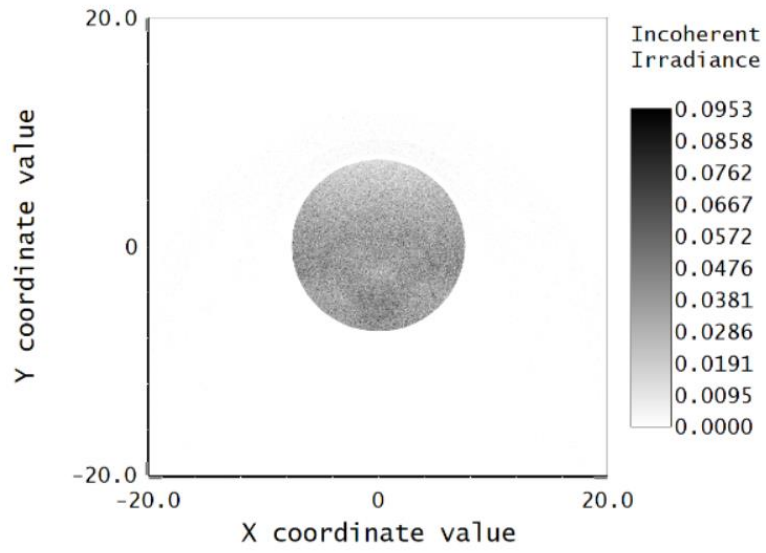

Figure 31: Image at the input of the light guide (Axes in mm)

The updated relay etendue (9×10^{-5} $\mathrm{m}^2\mathrm{sr}$) is compatible with the figure of merit defined in Table 3, however, the output power also depends on the source emissivity and the throughput. Literature data for the emissivity of the Al_2O_3 coating can be found in [88]. They show the emissivity is only ~0.5 at 800 K. Further losses are expected due to flux absorption/ scattering at the mirrors/light guide surface. Conservatively we assume 95% throughput per reflection off the gold mirror surface. The ray trace of the updated relay design (Figure 30 - Right) shows that typically ~6 reflections are required before light enters the sphere giving a total throughput of 0.74. Further losses are expected due to the chamber window. Calcium fluoride was chosen due to excellent (95%) transmittance out to 8 microns and low water solubility [89].

Combining all losses indicates a total source figure of merit of 3.2×10^{-5} $\mathrm{m}^2\mathrm{sr}$. This is marginally lower than the required 4.47×10^{-5} m^2 sr. However, the requirement calculations were performed assuming an 800 K source. The source temperature can be increased to 1200 K, giving five times margin in flux. Therefore, it will be possible to simulate the bright target flux with this design.

A design based on an Al_2O_3 button heater, two parabolic mirrors (Figure 30- Right) and a calcium fluoride window therefore is expected to meet the IR flux requirements with a considerable margin. This is achieved without the need for an additional vacuum-compatible mechanism, multiple

temperature zones in the chamber, and water cooling. This IR source design is, therefore, used for CDR.

3.1.2 VIS source relay

The throughput requirements derived in section 3.1 were also a driver for the VIS source relay. Before SRR the baseline VIS source was a 600-micron core fibre. The etendue of such a fibre would be ~29 times lower than would be needed to simulate the bright target. Because of this, the next simplest option of a 6.4 mm diameter solid core glass light pipe was used. This, however, presented challenges with the motion required between the chamber and the optical bench.

The need for motion between the optical bench and the chamber is driven by the need to accommodate misalignment of the CTR trolley (Figure 18) as well as changes in alignment during cooldown. To accommodate this misalignment, the optical bench can be translated with respect to the chamber by ± 2 cm. Because of this motion between the optical bench and the chamber[16], there was no practical way of implementing a light pipe feedthrough. Therefore, a mirrored relay was proposed that used two Off-Axis Parabolic mirrors (OAPs) to re-image the VIS source output onto the input of the sphere. The OAPs are accommodated on the ambient bench and inject a converging beam through the chamber window. This design is shown in Figure 20. There were two constraints that this relay must meet:

- Generate an image of the filament that is smaller than 1.5 cm in diameter (the light guide input size)
- Have a focal length greater than ~15 cm. This leaves a ~10 cm gap between the ambient optical bench and the shroud.

[16] In addition to the adjustability considerations, the optical bench can not be fixed with respect to the chamber for vibration isolation reasons. This is discussed further in section 5.2.1.2.

Reducing the F-number of the imaging OAP will reduce the image size, however, the focal length of the imaging OAP needs to be sufficiently large to accommodate the chamber wall and window (~15 cm). The combination of the long (~15 cm) focal length and the low F/# (~1.5) implies we need 100 mm diameter mirrors to satisfy both of these constraints. The use of 100 mm parabolic mirrors[17] to relay the VIS source into the chamber is the baseline in the run-up to CDR, currently planned for March 2024.

3.2 MONOCHROMATOR RADIOMETRIC MODEL

In addition to the broad-band sources, the OGSE design also features a monochromator for the wavelength calibration of the payload.

3.2.1 Monochromator design

It is planned that the OGSE will use a commercially available triple grating monochromator TMc300 from Bentham Instruments (Figure 32). At the entrance to the monochromator, there will be three light sources: A Quartz-Halogen bulb in the visible (>0.5 µm) and a SiN infrared source for use at wavelengths up to 7.8 µm. The transition between these sources is a free parameter to be optimised in this analysis. Both the SiN lamp and the quartz-halogen lamp have continuous spectra.

A mercury calibration lamp will also be used for wavelength calibration of the monochromator. The Hg lamp will only be used for internal OGSE wavelength calibration and not to illuminate the payload so is not discussed further in this modelling.

[17] Part no. 36-602 from Edmund optics.

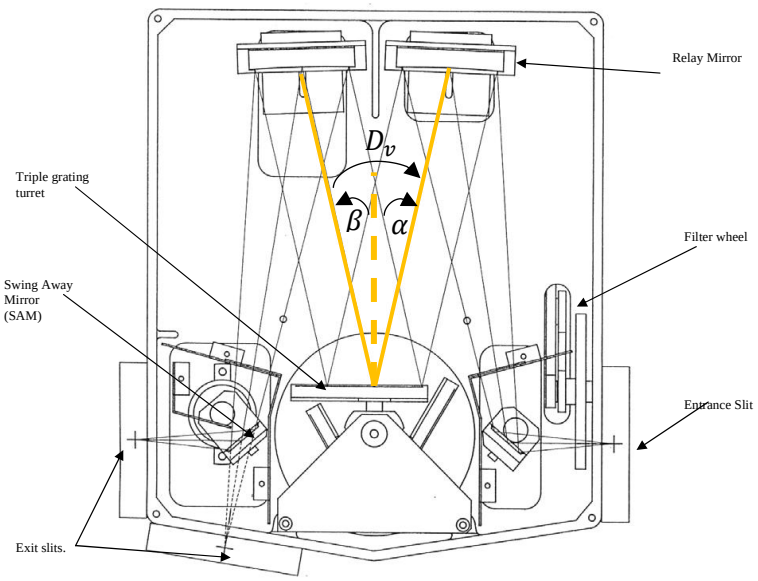

Figure 32. Bentham TM300 triple grating monochromator [Ref: Bentham, private communications]. The grating normal is shown by a dashed line.

The TMc300 monochromator can accommodate up to 3 gratings. The gratings must cover the spectral range of 0.5-7.8 µm. Whilst this is not formally defined in requirements, we also aim to choose these gratings to allow some out-of-band testing capacity. To attenuate higher diffraction orders, the light passes through an order sorting filter before being dispersed by the grating.

In this section, it will be described how the optical design evolved from the SRR baseline. At SRR, the baseline design was a fixed slit monochromator which fed light into a 30 cm Infragold-coated sphere. The monochromator had two gratings[18] one blazed at 1.2 µm, the other blazed at 3 µm. To assess the feasibility of achieving the flux requirements with the SRR design a simplified analytical model of the monochromator was created.

[18] T306R1U2 and T3015R3U0 from Bentham.

3.2.2 Analytical model

The monochromator output flux is required to be between the bright and faint stellar targets (HD 219134 and GJ 1214). This ensures that the flux seen by the detectors is representative of flight conditions, preventing any special ground test readout modes. Meeting the flux requirements for the stellar targets also ensures the calibration products can be measured to the required signal-to-noise in a time consistent with the stringent calibration schedule (~15 days). The analysis to simulate the calibration product generation with the OGSE is presented in [62].

To find the power leaving the monochromator we need to know the etendue of the monochromator. The etendue is determined by the slit width of the monochromator. This slit width is determined by the spectral resolution requirement.

To find the required slit width, the linear dispersion can be used. For a Czerny-Turner monochromator (such as the TMc300), the dispersion is given by:

$$\frac{dx}{d\lambda} = \frac{knf}{\cos\beta} \tag{3.6}$$

Where k is the diffraction order (operation in the first order assumed), n is the groove density, f is the exit focal length of the monochromator, β is the diffraction angle relative to the grating normal. For now, we make a small angle approximation that the diffraction angle is constant and equal to half the sum of the incident and reflected angle ($D_v/2$; further discussion in section 3.4). To ensure Nyquist sampling of a spectral resolution payload spectral resolution R, the slit width was set using:

$$w_{slit} = \frac{knf}{\cos\beta}\frac{\lambda}{2R} \tag{3.7}$$

It was found that the narrowest slit width was required at 2.3 microns (see Figure 33). Therefore, this fixed slit width was then used at all wavelengths.

In addition to the fixed slit case, a variable slit design was also considered. In this case, the slit is opened at wavelengths where the spectral resolution is less stringent. Nyquist sampling of the required spectral resolution gives a variable spectral width of $\Delta\lambda = \frac{\lambda}{2R}$.

The power leaving an ideal monochromator is then evaluated using[19]:

$$P_{ideal} = L_{source} h_{slit} w_{slit}\, \Omega_{mono} \Delta\lambda \tag{3.8}$$

Where $\Delta\lambda$ is evaluated using the dispersion relation (equation 3.6) and the known slit width (either constant or variable with wavelength); Ω_{mono} is the solid angle of the collimator that views the output of the monochromator (F/4), h_{slit} is the height of the slit.

The power that enters the integrating sphere is the ideal monochromator flux modulated by the grating efficiency and optical losses before the sphere i.e. $P_{in} = P_{ideal}\eta_{pre}$. Where η_{pre} is the spectral throughput of all the optics before the sphere – lens, mirrors, order sorting filter, grating, chamber window & light guide.

By combining equations 3.7 and 3.8 the sphere input power, P_{in}, can be calculated. Evaluation of the sphere radiance and propagation to the payload was calculated the same way as the broad-band

[19] Strictly, at this point we should be integrating the monochromator line shape function with respect to wavelength. However, the line shape function depends on the input and output slit dimensions as well as the internal PSF of the monochromator. This assumption is refined in section 3.4 with the numerical model that predicts the wavelength dependent line shape function.

sources (section 3.1) and uses variants of equation 3.1 and equation 3.2. In the variable slit case, the M1 equivalent input power[20] is given by:

$$P_{M1} = \frac{L_{source} h_{slit} \frac{knf}{2\cos\beta} \frac{\lambda}{R} \Omega_{mono} \frac{\lambda}{2R} \eta_{pre}}{\pi \, 4\pi r_{sphere}^2} \frac{\rho}{1-\rho\left(1-f_{port}\right)} A_{pin} \Omega_{col} \eta_{relay} \eta_{\exp} \tag{3.9}$$

At this stage, we have an estimate for the monochromator power injected into M1 for each line centre wavelength. By design, the monochromator spectrum is narrow compared to the Ariel spectral bins. For comparison, we evaluate the power collected by M1 when viewing the bright and faint targets. This stellar radiance is then binned to the spectral resolution of the payload. This is evaluated using:

$$P_{M1} = L_{star} A_{M1} \Omega_{star} \frac{\lambda}{R_{ARIEL}} \tag{3.10}$$

In this way, the monochromator power can be compared to the power in the corresponding spectral bin when the payload views the bright and faint targets. The bright and faint targets, along with the monochromator power are plotted in Figure 33.

[20] The M1 equivalent power is defined to be the power injected into M1 multiplied by the beam expander throughput.

3.2.2.1 Monochromator analytical model results

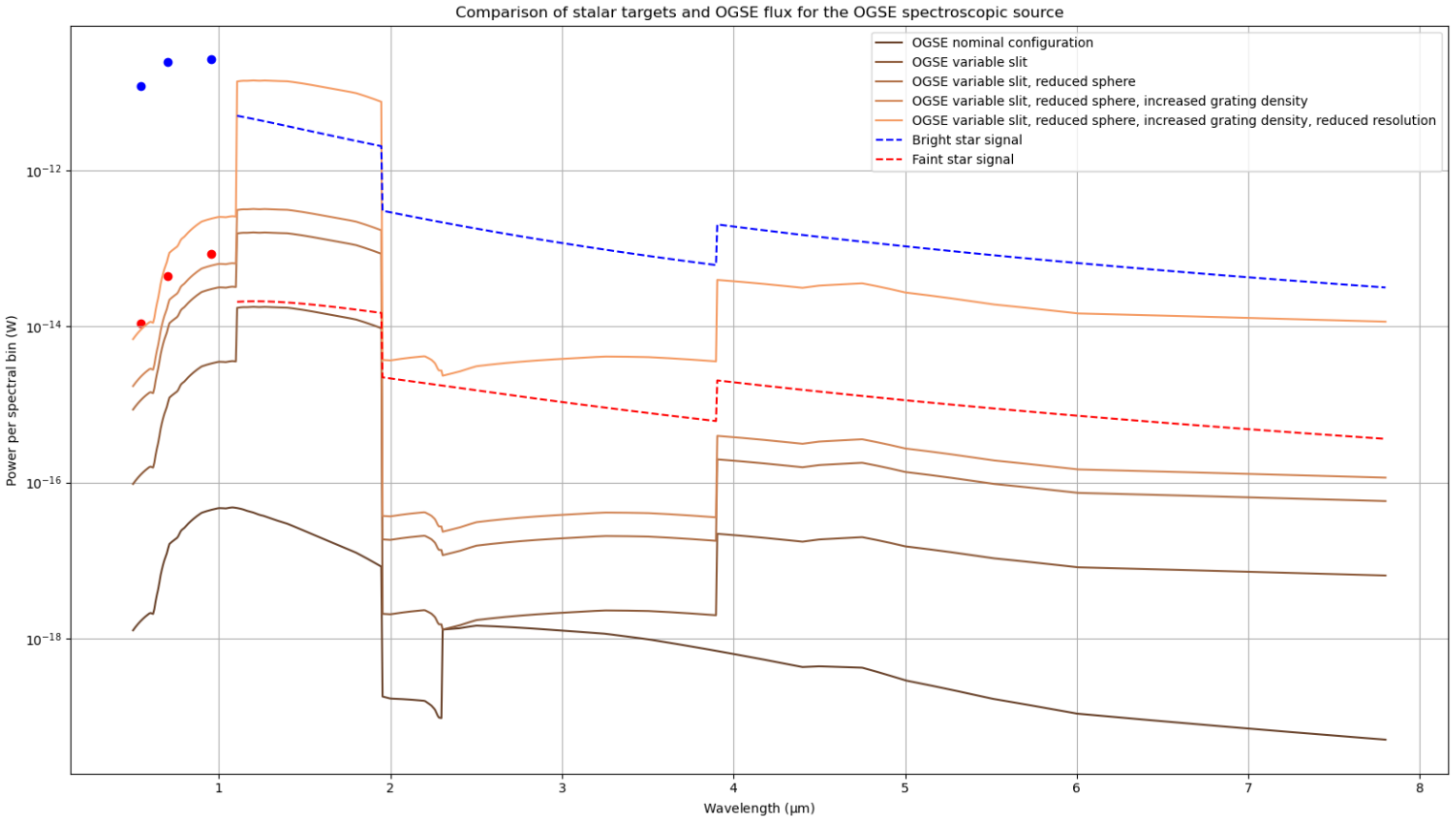

Figure 33: Comparison of the OGSE monochromator power (dark copper), to the stellar targets (dashed lines for spectrometers and dots for photometers). To increase the monochromator flux, the impact of a series of design changes is then assessed.

Figure 33 shows that the flux of the SRR design is ~4 orders of magnitude lower than the payload faint target. Significant tuning is therefore required to improve the output flux.

The first measure considered was the change from the fixed slit to the variable slit. AIRS CH0 drives the slit width size. By switching to a variable slit, the slit can be opened up in the FGS and Airs CH1. The impact of the variable slit is shown in Figure 33. This significant improvement is because of the quadratic scaling of power with the output slit size.

With the variable slit, the flux is still ~3 orders of magnitude lower than the faint target so further measures are required. The scaling of equation 3.9 can be used to optimise the sphere flux. Of particulate importance is that $P_{M1} \propto \frac{n}{r_{sphere}^2 R^2}$. These parameters are the parameters that are likely the easiest to tune/ trade-off to increase the flux.

Flux scales as the inverse square sphere radius. This high sensitivity can be utilised when optimising the flux. Figure 33 shows a case where the sphere is reduced from 30 cm to 10 cm[21]. This would lead to a 9x increase in sphere radiance. This is however a trade-off on the spatial uniformity of the sphere output. The implications of this are discussed in section 3.3.

The flux also scales as the square of the spectral resolution. The quadratic scaling comes from linearly from the larger exit slit, and linearly from the larger spectral width. If possible, it is therefore highly desirable to relax the spectral resolution requirements. The OGSE requirements at the time require Nyquist sampling of spectral resolutions that are ~10 times higher than Ariel's spectral resolution. This was more than was necessary, but not completely without motivation.

[21] It was later decided that a 15 cm sphere would provide a more acceptable compromise between flux and uniformity.

The driver for the monochromator resolution is the wavelength calibration requirement that requires calibration with an accuracy of 1/3 of a spectral bin (R-CAL-140). A spectral resolution to Nyquist sample 1/3 of a spectral bin would therefore be justified.

It is, however, important to make the distinction between the stepping resolution of the monochromator and the spectral width. The wavelength calibration measurement is a measurement of a spot centroid (see 2.2.14). The spectral stepping determines the centroid position of the spot. The spectral width determines the PSF broadening of the spot in the spectral detection. To meet the 1/3 spectral bin calibration, we need to be able to step the line centre position by $1/6^{th}$ of a spectral bin. The wavelength of the line centre also must be known to $1/6^{th}$ of a spectral bin.

The finite spectral width will have the effect of broadening the PSF. Provided the spectral width is small compared to the payload PSF it should not impact the centroid accuracy and, thus should not impact the wavelength calibration accuracy. Therefore a spectral width requirement of ½ spectral bin was chosen.

By requirement update and decoupling the spectral width and stepping resolution a factor of 10 relaxation in spectral width was possible. This corresponds to a factor of 100 increase in flux.

The final change was to increase the line density of the grating. A higher line density implies a wider slit can be used for the same spectral resolution. A case with double the line density was also evaluated (and is shown in Figure 33). This led to a factor of 2 increase in flux.

From Figure 33, one can see that even with all of the above-mentioned changes, the monochromator flux is fairly marginal on the faint target flux in AIRS CH0. This is due to the fainter IR source and the R>100 resolution in this channel. To address this, it is desirable to extend the usable wavelength of the brighter QTH source into the AIRS CH0 band. This can be done by exchanging the SiO_2 condenser for a CaF_2 condenser provided. This extended the quoted source operation to 4 microns. The impact of this is shown in Figure 34.

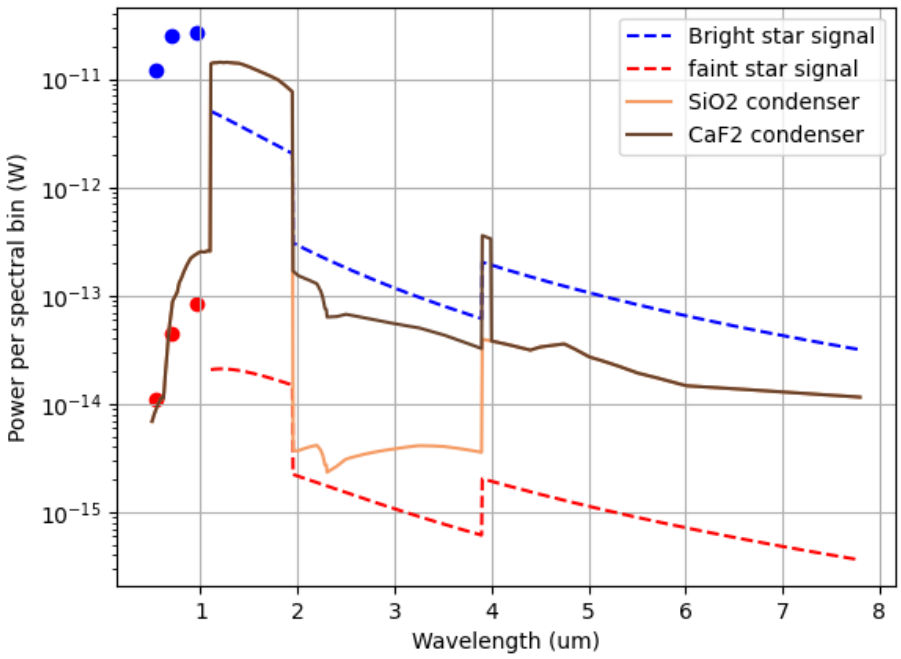

Figure 34: Using a CaF2 lens to extend the spectral range of the VIS source. This was modelled by changing the IR to VIS source transition wavelength from 1.95 µm to 4 µm. Note this plot assumes all the other measures discussed above have been enacted.

This simplified analytical model provided early indications about the challenges of meeting the output flux with a Bentham TMC300 monochromator (by ~4 orders of magnitude with the SRR baseline). Five measures were presented (1) the use of a variable slit to improve performance in FGS and Airs CH1 (2) the use of a CaF2 condenser to improve the throughput in AIRS CH0; (3) the decoupling of the spectral stepping and spectral width requirements to enable relaxation of the spectral width requirements; (4) increase in the grating line density; (5) a reduction in the sphere size.

The results shown in Figure 34 still show a marginal flux in VISPhot (the short-wave photometric channel). This will be addressed in section 3.4.

3.3 SPHERE RADIUS TRADE-OFF

Section 3.2 described the challenges of achieving a flux greater than the faint target with the F/4 Bentham monochromator. Because of this, a reduced sphere size was considered.

This decision was also influenced by the broad-band sources. The source etendue requirements stated in Table 3 would be four times larger with a 30 cm sphere. This would imply challenging low F-number optics for the sources (~F/0.5 for the IR source). With these low F/# source relays, the source power is a significant thermal load on the sphere (~11 W when both sources are operated simultaneously). This would require a >12 m^2 Radiator to dissipate this energy at 70 K. Therefore, in addition to helping solve the monochromator flux challenges, a reduced sphere simplifies the broad-band relay optics and reduces the thermal challenges on the cryogenic optical bench.

Reducing the sphere radius is, however, a trade-off against the uniformity at the output of the integrating sphere. A uniformity of better than 0.5% is beneficial[22] for flat fielding of the payload (section 2.2.11). To assess the feasibility of meeting the 0.5% uniformity requirement with a 15 cm sphere, a ray-tracing model was evaluated. The model considers a simplified on-axis system with a single entrance and exit port that are separated by a centrally located 9 cm square baffle (Figure 35). The sphere CAD has three entrance ports (shown in Figure 35- Right). These were combined into a single 3.5 cm port (equal to the area of 3×2 cm ports). A 1 cm output port was used (approximately two times oversized relative to the 50'' Ariel unvignetted field).

[22] It is also possible to flat field the detector by raster scanning the point source over the detector.

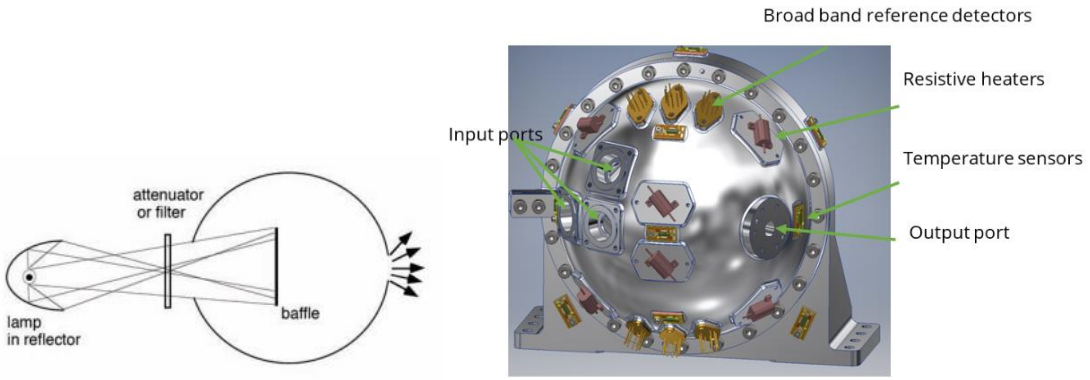

Figure 35: Left shows the port layout in the simplified model [86], right shows the baseline sphere layout [51].

The impact of the reference detectors on the number of photon scatterings in the sphere is handled implicitly by defining a reduced reflectivity. Pessimistically the reference detectors are modelled as black ($\epsilon = 1$) leading to a reduced effective sphere reflectivity of $\eta_{eff} = 0.94 \times (1 - 11.7/707) = 0.924$.

The model uses a radiometric ray tracing method. To describe the geometry, the sphere walls use a polar mesh[23]. The centrally located baffle is described by a rectangular mesh composed of 50 facets. View factors are calculated from each facet to each other facet. The light then undergoes scattering in a series of time steps. At each time step light is injected into the input, shining on the baffle. The flux landing on each facet is then calculated. A fraction $1 - \eta_{eff}$ is absorbed. The remainder is scattered to other facets in the next time step. Scattering is assumed to be Lambertian, and coupling is determined by the previously calculated view factors.

After ~100 time steps, the intensity distribution reaches a steady state equilibrium. The output is then measured in the equilibrium state. The radiance at the output port is integrated over the F/24 collimator cone angle to calculate the flux at the output port.

[23] 400 bins in the polar direction and 24 bins in the azimuthal direction

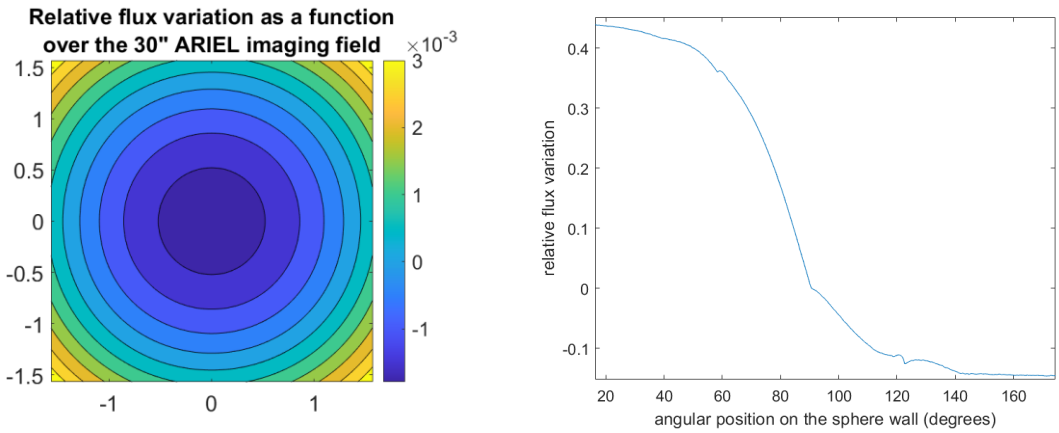

Figure 36: Left shows the sphere output uniformity across the extended port of the sphere. Right shows the angular variation in flux across the sphere wall.

The estimated uniformity is shown in Figure 36 – left. From this, the peak-to-valley non-uniformity over the circular 30'' field is ~0.2%, consistent with the 0.5% requirement. The analyses also implied the dominant source of the non-uniformity was caused by baffle shadowing. The baffle shadow leads to a flux gradient along the sphere wall (Figure 36 – Right), this, in turn, causes a gradient on the baffle which is seen at the output. This may be exaggerated by the pessimistic representation of the baffle as a 9 cm central baffle, but it is likely the dominant driver of non-uniformity for the on-axis system.

The model was, however, found to be very sensitive to the geometry of the system. Given the simplified handling of the geometry, the results should only be considered an order-of-magnitude feasibility assessment of the reduced sphere size. However, this model does show promising indications that the uniformity requirements should be achievable with the reduced sphere.

We can also compare it to the experimental data from Labsphere (Figure 37). Our exit port ratio is ~0.06, significantly smaller than the 0.3 port ratio shown on the graph which meets our uniformity requirements. This further provides evidence that a 15 cm sphere should be sufficient to meet the uniformity requirement.

Finally, it is worth noting the total port area ratio (including reference detectors). For the 15cm sphere, the port ratio is ~3% this is less than the 5% rule of thumb maximum port fraction specified by

Labsphere [RD2]. Beyond this area ratio, flux leaving the sphere through ports becomes comparable to the flux absorbed onto the sphere walls ($\epsilon \sim 0.06$). Therefore, the current design is below the threshold where the port fraction significantly impacts the mean number of photon scatterings.

Figure 37: Compilation of measured uniformities for previously designed spheres. Figure from Labsphere.

(figure redacted from ORA version)

It is planned to manufacture an integrating sphere breadboard which will allow the experimental assessment of the uniformity. The design also features a removable baffle so multiple baffle sizes and locations can be explored.

Based on this analysis it was decided that the baseline OGSE integrating sphere should be reduced from 30 cm to 15 cm in diameter. This provides a significant (four times) increase in throughput for the monochromator where throughput is marginal. This simplifies the low F/# relays for the broad-band sources and reduces dominant thermal loads (~11W to 3W source absorption). This is potentially at the cost of spatial uniformity, however, current models and literature data imply that a 15cm sphere should be able to provide the required 0.5% uniformity.

3.4 NUMERICAL MONOCHROMATOR MODEL

The analytical monochromator model presented in section 3.2 provided a useful tool for demonstrating the monochromator flux challenges. The analytical form also highlighted the parameters that could be tuned to improve flux. In preparation for PDR, a numerical model was developed to refine some of the simplifications in the analytical model. In particular:

- Improved handling of the entrance and exit slit vignetting.
- Prediction of the output line shape function.
- The small diffraction angle assumption no longer applies.
- Addition of broad-band stray light.
- End-to-end simulations to predict the payload focal plane response.

Beyond the reduced model uncertainty, the numerical model had several implications. The line shape function provides a direct comparison to the spectral width requirements. The broad-band stray light analysis led to an improved relay design featuring cryogenic focal and pupil stops. The end-to-end analysis provided focal plane signal to noise and saturation time estimates. These S/R and saturation times were then used to simulate the planned calibration measurements to assess the feasibility of completing the whole test campaign in the very restrictive 15 days allocated (driven by programmatic/cost constraints). The end-to-end flux simulations also led to the addition of an additional modulator to attenuate the sources by a further ~100 times when the extended source is in use.

3.4.1 Method

The end-to-end optical path is described in Figure 38. The optical path starts with the source filaments. The QTH and SiN sources are represented as black bodies with a defined emitting area and emissivity. The light from the filament is then collected by a condenser. Unlike the rest of the OGSE optical chain, this condenser is planned to be a transmissive lens. This lens also sets the size of the image of the

filament at the monochromator entrance slit (calculated using the abbe invariant). The image of the filament then gets vignetted by the entrance slit.

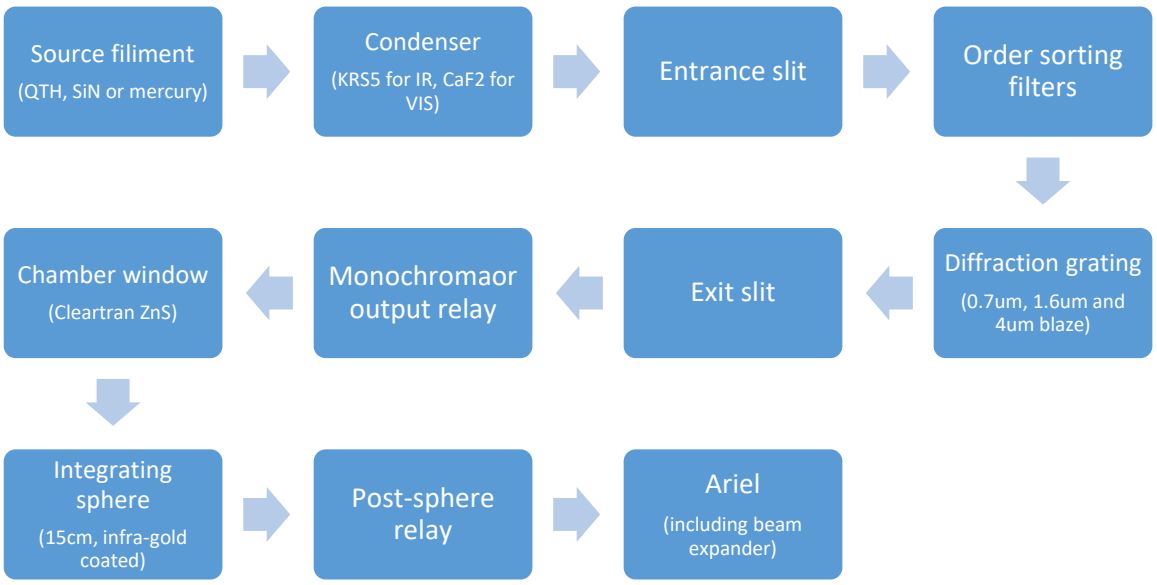

Figure 38: Monochromator optical path.

Light passing through the entrance slit is then filtered by an order sorting filter. A toroidal mirror collimates the beam and relays the beam onto a reflective diffraction grating. A second toroidal mirror images the dispersed light onto the output slit plane, creating a spectrum at this surface. The exit slit then vignettes the beam allowing only the selected wavelength to pass. Light from the monochromator is then relayed through a window into the chamber, into the sphere and onwards to Ariel.

3.4.1.1 Lineshape prediction

The spectral radiance at the input slit is defined to be $L_{in}(x,\lambda)$ ($Wm^{-2}sr^{-1}\mu m^{-1}$) where x is the position in the dispersive direction. $L_{in}(x,\lambda)\delta x\ h\ \Omega\Delta\lambda$, therefore is a 2D matrix with each element describing

the power within a spatial bin δx and a spectral bin $\Delta\lambda$. The sum over the spatial index provides the total power injected per spectral bin.

If we assume that the source is uniform in temperature across the emitting surface, we can separate the spatial and spectral parts of $L_{in}(\lambda, x) = I(\lambda)\Pi_{\text{in}}(x)$. We further assume homogeneous illumination of the input slit in the spectral direction. In this case, $I(\lambda)$ is the input radiance, and $\Pi(x)$ is a unity top-hat function.

To ensure the correct normalisation, $\sum \Pi_{in}(x)\, \delta x = w_{in} \equiv N\Delta x$ where N is the number of spatial samples across the slit, δx is the width of the spatial sampling and w_{in} is the width of the input slit or the size of the image of the filament, whichever is less.

In this notation, we can rewrite the input spectral power per spatial bin as:

$$\delta\Phi_{in}(\lambda, x) = I(\lambda)\delta x\, h\, \Omega\, \Pi(x) \tag{3.11}$$

For light at the nominal wavelength solution, the monochromator will image the input slit onto the output slit. For other wavelengths, the input slit image will be displaced by x_λ. Therefore, for a given grating angle, the ideal spatial power distribution at the output is:

$$\delta\Phi_{exit_{ideal}}(\lambda, x) = I(\lambda)\delta x\, h\, \Omega\, \Pi(x - x_\lambda) \tag{3.12}$$

The true monochromator output will differ from the ideal monochromator due to the internal throughput (η_{mono}). Therefore, at the exit of a real monochromator, the spectral power distribution will be $\Phi_{out}(\lambda, x) = \Phi_{exit\_ideal}(\lambda, x)\eta_{mono}$.

The monochromator will also have a non-zero internal point spread function which can have the effect of broadening the line shape. However, given the diffraction-limited point spread function is negligible relative to the line shape, and experimental data on geometric distortions was not available, this effect was omitted. At this point we have the spectral power falling at each point on the output plane. We now need to mask this by the output slit to obtain the spatial power at the monochromator output. $\Pi_{\text{out}}(x)$ is the top hat mask representing the output slit transmission.

$$\delta\Phi_{out}(\lambda, x) = \eta_{mono}(\lambda)I(\lambda)\delta x\ h\ \Omega\Pi_{\text{in}}(x - x_{\lambda})\Pi_{\text{out}}(x) \tag{3.13}$$

Integrating across the slit:

$$\Phi_{out}(\lambda) = \eta_{mono}(\lambda)I(\lambda)\Omega\ h\delta x \sum_{\text{x}} \Pi_{\text{in}}(x - x_{\lambda})\Pi_{\text{out}}(x) \tag{3.14}$$

This is the numerical convolution of the image of the input onto the output slit. Therefore the output power line shape can be described as:

$$\Phi_{out}(\lambda) = \eta_{mono}(\lambda)I(\lambda)\delta x\ h\ \Omega\ (\Pi_{\text{in}} * \Pi_{\text{out}})\big(x_{\lambda}(\lambda)\big) \tag{3.15}$$

Equation 3.15, determines the output line shape. This is plotted in Figure 39. One can see that the output line shape is determined by the overlap area of the input and output slits. The grating dispersion means that exact optical mapping from the input slit to the output slit only occurs at a single wavelength[24], λ_0. At wavelengths different from λ_0, the image of the input slit is displaced relative to the output slit. The mismatch between the input slit image and the output slit location causes vignetting and reduced throughput away from λ_0. In the optimised case where the input and output slit have the same width, this throughput has a triangular functional form (Figure 39).

[24] For first order diffraction

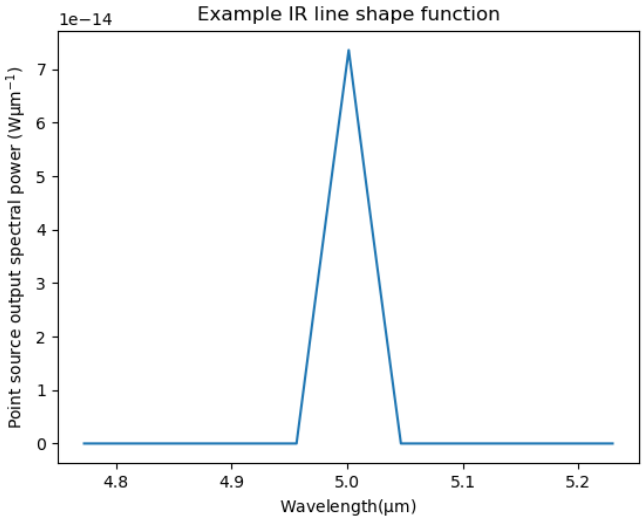

Figure 39: example output line shape function

3.4.1.2 Grating dispersion

As seen in equation 3.15, the output lineshape function depends on the image separation of the input slit relative to the output slit, $x_\lambda(\lambda)$. The image separation is determined by the dispersion characteristics of the grating. The image separation can be calculated based on standard expressions for the grating dispersion and the turret angle solution of the grating e.g. [90]. Constructive interference from a grating monochromator occurs when the following equation is satisfied:

$$\sin\alpha + \sin\beta = k n \lambda_0 \tag{3.16}$$

The Czerny-Turner monochromator has a fixed input and output slit locations. Therefore, $D_v = \beta - \alpha$, where D_v is the constant, known, angle subtended between the entrance and exit slits (Figure 32). By trigonometrical manipulation, a more useful form of 3.16 can be derived:

$$\beta = \arcsin\left(\frac{kn\lambda_0}{2\cos\left(\frac{D_v}{2}\right)}\right) + \frac{D_v}{2} \tag{3.17}$$

In this way, the grating angle can be calculated for each chosen wavelength.

The offset between the input slit image and the output slit is given by:

$$x_\lambda(\lambda) = \frac{dx}{d\lambda}(\lambda - \lambda_0) = \frac{knf}{\cos\beta}(\lambda - \lambda_0) \tag{3.18}$$

Equation 3.18 provides the slit image separation, equation 3.17 provides the grating angle for the chosen wavelength λ_0 and equation 3.15 predicts the spectral output power of the monochromator-based on slit image separation. This set of equations, therefore, predicts the spectral output power of the monochromator. The monochromator output power is then propagated through a window, into the sphere, and onwards to the payload. The method for doing this is as described for the broad-band sources in section 3.1.

3.4.2 Numerical monochromator model results

The results presented in this section are based on parameters/ data described in Appendix A. Where raw data for spectral throughput was available this was incorporated into the model. In other cases, simplified step function spectra were implemented that represented the cut-on/ cut-off wavelengths of coatings/ windows/ lenses.

Previous model iterations showed that the throughput of the monochromator system is going to be challenging. For this reason, the analysed design includes the use of a custom source system. This source uses F/1 condensers that magnify the image of the filament by four times at the input slit. This allows utilisation of the full slit height and width (20 mm by 8 mm maximum) [25].

[25] The design created in preparation for CDR baselines a pre-exiting off the shelf Bentham source module. This switch is largely enabled by finding a supplier that can produce silver coated integrating spheres (Artifex). This partially mitigates the short wave flux deficit. Flux is still expected to be marginal relative to the faint target, and it still plausible a custom source module will be required. If required, this will a straightforward switch which can be developed for payload flight model testing.

3.4.2.1 Spectral width

By evaluating the output lineshape, the slit width was optimised to match the spectral width requirements of the OGSE (R-OGSE-SPEC-0150, R-OGSE-SPEC-0160; see Figure 40 - Left). The optimised slit width vs wavelength is shown in Figure 40 – Right. The slit width is undersized to give at least a 25% margin on the spectral width relative to the requirement. This margin is to account for the internal point spread function of the monochromator. Blurring of the entrance slit image will broaden the line shape function. The spectral resolution of the monochromator will be measured by test using an FTIR to verify the impact of unknown optical aberrations on the spectral resolution.

The discontinuous jumps in the slit width (Figure 40) correspond either to different instrument channels' resolution or changes in grating.

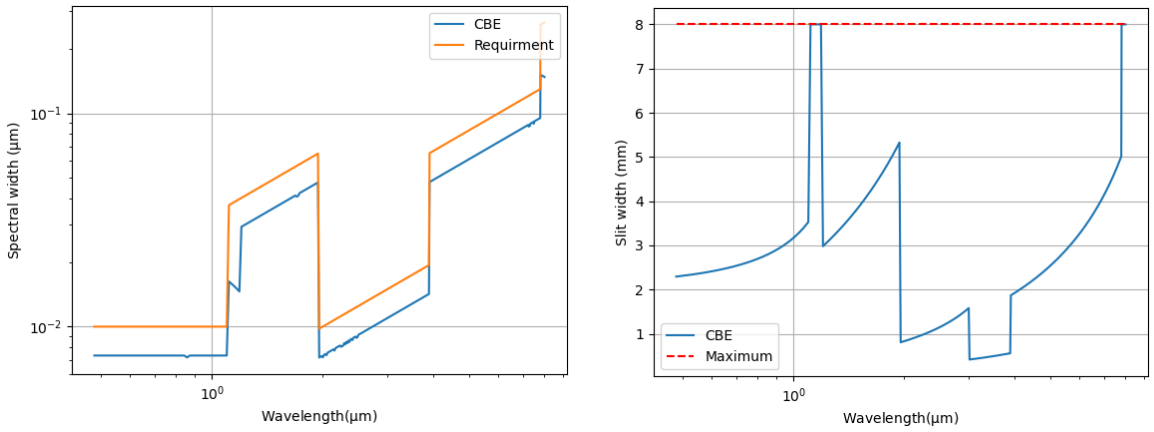

Figure 40: Slit width (left) and spectral width (right) as a function of wavelength. The maximum shown on the right plot is a mechanical constraint of the slit actuator.

3.4.2.2 Output power

For every grating angle, the output line shape was evaluated. The output power was then calculated by spectrally integrating the line shape. Output power was evaluated for the pinhole configuration (Figure 41- Right). An output radiance was evaluated for the extended source (Figure 41- Left). In the case of the pinhole configuration, the monochromator power can be compared to the power the payload receives when viewing the defined bright and faint targes (binned at the Ariel spectral

resolution). One can see there is a comfortable margin relative to the faint target in AIRS, however, in the three photometric channels, performance is compliant albeit marginal.

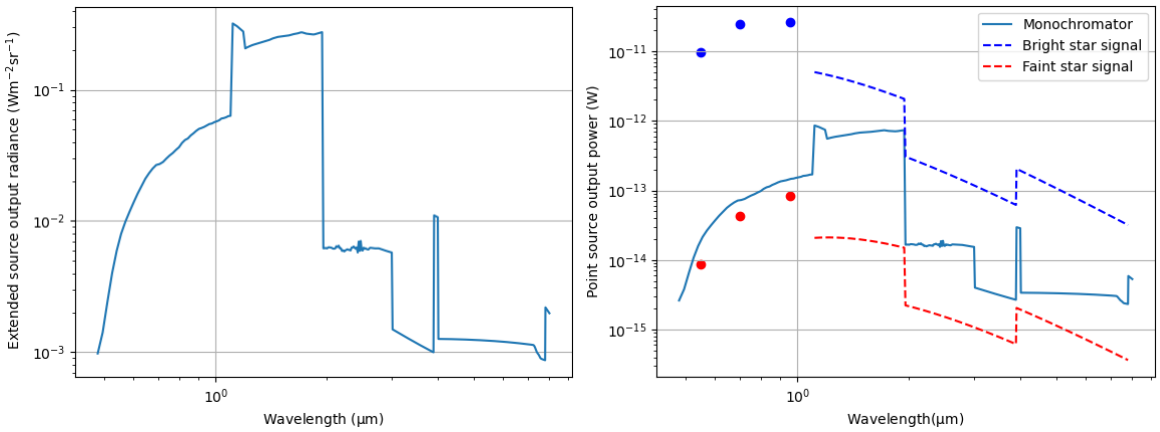

Figure 41: Extended source radiance (Left) and point source ouput power (Right).

Now the OGSE output spectral power is known, the next step is to inject this into Ariel to produce simulated focal plane spectra.

3.4.3 End-to-end simulations using ArielRad

To enable simulations of the focal plane response during calibration measurements, the monochromator model output was input into the Ariel end-to-end radiometric simulator (ArielRad, [91]). The following sections describe the results of the end-to-end ArielRad simulations.

3.4.3.1 Point source vs extended source

For the point source (Figure 19), it is relatively straightforward to demonstrate the OGSE output power is within acceptable bounds. This can be done by direct comparison to the bright and faint stellar targets. For the extended source, it is less straightforward to demonstrate the OGSE output flux is within usable ranges. To do this, end-to-end simulations are required to determine the focal plane saturation times.

The focal plane flux can then be estimated and can be compared to maximum and minimum saturation times for the bright and faint targets. A saturation time of less than 0.1 s would saturate the detectors

faster than they can be read out. Long ($\gg 10^3$ s) saturation times would lead to measurement times being inconsistent with the two weak calibration window in the RAL chamber. For comparison, the range of saturation times for the payload observing the bright and faint targets is 0.1 s to 4000 s [91].

Figure 42 shows the output power when the monochromator is used. Figure 43 shows the output power when the broad-band sources are used. For the broad-band sources, it was found that considerable excess in flux arrives at the focal plane. With the point source, there is a one-to-one wavelength mapping so each pixel only receives a narrow spectral width. For the extended source, the focal plane signal is the convolution of the spectrometer slit extent (top-hat function) with the point source spectrum. This implies a broad range of wavelengths land on each pixel leading to a ~100 times increase in flux.

Calibration measurements such as the pixel gain (section 2.2.17) rely on being able to measure the Poisson characteristics of photon noise. The variance of the noise provides a direct measurement of the number of detected photons. The measured signal (in Volts) can be used to predict the gain. However to see the photon noise above the intrinsic ~0.5% source variability the focal plane fluence needs to be less than $\sim \frac{1}{0.005^2} = 4 \times 10^4$ electrons. It is therefore necessary to be able to generate low-flux extended source measurements. To achieve this, an additional 100 times modulator was incorporated into the shutter blade. The design of this shutter is discussed in section 6.2.4.3.

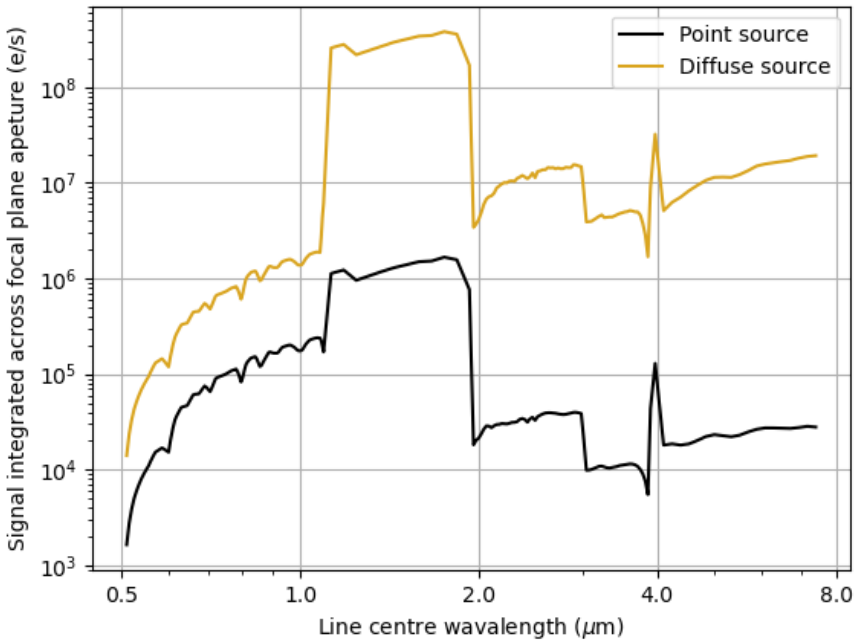

Figure 42: monochromator output power

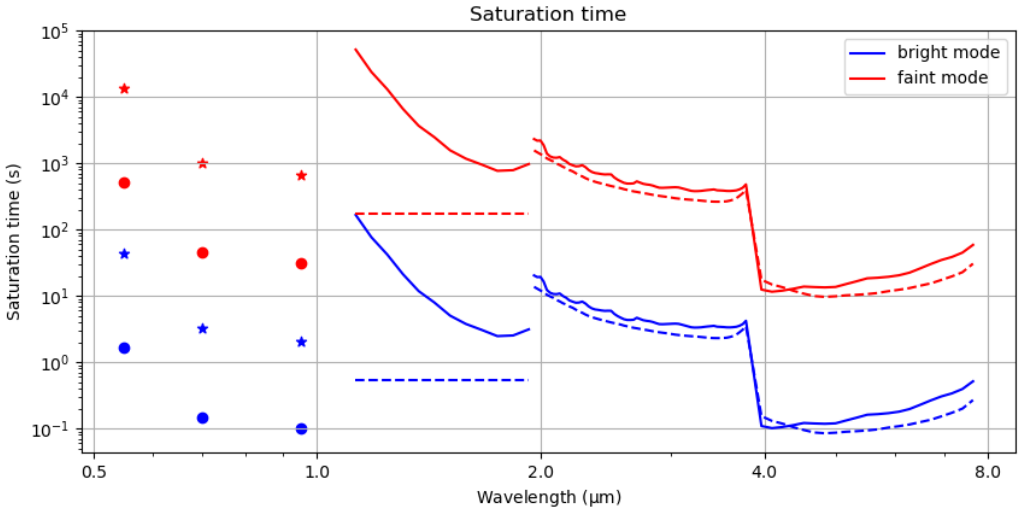

Figure 43: Focal plane signal when the payload is illuminated by the OGSE broadband sources. The diffuse output is shown with the dashed line and stars, the point sphere output is shown with the solid line and dots. The blue shows the limiting bright case, and the red shows the limiting faint case when the source is maximally attenuated. The extended source is shown with the 100 times modulator applied.

3.4.3.2 Flat fielding

Another output of the end-to-end simulations was the validation of the planned flat field method. To measure pixel response non-uniformity, it is desirable to illuminate the focal planes with a flat intensity distribution. Given a flat (or known) intensity distribution, any measured variability between pixels can be attributed to pixel response non-uniformity.

The flat field measurement is particularly challenging for the spectroscopic channels as the dispersive element will impact the flat field. If the extended sphere source was used with the broad-band sources, a ~black body intensity distribution would be seen across the focal plane (e.g. Figure 64) – not a flat intensity distribution. Given typical uncertainties in radiometric calibration standards[26], correcting the spectral flux dependence to the level of 0.5% will not be possible. Therefore, the broad-band sources can only be used to flat field the detectors in the spatial direction, not the spectral direction.

To Flat field the Ariel spectrometers an alternative method must be used. The method chosen is to use the monochromator and the extended sphere output. This can be used to generate local top-hat flat fields. As discussed in 3.4.2.1, the focal plane response is the convolution of the payload spectrometer slit extent (top-hat) and the OGSE point source spectral response. When a monochromator is used, the point source spectral response is small compared to the slit extent. The focal plane signal is therefore the convolution of a top-hat with a Dirac delta giving a top-hat intensity distribution at the focal plane. This was confirmed by injecting the line shape (e.g. Figure 39) into the end-to-end payload simulator the resulting focal plane intensity distribution is seen in Figure 44-left).

[26] ~3% is typical for a commercial, traceable, radiance standard (e.g. a Bentham SRS8)

The top hat is centred on the wavelength solution of the monochromator wavelength. This top hat can be used to create a local flat field. Verification of the global flat field is not possible at payload level. By scanning the monochromator wavelength, the top hat can be shifted across the focal plane allowing other regions of the focal planes to be flat fielded (Figure 44-Right). This scanning top-hat technique will also be used to verify the payload non-linearity where flat illumination is required.

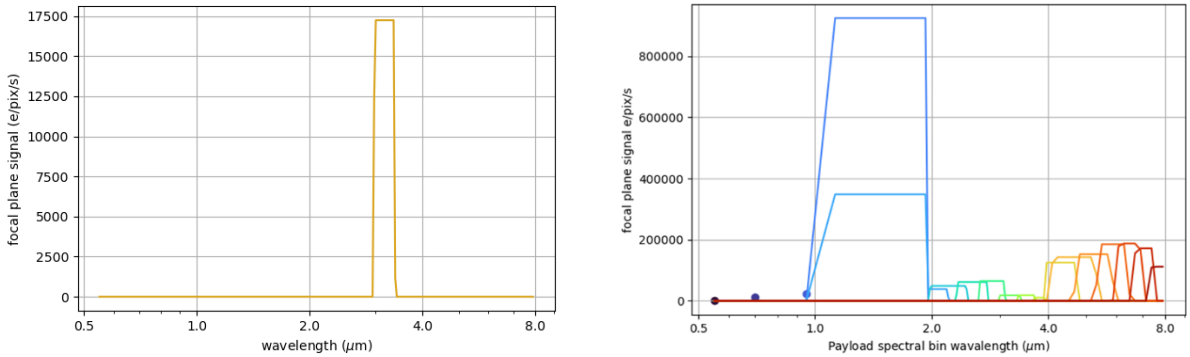

Figure 44: flat field generation using the OGSE monochromator and the extended sphere output. This generates top-hat intensity distribution at the focal plane (e.g. Left figure). The Right figure shows how flat fields can be built up over the full wavelength range by scanning the monochromator. Each colour corresponds to a different monochromator wavelength.

3.5 MONOCHROMATOR CONTINUUM STRAY LIGHT

The monochromator is designed to produce a line shape (Figure 39) that is narrow compared to the payload spectral resolution. However, continuum sources could contaminate this monochromatic signal – impacting calibration measurements such as wavelength calibration. The monochromator relay presented at PDR is shown in Figure 45 – left. This used a pair of 30° off-axis parabolic mirrors and a pair of folds to image the monochromator output to the input of a 15 mm diameter light guide situated on the ambient optical bench within the vacuum chamber. The light guides were used primarily for accommodation reasons. To maximise the uniformity of sphere output there must not be a direct line of sight between the output and the input. This means the inputs must all be located

close together on the sphere wall. Generating three close images with low F/# optics is challenging so light pipes were used to inject light into the sphere.

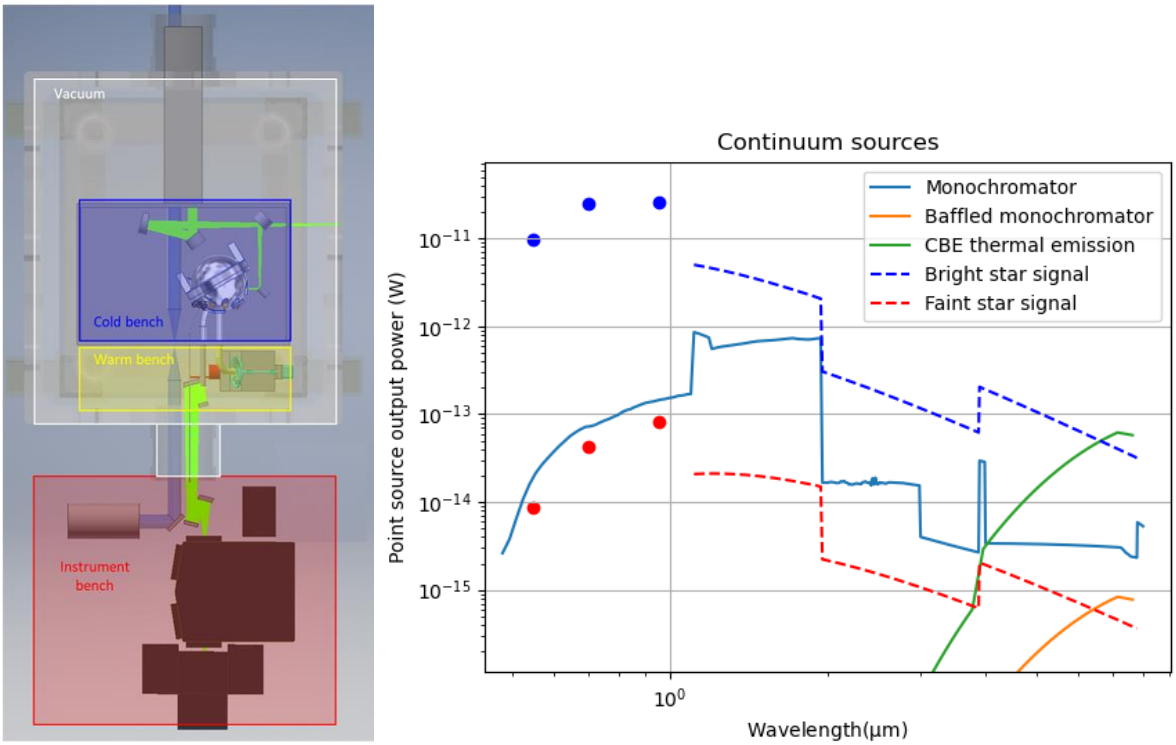

Figure 45: Illumination module design at PDR [51]. Right shows the monochromator output power as well as contributions from ambient stray light. The green line represents the stray light in the PDR relay. The orange line shows the stray light in the CDR design.

The drawback of the light guide concept is the management of stray light. The hollow core light guides are capable of transmitting light at all entrance angles[27] and transmit light over the full entrance aperture. This gives the light pipe an effective etendue of $\pi \times \pi\,(7.5)^2\ \mathrm{mm^2 sr} = 6 \times 10^{-4}\ \mathrm{m^2 sr}$. This orders of magnitude larger than the etendue of the monochromator relay ($2 \times 10^{-5}\ \mathrm{m^2 sr}$). At PDR, the entrance of the light pipe was on the ambient optical bench and the light guide entrance

[27] Albeit with somewhat reduced throughput at large incident angles due to the larger number of reflections.

faced entirely ambient surfaces. The resulting thermal emission entering the light guide is shown Figure 45. This shows that thermal emission will be an order of magnitude larger than the monochromator signal at 7.8 microns.

To reduce the thermal emission entering the light pipe, the ambient optical bench was removed from the design and all relay optics in the chamber were accommodated on an extended cryogenic bench (Figure 20). By placing the mirrors on the cryogenic bench, cryogenic focal and pupil stops can be used to drastically restrict the etendue of thermal emission ($2 \times 10^{-5}\ \mathrm{m^2 sr}$). The resulting reduction in thermal emission is shown in Figure 45.

The addition of cryogenic stops (Figure 47), will therefore bring thermal emission to a regime where it is lower than the monochromator signal. It, will, however, still be a measurable effect and will, for example, be seen when performing the flat field measurement (Figure 46). The monochromator does, however, have a shutter at the input. By sequential background subtraction, the thermal background coming from the monochromator relay should be correctable to an acceptable level.

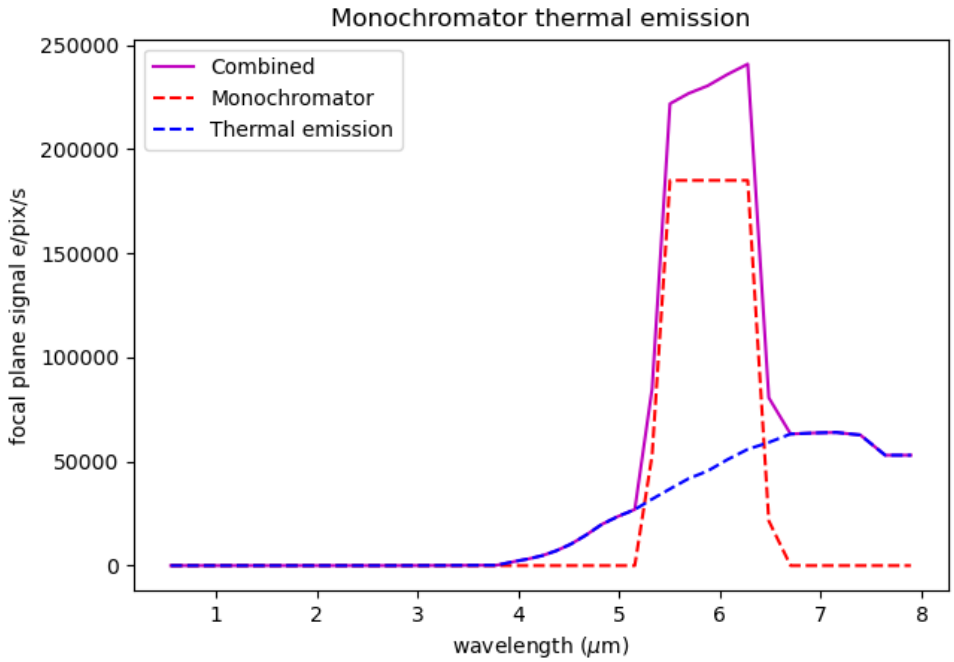

Figure 46: flat field simulation with broad-band spectral contamination (blue). The red dashed line shows the focal plane response when the monochromator and the extended source are used. The blue line shows the effect of thermal emission entering through the monochromator realy optical path. Purple shows the combined signal binned at the payload resolution.

This model shows the effect of thermal continuum contamination. It does not consider scattering off the grating which will likely dominate the continuum in the visible. It is extremely difficult to make predictions about the grating scattering characteristics without detailed knowledge of manufacturing defects/ contamination. Because of this, this effect is best validated by test.

3.5.1 Updated relay design

Figure 47 shows the updated relay design, needed to reduce the thermal emission in the system. To enable early breadboarding of the monochromator system, it was desired to use commercially available mirrors. A <0.75 times magnification in the system was required to map the 2 cm monochromator slit to the 1.5 cm diameter light guide. It was found that 2 inch mirrors were found to be sufficiently large to relay the large (2 cm) object over a long (~30 cm) collimated stretch with

negligible vignetting. Since these optics are before the sphere, imaging quality is not important, except where it causes vignetting.

A pair of 90-degree off-axis parabolic mirrors satisfies the above considerations. The collimating mirror has an apparent focal length of 154.2 mm, the imaging parabola has a focal length of 101.6 mm. By using 90-degree parabolas, and switching the monochromator output, three fold mirrors were eliminated from the optical path, improving throughput.

Given these parabolas, the only remaining free parameter was the orientation. Figure 47 shows two possible orientations. The top configuration uses a 'C' configuration, the bottom uses a 'S' configuration. When the 'C' configuration is addopted, there is a smaller point spread function, however, there is significant field distortion. The crescent shape image causes slight (~1%) vignetting at the left edge of the focal stop. A 0.6 mm decenter was applied to the light pipe entrance to minimize this vignetting.

With the opposite folding, a significantly larger PSF is seen. There is, however, negligible field distortion. However, even with this large PSF, both options produce a similar geometrical throughput of 82% vs 84%[28]. This is because in both cases the throughput losses are dominated by vignetting on the pupil stop. This is caused by the long collimated stretch (440 mm) required to relay the beam from the ambient optical bench to the cryogenic bench. To improve the throughput, longer focal length, and larger diameter, parabolas could be used. These would, however, have to be custom and the marginal gain in throughput from reduced vignetting would be offset by increased absorption from additional folds required to accommodate these longer focal lengths. The larger diameters would also

[28] This throughput calculation assumes uniform illumination across the slit. This is a worst case assumption, and is known to be pessimistic as the monochromator which brighter in the centre than at the edges of the slit.

imply larger chamber windows and a larger hole in the cryo-shroud. For these reasons, the left relay shown in Figure 47 is seen as the optimal solution.

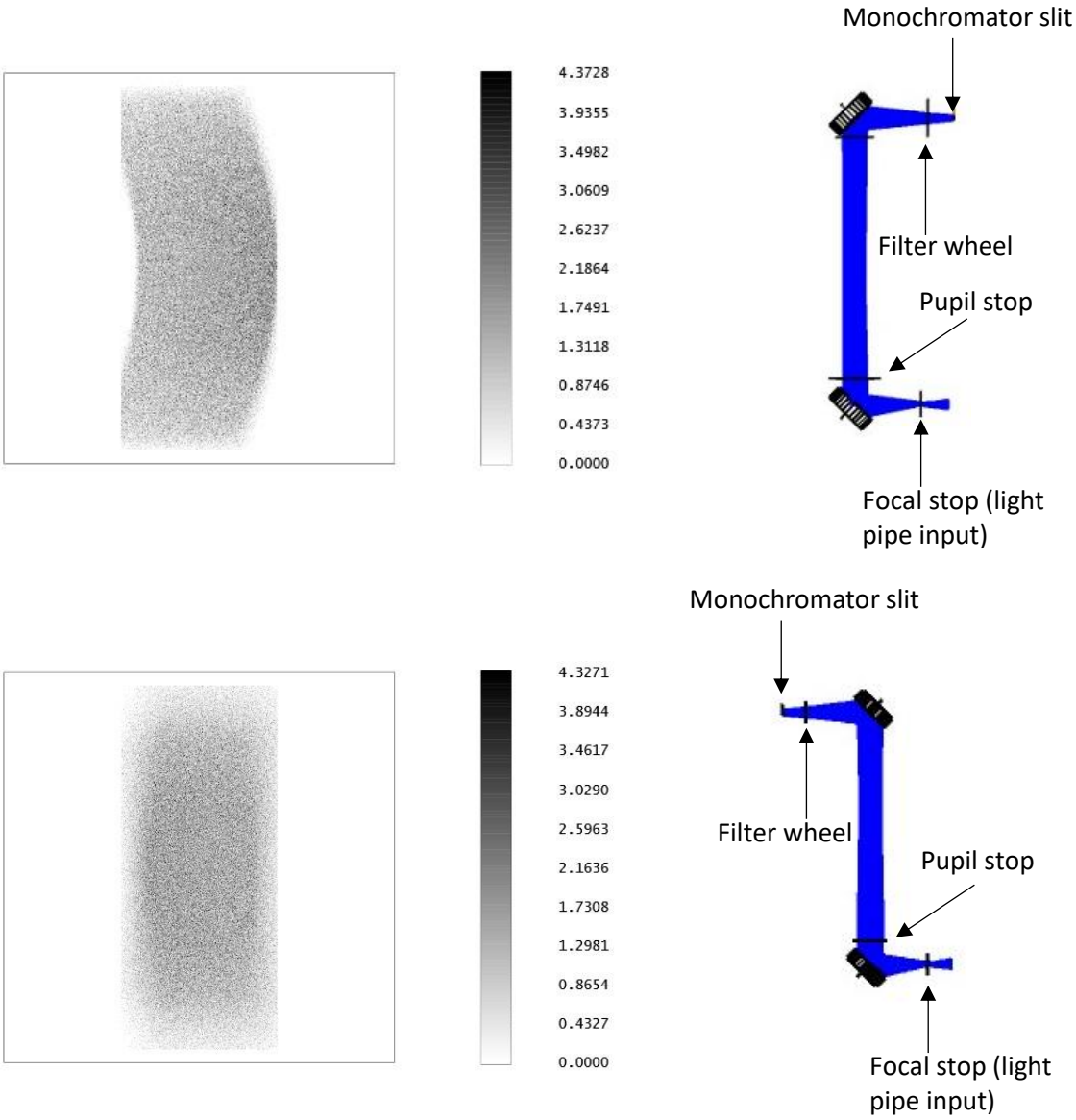

Figure 47: The impact on the monochromator relay image with different parabola orientations.

3.6 CONCLUSIONS

In this chapter, it was shown how Ariel's stellar targets (HD 219134 and GJ 1214) have influenced the OGSE design. In particular, meeting the bright target (HD 219134) flux whilst having a pinhole that is small compared to the Ariel telescope point spread function proved challenging. This had several design implications.

It was shown how representative fluxes for the Ariel stellar targets were flown down requirements on the source relays. Designs of these relays were presented. In the case of the monochromator (Figure 20), the flux is constrained by F/# limitations of the off-the-shelf Bentham TMC300 monochromator. A monochromator radiometric model was created to optimize the output flux. This was used to select the gratings, filters, slit width and mirror coating material. This model also highlighted the importance of out-of-band stray light control, leading to an improved realy design

Despite all of these measures to improve the monochromator flux, it was found that the flux was still non-compliant relative to the Ariel faint target. Because of this, it was desirable to reduce the sphere in size. A reduction in sphere radius is a tradeoff against the spatial uniformity at the output of the sphere. To check the feasibility of meeting the spatial uniformity requirements with a smaller 15 cm sphere, a simplified raytracing model of the sphere was created. Based on these results the sphere was results, the diameter of the sphere was reduced to 15 cm leading to a four times increase in output flux.

To simulate the focal plane response during ground testing, the output of the monochromator and broad-band models was fed into the payload's end-to-end radiometric simulator (ArielRad). This allowed focal plane spectra to be generated. Of particular importance was S/N and saturation times which were used to assess the feasibility of the proposed calibration methods.

4 PHOTOMETRIC STABILITY

Ariel's science goal is to characterise exoplanet atmospheres. The spectral features Ariel will measure are typically tens of ppm relative to the flux of the host star (see Figure 6). Transit depth measurements evaluate the difference between the in-transit and the out-of-transit flux. The time domain nature of transit measurements means the photometric stability of the payload directly translates to the uncertainty in the measured transit depth and therefore the spectral signals of interest. Ariel's photometric stability is therefore critical to its science case, for this reason, the OGSE is required to test the payload gain stability at the payload level (R-CAL-080).

The OGSE must verify the payload is stable to 40 $\mathrm{ppm}\ \sqrt{\mathrm{hr}}$ over a 10hr timescale. As will be discussed, this is an extremely challenging measurement to make. In this chapter, the feasibility of making this measurement at payload level will be assessed. It will also be shown how this test flows to requirements on the OGSE source, reference detectors as well as thermal stability requirements for the integrating sphere.

To estimate the performance required by the OGSE additional modules were added to the Ariel end-to-end simulator [92]. It will be discussed how OGSE source variability can impact the payload photometric stability measurements. The end-to-end simulation allowed time-varying OGSE spectra to be simulated. Moreover, pipeline modules were created to assess how well OGSE source variability could be corrected. It will be shown that a combination of source temperature monitoring and broad-band reference detectors will be required to correct source variability. Moreover, this analysis will be used to place constraints on the detectors and source performance.

Literature data will then be used to assess OGSE detector candidates. Literature measurements will also be used to motivate requirements on the temperature stability of the OGSE detectors. Thermal control models will then be presented to assess if the required thermal stability can be met.

The work completed in this chapter was conducted to define the driving performance requirements of the OGSE for system requirements review (SRR). Results are reported in the following documents

[93, 94]. The assessment of meeting the required thermal stability was completed for PDR and is reported in [95].

4.1 FEASIBILITY OF PERFORMING GAIN STABILITY TESTS AT PAYLOAD LEVEL

Correction of the source variability to 40 $\mathrm{ppm}\sqrt{\mathrm{hr}}$ remains a challenging test. To our knowledge, stability characterisation to this level has never been done before for a spectrometer. Clanton et al. [96] performed detector-level testing of MCT arrays. However, their work was in the context of a wide-field photometric transit survey mission which enables the use of common-mode rejection to detrend source variability. This is not possible for Ariel where only a single star is present in the telescope's field of view during an observation.

For CHEOPS, a payload that photometrically observes single targets, stability was measured at payload level with a precision of 20 ppm over 6 hours [97, 98]. They used a source stabilised to better than 20 ppm which was achieved using a monitoring system and a vignetting knife that attenuates the beam in a closed feedback loop. Such a system will, however, be shown to not be sufficient for Ariel. At the level of 40 $\mathrm{ppm}\sqrt{\mathrm{hr}}$, it is not sufficient to only modulate the amplitude since the spectral dependence of e.g., a drifting black body then becomes important (section 4.2.3.1). Moreover, CHEOPS had the technical advantage of operating from 400 – 1100 nm. This meant the OGSE could be operated at ambient.

For Ariel, payload level gain noise verification will be carried out using illumination from the OGSE (section 1.4). The OGSE will illuminate the detectors, and the variability in the measured signal will be used to assess the stability of the payload. The challenge with performing this test is that the OGSE source is expected to be stable to $\sim 0.5\%$ over 10h [See Bentham IL1 datasheet]. This stability is orders of magnitude worse than the 40 $\mathrm{ppm}\sqrt{\mathrm{hr}}$ stability the OGSE aims to measure (R-CAL-080). Therefore, the source variability must be corrected using knowledge from the reference detectors (Figure 19). In this way, the OGSE source variability will be known and correctable to 40 $\mathrm{ppm}\sqrt{\mathrm{hr}}$.

The OGSE reference detectors are accommodated on the integrating sphere (see Figure 19). To cover the spectral range, OGSE will have three types of reference detectors: A photovoltaic InGaAs for coverage between 0.5 µm -1.95 µm [99], a photovoltaic InSb for coverage between for coverage from 1.95 µm to 5.5 µm, and a photoconductive MCT for coverage between 5.5 µm to 7.8 µm [94].

4.2 PHOTOMETRIC VARIABILITY CORRECTION

Verifying Ariel is photometrically stable to the level required for atmospheric characterisation (40 $\mathrm{ppm}\sqrt{\mathrm{hr}}$, R-CAL-080) has several implications for components within the OGSE design. In this section, we explore the consequences of the gain stability measurement on the parts of the OGSE. Specifically, we define the requirements for the OGSE sources and reference detectors. To address this, two questions must be addressed:

1. How effectively can the raw OGSE variability be corrected by broad-band reference detector data alone?
2. How sensitive is the OGSE detrending pipeline to different types of monitoring uncertainty?

To test how well OGSE source variability can be corrected, a provisional on-ground detrending pipeline has been created. By a combination of sensitivity analysis of the pipeline and prior estimates of uncertainties, individual uncertainty sources can be constrained such that the overall noise budget is consistent with verifying the Ariel gain noise. This pipeline was implemented in ExoSim.

4.2.1 Intro to ExoSim

ExoSim [92] together with ArielRad [91] are the main tools used by the Ariel simulations team to model instrumental noise and systematics. ArielRad was used in Chapter 3 for the radiometric modelling of the OGSE + payload. Whilst ArielRad can predict signal-to-noise and flux vs wavelength, it can not produce 2D spectra nor can it simulate time domain effects (e.g. source drifts). Here we are interested in assessing the effects of OGSE source variability, therefore, a different tool must be used: ExoSim.

ExoSim has a modular structure shown in Figure 48. The first module is the astroscene. This generates the transit light curve given the stellar and orbital parameters of the exosystem. In addition to the light from the exosystem, the zodiacal light can then be added as well as a (time-independent) thermal emission from optical surfaces in Ariel. The star flux, zodi, and self-emission are then propagated through the optical surfaces, accounting for a wavelength-dependent throughput. The light then either arrives at a photometric focal plane or is dispersed by a prism. This focal plane image is then convolved with a wavelength-dependent PSF to produce the irradiance distribution at the focal plane.

The photons are then detected by the focal plane. However, there will be noise sources associated with this detection. The random arrival time of photons will lead to photon noise. Thermal charge excitation will lead to dark current. Finally, there will be stochastic variations in the readout electronics. These three noise processes are all implemented as Gaussian random sources. There are also correlated noise sources that must be accounted for. There is the possibility of gain drifts, e.g. caused by detector temperature variations. Finally, there is the possibility of pointing Jitter. This is implemented by translating the focal plane image with time based on a pointing PSD.

The focal plane signal is then sampled in the desired mode, correlated double sampling or up the ramp, to produce sample Ariel science frames. This simulates the full onboard signal processing chain up to, but not including data compression and the conversion to telemetry [63]. The science frames are then processed through the detrending pipeline [70]. At the time of performing this analysis, most payload detrending steps were still under development.

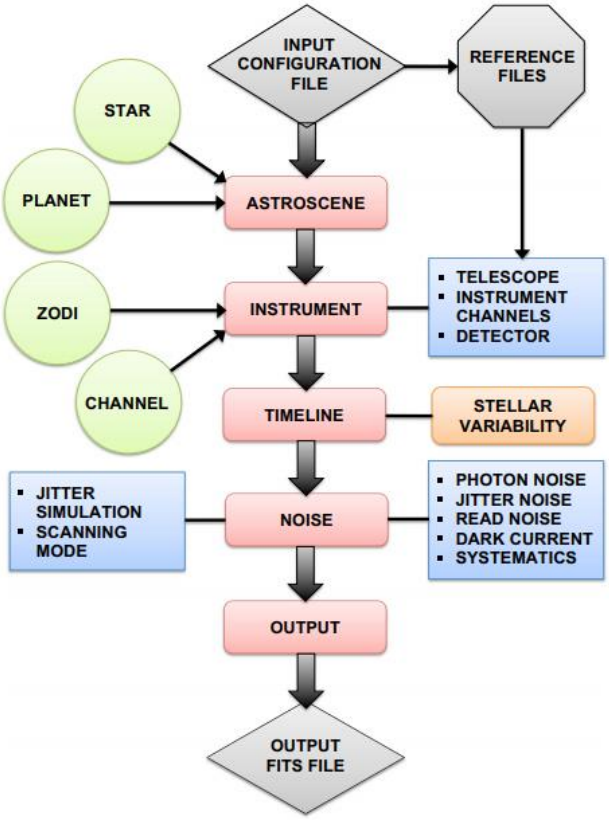

Figure 48: ExoSim structure. Figure from [92].

The pre-existing ExoSim framework was adapted such that the focal plane response of Ariel during ground testing could be simulated. The first change required was to replace the astroscene module (Figure 48) with the OGSE time-varying output flux (section 4.2.2.1). To allow variability correction, the OGSE source flux is then measured by OGSE reference detectors (section 4.2.2.2). In this chapter, it will be discussed if reference detectors alone are enough to correct the time-varying flux. It may also be necessary to monitor the source temperature to provide an additional monitoring constraint (section 4.2.2.3).

In addition to the source, emission from OGSE optics was also simulated (section 4.2.2.4). Pipeline steps were then created to assess how well source variability can be corrected given knowledge from the OGSE reference detectors and source temperature monitoring (section 4.2.2.5).

4.2.2 OGSE ExoSim modules

4.2.2.1 Source module

The OGSE source was modelled as a black body $B(T_{source}(t), \lambda)$ with a time-varying source temperature $T_{source}(t)$. The source flux is then propagated to the sphere through relay optics (Figure 20), and the sphere radiance is calculated. The sphere radiance calculation follows the method described in section 3.1. Using equations 3.2 and 3.1:

$$L_{sphere} = \frac{\eta_{sor}\varepsilon_{source}\, A_s\Omega_s}{\pi A_{sphere}} \frac{\rho}{1-\rho(1-f)} B(T_{source}, \lambda) \equiv \kappa(\lambda) B(T_{source}, \lambda) \tag{4.1}$$

Here we adopt a condensed notation where all the time-invariant constants are grouped into a wavelength-dependent function $\kappa(\lambda)$. $\kappa(\lambda)$ is the proportionality between the source and sphere radiance and can be evaluated using the requirements derived in Table 3.

In addition to source temperature variability, we also model vignetting-induced variability. The OGSE sources are known to vignette at various points before the sphere (e.g. Figure 30). If there are also any drifts/jitter in the alignment, this will cause a time-varying flux variation that may be important at the level of tens of ppm. This time-varying vignetting is represented as a wavelength-independent attenuation $\delta\alpha(t)$.

$$L_{sphere}(t, \lambda) = \big(1 + \delta\alpha(t)\big)\kappa(\lambda) B(T_{source}(t), \lambda) \tag{4.2}$$

Not modelled, but also of interest is variability introduced by changes in gas composition (e.g. humidity). This will have a different spectral signature to vignetting or temperature drifts. To minimise this effect, the optics outside the chamber will be operated in a nitrogen purge.

An example AIRS CH1 focal plane spectrum with the OGSE IR source is shown in Figure 49.

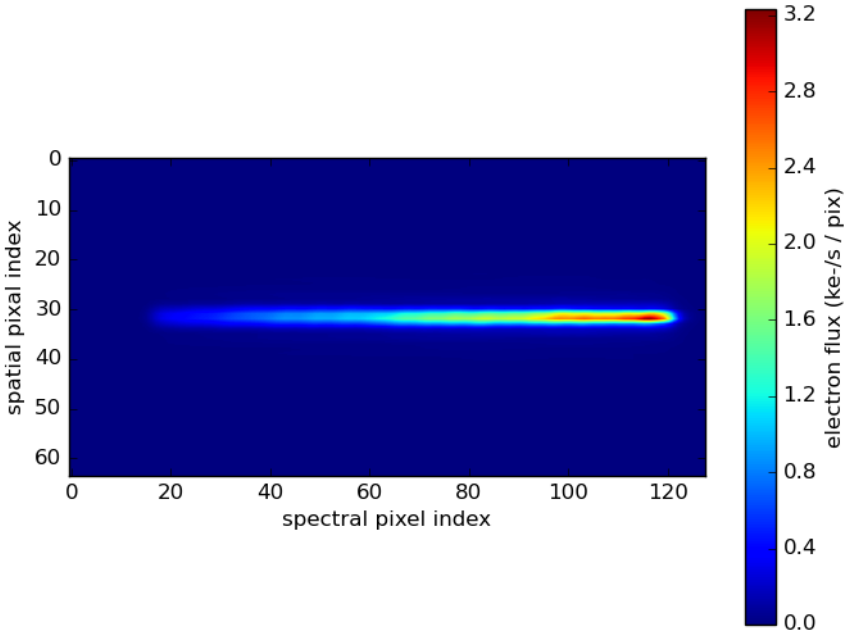

Figure 49: Focal plane electron flux when illuminated with the OGSE IR source. This observation is in the faint observing mode which matches the band-averaged flux of the faint target (R-OGSE-5200).

4.2.2.2 Sphere reference detector module

To enable correction of the OGSE source variability, the integrating sphere features broad-band reference detectors. The power incident on these detectors is governed by the sphere radiance, L_{sphere}, and the etendue of the detector, $A\Omega$. The detector will map the incident power (W) into a signal in arbitrary digital units (ADU). The conversion between the innocent power and the measured signal is described by the detector responsivity, $R(\lambda)$. For simplicity, this was modelled as being spectrally independent e.g. representing a gold-black coated thermopile. Later, semiconductor-based detectors were selected. The characteristics of the chosen detectors will be described in section 4.3.

The OGSE reference detectors will have non-ideal characteristics. To place bounds on the maximum allowable detector noise, stochastic noise sources were applied to the ideal detector signal. This included additive noise, $\delta_{add}(t)$ (e.g. Johnson noise, photon noise…), and stochastic gain variations ($\delta_{gain}(\lambda, t, T, \Phi)$). This noise breakdown follows the approach used in the Ariel noise model [68] and is discussed in section 2.2.6.

The measured reference detector signal in arbitrary digital units (ADU) is:

$$V_m(t) = (1 + \delta\alpha) \int_0^\infty A\Omega\kappa(\lambda) SED(T_{source}(t), \lambda) R(\lambda) \left(1 + \delta_{gain}(\lambda, t, T, \Phi)\right) d\lambda \; + \delta_{add}(t) \quad (4.3)$$

4.2.2.3 Source temperature monitoring module

In addition to reference detectors, it is planned to directly monitor the source temperatures. This provides an additional constraint when correcting flux variability. For the IR source, the temperature will be measured directly with a thermocouple on the source. For the VIS source, this is not possible. The colour temperature will therefore be measured spectroscopically.

To define the required measurement accuracy, a stochastic temperature measurement error was added to the model as well as a systematic monitoring offset.

4.2.2.4 OGSE thermal emission module

Thermal emission from OGSE optical surfaces is modelled as a black body with a defined emissivity (0.03[29]). Emission is assumed to be homogeneous across the optical elements' surfaces and isotropic across the payload FOV. The black body spectrum is propagated through the telescope optics and attenuated by dichroic and mirror absorption.

ExoSim then disperses the signal through the focal plane prism. The focal plane intensity distribution is the convolution of the spatial intensity distribution (flat over the AIRS FOV, zero elsewhere) with the prism spectral response function. The resulting thermal background electron count for a single Non-Destructive-Read (NDR) is shown in Figure 50.

[29] Assumed wavelength independent at this stage. When this analysis was conducted the mirror coatings were still to be confirmed.

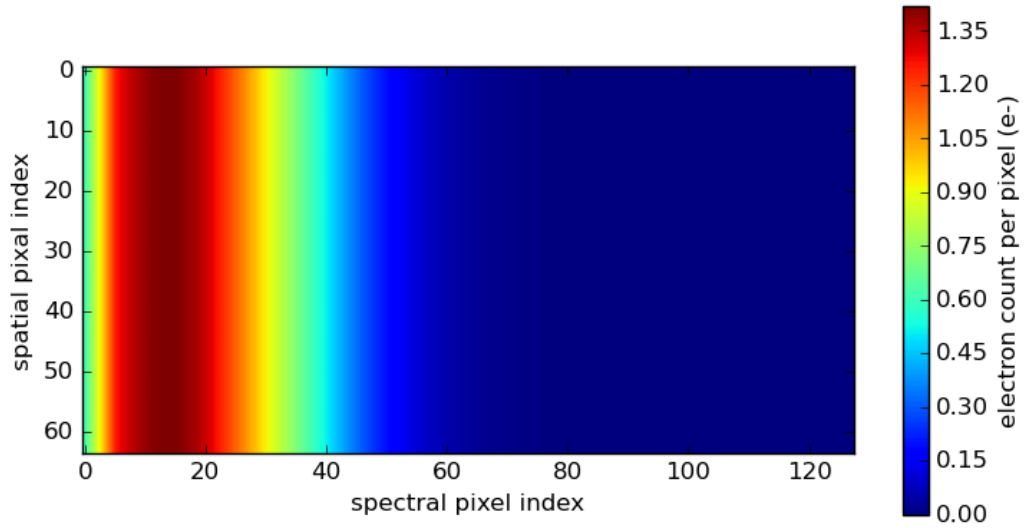

Figure 50: Example AIRS CH1 thermal background NDR. Calculated for a 70K sphere with 12s integration time.

For validation and understanding of the functional dependence of the ExoSim model, the AIRS slit convolution was also evaluated in the thin slit limit. Under this assumption, the top hat convolution can be replaced with a Dirac delta. This provides the following expression for the electron flux, F per pixel:

$$F(x) = \eta(\lambda)\varepsilon B(T,\lambda)\frac{d\lambda}{dx}\Delta x_{pix} A_{pix}\Omega_f R(\lambda) N_{spec} \tag{4.4}$$

Where $\eta(\lambda)$ is the attenuation of the payload optics, ε is the emissivity of the emitting surface, $B(T,\lambda)$ is the standard blackbody function, $\lambda(x)$ is the wavelength solution of the prism[30], Δx_{pix} is the width of the pixel (spectral direction), A_{pix} is the area of the pixel, Ω_f is the solid angle of the focusing mirror as viewed at the focal plane, $R(\lambda)$ is the responsivity of the detector, $N_{spec}$is the size of the AIRS slit in the spectral direction in units of pixels.

[30] The wavelength corresponding to each pixel for on-axis point source illumination.

The agreement of the thin slit analytical model (equation 4.4) with the ExoSim implementation that uses the full tophat convolution can be seen in Figure 51. At 8 microns the thin slit approximation breaks down. This occurs when the pixel position is less than the slit width of the edge of the detector. However, this is outside of the defined wavelength range of Ariel (<7.8 μm) so is not of concern for this analysis. Moreover, in the analytical formulation, one can see ripples coming from spectral throughput variations. These ripples get smoothed out by the slit convolution but not in the thin slit limit. This only causes a few per cent deviation from the ExoSim calculation though.

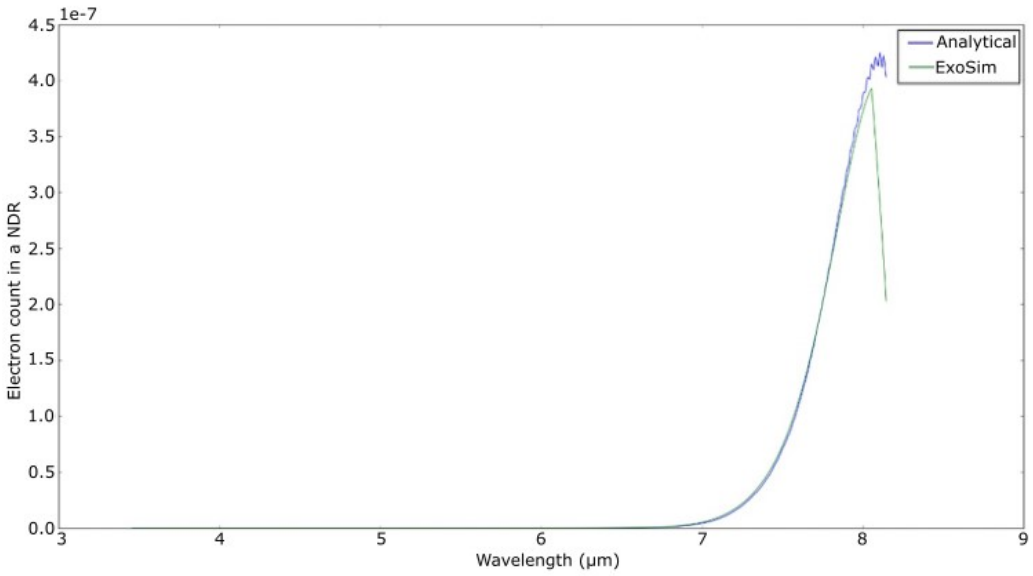

Figure 51: Comparison of the numerical ExoSim model with the analytical expression described in eq 4.4. The ripples seen in the analytical are due to absorption within the PLM.

The results of the OGSE thermal background module will be discussed further in section 5.1. In particular, it will be shown how the thermal backgrounds impact the required mirror temperature. In this chapter, we focus on the definition of the source monitoring requirements.

4.2.2.5 Pipeline modules

As discussed above, it is not expected that the OGSE sources will be stable to the level required to verify the gain stability (40 $\mathrm{ppm}\ \sqrt{\mathrm{hr}}$) without correction. Therefore, an assessment must be made of

how well source variability can be corrected. The following steps of the payload pipeline[70] are of particular importance when correcting OGSE systematics:

- Background subtraction using off-science pixels.
- Masking off high background regions of the array.
- Residual systematics correction – time-domain fitting of data to a transit model

The first two of these steps can be used to reduce the impact of OGSE thermal emission and stray light. The final step can be used to reduce the impact slowly (hrs) varying source drifts. This uses the time correlation of long-period systematics, essentially short-pass filtering the data (see [100]).

In addition to the flight pipeline steps. The OGSE will also use a reference detector and source temperature data to correct source variation.

4.2.2.5.1 Correction method 1 – Physics agnostic method

Section 4.2.2.1 describes the sphere variability model which includes amplitude and temperature variations. The first approach explored to correct the signal variability was to scale all focal plane pixels by an amount proportional to the sphere flux variability (as measured by a broad-band reference detector). For example, if the reference detector signal increased by 1%, at some time, all focal plane pixels get divided by 1.01. The advantage of this approach is the correction makes no assumption about the origin of the drift. Moreover, given only a single observable, a bolometric correction is likely the best that can be performed.

4.2.2.5.2 Correction method 2 – noisy reference detector data

In section 4.2.2.5.1 a physics-agnostic correction was presented. It will be shown, however, that without some knowledge of the underlying cause of the variability, correction to the level of tens of ppm will likely not be possible. Here we consider an alternative correction. This method allows us to combine information from temperature sensors and reference detectors. This method, does, however, suffer from the problem that the forward and correction models are the same. Therefore, it

may overpredict the correction efficacy if physics not included in the model is important (e.g. humidity variation).

This model, does, however, allow a quantitative prediction of how OGSE detector and temperature monitoring errors propagate to the uncertainty in the payload gain stability.

The correction takes the form of a matrix (M) with the wavelength in one direction and time in the other. It describes how, at a given wavelength, subsequent radiances compare to the initial radiance[31]. For convenience, we define matrix to be the fractional change in flux from the initial radiance. It is, therefore, filled with values close ($\lesssim 1\%$ deviation) to one.

$$M \equiv \frac{L(t,\lambda)}{L(0,\lambda)} = 1 + \frac{\Delta L(t,\lambda)}{L(0,\lambda)} \tag{4.5}$$

To correct the OGSE source variation, the focal plane image stack is divided by this correction matrix[32]. It is assumed this correction will be applied after payload systematics such as dark current, point jitter, etc. have already been accounted for (at the end of level 1.5 using the notation in [70]).

This method allows knowledge to be combined from two sources. The two observables known to the observer are the reference detector signal (V_p) and the source temperature drift ΔT. The correction matrix will, therefore, be some function $\mathrm{M}(\mathrm{V_p}, \Delta T)$. For the correction, we assume the same source variability as the forward model (4.2). This implies the following form for the correction:

[31] The choice of normalising to the initial value is arbitrary and is chosen for ease of explanation. However experimentally, the initial value is often less stable e.g. due to some settling time being required, therefore, in practice, another normalisation may be preferred.

[32] After resizing this matrix to a 3D array. This implicitly assumes flux variability is correlated in the spatial direction of the array.

$$M \approx 1 + \frac{\frac{dB}{dT}\Delta\mathrm{T} + \big(\delta\alpha(t) - \delta\alpha(0)\big)B(T_0, \lambda)}{\big(1 + \delta\alpha(0)\big)B(T_0, \lambda)} \tag{4.6}$$

From the form of the correction matrix shown in equation 4.6, one can explicitly see the contribution from a predicted thermal drift, $\frac{dB}{dT}\Delta\mathrm{T}$, and the contribution from a vignetting variation, $\big(\delta\alpha(t) - \delta\alpha(0)\big)B(T_0, \lambda)$, to the correction that is being applied. This also shows how information from two sources, the photometric reference detector and source temperature monitoring, can be combined to provide a correction that can distinguish amplitude variations from source drifts. Moreover, one can see how different sources of uncertainty propagate and impact the final correction efficacy.

To predict the relative contributions of vignetting $\big(\delta\alpha(t) - \delta\alpha(0)\big)$ and source drifts ΔT, the reference detector model (section 4.2.2.2) can be used:

$$V_p(t) = \big(1 + \delta\alpha(t)\big)\int_0^\infty A\Omega\kappa(\lambda)\left(B(T_0, \lambda) + \frac{dB}{dT}\Delta T\right)R(\lambda)\, d\lambda \tag{4.7}$$

This can be rearranged to estimate the vignetting variation at some time t

$$\delta\alpha(t) = \frac{V_p(t)}{\int_0^\infty A\Omega\alpha_\lambda\left(B(T_0, \lambda) + \frac{dB}{dT}\Delta T\right)R(\lambda)d\lambda} - 1 \tag{4.8}$$

By substituting 4.8 into 4.6 a matrix to correct source variability can be derived.

This concludes the additional ExoSim modules required to define the source monitoring requirements.

4.2.3 Flux variation correction results

The source, monitoring and correction models described in 4.2.2 were then used to simulate the gain stability measurements of the payload using the OGSE. Multiple cases will be explored here to quantify how well it will be possible to monitor and correct the OGSE spectrum. In the first case, we consider ideal noise-free reference detectors. Even in the noise-free case, it is non-trivial to recover the OGSE output power since there is no guarantee the flux will change by the same amount at all wavelengths.

If the flux changes by different amounts at different wavelengths, it may not be able to recover the spectrum given only a broad-band reference detector information. To investigate this, we consider an example where the source experiences both a temperature drift as well time-dependent vignetting.

For subsequent cases, detector noise will be added. This allows requirements to be placed on the maximum OGSE detector noise and the required OGSE detector gain stability.

When the payload is illuminated in the OGSE bright mode, the payload has the lowest noise to signal ratio (40 $\mathrm{ppm}\sqrt{\mathrm{hr}}$ [101]). This will be used to drive the gain stability of the OGSE reference detectors.

When the payload is illuminated in the OGSE faint mode, the payload is photon noise limited (e.g. 200 $\mathrm{ppm}\sqrt{\mathrm{hr}}$ at wavelengths longer than 1.95 μm [101]). The correction in the faint mode, therefore, is less stringent than the bright case. However, the lower source flux means effects such as dark current in the OGSE reference detectors become more significant. The faint case will therefore be used to drive the maximum additive noise in the OGSE detectors.

4.2.3.1 Physics-agnostic correction

The first correction case considered follows the method described in 4.2.2.5.1. The goal of this method is to assess if knowledge of the underlying physical mechanism is required to correct the signal to the level of tens of ppm. Equivalently, if a principal component style correction ends up being used, here we are assessing if we should expect >1 principal component to be important.

The simplest correction to apply, which requires no knowledge of the underlying mechanism of the variability would be to scale the measured signal by the change in the reference detector signal. This correction is shown in Figure 52 - right. To model the source drift a 0.5% drift[33] in bolometric flux was

[33] See Bentham IL1 datasheet

assumed, and was implemented as a change in the emitting filament temperature. The functional form of the drift is not yet known so was nominally implemented as a sinusoidal function (e.g. driven by changes in the ambient air temperature).

The effectiveness of the correction described in 4.2.2.5.1 depends strongly on the assumption made about the origin of the radiance variability. If the radiance variation is dominated by vignetting, then this correction could, in the absence of any reference detector noise, be perfect (since this should affect all wavelengths equally). However, if this spectrally independent correction was applied to variation caused by a temperature drift, a perfect correction at all wavelengths would not be possible (even in the absence of any reference detector noise). Since, at this point, we only have one observable, the broad-band reference detector signal, it is not possible to distinguish a source temperature drift from an amplitude variation, therefore, here we make the worst-case assumption of correcting a source temperature drift with a spectrally invariant amplitude correction. From this one can infer whether a correction model with one free parameter is sufficient.

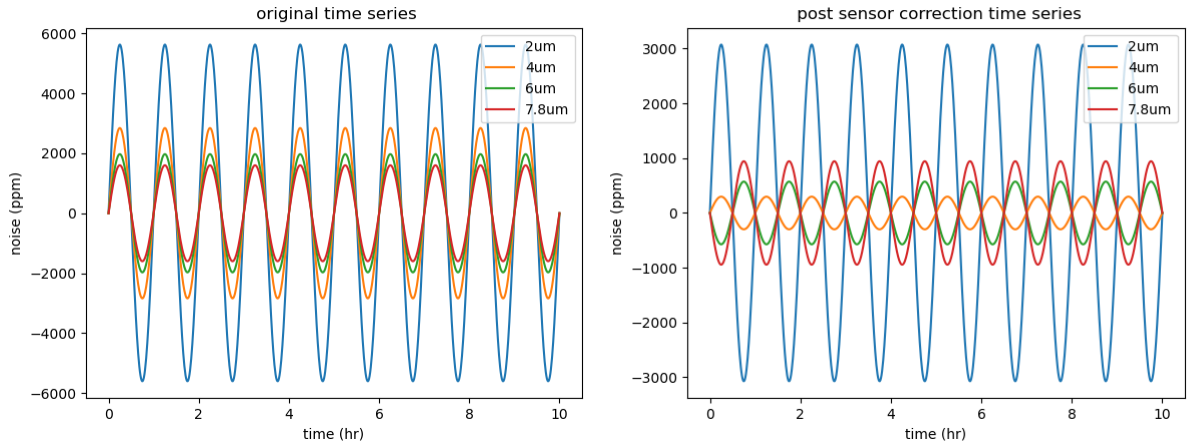

Figure 52: Left shows the original time series that is injected. Right shows the residual variation post-correction.

From Figure 52, one can see that some wavelengths ($> 4\mu m$) are overcorrected, and other wavelengths are significantly undercorrected. This leaves a residual uncertainty that is likely too large to verify the Ariel gain drift. *Therefore, we need more than one piece of information so that we can*

distinguish between amplitude and source temperature variations. This motivates the source temperature monitoring requirement.

4.2.3.2 Bright Mode correction (random noise only)

Subsequent models used the correction described in 4.2.2.5.2. This enables information from source temperature monitoring to be combined with reference detector information, leading to a more effective correction. Noise is also added to the reference detectors and the temperature sensors (Table 5 & Table 6) to place bounds on the maximum allowable noise.

To place constraints on the required OGSE detector gain stability, the correction of the OGSE in the bright mode is considered. Here, only white noise sources are included. The assumed source and monitoring parameters are shown in Table 4, Table 5 & Table 6. The following plots (Figure 53 & Figure 54) were evaluated for the 800 K IR source and a 3360 K VIS source [51]. The integration time used for this simulation was 45 s (corresponding to the maximum frequency defined in the Ariel noise band, R-PRD-0470).

Pre-correction thermal drift (peak-to-peak)	1K / 4.2K for the IR/VIS sources (0.5% variation in bolometric flux)
Pre-correction amplitude type variation (1σ)	0.5%

Table 4: Source parameters used for bright mode simulations.

The source parameters are conservatively motivated by the Bentham IL1 Halogen Source spec for the vis source and discussions with HeatWave Labs for the IR source.

Reference detector additive nose (1σ)	79 ppm$\sqrt{s}$ (1.3 ppm$\sqrt{hr}$)
Reference detector gain nose (1σ)	1440 ppm$\sqrt{s}$ (24 ppm$\sqrt{hr}$)
Source temperature monitoring relative uncertainty (1σ)	0.5 K$\sqrt{s}$

Table 5: Monitoring parameters used for the bright mode simulations (IR band).

Reference detector additive nose (1σ)	6.4 ppm$\sqrt{s}$ (0.11 ppm$\sqrt{hr}$)
Reference detector gain nose (1σ)	1400 ppm$\sqrt{s}$ (24 ppm$\sqrt{hr}$)
Source temperature monitoring relative uncertainty (1σ)	2.5 K$\sqrt{s}$

Table 6: Monitoring parameters used for the bright mode simulations (VIS band).

The sub-allocation of uncertainty between the different noise sources (Table 5 & Table 6) was done by sensitivity analysis. This ensured the relative impact of the colour temperature monitoring uncertainty and gain noise was roughly equal whilst ensuring the total post-correction variability did not exceed 40 ppm$\sqrt{hr}$. The additive noise was set by faint mode considerations (see section 4.2.3.3).

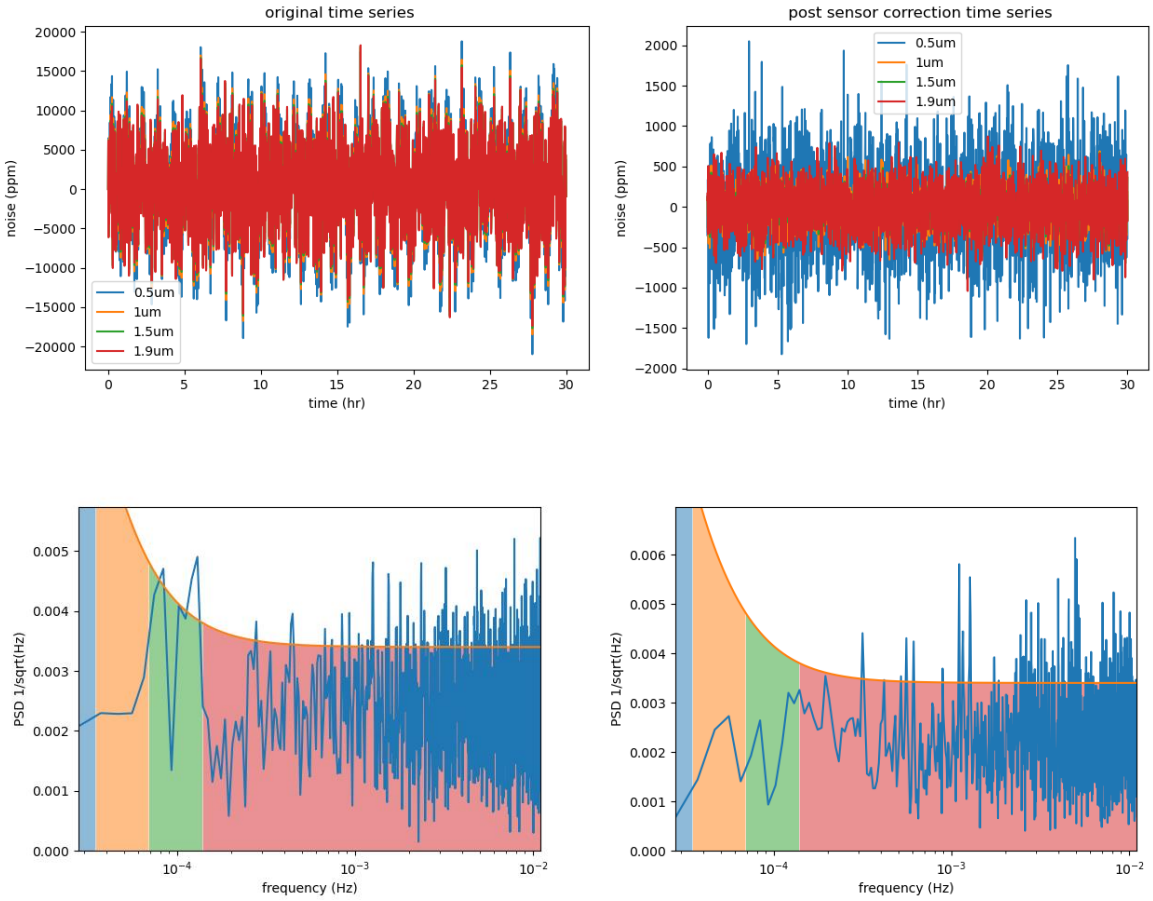

Figure 53: Top left shows the VIS source time series (a normalised version of equation 4.2), top right shows the VIS source variability after correction with a reference detector and temperature sensor (as described in 4.2.2.5.2). Bottom left shows the PSD of the VIS source, post-correction. Bottom right shows the PSD of the IR source, post-correction. These figures are calculated using the parameters listed in Table 4, Table 5 & Table 6.

The lower plots of Figure 53 show the noise power spectrum after correction. The highlighted region in the lower plots shows the required noise after correction (R-PRD-8818). By comparing the post-correction source variability to the PSD requirements, it can be determined if the monitoring uncertainties described in Table 4, Table 5 & Table 6 are consistent with detrending source variability to 40 $\mathrm{ppm}\ \sqrt{\mathrm{hr}}$. From the PSDs shown in Figure 53, the integral of the PSD^2 was evaluated over the red region and compared to 356 ppm (see R-PRD-8818). The red region was chosen as it is the most stringent driver for the white noise analysis presented here.

For the parameters described in Table 4, Table 5 & Table 6, the VIS source integral was evaluated to be 270 ppm, and the IR was evaluated to be 262 ppm. These are both consistent with the 356 ppm requirement with ~25% margin to account for photometric error due to optomechanical vibrations after the integrating sphere which are not included in this model. The assumed parameters (Table 4, Table 5 & Table 6) are, therefore, consistent with the payload gain stability measurement.

4.2.3.3 Faint mode correction (random noise only)

The second case of interest is the faint mode detrending of the OGSE since this drives the additive noise requirement for the reference detectors. In the faint mode, the broadband sources are fainter by a factor of 114 and 311 in the IR and VIS bands respectively. Therefore, whilst the OGSE gain noise and colour temperature monitoring uncertainty remain unchanged, the impact of additive noise is increased by this factor. It is with this increased additive noise, that the OGSE must be able to detrend to the Ariel photon noise limit. The faint mode photon noise limit is, however, less stringent than 40 $\mathrm{ppm}\ \sqrt{\mathrm{hr}}$.

In the faint mode, the OGSE needs to verify Ariel's photometric stability to the Ariel photon noise limit. For design purposes, we defined this to be 200 $\mathrm{ppm}\ \sqrt{\mathrm{hr}}$ in the IR (>1.95µm) and 60 $\mathrm{ppm}\ \sqrt{\mathrm{hr}}$ in the VIS band (<1.95 µm) [101]. The method used throughout this analysis to assess compliance was to compare to the tiger team PSD (see R-PRD-8818; Appendix C), this PSD is, however, defined for the bright mode and must be generalised to describe the acceptable level of variability in the faint mode. This was done by scaling the PSD by 200 $\mathrm{ppm}\ \sqrt{\mathrm{hr}}$/40 $\mathrm{ppm}\ \sqrt{\mathrm{hr}}$ and 60 $\mathrm{ppm}\ \sqrt{\mathrm{hr}}$/40 $\mathrm{ppm}\ \sqrt{\mathrm{hr}}$ in the IR and VIS bands respectively. This ensures the high-frequency tail tends towards the photon noise limit.

The source variability parameters used were the same as those described for the bright mode (Table 4), as were the assumed gain stability and colour monitoring uncertainty. The additive noise was then tuned to give a post-correction variability that was consistent with the faint mode PSD (see Figure 54).

Reference detector additive nose (1σ)	9,000 ppm $\sqrt{s}$ (150 ppm $\sqrt{hr}$)
Reference detector gain nose (1σ)	1440 ppm $\sqrt{s}$ (24 ppm $\sqrt{hr}$)
Source temperature monitoring relative uncertainty (1σ)	0.5K $\sqrt{s}$

Table 7: Monitoring uncertainties used for the faint mode analysis (IR band).

Reference detector additive nose (1σ)	2000 ppm $\sqrt{s}$ (33 ppm $\sqrt{hr}$)
Reference detector gain nose (1σ)	1400 ppm $\sqrt{s}$ (24 ppm $\sqrt{hr}$)
Source temperature monitoring relative uncertainty (1σ)	2.5 K $\sqrt{s}$

Table 8: Monitoring uncertainties used for the faint mode analysis (VIS band).

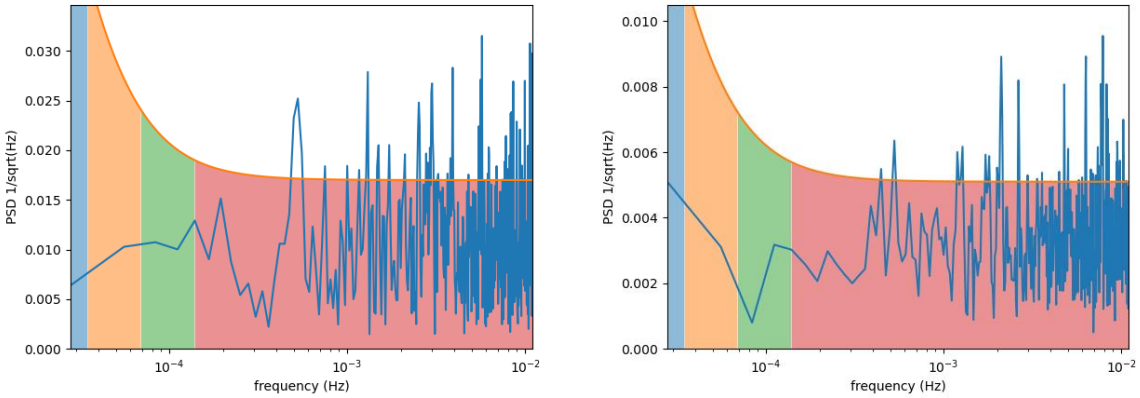

Figure 54: Faint mode correction efficacy resulting from the monitoring uncertainties described in Table 7 & Table 8. This is shown as the post-correction PSD of the VIS (left) and the IR (right) sources.

Similarly to the bright mode, the corrected source variability (Figure 54) can be compared to the photon noise limit using PSD integrals. The 60 ppm $\sqrt{hr}$ and 200 ppm $\sqrt{hr}$ photon noise threshold corresponds to a required PSD integral of 534ppm in the VIS and 1780ppm in the IR. The integral of the post-correction time series has a variability of 400ppm and 1348ppm for the VIS and IR. This is consistent with the photon noise limit with a ~25% margin. Therefore, 33 ppm $\sqrt{hr}$ & 150 ppm $\sqrt{hr}$ reference detector additive noise requirements are proposed for the VIS and IR reference detectors respectively (defined relative to the source signal in the faint mode).

4.2.4 Source correction pipeline conclusions

The gain drift requirement (R-CAL-080) is defined in terms of post-correction noise (40 ppm $\sqrt{\text{hr}}$ in the bright mode and the photon noise in the faint mode). To verify Ariel gain drifts, the OGSE source variability must be corrected to a level less than the Ariel stability. The purpose of this work is to place source monitoring requirements such that a detrending pipeline can correct to this level.

In section 4.2.3.1, a correction model was presented that only utilised a broad-band reference detector. It was found that if the sphere radiance can vary in both amplitude (as caused e.g. by vignetting) and due to source temperature drifts, a broad-band reference detector alone was insufficient to correct the spectrum to the level required to verify the Ariel gain noise. Therefore, colour temperature monitoring, in addition to broad-band photometric monitoring, is likely necessary to correct the spectrum to 40 ppm $\sqrt{\text{hr}}$. This provides two constraints to correct the OGSE spectrum variability.

It is still possible, however, that if three state variables are important (e.g. source temperature + vignetting + humidity), two observables may still not be sufficient to correct to the level of 40 ppm $\sqrt{\text{hr}}$. Though predicting the number of state variables is extremely challenging a priori. This is best assessed by assessing the spectral dependence of the payload variability during payload EM testing.

In section 4.2.2.5.2 a more general framework was described for combining knowledge from both source temperature monitoring as well as broad-band photometric monitoring. Given both these pieces of information, an adequate level of correction can be reached provided monitoring uncertainties can be made sufficiently small (Table 9, Table 10). This defines the reference detector noise and source temperature monitoring requirements.

IR band monitoring requirements

Faint mode reference detector additive nose (1σ)	9,000 ppm $\sqrt{s}$ (150 ppm $\sqrt{hr}$)
Reference detector gain nose (1σ)	1,440 ppm $\sqrt{s}$ (24 ppm $\sqrt{hr}$)
Source temperature relative monitoring uncertainty (1σ)	0.5 K $\sqrt{s}$

Table 9: IR monitoring requirements

VIS band monitoring requirements

Faint mode reference detector additive nose (1σ)	2,000 ppm $\sqrt{s}$ (33 ppm $\sqrt{hr}$)
Reference detector gain nose (1σ)	1,440 ppm $\sqrt{s}$ (24 ppm $\sqrt{hr}$)
Source temperature relative monitoring uncertainty (1σ)	2.5 K $\sqrt{s}$

Table 10: VIS monitoring requirements.

4.3 DETECTOR SELECTION

The OGSE is required to verify Ariel's photometric stability[34]. To do this, OGSE source variability must be detrended to this level. This drives the source monitoring requirements. The OGSE gain noise budget (section 4.2) explored a possible method of detrending OGSE source variability. This determined the required level of colour temperature monitoring, reference detector noise and reference detector stability. It was found that to detrend the IR source variability, the monitoring uncertainties need to be less than the values in Table 9.

In the IR, it is planned that this source monitoring will be achieved using a broad-band InSb reference detector (for coverage from 1.95 µm to ~5.5 µm). Colour temperature monitoring will be achieved by direct monitoring of the source with a thermocouple. An additional broad-band 12 µm cut-off MCT

[34] 40 ppm $\sqrt{hr}$ in the bright mode and the photon noise limit in the faint mode (R-CAL-080).

will provide an additional colour constraint on the source with the goal that this additional MCT also follows the noise and stability parameters described in Table 9. This section assesses the feasibility of using MCT and InSb detectors for source monitoring. The monitoring of the VIS source is the responsibility of the Lisbon team and is described in [99]. Here we focus on the IR detectors (> 1.95 microns).

Various sources of uncertainty can contribute to the reference detector monitoring uncertainty. We break these into two classes:

- Additive noise sources (sources of noise that add to the measured signal independent of the signal). For example, dark current.
- Gain variations (sources of variability that multiply the signal). For example, QE variations & amplification gain drifts, vignetting.

Here we focus only on quantifying the expected detector additive and gain stability given literature data. It is assumed that the performance of the monitoring system will be limited by the detector element. Assessment of the amplification electronics performance will be the subject of future work.

The manufacturer provides D* information on the source. However, for further information on other effects that may impact stability, literature data must be used. This data is then used to place an order of magnitude constraints on the expected photon noise, QE stability, dark current shot noise & dark current drifts. Given the expected QE stability and dark current, constraints can be placed on the sphere temperature and the temperature stability.

4.3.1 Sources of uncertainty

4.3.1.1 Photon noise

The first noise source to consider comes from the random arrival time of photons at the reference detector. The photon noise on the reference detector will be highest (relative to the signal) in the

OGSE faint mode (Table 3). There are also two types of detectors. The MCT has a 0.1 mm active area and the InSb with a 0.25 mm active area.

The photon noise will be worse for the smaller 0.1mm MCT. The signal power absorbed will be on the order ~ 3×10^{-9} W (see Table 3). Assuming a characteristic QE of 0.7 [102] , and a characteristic photon energy of $\frac{hc}{\lambda}$ where $\lambda = 2\ \mu\text{m}$[35], the measured electron flux is $\Phi_{\text{MCT}} = 2 \times 10^{10}\ \text{es}^{-1}$. Therefore, the photon noise-to-signal ratio is $\frac{1}{\sqrt{\Phi_{\text{MCT}}}} = 7\ \text{ppm}\ \sqrt{\text{s}} = 0.1\ \text{ppm}\ \sqrt{\text{hr}}$.

Therefore, for both the InSb and the MCT, photon noise will contribute negligibly to the reference detector noise budget.

4.3.1.2 D* comparison

A standard metric for detector performance is the specific detecivity. The specific detectivity D^* is defined to be:

$$D^* = \frac{\sqrt{A\Delta f}}{NEP} \tag{4.9}$$

Without loss of generality, we evaluate the NEP at 1Hz. This corresponds to a 0.5 s integration time. At 0.5 s integration time, the additive noise requirement ($150\ \text{ppm}\sqrt{\text{hr}}$) corresponds to a noise-to-signal ratio of $18000\ \text{ppm}$. This can then be converted to a NEP, and a required D*. These are shown in Table 11.

	Detector size (m)	Power incident on detector (W)	NEP @1Hz (W)	D* ($\text{cmHz}^{0.5}\text{W}^{-1}$)
InSb	2.50×10^{-4}	1.66×10^{-8}	2.99×10^{-10}	8.35×10^{-7}
MCT	1.00×10^{-4}	2.66×10^{-9}	4.79×10^{-11}	2.09×10^{8}

Table 11: D* requirements.

[35] Worst case assumption for the IR band (2-8 microns)

The manufacturer quoted D* (Figure 55) are approximately two orders of magnitude better than those needed to meet the reference detector additive noise performance specification.

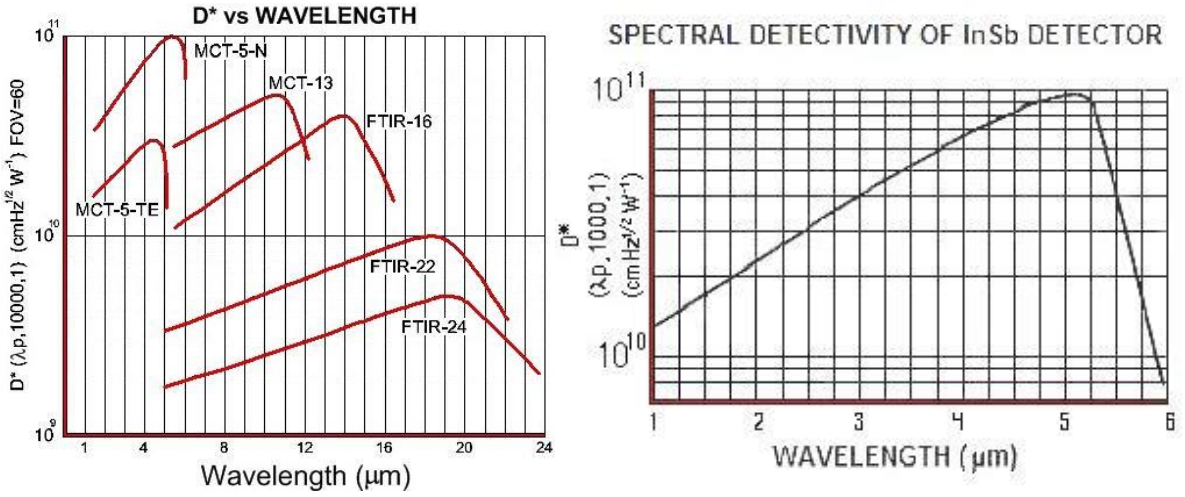

Figure 55: Left shows the quoted D performance for the MCT-13. Right shows the D* performance of the InSb detector. Data from IR associates.*

4.3.1.3 QE stability

To assess any further non-ideal detector characteristics, literature data must be used. An effect that could impact the OGSE's ability to detrend the source variability would be any drift in our detector's quantum efficiency (caused by a drift in detector temperature). This is of particular concern, as a drift in QE could be mistaken for a drift in OGSE source flux.

QE drifts can be caused by a drift in the detector temperature. The QE temperature sensitivity can then be used to place a provisional constraint on the sphere temperature stability/monitoring.

The long wave (up to ~12 μm) MCT detectors were extensively characterised as a part of the EChO mission [102, 103]. Data on the QE temperature sensitivity of InSb detectors was measured as a part of the Spitzer mission [104].

4.3.1.3.1 MCT QE stability

From [102], we see that the QE of the tested MCT detectors varies by ~0.03 over 5 K (70 – 65 K). Therefore, the normalised QE temperature sensitivity is $S \approx 8600\ \mathrm{ppm\ K^{-1}}$. Since a drift in QE is seen

as a drift in the measured signal, we require that the product of the thermal stability and the QE sensitivity to be less than required gain stability.

To achieve $24\ \mathrm{ppm}\sqrt{\mathrm{hr}}$ QE stability (the total stability allocation to all gain type effects), the temperature stability/ monitoring needs to be:

$$S\Delta T = 24\ \mathrm{ppm}\sqrt{\mathrm{hr}}$$

$$\rightarrow \Delta T = 2.8\ \mathrm{mK}\ \sqrt{\mathrm{hr}}$$

4.3.1.3.2 InSb QE stability

The temperature dependence of the InSb QE was measured as a part of the Spitzer test campaign [104]. They quote a change in QE of <2% change over the temperature range 15 K to 35 K. Whilst this is colder than the temperature range of interest, this can be used to predict a QE temperature sensitivity of $1000\ \mathrm{ppm\ K^{-1}}$.

Given this QE temperature sensitivity, to achieve $24\ \mathrm{ppm}\sqrt{\mathrm{hr}}$ QE stability, the temperature stability/ monitoring needs to be $24\ \mathrm{mK}\ \sqrt{\mathrm{hr}}$.

4.3.1.3.3 Thermal stability requirement

For the InSb detectors, ~24 mK $\sqrt{\mathrm{hr}}$ stability/ monitoring would be needed to negate the impact of QE variations. For the MCT detectors, the stability would need to be ~2.8 mK $\sqrt{\mathrm{hr}}$. It was, therefore, proposed that a thermal stability requirement of 5 mK $\sqrt{\mathrm{hr}}$ be defined[36]. This would allow the required

[36] This representation of the thermal stability in terms of a stochastic temperature profile is intended to capture any thermal ripples that are uncorrelated on timescales of hours or less (e.g. introduced by the

stability of the InSb to be met without correction and the goal stability of the MCT to likely be met by correction with temperature sensor data. $5\ \mathrm{mK}\sqrt{\mathrm{hr}}$ is also the stability requirement on the focal planes [105] so if similar amplification electronics were used, any temperature gain should be consistent with the stability budget. The feasibility of achieving this level of stability will be discussed in section 4.4.

4.3.1.4 Dark current shot noise

Quantum efficiency is not the only effect known to have a strong temperature dependence. The detector's dark current may also cause temperature-correlated drifts. Dark current will also contribute shot noise to the measurement. These effects are considered here and are compared to the total reference detector additive noise allocation of 150 ppm $\sqrt{\mathrm{hr}}$ (defined relative to the OGSE faint target signal, see Table 9).

4.3.1.4.1 MCT dark current shot noise

Using literature data from EChO [102, 103], the typical dark current as a function of temperature can be estimated for the long-wave (12.5 µm cut-off) MCT reference detectors. From Figure 56, at 70 K, $I_{dark} = 7 \times 10^{-9}$ A. Bounab et al. [103] measured the dark current using eighty 30 µm pitch diodes giving a total detector area of $A_{det} = 7.2 \times 10^{4}\ \mu\mathrm{m}^2$. Therefore, the dark current flux is $\frac{I_{dark}}{A_{det}e} = 6.08 \times 10^{5}\ \mathrm{es}^{-1}\mu\mathrm{m}^{-2}$.

PID thermal controller). These are expected to be particularly problematic for detrending source variability. For ease of budgeting, it is this 5mk $\sqrt{\mathrm{hr}}$ thermal variability that is used throughout the rest of this document. It is, however, also important to assess the impact of thermal drifts which occur on time scales longer than the measurement.

Assuming the dark current scales linearly with the detector area, over the 0.1 mm OGSE reference detectors we expect a dark current of $D_{MCT} = 6 \times 10^{9}\ \mathrm{es}^{-1}$. This is a factor of two smaller than the predicted source signal (section 4.3.1.1).

This will result in a dark current shot noise-to-signal ratio of $\frac{\sqrt{D_{MCT}}}{\Phi_{MCT}} = 4.1\ \mathrm{ppm}\ \sqrt{\mathrm{s}} = 0.07\ \mathrm{ppm}\ \sqrt{\mathrm{hr}}$. Therefore, the dark current shot noise will also contribute negligibly to the noise budget for the 12-micron cut-off MCT detector.

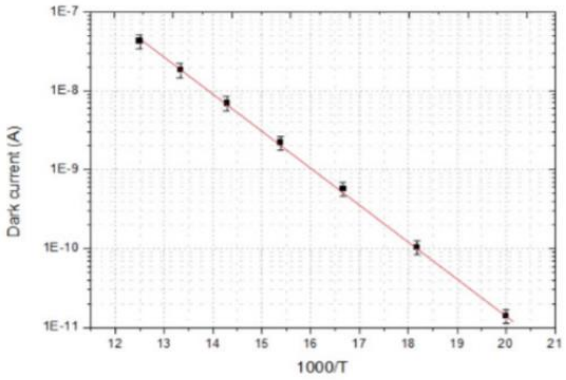

Figure 56: MCT dark current as a function of temperature [103].

4.3.1.4.2 InSb dark current shot noise

For the 5-micron cut-off InSb detectors, we use data collected in the Spitzer test campaign [104], as well as during the JWST prototyping [106]. However, this data was not measured up to 70 K. To estimate the dark current at 70 K, the known exponential dark current scaling can be used (e.g. [107]).

$$D = ae^{-\frac{b}{T}} \tag{4.10}$$

Data from [106] can be used to fit the two free parameters (a, b). Using the 40 K and 45 K data points from [106] and scaling their data to the OGSE 250 µm detector area gives coefficients of $a = 7.23 \times 10^{12}\ \mathrm{es}^{-1}$ and $b = 928.39\ \mathrm{K}$. At 70 K this gives a dark current of $1.3 \times 10^{7}\ \mathrm{es}^{-1}$ for our InSb detector. This gives a dark current-to-signal ratio of $\frac{1.3\times10^{7}}{1.18\times10^{11}} = 10^{-4}$. Therefore, given the photon

noise of the signal on the detector is negligible relative to the noise budget (section 4.3.1.1), the shot noise from the dark current will be completely insignificant for the InSb detector.

4.3.1.4.3 MCT Dark current drifts

Shot noise, however, is not the only way dark current can cause measurement uncertainty. A more significant source of variability coming from the dark current could be temperature-correlated dark current drifts. To investigate this, the exponential form (equation 4.10) can be differentiated to give a dark current temperature sensitivity.

$$\frac{dD}{dT} = \frac{ab}{T^2} e^{-\frac{b}{T}} = \frac{b}{T^2} D \tag{4.11}$$

$$b = \frac{\ln \frac{D_2}{D_1}}{\frac{1}{T_1} - \frac{1}{T_2}} \tag{4.12}$$

Empirical values to constrain equation 4.11 were extracted from Figure 56 ($T_1 = 63\ \mathrm{K}, T_2 = 53\ \mathrm{K}, D_1 = 1 \times 10^{-9}\ \mathrm{A}, D_2 = 4 \times 10^{-11}\ \mathrm{A}$) giving a value of $b = 1073\ \mathrm{K}$.

Therefore, given also the dark current, D, at 70 K is $6.08 \times 10^9\ \mathrm{es}^{-1}$ (section 4.3.1.4.1), the dark current variability caused by a $\Delta T = 5\ \mathrm{mK}\sqrt{\mathrm{hr}}$ thermal variations will be:

$$\Delta D = \frac{dD}{dT} \Delta T = \frac{b}{T^2} D \Delta T = 6.66 \times 10^6\ \mathrm{es}^{-1}\sqrt{\mathrm{hr}} \tag{4.13}$$

Therefore, the dark current variability to signal ratio is: $\frac{\Delta D}{\Phi_{MCT}} = 354\ \mathrm{ppm}\sqrt{\mathrm{hr}}$

This would then need to be corrected using temperature sensor data to meet the 150 $\mathrm{ppm}\sqrt{\mathrm{hr}}$ additive noise goal for the MCT detector.

4.3.1.4.4 InSb dark current drifts

Similarly to the MCT detectors, the expected impact of dark current drifts can be assessed for the InSb detectors using the known exponential dependence of the dark current (recall equations 4.10 and 4.11 and the dark current coefficients evaluated in 4.3.1.4.2). Therefore, assuming a $5\ \mathrm{mK}\sqrt{\mathrm{hr}}$ thermal

drift and a 70 K operating temperature, the temperature-correlated dark current drift for an InSb detector is expected to be :

$$\Delta D = \frac{dD}{dT}\Delta T = \frac{b}{T^2} D\Delta T = 1.23 \times 10^4 \text{ es}^{-1}\sqrt{\text{hr}} \tag{4.14}$$

This gives a dark current drift-to-signal ratio is:

$$\frac{1.23 \times 10^4 \text{ es}^{-1}\sqrt{\text{hr}}}{1.18 \times 10^{11}\text{es}^{-1}} = 0.1 \text{ ppm}\sqrt{\text{hr}} \tag{4.15}$$

Therefore, for the InSb detectors, dark current drifts will contribute negligibly to the additive noise budget.

4.3.2 Detector selection conclusions

In this section, literature data was used to make an order of magnitude estimates of different noise sources. The impact of noise sources was compared to the IR source monitoring requirements. The sources of variability are summarised in Table 12. It was shown that the sphere radiance is sufficiently large to make the photon noise negligible. Moreover, the sphere will be sufficiently cold to make dark current shot noise negligible. However, it was shown that temperature-correlated QE and dark current drifts would be significant, especially for the MCT. This analysis, therefore, motivated the need for stringent (~5 mK$\sqrt{\text{hr}}$) thermal stability of the OGSE reference detectors.

	InSb	MCT
Photon noise	0.05 ppm $\sqrt{\text{hr}}$	0.1 ppm $\sqrt{\text{hr}}$
QE drifts	5 ppm $\sqrt{\text{hr}}$	40 ppm $\sqrt{\text{hr}}$
Dark current shot noise	5×10^{-4} ppm $\sqrt{\text{hr}}$	0.07 ppm $\sqrt{\text{hr}}$
Dark current drifts	0.1 ppm $\sqrt{\text{hr}}$	400 ppm $\sqrt{\text{hr}}$
D* (required/expected)	8×10^7 / 10^{10}	2×10^8 / 10^{10}

Table 12: Sources of variability in OGSE detectors.

With this level of thermal stability, it was found that the InSb detector will be able to constrain source variations to the required level. When combined with the source temperature monitoring with a

thermocouple, this should provide sufficient information to correct the source to 40 ppm $\sqrt{\text{hr}}$ (bright mode) and thus the verification of Ariel's gain stability.

As a goal, the OGSE also aims to provide an extra 12 µm MCT detector to provide an additional colour constraint on the source. The literature data suggests a more marginal performance is to be expected with this detector, with dark current drifts (pre-correction) becoming important at the level of $\sim$400 ppm $\sqrt{\text{hr}}$ (relative to the faint stellar target), and QE drifts becoming important at the level of $\sim$40 ppm $\sqrt{\text{hr}}$. However, given both of these effects are temperature correlated, it is likely the MCT performance goals can be met by correction with temperature monitoring of the detectors.

4.4 THERMAL CONTROL

In section 4.3, it was shown that ~5 mK[37] stability of the detectors would likely be needed to verify the Ariel gain stability. In this section, we will explore the feasibility of achieving mK stability.

Achieving this level of thermal stability in a time consistent with the approximately two week test schedule raises multiple questions:

1. How long does it take for the sphere to stabilise after the initial cooldown?

[37] The 5 mK $\sqrt{\text{hr}}$ stochastic representation is used for simplicity of budgeting. A 5 mK ppeak-to-peakdrift is conservative relative to this stochastic requirement since the frequency-domain power is biased to lower frequencies than Ariel is interested in (>10hrs). See ARIEL-OXF-PL-TN-036 for quantitative discussion. 5 mK peak-to-peak is likely overly stringent, however, in this work the time needed to reach this (likely overly stringent) goal after a perturbation is found to not impact the test schedule. Therefore, in this work, we consider the integrating sphere to be sufficiently stable to perform photometric stability measurements when the sphere reaches 5 mK of the equilibrium temperature and has an RMS variability less than 5 mK $\sqrt{\text{hr}}$.

2. How long does the sphere take to stabilise after a source change?
3. Given PID parameters are found that satisfy the stabilisation timescale constraints, are these PID parameters robust to temperature sensor noise?
4. With the chosen PID parameters, is the sphere temperature-sensitive to 6K ambient temperature variations?

4.4.1.1 PDR illumination module thermal architecture

The illumination module PDR thermal design is shown in Figure 57. It consists of a ~70 K sphere and optical bench which is separated from the ambient using GRP support blades. The cooling of the optical bench is achieved using copper flex links which couple to a ~40 K cold head. The cold head and optical bench are also both fitted with interlocking fins that provide radiative cooling of the optical bench. Finally, there is a ~40 K shroud that directly couples to the cold head. This surrounds the whole 70 K optical bench and sphere. Thermal stabilisation is achieved by PRT monitoring and resistive heating using a PID feedback loop. The key thermal parameters are summarised in Table 13.

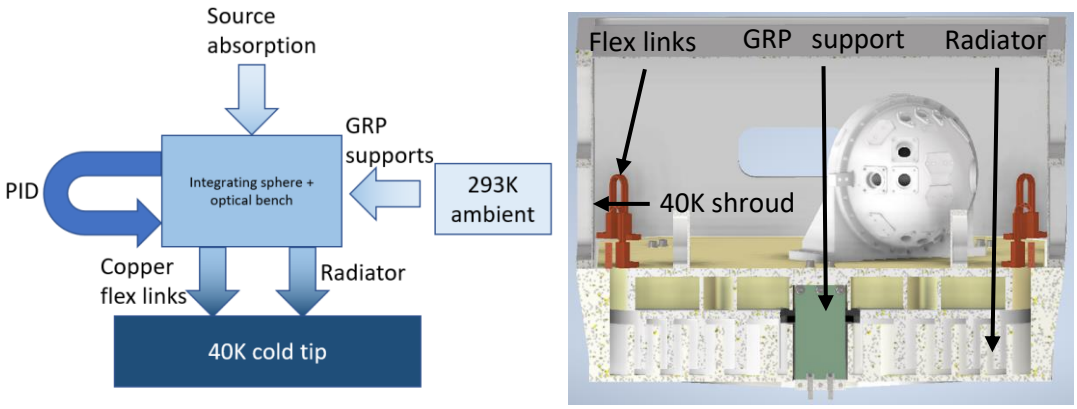

Figure 57: Schematic and CAD representations of the illumination module thermal design [51].

Exchanger effective emitting area	3 m^2
Black paint emissivity	0.8
Copper flex link conductance	0.28 WK^{-1} × 4 (quoted at 40K)
GRP blade cross-section	60 mm × 2.5 mm × 3
GRP blade thickness	101 mm
GRP thermal conductivity	0.5 $Wm^{-1}K^{-1}$ (typical room temperature value – worst case)
Sphere + optical bench + top radiator mass	36 kg
AL specific heat capacity	336 $Jkg^{-1}K^{-1}$ (data quoted at 77 K)
Bright mode source absorption	2.75 W
Ambient temperature	19°C to 25°C (set point 20°C)

Table 13: Thermal parameters assumed in the model

4.4.1.2 Illumination module optical bench stability

4.4.1.2.1 Nodal illumination module representation

To enable thermal control simulations and PID optimisation a Simulink nodal model of the illumination module was used. This assumed an isothermal integrating sphere and optical bench. This assumption is motivated by the conductance across the integrating sphere being large compared to the conductance across the flex links. Therefore, the time for thermal perturbations to stabilise across the integrating sphere should be shorter than the time taken for thermal perturbations to stabilise across the flex links.

The reduced nodal model includes:

- The sphere + optical bench thermal mass (36kg).
- The conductive cooling of the sphere through the copper flex links (Figure 57)
- The radiative heat exchange between the cold head and the optical bench modelled by $\frac{\sigma\epsilon}{2-\epsilon}A_{eff}\left(T_{sp}^4 - T_{cold}^4\right)$ over a $3\ \mathrm{m}^2$ effective radiating area. Where $T_{cold} = 40\ \mathrm{K}$
- The conductive link between the ambient and the optical bench via the GRP support blades.
- The absorption of source flux within the sphere.

4.4.1.2.2 PID optimisation and low-pass filtering

To control the sphere temperature a standard PID control loop was assumed. This uses the following transfer function:

$$C(s) = P + I\left(\frac{1}{s}\right) + D\left(\frac{s}{sT+1}\right) \tag{4.16}$$

Where P, I and D are the weightings between the proportional, integral and differential terms and T is the derivative smoothing time constant. The PID optimisation was handled using the MATLAB PID tuning toolbox. A solution was chosen that prioritised a rapid response at the cost of overshoot. This gave the following provisional parameters:

P	124 WK^{-1}
I	0.237 $WK^{-1}s^{-1}$ (853 $WK^{-1}hr^{-1}$)
D	60,000 WsK^{-1} (16.7 $WhrK^{-1}$)
T	300 s (0.08 hr)

Table 14: Provisional PID parameters used in this stabilisation analysis.

However, with these parameters (Table 14), it was found that 5 $\mathrm{mK}\sqrt{\mathrm{hr}}$ temperature sensor noise[38] caused large heater power variations (~30 W variability[39], relative to a ~35 W steady-state). Whilst the sphere thermal mass does smooth the short timescale power variability to an acceptable level (5 $\mathrm{mK}\sqrt{\mathrm{hr}}$), this power variability could be a source of EM noise.

The output power variability was primarily caused by the proportional term in the above expression (equation 4.16). To overcome this, a low-pass filter was added to the control loop. To set the smoothing time constant of the low pass filter, a noise-free simulation was run without the filter added

[38] 5 mK $\sqrt{\mathrm{hr}}$ temperature sensor noise was chosen as this is the worst-case noise that is consistent with stabilising the sphere to 5 mK $\sqrt{\mathrm{hr}}$.

[39] When a 1 minute update time was used

(Figure 58). The system was initially in equilibrium with the bright target sphere radiance. The source was then shuttered reducing the source flux absorbed by the sphere to zero. It was found that the system stabilises in ~20 minutes. This was therefore used as the characteristic timescale, below which any variability can reasonably be assumed to be noise. Therefore, 20 minutes was chosen as the smoothing time constant for the low pass filter.

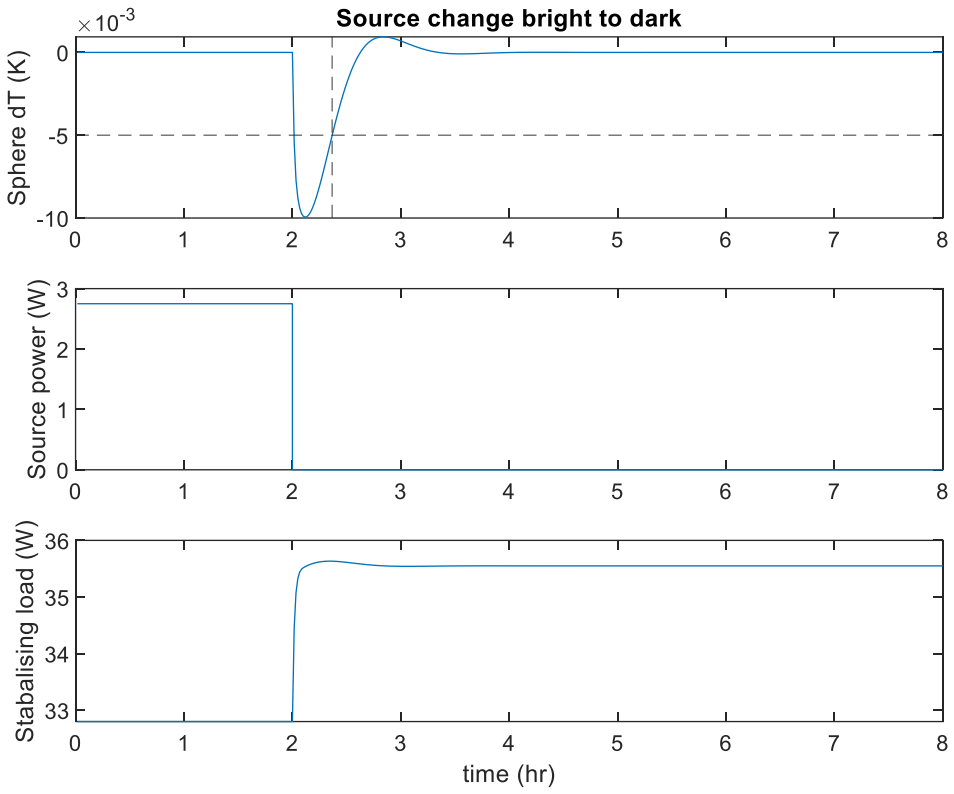

Figure 58: Unfiltered, noise-free, simulation of the thermal stability when the source is changed from the bright target to the dark.

The filter makes the system more robust to noise, however, it is detrimental to the response time. The impact on the stabilisation time can be seen to be small by comparing (Figure 58 – unfiltered & Figure 61 – filtered).

The parameters in Table 14 were then used to assess the initial stabilisation time, the stabilisation after a source change and the robustness of the PID controller to noise.

4.4.1.2.3 Initial cooldown

Members of the wider OGSE team conducted a preliminary FEA analysis to assess the time it will take for the sphere to go from ambient to 70 K (see [51]). It was found that it would take ~2 days for the cooldown to occur. However, the time taken to reach the required level of thermal stability is also an important consideration. The planned procedure for cooldown is to allow the sphere to cool with the heaters turned off until the sphere reaches close (e.g. ~2 K) to the planned 70 K operating temperature. At this point, the PID control system will be activated such that the sphere tends to this equilibrium point.

To assess the stabilisation, a 72 K initial condition was applied to the sphere and the PID controller was used to bring the sphere temperature to equilibrium. The resulting time series is shown in Figure *59*. The sphere stabilises to 5 mK after ~2 hrs. Given it is not planned to perform a gain stability test at the beginning of the sequence, the initial stabilisation should not cause problems for the test schedule.

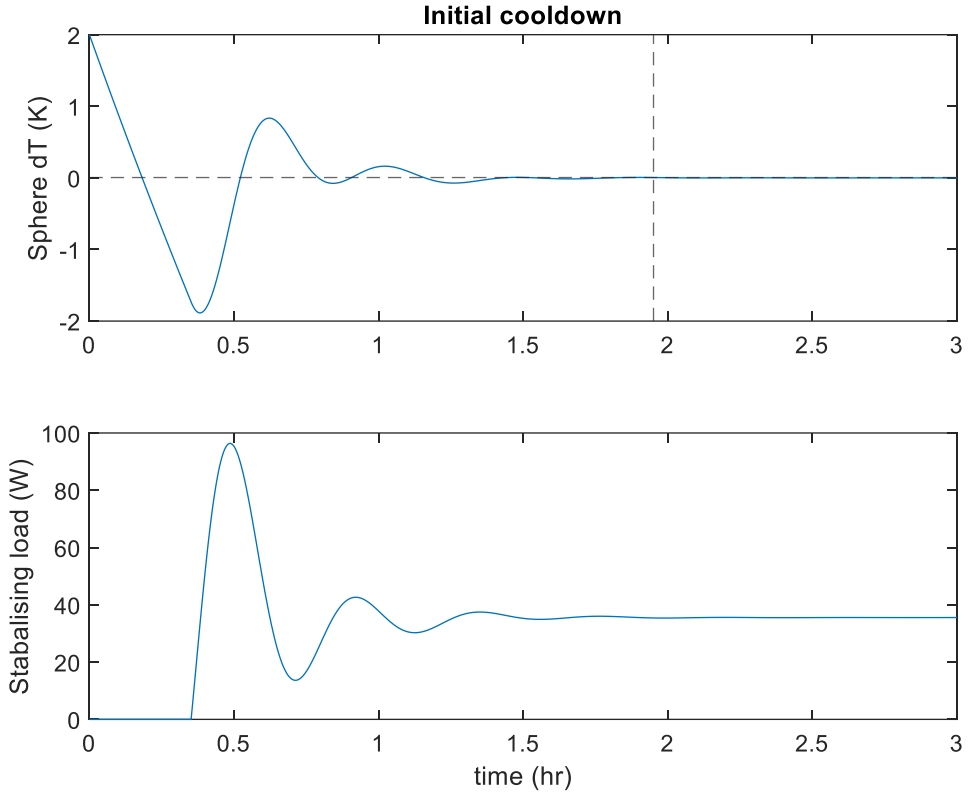

Figure 59: Top - temperature as a function of time for the initial stabilisation of the illumination module. A horizontal 5 mK dashed line is shown and a vertical dashed line shows the time at which the sphere stabilises to less than 5 mK of equilibrium. Also shown is the power supplied by resistive heaters that are used to stabilise the system.

4.4.1.2.4 Thermal drifts due to a source mode change

Due to the need for a flight-like spot size, the OGSE uses a small (50 μm) pinhole at the sphere exit. This in turn drives the need for a large radiance within the sphere (see Table 3). When observing the VIS and IR sources simultaneously in the bright mode, the flux absorbed by the sphere is expected to be ~2.75 W. When the sources are shuttered the absorbed source flux becomes zero. This change in flux may introduce thermal drifts within the integrating sphere.

This was simulated using a 2.75 W step change in the sphere load. The resulting thermal drifts can be seen in Figure 60 and Figure 61. Even in the worst case when we are changing between the bright and dark observing modes, the peak-to-peak thermal drift is only expected to be ~10 mK. Moreover, the system stabilises to 5 mK in ~20 minutes. Therefore, given the limited number of tests that will require

the 5 mK $\sqrt{hr}$ stability, 20-minute stabilisation after a source change is not expected to significantly impact the schedule.

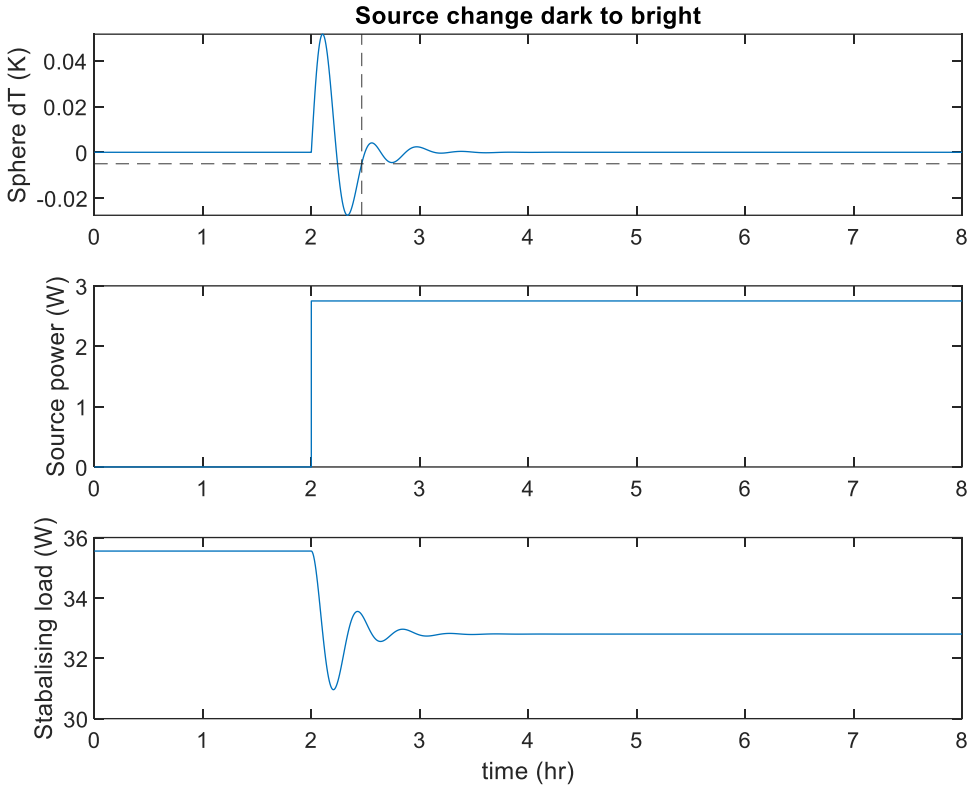

Figure 60: Sphere temperature as a function of time after a step change in source flux is added.

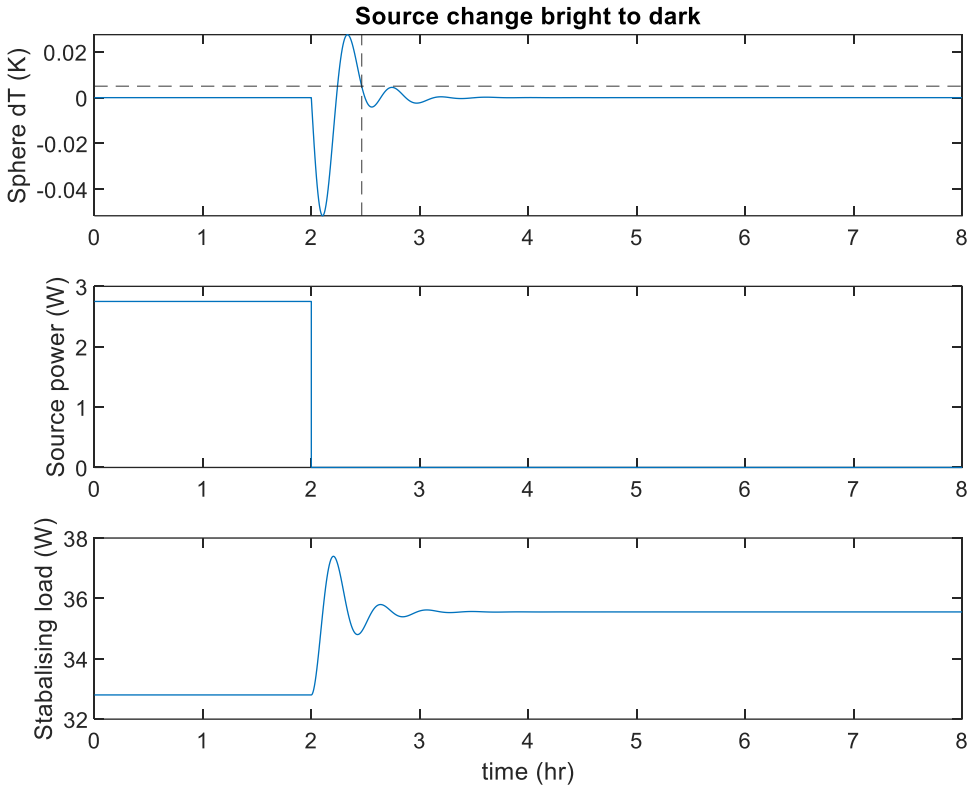

Figure 61: Sphere temperature as a function of time after a step change in source flux is added.

4.4.1.2.5 Temperature sensor noise

When tuning the PID parameters, there is a trade-off between rapid response and robustness to noise. We have demonstrated that the PID parameters provide a sufficiently rapid response for cool down and a source change (Figure *59*, Figure 60 & Figure 61). Here we will assess if the PID parameters were robust to temperature sensor noise. At the time of performing this analysis, the sensor noise floor was still to be measured. However, given the need to stabilise to 5 mK $\sqrt{\text{hr}}$, the temperature monitoring noise floor will need to be better than this. We, therefore, choose the temperature monitoring noise to be 2.5 mK $\sqrt{\text{hr}}$. This was implemented in the model as 150 mK stochastic noise evaluated at 1 s integration time (Figure 62).

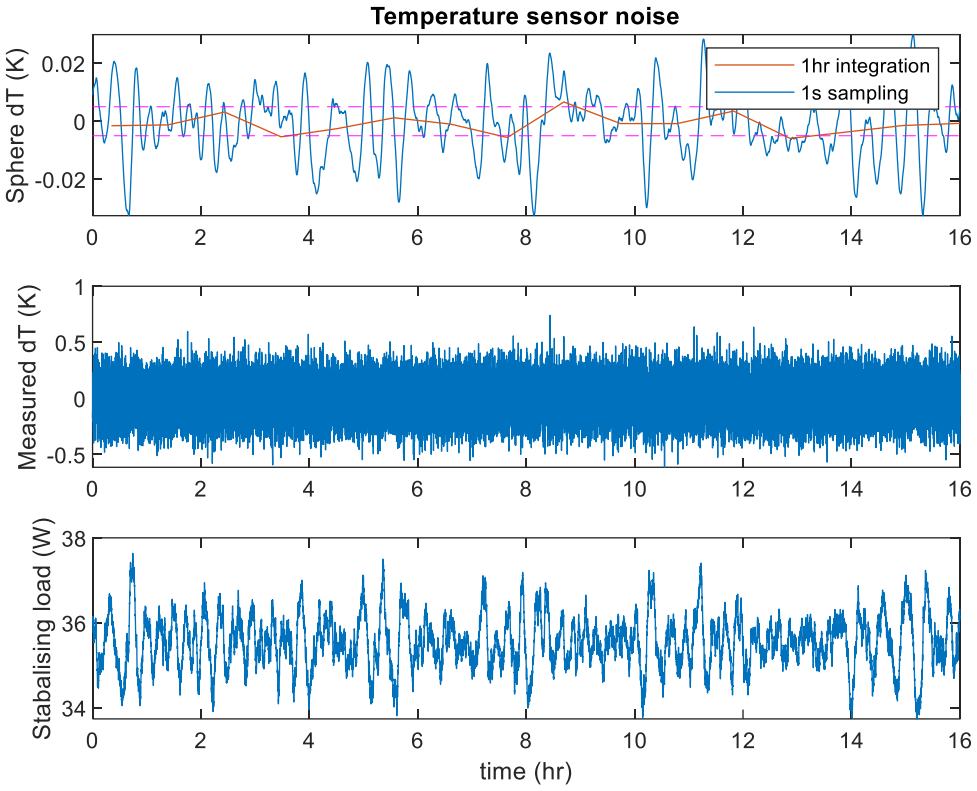

Figure 62: Sphere temperature vs time when temperature sensor noise is added to the monitoring system. ±5mK dotted lines are also shown.

It was found that with 2.5 mK $\sqrt{\text{hr}}$ temperature sensor noise, 3.4 mK sphere temperature stability at 1 hr integration time can be obtained (Figure 62). This is only marginally worse than the noise floor and consistent with the 5 mk $\sqrt{\text{hr}}$ requirement. Therefore, the provisional PID parameters are seen to be robust to the expected temperature sensor noise.

The lakeshore model 336 was chosen to perform temperature monitoring and control. This quotes 1 mK stability when using a PRT at 77 K for "an ideal thermal system"[108]. This further indicates temperature sensor readout noise will not limit thermal control accuracy.

4.4.1.2.6 Ambient temperature variations

The RAL test facility quotes large (6 K) variations in the ambient thermal environment [109] in the clean room area that services the 5 m diameter test chamber. The final effect to check is, therefore, whether the 6 K ambient variations will propagate onto the optical bench. The optical bench is

supported from the ambient with 3 GRP blades. Changes in the ambient temperature will change the conductive flux along these supports, potentially leading to temperature variations in the optical bench.

The RAL test facility quotes 19-25 ℃ temperature range [109] (20 ℃ setpoint) for the room temperature. Here we assume the functional form of this drift is a saw tooth i.e. the temperature gradually drifts up until a temperature threshold is met then the AC switches on rapidly bringing the temperature down to a lower threshold.

The sphere temperature variations that result from the ambient drift are shown in Figure 63. One can see that the sphere temperature perturbations are ~0.2 mK so are negligible relative to the 5 mK requirement.

There is the possibility that ambient temperature variations could change the efficiency of the cold head compressor causing variability in the 40 K boundary condition. The impact of this is best assessed by testing. In the event, that this is a problem, a two-stage stabilisation scheme could be implemented.

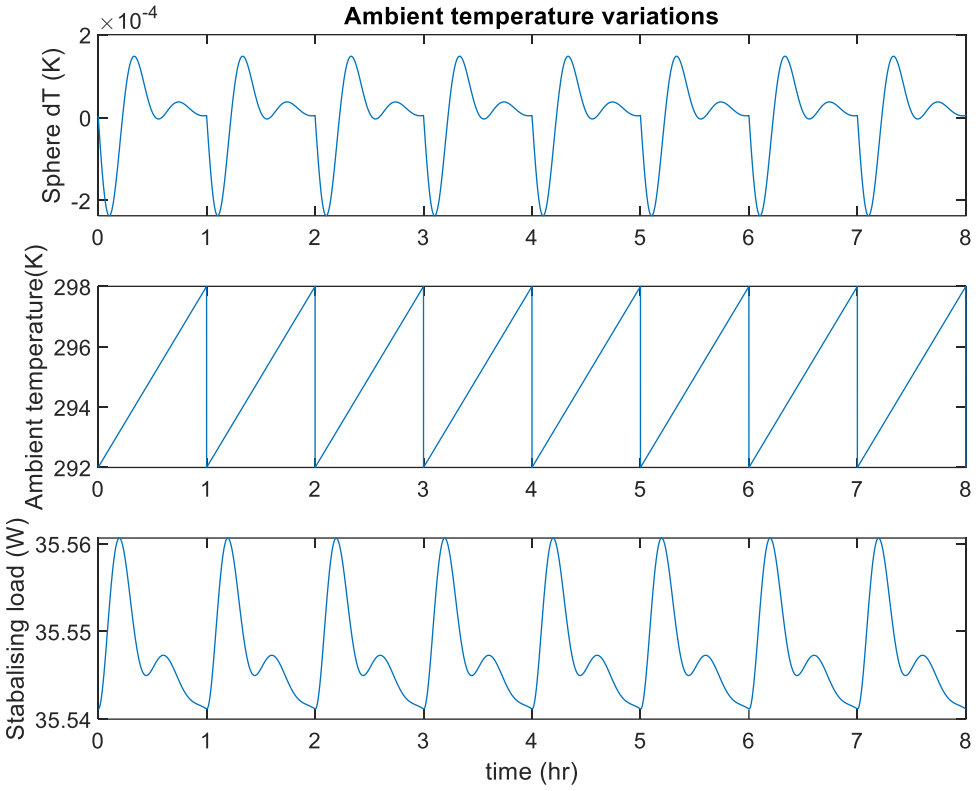

Figure 63: Sphere temperature vs time when 6K ambient drifts are included.

4.4.1.3 Thermal control conclusions

To assess the stabilisation of transient effects, a nodal thermal model of the illumination module optical bench was created. A provisional set of PID parameters have been shown to be sufficiently aggressive to correct perturbations in a reasonable time frame (hrs) whilst being robust to temperature senor noise & expected flux perturbations. It was also shown that these PID parameters can stabilise 6 K ambient temperature variations to a level constant with the 5 mK $\sqrt{\text{hr}}$ requirement.

For the initial cooldown, ~2 hr stabilisation (plus ~2 days to reach ~72 K from ambient) would be needed to reach the level of stability needed to perform gain stability measurements. After a source change, ~20 minutes of stabilisation would be required to reach 5mK stability. The source change introduced a 10 mK peak-to-peak drift which is expected to be negligible for all tests that do not require 40 $\text{ppm}\sqrt{\text{hr}}$ source correction.

Therefore, given: (1) the photometric stability tests are not planned to be conducted at the start of the test sequence, (2) the small number of tests that require 40 $\mathrm{ppm}\sqrt{\mathrm{hr}}$ source correction (only end-to-end noise budget tests), and (3) the 20-minute stabilisation time after a source change, neither stabilisation after a source change nor the initial cooldown is expected to significantly impact the test schedule.

It is planned to produce a Structural-Thermal Model (STM) of the illumination module integrating sphere which will allow validation of this thermal control model and further optimisation of the PID parameters. It will also allow the assessment of any spatial thermal waves which are not included in this model.

Further optimisation of the PID parameters will be the subject of future work however it will be shown that these parameters provide a sufficiently fast response time whilst being robust to expected noise sources & perturbations and, therefore, provide a satisfactory baseline.

4.5 CHAPTER SUMMARY

In section 4.2, the requirement to verify the Ariel gain stability was flowed to OGSE source monitoring requirements. To do this requirement flow, a source variability and correction model was created and incorporated within the ExoSim framework. It was shown that to correct the OGSE source variability to a level less than the Ariel noise floor (40 $\mathrm{ppm}\sqrt{\mathrm{hr}}$ - bright mode only), high-stability OGSE reference detectors would be required as well as source temperature monitoring. The required levels of stability and noise for the OGSE reference detectors are described in Table 9 & Table 10.

To enable the selection of the OGSE detectors, a literature review was then conducted to assess the likely performance of the InSb and MCT detector candidates. It was shown that these detectors will exhibit a noise performance consistent with verifying the Ariel noise floor. However, the temperature dependence of the quantum efficiency was identified as a key effect. Since the QE is degenerate with

the source flux, drifts in QE could cause spurious measurement of the source variability. To achieve 40 ppm $\sqrt{\text{hr}}$ monitoring it was shown that 5 mk $\sqrt{\text{hr}}$ stability of the detectors was required.

Achieving 5 mk stability on hr timescales is challenging, so an assessment level of the achievable thermal stability was made. It was shown that PID parameters exist which can stabilise transient effects in a reasonable time (20 minutes) whilst being robust to temperature sensor noise.

The Ariel gain stability test has therefore been flowed to requirements on the source monitoring, as well as thermal control requirements. The feasibility of meeting these requirements has also been assessed.

An effect that can affect transit spectroscopy is dark current. It is required The Ariel dark current at payload-level testing (R-CAL-060, see appendix C). There are two contributing factors to the payload dark current: thermally liberated electrons within the detector, but also thermal backgrounds within the payload instrument cavity. The detector's dark current will be verified at lower levels (component, unit and sub-system level). However, the instrument cavity emission, in a flight-like thermal environment, is uniquely testable at payload level.

Both sources of dark current cause a spurious signal that adds to the stellar signal. This is primarily of importance due to possible photometric errors it may introduce, leading to uncertainty in the measured transit depth. The stochastic liberation of dark current electrons will contribute shot noise to science frames. Additionally, the dark current could drift causing a change in the measured signal. Dark current is a term in the payload noise budget, the sum of which must be correctable to ~tens of ppm to enable the detection of atmospheric spectral features. It is for this reason that the OGSE will verify the dark current at payload-level testing.

The payload dark current will be measured with the OGSE output shuttered. This is enabled by a flip mirror that relays the payload line of sight to a cryogenic beam dump (see section 6.2.4.1 for further details). Thermal emission from the beam dump, as well as any optics after the beam dump will lead to an additive signal that may not be distinguishable with the payload dark current. Therefore, for the OGSE to be able to verify the Ariel dark current, we require the thermal emission from optical surfaces + the beam dump (Figure 19) to be comparable to or less than the Ariel dark current[40].

[40] Ensuring OGSE emission is less than the payload dark current also ensures that OGSE emission will not significantly impact any of the other calibration measurements.

Demonstrating that the OGSE design is compatible with testing the payload dark current will be the subject of this chapter. Firstly, analysis will be presented to determine the required temperature of the optics. Secondly, thermal designs will be presented as well and FEA modelling will be used to assess if the optics will reach the required temperature. Finally, the impact of thermal stray light will be assessed.

The thermal requirements were derived for SRR and are reported in [110]. The stray light analysis is reported in [111]. The illumination module thermal design and analysis is ongoing work in preparation for CDR.

5.1 EXOSIM DARK SIMULATIONS

The requirement to have OGSE emission less than the payload dark current then must be flowed to thermal requirements on the OGSE beam dump and mirrors. To achieve this, the author added a module to an Ariel end-to-end simulator (ExoSim [92]). This allowed simulated focal plane spectra to be generated for different OGSE mirror temperatures. This was then used to address 3 design questions:

(1) To enable full aperture illumination, can a mirror with a room-temperature optical surface be used as a part of the OGSE?
(2) If not, what temperature do all the OGSE mirrors need to be cooled to?
(3) Is a shutter mounted on the illumination module optical bench cold enough to be used for dark observations or is there a need for a separate dark target e.g. mounted on the ~40K shroud?

To simulate the OGSE thermal emission, a modified ExoSim implementation was used. A description of the ExoSim is contained in [92]. A summary of ExoSim, as well as a description of the OGSE modules, is described in Chapter 4. ExoSim was used to predict the signal generated from thermal photons and

was evaluated in AIRS CH1. The magnitude was compared to Ariel's detector dark current requirements (<1 $e^{-}pix^{-1}s^{-1}$; R-PRD-8813).

5.1.1 ExoSim thermal background results

5.1.1.1 The Euclid mirror

The first of the three questions was motivated by the possible use of a 1.2 m flat mirror from the Euclid test campaign (near IR ESA mission [112]).

As discussed in Chapter 6, the sub-aperture OGSE design + beam expander significantly compromises multiple tests including the telescope to focal plane alignment, the payload PSF and stray light verification. These are tests that are only fully verifiable at payload level. The decision to go to a sub-aperture beam was mainly programmatic due to the cost of a 1 m cryo-compatible OAP. All avenues were therefore explored to obtain a full aperture mirror.

A 1.2 m collimator built for the Euclid mission ground test campaign could allow full aperture illumination of M1 under vacuum and cryo conditions. However, to maintain WFE and alignment, the Euclid collimator mirror was designed to operate in the temperature range of $286 - 294$ K. At Ariel's operating wavelengths (up to 7.8 μm) this will produce a significant thermal background.

A priori it was not expected to be able to do low signal level testing, such as dark current measurements, with an ambient mirror. However, dark current can be partially verified at sub-system levels. Sacrificing dark current testing for PSF, alignment and stray light verification of the payload would likely be a worthwhile trade. The open question was whether an ambient mirror would prevent any functional testing in Airs CH1.

It was assumed that the Euclid collimator's optical surface would be maintained at 290 K and has a black body spectral radiance with an emissivity of 0.03. The resulting thermal signal in AIRS channel 1 is shown in Figure 64. This simulation only included the Euclid mirror thermal background, with no source. No other noise sources were applied.

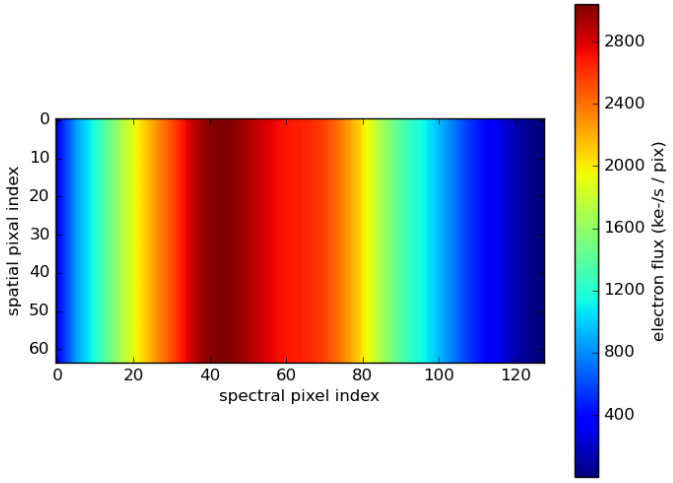

Figure 64: AIRS channel 1 focal plane electron flux due to the thermal background. The wavelength range in this channel is $8.15 \mu m$ *to* $3.46 \mu m$ *with the longwave end being on the left side of the array.*

The electron flux due to the Euclid mirror reaches 3×10^6 $\mathrm{e^- pix^{-1} s^{-1}}$ (Figure 64). Airs CH1 has a full well depth of 50,000 electrons (R-PRD-8814). The detector would therefore saturate in 0.02 s. This is faster than the 10 Hz maximum readout rate of the detector. The detector would, therefore, likely be in-operable with an ambient mirror. For this reason, the sub-aperture cryogenic configuration remained the baseline (see 1.4.4.1).

5.1.1.2 Mirror temperature requirements

Given the thermal background from the Euclid mirror is significantly ($\sim 10^6 \times$) greater than the AIRS CH1 dark current, the immediate question is how cold does a mirror need to get for the dark current to be verified? To explore this a series of focal plane images were generated using ExoSim for a range of mirror temperatures (e.g. Figure 64). From these images, the electron flux as a function of wavelength was calculated (Figure 65). Figure 65 shows that the mirror temperature needs to be less than or comparable to ~ 80 K for the thermal background to be less than 1 $\mathrm{e^- pix^{-1} s^{-1}}$ (for an optical system with a single mirror). A budget that includes the thermal contribution from all OGSE optical surfaces is discussed in section 5.1.1.4.

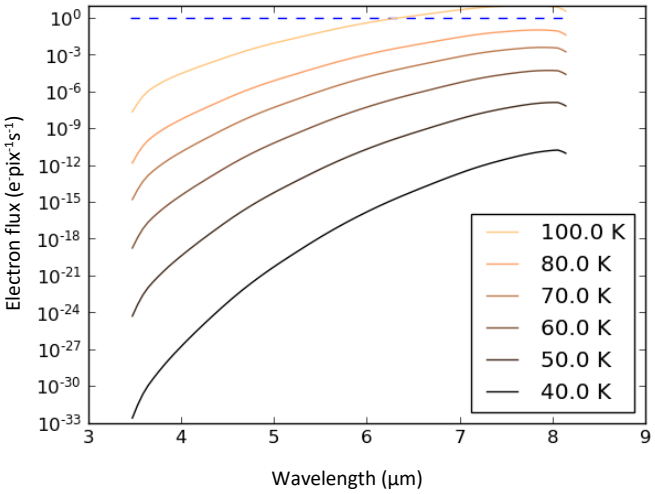

Figure 65: AIRS channel 1 focal plane electron flux as a function of wavelength, plotted for a range of mirror temperatures. Also plotted is a $1\ e^{-}pix^{-1}s^{-1}$ *horizontal line.*

mirror temperature (K)	**100**	**80**	**70**	**60**	**50**	**40**
7.8 µm thermal signal per mirror (e^{-} $pix^{-1}s^{-1}$)	9.9	0.099	0.0037	4.5×10^{-5}	9.7×10^{-8}	9.7×10^{-12}

Table 15: peak thermal signal per mirror for a range of mirror temperatures.

5.1.1.3 Dark target temperature requirements

During dark observations, the payload line of sight is pointed at a black-painted[41] a-focal beam dump (see section 6.2.4.1). To place thermal constraints on the beam dump, the analysis described in section 5.1.1.2 was re-evaluated for a dark target. From Figure 66, the thermal emission becomes negligible compared to the dark current at target temperatures less than ~70 K.

[41] 0.94 emissivity assumed.

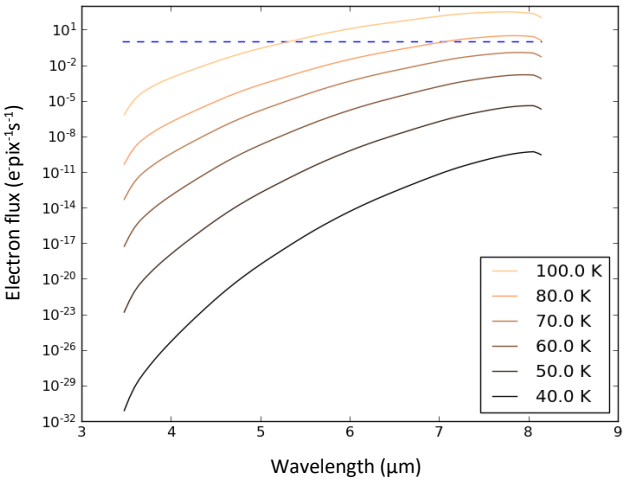

Figure 66: AIRS channel 1 focal plane electron flux as a function of wavelength, plotted for a range of dark target temperatures. Also plotted is a $1\ e^{-}pix^{-1}s^{-1}$ *horizontal line.*

Target temperature (K)	**100**	**80**	**70**	**60**	**50**	**40**
7.8 μm thermal signal ($e^{-}pix^{-1}s^{-1}$)	310	3.1	0.11	1.4×10^{-3}	3.0×10^{-6}	3.0×10^{-10}

Table 16: peak thermal signal for a range of dark target temperatures.

5.1.1.4 Mirrors + dark target temperature budgeting

Since the mirrors' emissivities are <<1, the thermal signal from each mirror will add approximately linearly. After the beam dump, there are 7 illumination module mirrors (Figure 20), 2 periscope mirrors (Figure 21) and 6 beam expander mirrors (Figure 22). By inspecting Table 15 & Table 16 a budget can be constructed.

The beam expander is accommodated on the Telescope Optical Bench (TOB) which is cooled to ~55 K [37]. The beam expander will therefore contribute negligibly to the thermal emission budget (10^{-7} $e^{-}pix^{-1}s^{-1}$ per mirror).

For simplicity, we assume the same thermal requirement for the illumination module and the periscope. An 80K beam dump would already exceed the thermal requirement ($1\ e^{-}pix^{-1}s^{-1}$). A 70 K

beam dump + 9 mirrors would contribute 0.14 $e^{-}pix^{-1}s^{-1}$. Therefore, A 70 K requirement was placed on all OGSE optics.

This 70 K mirror temperature requirement ensures the payload dark current will be verifiable at payload level. Moreover, this ensures OGSE backgrounds are less than the payload backgrounds (thermal emission + dark current), enabling the same signal-to-background ratio during ground testing as in flight. This ensures diffuse backgrounds from OGSE mirrors will not impact the verification of other calibration products.

5.2 ILLUMINATION MODULE THERMAL DESIGN

In the previous section (5.1) it was shown that to enable testing of the payload dark current, the OGSE optics must be maintained at <70K. In this section, the thermal design of the illumination module to enable the low background testing will be discussed, as well as finite element analysis to assess compliance. The author's responsibility was the thermal re-design between PDR and CDR.

The PDR thermal design, led by the wider OGSE team, is shown in Figure 67 and is discussed further in [51]. The design was based on a 3.5 m^2radiator. This radiator exchanges heat from the optical bench to the shroud. The shroud was cooled conductively by the cold head. To improve the cooldown time, copper flex links were used to provide additional cooling of the optical bench.

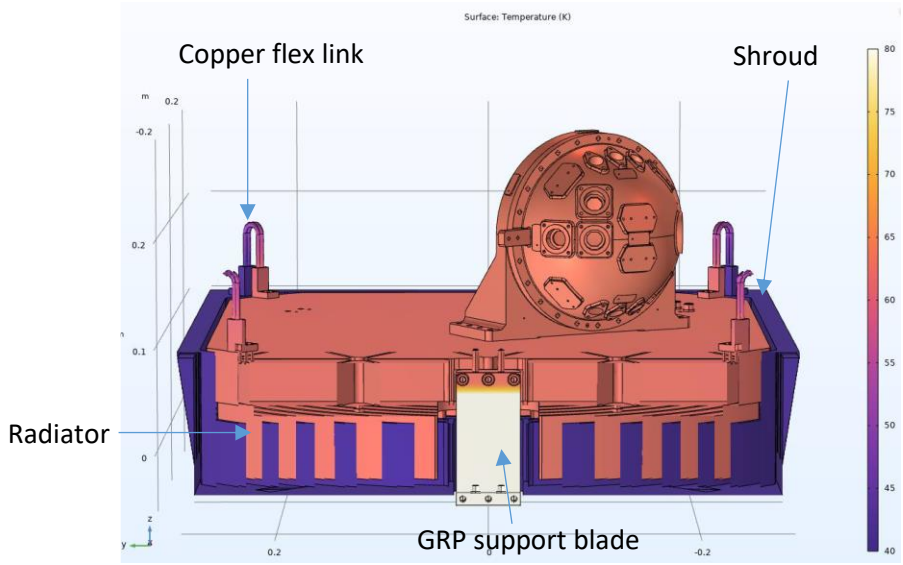

Figure 67: Thermal architecture at PDR [51].

5.2.1 Illumination module thermal architecture

5.2.1.1 Post-PDR design evolution

The updated illumination module thermal architecture is shown in Figure 68. The updated thermal design was driven by the need to accommodate the significantly larger optical bench (1.1 m^2 vs 0.3 m^2). The motivation for the enlarged bench will be discussed in chapter 6. As before, the illumination optical bench is enclosed in a cryogenic radiation shield. Cooling of the shroud is achieved by a closed loop RDK-500B cold head which is hard mounted to the base of the shroud. The optical bench is then conductively cooled from the shroud via flexible copper links. Beyond the change in scale of the system (1.1 m^2 vs 0.3 m^2 optical bench), the main change between the PDR and CDR design was the removal of the radiator.

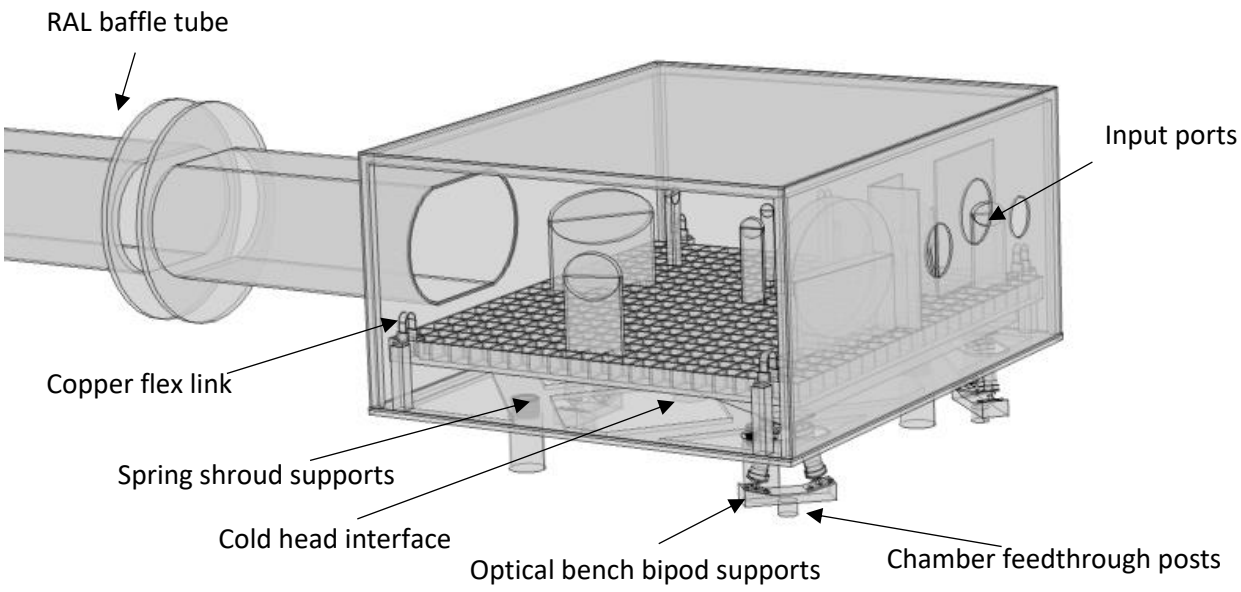

Figure 68: Simplified CAD for thermal simulations.

The decision to remove the radiator was based on (1) the steady-state performance and (2) the thermal mass. In the steady state, the radiator dissipated 4 W. For comparison, the copper flex links dissipated ~20 W. Therefore, in the steady state, the radiator performance is negligible compared to the flex links.

The second motivation for removing the radiator was the thermal mass. In the PDR design, the mass of the optical bench was 15 kg. The radiator weighed 20.9 kg. Whilst the radiator does dominate the cooling of the optical bench at ambient temperatures, helping the cooldown time, this effect is offset by the considerable increase in the thermal mass of the system.

Therefore, based on the driving thermal mass, and negligible steady-state performance, the decision was taken to remove the radiator from the design. The deep (50 mm) and narrow, (15 mm) interlocking fins were also expected to be challenging to machine, coat and assemble. The radiator removal was, therefore, also a considerable reduction in complexity.

5.2.1.2 Micro-vibration implications on the thermal design

The thermal design shown in Figure 68 is largely driven by micro-vibration isolation considerations. The cold head will be a significant source of micro-vibrations. If these are transmitted onto the optical bench this could lead to jittering of the OGSE spot on the focal planes. Ariel's narrow (~30'') FOV makes pointing jitter of particular concern for this mission. ~1 arcsecond optical bench stability is required to not cause significant pointing jitter[42]. The system has, therefore, been designed to minimise the coupling of micro-vibrations onto the optical bench. Micro vibrations were the original motivation behind the complex radiator concept. This later evolved into a hybrid radiative-conductive design and finally a solely conductive design.

The support structure to enable the micro-vibration isolation is being developed in collaboration with Bob Watkins and is shown in Figure 69. The cold head is supported and hard-mounted to the illumination module chamber. The chamber is, therefore, expected to be vibrationally noisy. Similarly, the shroud is hard mounted to the cold head, so must also be isolated from the optical bench.

To enable this isolation, the optical bench bipods pass through holes in the shroud. The base of the bipods then passes through the chamber via flexible bellows. The base of the bellows is then supported off the RAL seismic block. The chamber is separately supported by a frame that straddles the seismic block and is held up by the structural ground. In this way the optical bench floats with respect to the chamber.

[42] Small compared to the spot size.

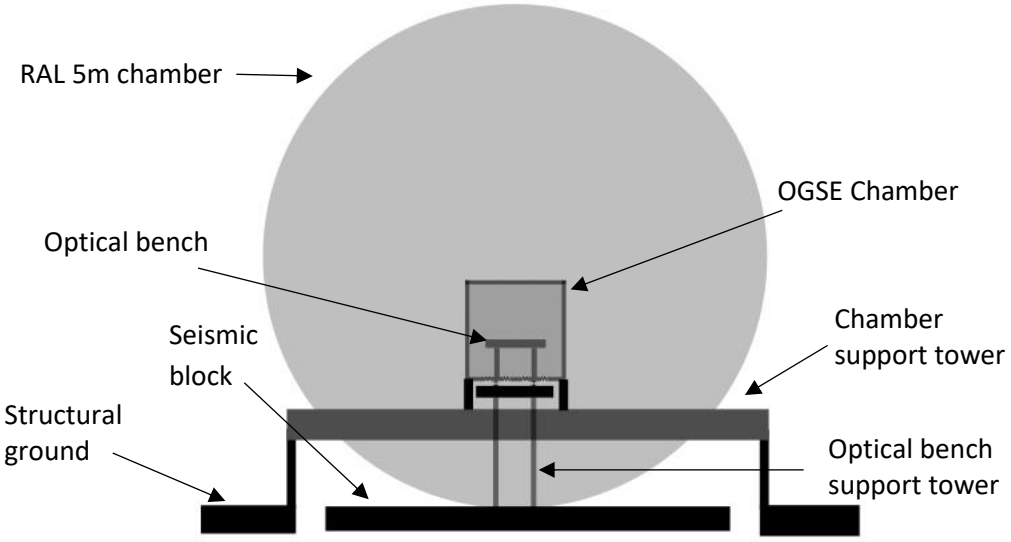

Figure 69: micro-vibration isolation schematic representation

This micro-vibration concept has thermal implications. It drives the need for separate quiet and noisy support supports within the chamber as well as the need for flexible straps to connect the shroud to the optical bench. The cross-section of these straps has been minimised to avoid vibration coupling.

5.2.1.3 Thermally important structural components

The optical bench is supported by low-conductivity G-11 bipods (Figure 68). For simplicity, the GRP and titanium end caps duplicate those designed for the target projector. The titanium end caps feature flexures to account for the thermal contraction of the optical bench. Initially, the simplest solution of three vertical GRP posts was explored. However, a modal analysis showed this would lead to a wobbly optical bench with low (<10 Hz) eigenmodes. Therefore, a bipod solution was adopted. The bipod concept suppressed the low-energy rotation modes whilst maintaining the radial compliance required to account for the thermal contraction of the optical bench.

Separate supports are required for the shroud assembly. Since the cold head is fixed to the chamber and the shroud, the shroud supports need to be vertically compliant to account for the contraction of the cold head. The shroud is, therefore, supported using low-conductivity stainless steel springs (Figure 68).

In addition to the conductive interfaces provided by the supports, flex links and cold head, there are significant radiative interfaces. The shroud is accommodated within an ambient chamber. The shroud features ~100 mm holes to allow the injection of the sources into the sphere (Figure 68). There are also holes in the shroud surrounding the bipod feet. These holes are oversized to account for the required ±2 cm adjustment range of the optical bench. The sphere input and bipod holes both lead to radiative load on the optical bench.

At the output of the optical bench, there is a baffle tube. This is fixed to and cooled by the OGSE shroud. This tube extends to the OGSE gate valve where it is met by an opposite-facing baffle tube (Figure 68). The second baffle tube segment is mounted to and cooled by the RAL liquid nitrogen shroud.

To minimise the radiative load, the outside of the shroud and baffle tube will be coated in Multi-Layer insulation (MLI). To reduce stray light, the optical bench, the interior of the shroud, and the inside of the baffle tube will be coated in Aeroglaze Z307 high (~0.85) emissivity paint.

5.2.2 Illumination module thermal FEA analysis

5.2.2.1 Boundary conditions & material properties

A COMSOL finite element model was then used to assess the thermal performance of the design (shown in Figure 68). Also simulated, but not shown above, was the OGSE illumination module chamber. The chamber interior was assumed to have a surface emissivity of 0.2 and was held at a uniform 293 K.

The cold head performance was explicitly modelled as a flux boundary condition with a temperature-dependent cooling power shown in Figure 70.

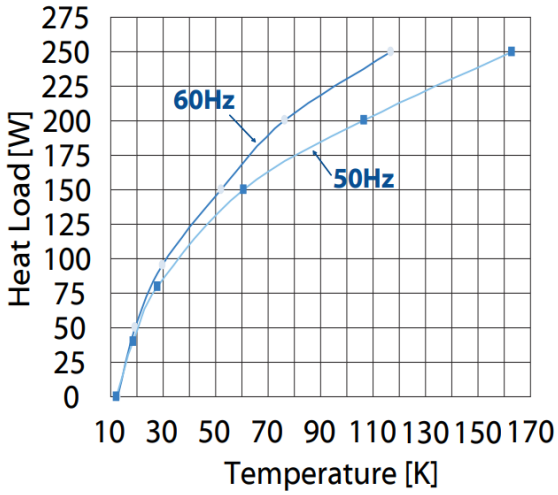

Figure 70: RDK-500B cold heat cooling power [113]. The two curves shown correspond to different power supply frequencies.

The temperature of the RAL baffle tube is somewhat uncertain but is known to be somewhat greater than 77 K. This was nominally simulated at a fixed 100 K temperature.

Many materials show considerable variation in conductivity and heat capacity at cryogenic temperatures. The assumed heat capacities and conductivities are shown in Figure 71 and Table 17. In the absence of heat capacity data for AL 6082 and 1050, temperature-dependent heat capacity data for 6061 was assumed. However, [114] shows a negligible change in heat capacity between vastly different grades of AL (3003, 5083 & 6061) so the use of 6061 heat capacity data is not expected to be a dominant source of uncertainty[43]. Aluminium dominates the thermal mass of the system (tens of kilograms vs hundreds of grams of other materials), therefore room temperature heat capacities were assumed for all materials with negligible mass. In all cases, temperature dependant thermal

[43] The heat capacity is only an issue for the cooldown time. The uncertainty in the cooldown time is dominated by the mass missing structural members/ additional lightweighting that could be possible to the current design.

conductivities were used. In cases where thermal conductivity data was not available for the specific grade, the closest available grade was assumed. This included the use of AL 1100 data for AL 1050 and the use of AL 6061 in place of AL 6082.

The assumed surface properties are shown in Table 18.

Figure 71: Material properties used in the FEA model. References are provided in Table 17. (Figure redacted from ORA version)

Material	Conductivity	Heat capacity
Aluminium 6082	Temperature-dependent function from [115]	Temperature-dependent function from [116]
AL 1050	Temperature-dependent function from [117]	Temperature-dependent function from [116]
P6 504 copper strap (100mm length) from TAI	Temperature-dependent function from [118]	386 $Jkg^{-1}K^{-1}$
G-11	Temperature-dependent function from [116][44]	999 $Jkg^{-1}K^{-1}$
17-7 Stainless steel	Temperature-dependent function from [116][45]	480 $Jkg^{-1}K^{-1}$
Ti 6AL4V	Temperature-dependent function from [116]	529 $Jkg^{-1}K^{-1}$

Table 17: Assumed material properties

Material	Emissivity	Reference
Aluminium	0.2	[37]
GRP	0.84	[37][46]
Steel	0.5	Grade/ roughness were not yet defined however this material has a tiny contribution to thermal balance
Titanium	0.5	Grade/ roughness were not yet defined however this material has a tiny contribution to thermal balance
MLI	0.02	[119, 120]
Aeroglaze Z307	0.85	[121]

Table 18: Assumed emissivities

[44] Data for G-10

[45] Data for grades 304/ 316

[46] Reference for CFRP

5.2.2.2 Simple shroud-only model

Early simulations focused only on the shroud assembly, without the optical bench present in Figure 72. These were primarily used to get an intuition for the flux balance of the system and the anticipated gradients. Initially, it was still TBD the AL grade that would be required so a temperature-independent 150 $Wm^{-1}K^{-1}$ was applied. Initially, a 1 cm thick uniform baseplate was assumed (shown in Figure 72 – Left). The uniform baseplate shows 30 K gradients between the cold head and the warm side of the copper flex links. Such gradients would be incompatible with a 70 K optical bench (R-OGSE-ILL-0070; Appendix C). Therefore, it was clear the baseplate design needed to be optimised to minimise gradients.

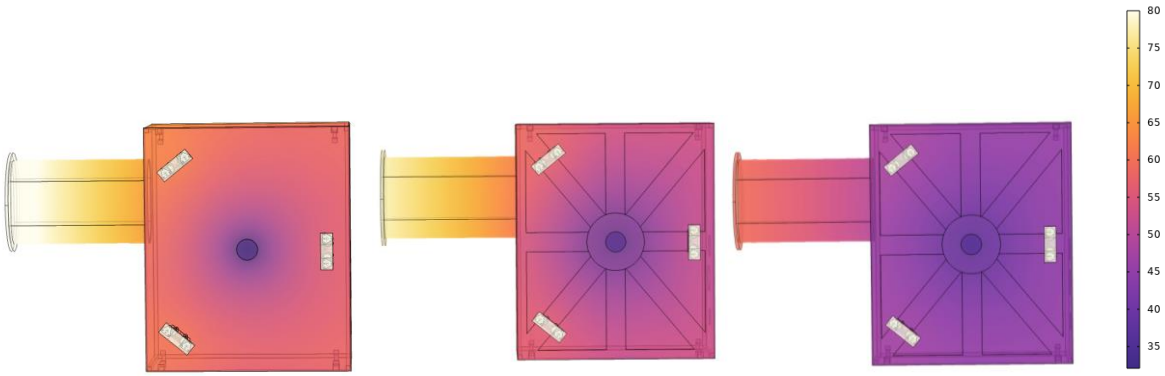

Figure 72: Shroud gradient mitigation (temperatures in K).

For a constant heat flux, the gradient scales as the inverse of the cross-sectional area. For a flat metal base plate and a radial flux, the conductive cross-section is a cylinder with an area that scales as the distance from the cold head squared. It is this inverse square cross-section scaling that gives rise to the vast gradients close to the cold head (Figure 72-left). An improved baseplate would, therefore, have a cross-sectional area independent of the radius from the cold head. This inspires the radial design shown in Figure 72 – centre. This provided a 7 K improvement to the gradient, however, it was clear that a thermally optimised aluminium grade would also be required. Figure 73 shows the conductivity of different grades of aluminium. 6063 was preferred as this is sufficiently rigid to be used for structural members whilst having a conductivity only marginally less than pure 1000 series

Aluminium. The results with improved lightweighting and 6063 conductivity are shown in Figure 73 – Right showing gradients could be made negligible.

The simple, shroud-only model highlighted that radiative loads on the shroud (even with MLI) would cause considerable gradients and that the conductive path will need to be optimised to enable at 70K bench (Figure 73).

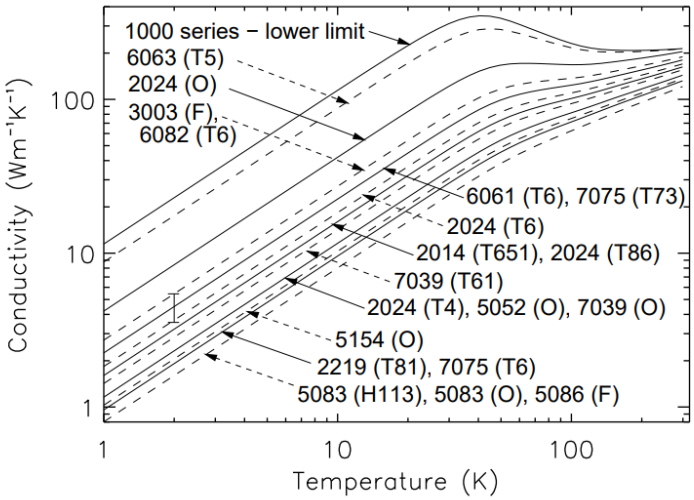

Figure 73: Thermal conductivity of different grades of AL from [122].

5.2.2.3 Full illumination module geometry

Having assessed the thermal balance of the shroud, the next step, was to incorporate the full geometry of the optical bench and support structure (shown in Figure 68). The resulting temperature distribution is seen in Figure 74. With this design the optical bench reaches 90 K. This is 20 K above the required temperature.

Part of the reduction in performance between Figure 74 and Figure 72 is due to a switch in the AL grade. Due to limited supplies of large enough plates AL 6063, a hybrid solution was needed. AL 6082 would be used for structural members of the shroud and 5mm sheet 1050 would be used for thermal performance.

In this version, the cold head reaches 38 K. However, due to gradients along the shroud, the cold side of the copper strap (Figure 68) reaches 62 K. There is then a further 28 K temperature increase across the strap giving a 90 K bench.

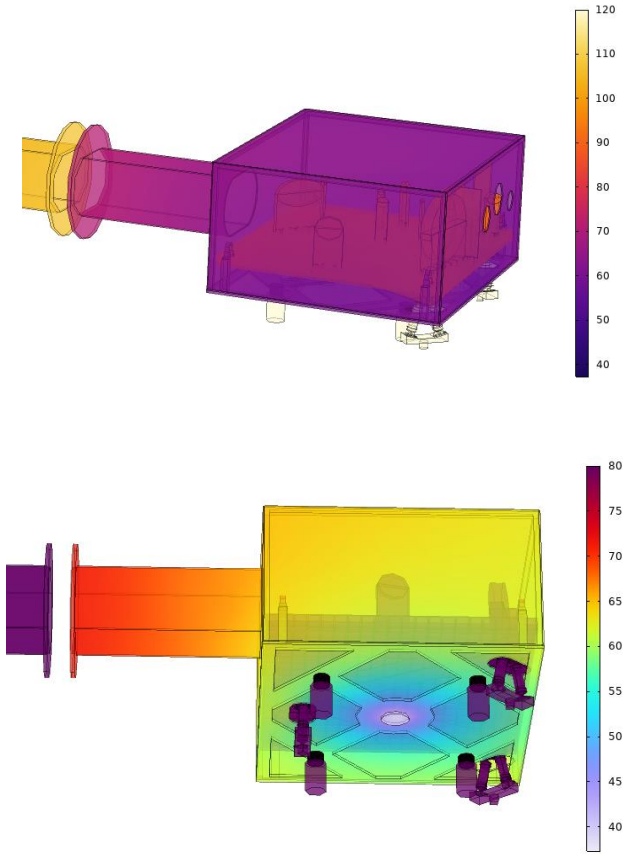

Figure 74: Equilibrium temperature distribution. The lower plot is re-scaled to emphasise the thermal distribution across the shroud (temperature shown in K).

A combination of measures could be used to bring the optical bench to below the required 70 K. By increasing the 1050 thickness in the baseplate, gradients can be reduced. However, the shroud already weighs 83 kg[47], with the baseplate already contributing 33 kg of that. Significantly changes to the

[47] This should be seen as a minimum mass at this stage. At the time of thermal modelling, certain structural members were still to be defined (including the baffle tube support).

baseplate thickness are therefore not an insignificant mass driver. This has cooldown time implications. An alternative approach would involve routing the optical bench thermal flux via a path independent of the shroud. This would reduce the temperature gradient between the cold head and the copper strap without a major mass increase.

In combination with the measures to reduce cold head to straps gradients, the delta T across the straps also needs to be reduced. A factor of approximately two increase in strap cross-section should give an acceptable ΔT across the strap (~15 K). These two measures would likely bring the optical bench to acceptable temperatures.

5.2.2.4 Illumination module flux balance

In addition to thermal gradients, the flux balance of the system is the other driver of the steady-state temperature distribution. The cold head exhibits a temperature-dependent cooling power (Figure 71) By reducing the parasitic loads on the system, the cold head temperature could be reduced. To assess if any parasitic loads could be optimised, a thermal budget was created. This is shown in Table 19.

In most cases, thermal loads were evaluated by integrating conductive fluxes over key interface surfaces. In the case of the radiative load on the optical bench, this was not possible to determine by direct flux integration so it was estimated by differencing the total cooling power of the optical bench from the conductive load from the GRP supports. Cooling of the optical bench is provided by the copper straps as well as radiative emission from the bench. At 90 K, this corresponds to 13.6 W and 7.4 W respectively.

The steady-state temperature profile was evaluated with the sources and thermal control heaters turned off. Further margin must be added to account for the source flux (~3 W; Table 3) as well as the thermal control heaters (~10 W was assumed).

Load	Power (W)
Baffle tube (radiative)	20.6
Top/base shroud panel (radiative)	9.6×2
Front/ back shroud panel (radiative)	4.7×2
Side panels(radiative)	4.4×2
Bipods	2.64×3
Radiative load on the optical bench	13.1
Spring supports	1.1×4
Cold head cooling	-91

Table 19: Thermal fluxes estimated from COMSOL

Table 19 shows that the dominant loads on the system are all radiative. In particular, the balance is being driven by the load from the ambient chamber walls onto the MLI-covered shroud. Unfortunately, this means the model results are extremely sensitive to the assumed effective emissivity of MLI. The effective emissivity is notoriously hard to predict for the following reasons: In addition to the layer material and number of layers, the effective emissivity depends strongly on the inter-layer conduction as well as edge effects. Inter-layer conduction strongly depends on compression due to e.g. corners, as well as fastening points [119, 120]. All of these effects make the MLI effective emissivity hard to predict (by at least an order of magnitude [123]). In this analysis, an effective emissivity of 0.02 was assumed this was measured by [119] and is the value recommended for design by [120]. The effective emissivity remains the driving source of uncertainty in the steady state temperature profile.

5.2.2.5 Cooldown time

In addition to the steady state temperature distribution, the cooldown time must be assessed. The illumination module cooldown time is being driven by test time considerations in Oxford. A couple of days is seen as the maximum feasible cooldown before this timescale will considerably impact optical and calibration testing in Oxford. The predicted cooldown time is shown in Figure 75. The results show a ~7-day cooldown time – longer than would be desirable.

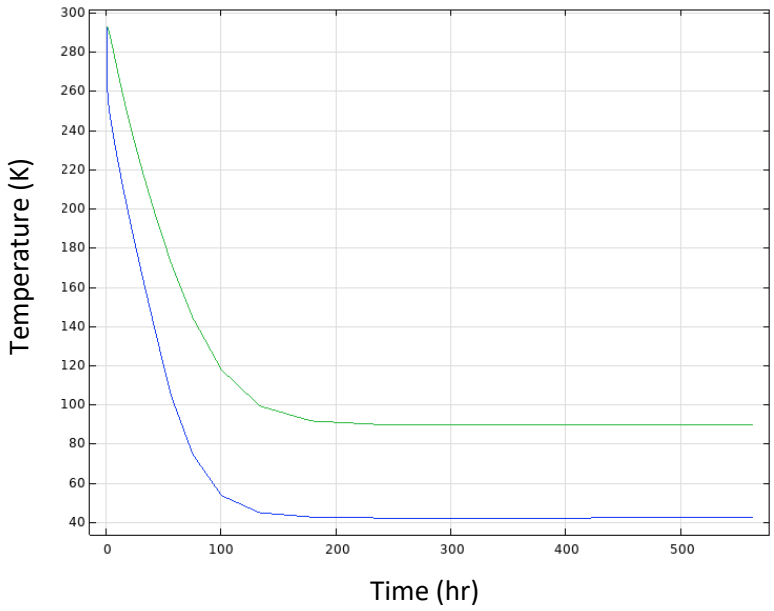

Figure 75: Cooldown time. The cold head temperature is shown in blue. The optical bench is shown in green.

5.2.2.6 Conclusions

The steady-state analysis showed a non-compliant thermal profile. However, solutions were proposed that would likely bring the optical bench temperature into marginal compliance. Of greater concern is that the flux budget is entirely driven by the highly uncertain MLI performance and the (un-tested) cold head power. This would only be de-risked by test when the full illumination module was constructed. In addition, the cooldown time is likely considerable (~7 days) with this single-stage thermal design. Because of the MLI risk and the cooldown time, an alternative solution is currently under consideration.

The alternative design uses liquid to cool the shroud and the cold head only to cool the optical bench. The vast ambient radiative load would therefore be dissipated by the liquid nitrogen. The load on the cold head would then be considerably reduced (~30 W total load) and would be less uncertain as this is not driven by the MLI performance. Liquid nitrogen cooling of the shroud would also significantly help the cooldown time which is currently driven by the thermal mass and the cooling power of the cold head (Figure 70). The trade-off between the two-stage liquid nitrogen design and the single-stage cold head design is the subject of immediate future work.

5.2.3 Target projector thermal design

The target projector has a comparably simple thermal architecture. The optics are supported on a cold (~70 K) table (Figure 76). This table is supported from the ~ambient trolley by a low conductivity GRP hexapod. The target projector is fully enclosed in a ~40 K shroud and has only small view factors of ambient surfaces (e.g. the target projector feet). The target projector is in a radiative-conductive balance with the dominant load coming from conduction along the GRP supports. This is balanced against thermal emission from the target projector table and mirror support structure.

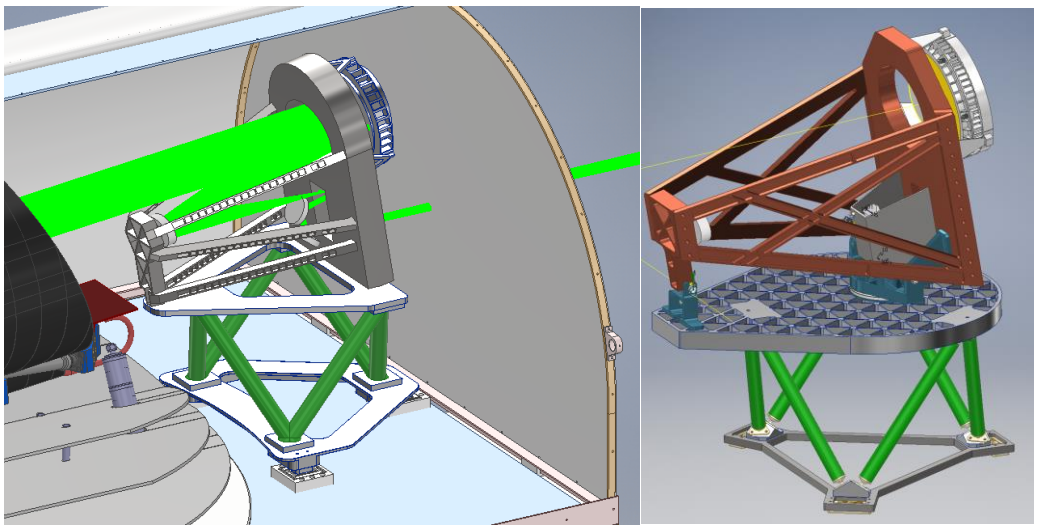

Figure 76: Early iterations of the target projector design (CAD by Rory Evens) [51]. Left shows the initial conceptual design as SRR. Right shows the updated, thermally optimised, table.

To study the thermal performance of the target projector, a nodal thermal model of the target projector was created. This was then used to validate and understand the detailed RAL FEA model[48] of the target projector within the CTR enclosure.

The nodal model assumed an isothermal optical bench. The optical bench + table radiatively exchanged flux with the 40 K shroud over a $1.75\ \mathrm{m}^2$ effective radiating area. The conductive load along the GRP posts was represented as a 1D conductive heat flux. The magnitude of the conductive load is determined by the combined cross-section of all GRP rods ($0.0014\ \mathrm{m}^2$) and the GRP length ($0.4\ \mathrm{m}$). To resolve the temperature-dependent thermal conductivity of the GRP, 7 nodes were used along the length of the GRP.

In addition to the conductive load on the table, a radiative short was also included. This modelled the radiative coupling between the ambient and cryogenic triangles seen in the table design (Figure 76-Left).

Early iterations of the target projector showed a non-compliant temperature (~92 K). This was significantly higher than the GRP conduction limited performance of the system. This indicated the presence of a significant radiative load on the upper table. This was mitigated by two factors: (1) the addition of a separator plate to prevent line of sight between the target projector and the approximately ambient payload PIP plate. Secondly, the results showed a significant radiative short between the ambient and cryogenic support triangles. To reduce this, the surface area of the lower support triangle was considerably reduced (Figure 76). The combination of these two measures brought the target projector into the conduction limited regime.

[48] FEA modelling conducted buy Samuel Tustain and Ediz Tunarli

The nodal model, however, also highlighted that even in the conduction-limited case, the target projector would still have marginal thermal performance (~75 K relative to a 70 K requirement). Because of this, two further design changes were made: (1) a factor of four reduction in the GRP cross section and (2) filling in the target projector table to give the teardrop shape shown in Figure 76. The teardrop increased the effective radiating area of the target projector from ~1 $\mathrm{m}^2$to ~1.75 m^2. The combination of the GRP optimisation and the enhanced radiating area brought the predicted equilibrium temperature from 75 K down to 59 K[49]. This provided ample margin relative to the 70 K requirement, including the margin required to add thermal control heaters. This design was, therefore, assumed at PDR.

5.3 THERMAL STRAY LIGHT DURING PAYLOAD-LEVEL TESTING

Having analysed if the OGSE optics can get sufficiently cold to verify the payload dark current, the remaining effect to be explored is thermal stray light. Thermal stray light similarly manifests as a spurious additive signal that may impact dark current measurements. In part, the stray light analysis was motivated by the extreme background seen when simulating the ambient mirror (Figure 64). This showed that an in-field, low emissivity mirror (0.03) would contribute 3×10^6 $\mathrm{e^-pix^{-1}s^{-1}}$ in Airs CH1. This shows the vast photon flux from ambient surfaces at ~8 microns. Given there are approximately ambient surfaces within the CTR, these will be emitting a vast flux at 8 microns. To be determined was how much of this flux would scatter off OGSE optics and arrive at the payload detectors.

The dominant sources of stray light are expected to be any ambient (or close to ambient surfaces) within the CTR. These include:

[49] This model also used a more conservative 0.5 $\mathrm{Wm^{-1}K^{-1}}$ CBE thermal conductivity to a 0.9 $\mathrm{Wm^{-1}K^{-1}}$ conductivity.

- The Payload Interface Plate (PIP) (293 K)
- The lower V-grooves (173 K & 117 K for VG1 and VG2 respectively)
- Exposed parts of the CTR trolly (ambient)
- The target projector feet and lower ring support (277 K – separated from the ambient trolly by a GRP spacer block)

To be detected, thermal emission from these surfaces must scatter into the OGSE beam. In principle, this could happen off any of the optics within the injection module, target projector or the payload. However, the injection module optics are enclosed in a ~65 K black painted box, therefore it is likely that the target projector optics will dominate any stray light budget over the injection module (see Figure 77). It is also important to assess the impact of thermal stray light scattering off the CTR shroud directly into M1.

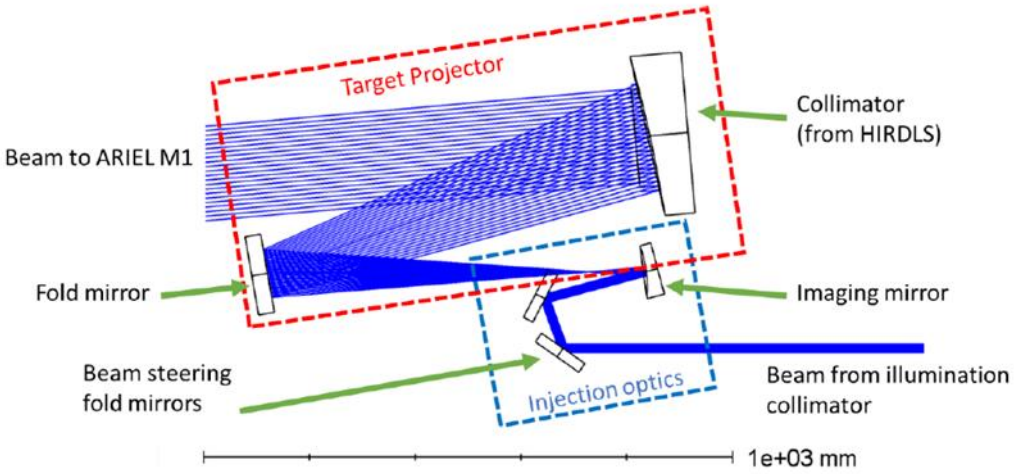

Figure 77: OGSE target projector and injection module optics [51].

5.3.1 Thermal stray light model

5.3.1.1 Thermal irradiance at a mirror's surface

To assess the impact of thermal stray light, the radiative coupling between the various elements within the CTR, PLM and OGSE must be evaluated. The radiative coupling between surfaces has been defined

in terms of the radiative heat transfer coefficient (from ESATAN). These have been provided by the CTR team and are given in Table 20.

. Our starting point is, therefore, the radiative heat transferred between surfaces. We want to convert this into the scattered stray light radiance. Therefore, the method used here is:

1. To use the radiative heat transfer coefficients to predict how much of the spectral power emitted by the PIP plate gets absorbed at a mirror's surface.
2. Given the emissivity of the mirror, the spectral power absorbed by the mirror can be used to predict the irradiance incident at the mirror's surface.
3. Finally, given the scattering properties of the mirror, the irradiance at the mirror's surface can be used to predict the stray light radiance that scatters into the OGSE beam.

Here a brief derivation is provided, for further details see Appendix B.

The radiative transfer between the PIP plate MLI and optical elements is described in terms of a radiative heat transfer coefficient G_R (defined by equation 5.1). The radiative transfer coefficient relates the net heat flux, Φ_{tot}, to the temperature of the respective surfaces:

$$\Phi_{net} = \Phi_{abs} - \Phi_{emit} = G_R\sigma\left(\mathrm{T}_{\mathrm{PIP}}^4 - T_{mirror}^4\right) \tag{5.1}$$

The absorbed flux is $\propto T_{pip}^4$ and the emitted flux is proportional to T_{mirror}^4. Therefore, by inspection, the radiative flux absorbed by a mirror is given by:

$$\Phi_{abs} = G_R\sigma\mathrm{T}_{\mathrm{PIP}}^4 \tag{5.2}$$

Therefore, the spectral power absorbed by the mirror, P_{abs} is:

$$\mathrm{P}_{abs}(\lambda) = G_R B\left(T_{pip}, \lambda\right)\pi \text{ sr} \tag{5.3}$$

To obtain the power incident on the mirror, P_{in}, the absorbed power can be normalised by the mirror emissivity ϵ_{mirror}.

$$\mathrm{P}_{in}(\lambda) = \frac{G_R B\left(T_{pip}, \lambda\right)\pi \text{ sr}}{\epsilon_{mirror}} \tag{5.4}$$

The irradiance on the mirror's surface I_{in} can then be elevated. $I_{in} = \frac{\mathrm{P}_{in}}{A_{mirror}}$, where A_{mirror} is the absorbing area of the mirror used in the view factor calculation.

$$\mathrm{I}_{in}(\lambda) = \frac{G_R B(T_{pip}, \lambda)\pi \text{ sr}}{A_{mirror}\epsilon_{mirror}} \tag{5.5}$$

This allows the spectral irradiance at a mirror's surface to be calculated in terms of quantities that are obtainable from the ESATAN thermal model (G_R and T_{pip}). Given the scattering properties of the mirror, the stray light radiance can now be calculated.

5.3.1.2 Scattering model

In this analysis, the ESATAN thermal model has been used to calculate the radiated coupling between facets. This tells us the spectral irradiance at a mirror's surface, however, gives us no information about the incident angle. Therefore, it is not possible to utilise the full angular dependence of the bidirectional reflectance distribution function (BRDF). We can, however, perform calculations in two limiting cases: (1) A model which is valid in the limit of isotropic irradiance of the mirror's surface; and (2) a best-case analysis where we assume a point source irradiance which occurs at an angle at which the BRDF has the minimum scattering.

5.3.1.2.1 Isotropic irradiance

Given there is no direct line of sight paths between the stray light sources (e.g. the PIP plate) and the mirror's surface, it is reasonable to expect that the irradiance will contain contributions from a wide range of incident angles. Therefore, we make the simplifying assumption of isotropic irradiance to place a zeroth-order estimate on the expected stray light rejection.

In general, the stray light radiance can be calculated as [124]:

$$\mathrm{L}_{stray}(\lambda, \theta_s) = \int BRDF(\theta_{in}, \theta_s)\, L_{in} \cos\theta_{in}\ d\Omega \tag{5.6}$$

Where the scattering angle, θ_s, is set by the optical geometry, e.g. the angle M2 subtends from M1 (in the case of scattering off M1). For isotropic incident radiance L_{in}:

$$\mathrm{L}_{stray}(\lambda) = L_{in} \int BRDF \ \cos\theta \ d\Omega \equiv \ L_{in} \ TIS \tag{5.7}$$

$$= \frac{I_{in}}{\pi} \ TIS \tag{5.8}$$

Therefore, from equation 5.5, the stray light radiance, scattered at a mirror's surface is given by:

$$\mathrm{L}_{stray}(\lambda) = \frac{TIS \ G_R BB(T_{pip}, \lambda)}{A_{mirror} \epsilon_{mirror}} \tag{5.9}$$

5.3.1.2.2 Total Integrated Scatter (TIS) from surface roughness

The stray light evaluated using equation 5.9 is defined in terms of the Total Integrated Scatter (TIS). There will be two contributing factors to the TIS of the mirrors. (1) micro-roughness and (2) particulate contamination. For micro-roughness, we assume a 5 nm [125] surface roughness and a Total Integrated Scatter (TIS) given by:

$$TIS = \left(\frac{4\pi\sigma \cos\theta_i}{\lambda}\right)^2 \tag{5.10}$$

At 7.8 μm, the TIS = 6.5×10^{-5}.

5.3.1.2.3 TIS from particulate contamination on optical surfaces

For particulate contamination, we assume a class one surface with a 0.08% Percentage Area Coverage (PAC) (R-OGSE-CRS-0080) upon delivery to RAL. Ekin [126] quotes 50 ppm contamination per T-VAC cycle. After delivery of the target projector, there are three planned T-vac cycles (CTR blank test, payload EM and payload PFM). Moreover, we assume 50 ppm contamination during AIT at RAL for each of the campaigns. We, therefore, define an end-of-life cleanliness ~800 ppm + 50 ppm × 6 = 1100 ppm. Defining the expected cryo-condensation remains highly uncertain and should be verified by test using witness samples during the CTR blank test.

By assuming that photons incident on contaminants scatter diffusely, the PAC can be converted into the TIS (≈PAC/100). However, diffraction effects can cause the TIS to be larger than the PAC/100 by a factor of two [124]. **Therefore, in this analysis, we assume a TIS of 0.2% for OGSE mirrors.**

Thermal stray light can also scatter into the beam from the payload optics, especially M1. Therefore, a TIS must also be assumed for the payload optics. Table 6 of the payload cleanliness and contamination control plan [127] quotes 994 ppm PAC for M1 at PLM delivery to the spacecraft AIT. As before, we multiply the PAC by two to account for diffraction effects. Therefore, 0.2% TIS is also assumed for M1.

5.3.1.2.4 Best-case scattering model

Without knowing the angular distribution of the incident irradiance it is challenging to estimate the uncertainty in the isotropic irradiance assumption. However, we can place a best-case bound on the minimum stray light we would expect to see. From Figure 78, one can see that the best stray light rejection would occur if all the incident irradiance was at 60 degrees. Therefore, we can place a best-case bound on the stray light rejection if we assume the stray light comes from a point source located at an incident angle of 60 degrees.

The BRDF shown in Figure 78 was created for M1, with a scattering angle set by the angle subtended by M2. However, the angle of the OGSE beam on e.g. the target projector fold mirror will be different from the M1- M2 angle. Therefore, it is not immediately obvious the BRDF remains valid for other mirrors such as the OGSE collimator and the fold mirror.

To justify the use of the M1 BRDF on mirrors with other scattering angles we first note that the scattering angle is similar and small in all cases ($< 14°$). Secondly, typical first-order BRDF representations are shift-invariant (see e.g. the Harvey or ABg BRDF representations [124]). A shift-invariant BRDF would preserve the minimum scattering amplitude but the minimum would occur at a different incident angle. This best-case analysis only depends on the minimum value of the BRDF and not the incident angle at which the minimum occurs. Therefore, the small discrepancy in scattering angles between M1, and e.g. the OGSE target projector fold mirror is not expected to significantly impact results.

The only other possible discrepancy between the OGSE BRDF and the payload M1 BRDF would be if the contamination level was different. However, as discussed in 5.3.1.2.1, the contamination of OGSE optics is expected to be similar to the contamination of M1. Therefore the Ariel BRDF (Figure 78) can be used not only to assess scattering off M1, but also to assess scattering of the OGSE collimator, and target projector fold mirror.

Figure 78: Full BRDF compared to clean mirror BRDF. Particle density 2000ppm, surface roughness 10nm RMS. Figure from [128]. (Figure redacted from ORA version)

To place a best-case bound on the stray light, all incident light is assumed to originate at a single angle, the angle at which the BRDF has its minimum value (see Figure 78). In other words, the incident radiance takes the form of a Dirac delta, $L_{in} \propto \delta(\theta_{in} - \theta_{\min})$. When this is the case, equation 5 simplifies to:

$$\mathrm{L}_{stray}(\lambda) = BRDF(\theta_{min}, \theta_s) \int L_{in} \cos\theta_{in} \; d\Omega \tag{5.11}$$

Therefore,

$$L_{stray} = BRDF(\theta_{min}, \theta_s) \times I_{in} = \frac{BRDF(\theta_{min})\,\pi \text{ sr } G_R B(T_{pip}, \lambda)}{A_{mirror}\epsilon_{mirror}} \quad (5.12)$$

This stray light radiance now needs to be propagated to the focal plane such that this can be compared to the detector's dark current (in e^-s^{-1}).

5.3.1.3 Radiance to focal plane signal conversion

The diffuse stray light is propagated to the instrument focal planes using an ArielRad-derived end-to-end radiometric calibration[50]. The end-to-end radiometric calibration can be described in the following form[51]:

$$E = \alpha L \eta_{\text{exp}} \quad (5.13)$$

Where E is the focal plane signal in e^-s^{-1} and L is the radiance of a diffuse source at M1 ($\mathrm{Wm^{-2}sr^{-1}\mu m^{-1}}$). The proportionality constant between them, α , defines the radiometric calibration. η_{exp} is the correction factor that is applied to account for the beam expander throughput.

The proportionality constant was derived using ArielRad IR diffuse source simulations. When the payload is illuminated by the IR diffuse source (bright mode), the focal plane signal in the longest

[50] Computed on ArielRad version dated 1st March 2022

[51] Strictly only valid for thin slits (thin compared to spectral resolution), but also agrees well for wide slits providing that the SED is smoothly varying. See ARIEL-OXF -PL-TN -005 for quantitative discussion.

spectral bin was found to be[52] 1.86×10^7 $\mathrm{e^{-}s^{-1}pix^{-1}}$. At 7.639 µm (midpoint of the longest spectral bin) the injected radiance was $0.425\ \mathrm{Wm^{-2}sr^{-1}\mu m^{-1}}$. Therefore, the radiometric calibration proportionality constant is given by $\alpha = 4.39 \times 10^7\ \mathrm{e^{-}}s^{-1}\mathrm{m^2\mu m\ srW^{-1}}$.

5.3.2 Thermal stray light results

The goal of this analysis is to calculate the focal plane signal that results from thermal stray light. To do this, the stray light must be evaluated for every combination of stray light source and mirror. This was achieved using the RAL thermal model to perform the ray trace to determine the radiative coupling between stray light sources and the mirror's surface. From this coupling, the incident irradiance at a mirror was calculated (equation 5.5). A scattering model was then required to determine how much light scatters into the payload FOV. The stray light radiance was predicted using equation 5.9 (isotropic model) and equation 5.12 (best case model). The resulting focal plane signal was then predicted using an ArielRad-derived end-to-end radiometric calibration (equation 5.13). This is shown below in Table 20.

[52] These simulations were evaluated without any OGSE modulation. 10^7 $\mathrm{e^{-}pix^{-1}s^{-1}}$ is larger than planned OGSE fluxes, however this can still be used to derive the radiometric calibration. To check we are not seeing saturation in the simulation, the calibration was cross-checked with diffuse ExoSim data at lower flux levels.

Emitting surface	Scattering surface	Radiative heat transfer coefficient (m^2)	Emitting temperature (K)	Emitting radiance ($Wm^{-2}sr^{-1}\mu m^{-1}$)	Mirror emissivity	Scattering mirror area (m^2)	Stray light radiance ($Wm^{-2}sr^{-1}\mu m^{-1}$)		Focal plane signal ($e^{-}pix^{-1}s^{-1}$)	
							Isotropic irradiance model	Best case model	Isotropic irradiance model	Best case model
VG1	Collimator	6.92×10^{-6}	170.2	8.10×10^{-2}	0.02	0.071	7.93×10^{-7}	3.74×10^{-7}	26	12
VG2	Collimator	7.48×10^{-6}	115.1	4.52×10^{-4}	0.02	0.071	4.79×10^{-9}	2.26×10^{-9}	0.16	7.4×10^{-2}
PIP plate	Collimator	1.17×10^{-5}	227.5	1.24	0.02	0.071	2.05×10^{-5}	9.68×10^{-6}	6.8×10^{2}	3.2×10^{2}
VG1	Fold mirror	0.00	170.2	8.10×10^{-2}	0.02	0.012	0.00	0.00	0.0	0.0
VG2	Fold mirror	0.00	115.1	4.52×10^{-4}	0.02	0.012	0.00	0.00	0.0	0.0
PIP plate	Fold mirror	1.45×10^{-6}	227.5	1.24	0.02	0.012	1.52×10^{-5}	7.17×10^{-6}	5.0×10^{2}	2.4×10^{2}
PIP plate	M1	1.51×10^{-3}	227.5	1.24	0.05	0.605	1.24×10^{-4}	5.83×10^{-5}	4.1×10^{3}	1.9×10^{3}
								Total	**5.3×10^{3}**	**2.5×10^{3}**

Table 20: Thermal stray light signal as measured at AIRS CH1 for various thermal stray light paths. The 'Collimator' and 'fold mirror' are shown in Figure 77.

The thermal stray light for the isotropic case is ~5000 $e^{-}pix^{-1}s^{-1}$ at 7.8 µm with a best-case limit of ~2000 $e^{-}pix^{-1}s^{-1}$. The dominant contributor is indirect scattering from the pip plate into M1[53]. There are also significant contributions from PIP plate scattering onto the OGSE collimator and fold mirror. The total stray light is significantly larger than the 1 $e^{-}pix^{-1}s^{-1}$ dark current requirement so would likely prevent dark characterisation of the payload in Airs CH1. This level of stray light would also be larger than the OGSE faint target signal (~1000 $\mathrm{es}^{-1}\mathrm{pix}^{-1}$ at 7.8µm; see Figure 49). To reduce the stray light, one option considered was to switch from reflective to black MLI the merits of this were assessed by sensitivity analysis.

5.3.2.1 PIP plate MLI sensitivity analysis

To assess the sensitivity of the stray light to the PIP MLI emissivity, two rounds of thermal analysis can be compared. The first was performed with black MLI, the second round was performed with low emissivity MLI (ϵ = 0.05). It was shown in section 5.3.1.1 that the thermal stay light is proportional to $G_R B(T_{PIP}, 7.8\ \mu\mathrm{m})$. Therefore, we can compare this stray light proxy in the two cases. This is shown in Table 21.

[53] Note, the M1 stray light radiance was evaluated as the mean radiance over the full pupil. However, only the centre ¼ of the pupil is sampled during ground testing.

	Low emissivity MLI	High emissivity MLI
Radiative transfer coefficient G_R	2.975×10^{-5} m^2	2.664$\times 10^{-4}$m^2
PIP top MLI layer temperature, T_{pip}	227.5 K	171.5 K
$B(T_{PIP}, 7.8\ \mu\text{m})$	1.22056 Wm^{-2}sr^{-1}μm^{-1}	0.0880 Wm^{-2}sr^{-1}μm^{-1}
Thermal stay light proxy $\propto G_R B(T_{PIP}, 7.8\ \mu\text{m})$	3.63×10^{-5} Wsr^{-1}μm^{-1}	2.34×10^{-5} Wsr^{-1}μm^{-1}

Table 21: Comparison of high and low emissivity MLI

The results shown in Table 21 can be understood by considering two effects. To first order, the radiative transfer coefficient, G_R, will scale linearly with the PIP MLI emissivity. However, due to increased self-absorption at higher emissivities, the scaling will be weaker than a simple proportionality. The higher emissivity also causes stronger coupling between the MLI top surface and the cold radiative environment, causing a cooler top-layer emitting temperature.

Therefore, switching from high to low emissivity MLI causes an order-of-magnitude reduction in the distribution factor, but an order-of-magnitude increase in 7.8 μm radiance. By coincidence, these effects cancel out such that the stray light radiance is largely insensitive to the emissivity of the PIP MLI (~30% less stray light with high emissivity MLI). Therefore, the stray light only weekly depends on the MLI coating emissivity. However, we are very sensitive to the MLI top layer temperature (and hence the MLI heat transfer model). The sensitivity to the top layer temperature is even larger in the high emissivity case.

5.3.2.2 Thermal stray light conclusions

Multiple rounds of stray light analysis were performed. In all cases, stray light was found to be considerably above the payload dark current level (~10^3 times more). Multiple options were, therefore, discussed to aid in the reduction of stray light.

Initial rounds of analysis focused on the target projector mirrors. It was found that the PIP plate was the dominant stray light source. A separator plate was therefore proposed to isolate the stray light

source (the PIP plate) from the OGSE optics. Subsequent rounds, however, showed that scattering off M1 was the dominant stray light path. An alternative skirt-based baffle was therefore proposed to contain the stray light at the source.

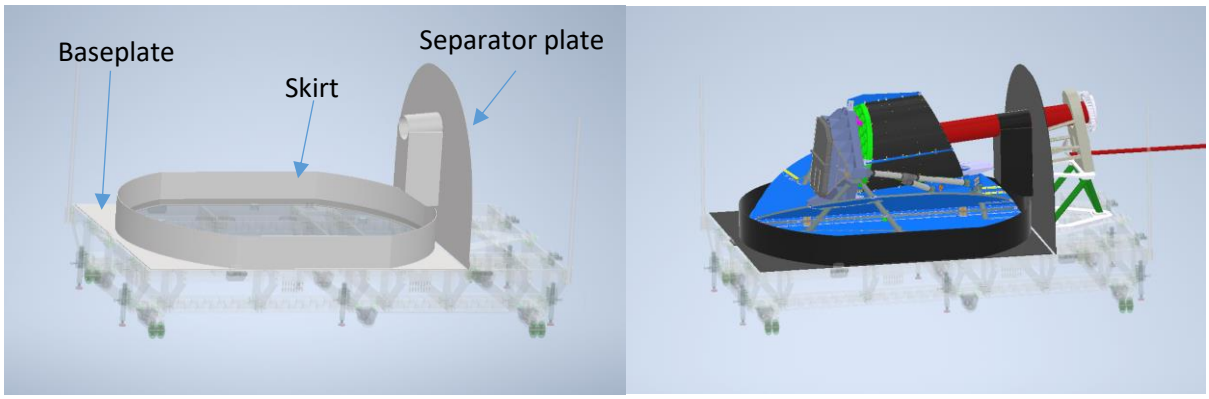

Figure 79: Conceptual design of possible baffling options to reduce thermal stray light. Both approaches attempt to restrict view factors between the PIP plate and optical surfaces.

In the end, an alternative solution was sought. This analysis showed that the dominant stray light paths were indirect, likely via the shroud. Therefore, improved stray light control may be achievable by improving the shroud emissivity. 0.81 was assumed in the RAL thermal model [129]. It was, therefore, decided to use a honeycomb shroud instead of flat shroud panels. This was also beneficial for thermal reasons. It is hoped that the improved stray control provided by the honeycomb will reduce stray light to closer to acceptable levels (1 e $s^{-1}pix^{-1}$).

The model presented in this section is intended to be an order-of-magnitude estimate. Achieving better than this at this stage will be challenging. This model relies on knowledge of mirror particulate contamination. The values modelled are those budgeted in the payload contamination budget. This remains highly uncertain until the contamination is measured using witness samples. Moreover, the use of the RAL thermal model to predict radiative coupling enables irradiance estimation but does not allow a full BRDF model to be used. A full end-to-end scattering model would be desirable. However, in all likelihood, thermal stray light will be verified by test during the EM test campaign.

5.4 CHAPTER SUMMARY

In this chapter, the OGSE thermal requirements were derived. It was shown that to test the dark current at the payload level, OGSE optics must be cooled to less than 70K. This was derived using end-to-end simulations using ExoSim.

To meet this 70 K requirement, an updated illumination module thermal design was created. A finite element analysis was conducted to assess the compliance of this design, however, it was found the enlarged illumination module design would be non-compliant largely due to thermal gradients on the shroud. Measures were presented to improve the conductive path from the cold head to the optical bench, this would likely bring the thermal design into marginal compliance.

Of greater concern was the flux balance analysis. This analysis showed the loads on the cold head are dominated by the radiative load on the MLI. Literature data shows order or magnitude variation in the effective emissivity of MLI [123], meaning, the dominant load in the thermal model is highly uncertain. This combined with the long (~1 week) cooldown time motivated an alternative thermal architecture. The new design uses liquid nitrogen to cool the shroud and the cold head only cools the optical bench. This liquid nitrogen design is currently under development.

In addition to thermal emission from optical elements, thermal stray light was also considered. It was found that thermal mission from the PIP plate indirectly scattering off M1 will lead to a considerable ($\sim 10^3$ e $s^{-1} pix^{-1}$) signal in Airs CH1. Improvements in the CTR shroud emissivity have been made, partially mitigating this effect, however, stray light remains the dominant risk to low background (~ 1 e $s^{-1} pix^{-1}$) measurements during payload-level testing.

6 ILLUMINATION MODULE OPTICAL DESIGN

Chapter 5 focuses on the thermal aspects of the illumination module design, in this chapter, the illumination module optical design will be motivated, and described. It will be shown why there was a need to change the OGSE optical architecture from the PDR design. The new optical design for the illumination module will be presented.

6.1 TARGET PROJECTOR TRADE-OFF

In the lead-up to CDR, there was a major revision to the OGSE architecture. At PDR the illumination module injected a 22 mm (major axis) beam into the main test chamber (Figure 17). The illumination module output was then expanded by 12.5 times in the target projector to provide a ¼ aperture beam at M1. The revised optical architecture has an illumination module that produces ¼ aperture beam ~28 cm in the major axis). The target projector module became two flat mirrors known as the periscope assembly. The motivation for the switch away from the PDR concept will be discussed here.

6.1.1 Degrees of freedom of the OGSE

The driving motivation for the target projector trade-off was the complexity associated with monitoring and adjusting all the degrees of freedom in the target projector design. The adjustment is required to ensure that:

- The target projector output is centred and on the axis with respect to the payload M1 optical axis.
- The output of the OGSE has an angular size less than the OGSE encircled energy requirement (R-OGSE-8630).
- The output of the illumination module is on-axis and centred with respect to the first powered mirror in the target projector.

The illumination module, target projector, and payload are each separate modules, each with their own support structures. During cooldown, each will independently contract by millimetres causing significant misalignment between modules. Moreover, deformations internal to the target projector could cause the powered mirrors to no longer be confocal leading to aberrations. To correct the inter-module alignment shifts and internal optical aberrations, the following degrees of freedom were assumed in the PDR design[54]:

Adjustment	Function
Tip-tilt on the illumination module output	Illumination module to target projector centration
Tip-tilt on the first target projector fold mirror	Illumination module to target projector angular correction
Tip-tilt-piston adjustment of the first target projector powered mirror	Target projector optical aberration correction
Global tilt of the whole target projector structure	Target projector to payload angular correction
Translation of the target projector pupil plate	Target projector to payload centration

Table 22: adjustment degrees of freedom in the PDR design

[54] At the time of this analysis, the exact number of degree of freedom in the target projector was still under discussion. This represents the minimum number under consideration.

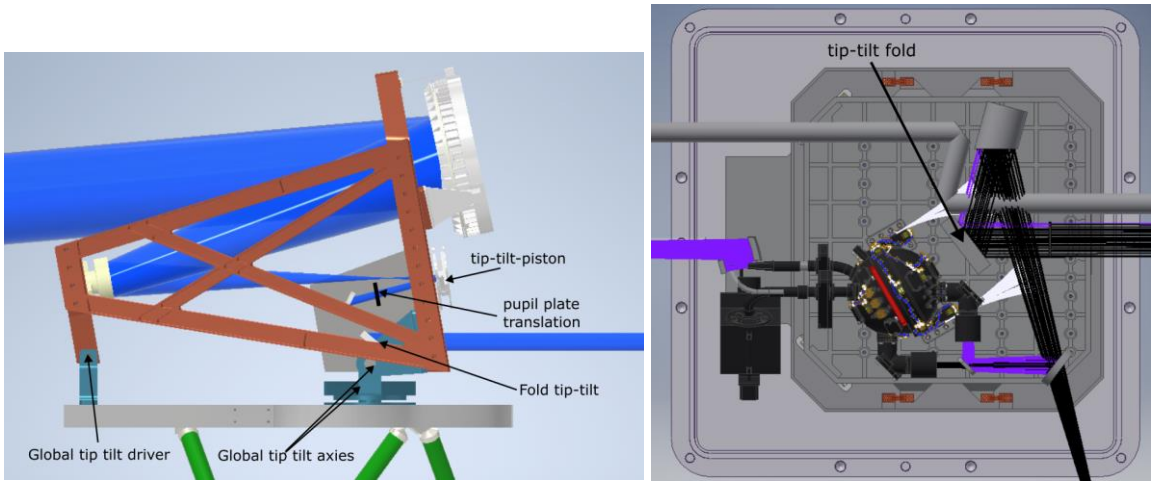

Figure 80: Actuated mechanisms in the target projector and PDR illumination model [51].

Even with these degrees of freedom, this does not guarantee all misalignment-induced WFE can be removed. These degrees of freedom do ensure the powered mirrors have parallel optical axis and that the powered mirrors are not defocused, it does not ensure that the optical axis of the first mirror is centred with respect to the optical axis of the second mirror. It may be necessary to tip-tilt the fold between the powered mirrors to ensure they remain co-axial (whether or not this was required was still to be confirmed).

6.1.2 Cooldown-induced optical aberrations

The list of adjusters presented in Table 22 provides a comprehensive set of adjusters to correct most cooldown-induced aberrations in the design. It was still, however, to be demonstrated whether all these degrees of freedom are required to correct the alignment-induced aberrations. It may be possible to reduce the number of degrees of freedom at the cost of optical quality. An assessment must be made of the optical quality with certain degrees of freedom removed from the design.

6.1.2.1 Powered mirror adjustment

To assess this, a thermoelastic analysis produced by Keith Nowicki was used (Figure 81). The author's responsibility was to use the thermoelastic analysis to predict the resulting optical aberrations.

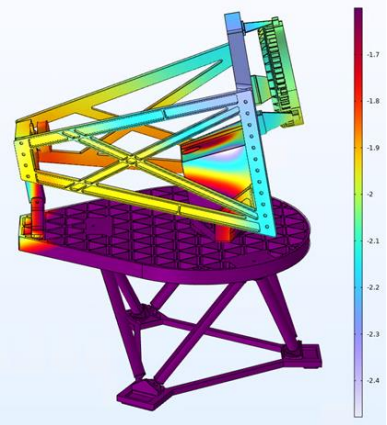

Figure 81: Y-deformation (vertical) of the target projector after 15 days of cooling (mm). The colour range is scaled to maximize deformations in the invar structure.

Positions and angles were measured from the COMSOL model and were used to perturb the optical model. The following deformations were seen in the thermoelastic analysis:

- 0.1 degree tilt of the front fold
- 0.03 degree tilt of the collimating mirror
- 300 μm displacement of the fold mirror (defocus)
- 200 μm centration offset of the collimating mirror

In the perturbation analysis, only the mirror positions were perturbed. The prescription of the powered mirrors was left unchanged. The contraction of an ideal isometric ZERODUR system would contract by 58 μm[55] (based on a 1.5 m focal length and a linear expansion coefficient of 39.3×10^{-6} [130]). The isometric contraction of the mirrors is, therefore, an order of magnitude smaller than the deformations seen in the thermoelastic analysis (600 μm change in focal length). Therefore, the change in powered mirror prescription was neglected.

[55] Based on a 1.5 m focal length and a linear expansion of 39.3×10^{-6}

In particular, defocus and tilt of the fold mirror were found to be dominant aberrations (Figure 82) and result in aberrations that are an order of magnitude larger than the OGSE rEE requirement (~15'' compared to a 0.9'' requirement the 28 cm beam, R-OGSE-8360). This confirmed the need for the tip-tilt-piston actuation of the imaging mirror in the PDR design (Table 22).

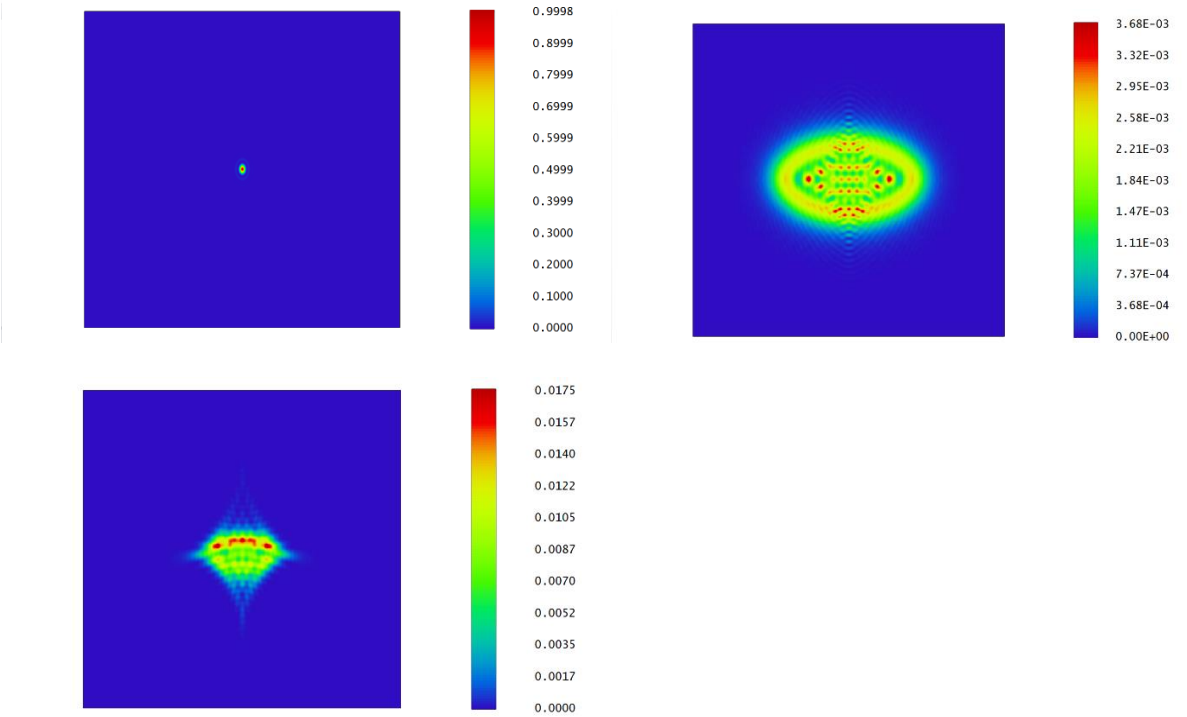

Figure 82: Optical model perturbations. Models were simulated with light at 550 nm. The image scale is 33 arcseconds square. Top left shows only the geometric aberrations (diffraction limited at 550 nm). Top right shows a 300 µm displacement of the front fold mirror. Bottom left shows 0.1 degree tilt of the front fold mirror.

6.1.2.2 Beam steering degrees of freedom

Having shown the powered mirror degrees of freedom are required, we now consider the beam steering degrees of freedom. Table 22 shows four degrees of freedom were assumed to align the target projector to the payload. The thermoelastic analysis used in 6.1.2.1 can also be used to assess if the target projector tilt/ centration degrees of freedom are required.

The OGSE must be able to steer the beam to the centre of the payload FOV with 4 arcsecond[56] resolution (SR-PER-215, [131]) and be centred to within 1 mm[57] (R-PRD-0610). The thermoelastic analysis showed ~2 mm translations and tilts of hundreds of arcseconds. Therefore, aligning the OGSE output with the required tolerances would require at least four degrees of freedom.

Also shown in Table 22 were four degrees of freedom to align the illumination module output to the target projector. At the time of performing this analysis, thermoelastic analysis/detailed tolerancing of the illumination module was still to be conducted. However, given the course (millimetre) tolerating of the CTR position relative to the illumination module, it was seen as extremely likely that adjusters would be required to align and centre the illumination module to the target projector.

The OGSE PDR design with the target projector, therefore, required eleven degrees of freedom [51]. Having this many mechanisms in the design already adds significant complicity. However, the real challenge is constraining these degrees of freedom.

Constraining the degrees of freedom is even harder for the OGSE than the payload. The payload has five degrees of freedom: three degrees of freedom provided by the M2 mechanism[132] and a further two degrees of freedom from the spacecraft to tip-tilt the payload. To constrain these degrees of freedom, the payload can observe the star on the detectors. There are three observables, the centroid of the spot (x & y) and the PSF. Through a combination of spot size minimization and centration, the optimum tilt and M2M position can be found.

[56] 1'' spacecraft absolute pointing requirement times four to account for the beam expander magnification.

[57] 0.1mm at the output of the beam expander times $55/4 = 1$ mm at the entrance of M1.

Not only does the OGSE have more degrees of freedom than the payload, but the OGSE can't use the payload detectors to focus the OGSE, since an aligned, collimated beam is required to focus the telescope. Because of this, the OGSE must find other ways to monitor and correct deformations during cooldown.

6.1.3 Monitoring optical aberrations - the pupil scanning autocollimator

To monitor alignment shifts, a pupil-scanning autocollimator design was proposed (Figure 83-Left). The autocollimator beam is injected above the test beam (Figure 83- Right) at the illumination module output. The laser follows the same optical path as the test beam through the target projector. The laser, therefore, acts as a decentered tracer ray. The laser can then be retroreflected off several alignment reference surfaces to monitor motion between key mirrors.

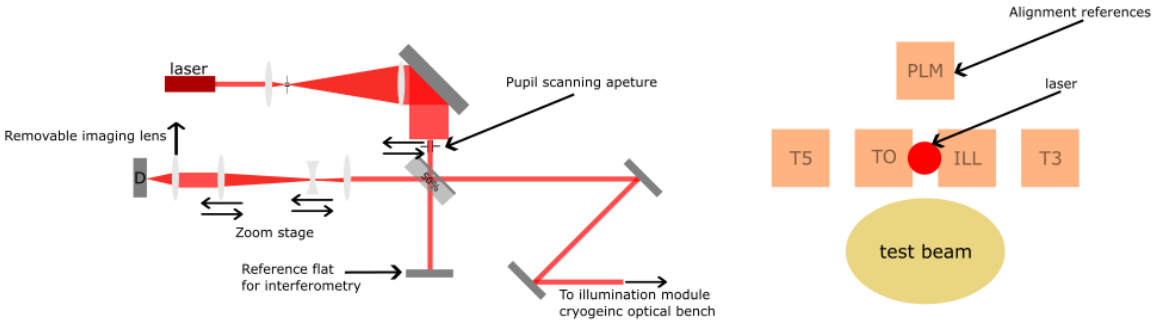

Figure 83: Pupil scanning autocollimator design. Left shows the autocollimator conceptual design. Right shows the pupil positions of the test beam and alignment surfaces.

The pupil-scanning autocollimator concept uses a laser with a long (e.g. 10 m) coherence length. The light passes through a spatial filter and beam expander to generate a ~50 mm beam (Figure 83 – Left). The beam then passes through an aperture mask mounted on an X-Y translation stage. This X-Y translation stage is used to change the centration of the laser, and thus view different alignment surfaces (Figure 83- Right). These reference surfaces are flat mirrors close to the test beam optical path but decentered from it (e.g. machined into the rims of the optical surfaces). The reference flats include:

- Illumination module reference surface (ILL) – An overhanging flat mirror after the illumination module tip-tilt mirror (Figure 80).
- Target projector output (TO) – an overhanging flat mirror at the target projector output.
- Target projector imaging mirror (T3) - a wedge machined into the mirror's rim
- Target projector collimating mirror (T5) - a wedge machined into the mirror's rim
- The payload alignment cube (PLM) – viewed via a pickoff mirror

By viewing combinations of these reference surfaces, the actuated degrees of freedom can be constrained. In each case the reference surfaces will have etchings, enabling them to define angle as well as centration. The interference fringes allow path length changes to be measured.

Actuator	Observable
Illumination module output tip-tilt	Illumination module optical bench (ILL) relative to T3
Tip-tilt on the first target projector fold	Illumination module optical bench (ILL) relative to T3
Powered mirror tip-tilt	T5 relative to T3
Powered mirror focus	Interference fringes from overhang flat
Target projector global tilt	T5 relative to PLM cube
Translation of the pupil plate to centre the OGSE pupil image onto the centre of M1.	T5 relative to PLM cube

Table 23: Monitoring constraints for the target projector design

With the alignment surfaces in Table 23, and the pupil scanning autocollimator (Figure 83), it theoretically would be possible to constrain all of the actuated degrees of freedom in the design. However, the design is complex, and it likely won't be possible to verify end-to-end cryogenic performance in Oxford. Therefore, the first time this system would be verified in cryogenic conditions would be during payload EM.

6.1.4 Target projector trade-off

Without a prohibitively complex alignment tracking system, it is impossible to constrain all ~11 degrees of freedom associated with the PDR OGSE design. The immediate question that then follows is whether it is possible to remove some of the degrees of freedom in the design. Three options were considered:

(1) The target projector PDR baseline (approximately eleven degrees of freedom)
(2) A redesigned target projector with the powered mirror degrees of freedom removed (approximately eight degrees of freedom)
(3) A switch from the target projector to the periscope design (approximately four degrees of freedom)

6.1.4.1 Option 1- PDR target projector baseline (complex laser system)

To align the illumination module to the target projector, the target projector to the payload, and to maintain a compliant PSF, eleven degrees of freedom were assumed (section 6.1.1). A complex laser alignment tracking system was proposed to monitor and constrain all these degrees of freedom (section 6.1.3). However, not only is this system complex to design, but it will also be hard to test and full cryogenic verification will likely not be possible before payload EM.

This option does, however, require the smallest number of changes to the design presented at PDR.

6.1.4.2 Option 2 – re-design the target projector structure (Significant mass increase)

By re-designing the target projector, it may be possible to ensure the powered mirrors remain confocal during cooldown. This would remove three degrees of freedom. The complex strain distribution seen in the target projector is largely a consequence of the significant light-weighting of the structure. This lightweighting was to help radiative cooldown times. One possibility to reduce the complexity of the

alignment tracking system would be to redesign the mechanical structure of the target projector such that the powered mirrors are guaranteed to remain confocal during cooldown.

The updated mechanical design would consist of a vertical monolithic optical bench. Likely made of aluminium with aluminium optics. The vertical optical bench would have a significant (TBD) mass increase relative to the current design which has thermal implications. It is likely we will require conductive cooling to the CTR shroud wall to cool down in a reasonable time frame (<2 weeks). With this option, we still need to track and control the motion of the target projector relative to the illumination module and then the target projector relative to the PLM.

6.1.4.3 Option 3 – bring the powered optics into the illumination module (enlarged CTR baffle tube)

The design with the fewest numbers of degrees of freedom would be if all the powered mirrors were incorporated on a single optical bench in the illumination module. The illumination module would output a ¼ aperture beam (28cm, major direction). This means the target projector can be replaced by two 30cm flat mirrors.

With this approach, the angle and centration of the illumination module relative to the periscope does not cause optical aberrations. Therefore, provided the periscope mirrors are sufficiently oversized, it is sufficient to only monitor the motion of the illumination module relative to the payload. This removes four degrees of freedom, previously for target projector position monitoring.

Moreover, as with option 2, by moving the powered optics to the illumination module, the optics can be mounted on a thick (e.g. 5 cm) optical bench. This bench will suffer from fewer thermoelastic distortions compared to the heavily lightweighted target projector. By having aluminium optics on an aluminium optical bench, it should remain con-focal during cooldown. In this way, it should be possible to remove the actuation between the powered mirrors – a further reduction of three degrees of freedom.

STOP analysis is still required to assess if an ideal isometric optical bench design is realizable in practice. If it turns out there is still a need for cryogenic focusing of the powered mirrors, this new optical design allows us to use the payload to focus the OGSE. The current baseline is to cool the OGSE at the same time as the payload. This means the OGSE experiences thermoelastic deformations at the same time as the payload making it extremely challenging to align both systems (as discussed in 6.1.3). If the powered optics are in a separate chamber, an alternative cooldown plan could be used:

1. Before cooldown, the illumination module will be aligned and verified by imaging the output using an imaging parabolic mirror
2. Cool the payload with the illumination module remaining ambient.
3. Focus the payload using the collimated OGSE beam.
4. Cool the illumination module.
5. Use the image on the payload detectors to focus the illumination module optics.

By decoupling the cooldowns, the OGSE can be used to focus the payload, then the payload can be used to focus the OGSE. This does, however, have programmatic consequences for the chamber time so parallel cooldown remains the baseline, though, this approach may prove necessary if OGSE focusing actuation is required. Using the payload to focus the OGSE is only possible if the OGSE powered mirrors are cooled after the payload.

This design is also significantly more testable. With this design, all the powered optics are now contained in the OGSE chamber, making derisking of the complex optics in possible in Oxford.

6.1.4.4 Target projector trade-off conclusions

	PDR baseline	Re-designed target projector	Bringing powered optics into the illumination module
Alignment degrees of freedom/risk	11 degrees of freedom	8 degrees of freedom	4 degrees of freedom
Impact on other teams	-	Conductive cooling of target projector	Enlarged baffle tube
Testability	No cryogenic end-to-end test	No cryogenic end-to-end test	All complex optics contained in one chamber
Design change from PDR	-	Updates to the mechanical and thermal design of the target projector	Significant updates to the illumination module including the chamber support structure, and optics.
Decoupled cooling of powered mirrors	No	No	yes

Table 24: target projector trade-off summary table

The benefits of the three OGSE optical designs are summarised in Table 24. It was decided that due to the vast complicity in monitoring all the degrees of freedom of the target projector, the periscope concept would be adopted. In this way, only the illumination module to payload alignment needs to be tracked – greatly simplifying the design. This design also improved the testability of the system by bringing all high-risk components into the illumination module, where they can be tested in Oxford.

The drawback of this outcome is it required a major re-design of the illumination module and target projector. The updated thermal design was discussed in section 5.2. The updated optical design will be discussed here.

6.2 ILLUMINATION MODULE OPTICAL DESIGN

6.2.1 Illumination module optical requirements

The illumination module's optical design is driven by the optical performance requirements. Before the sphere, we have 'light bucket' optics where imaging quality is largely unimportant[58] and the driving requirement is throughput. The design of the source optics to meet the throughput requirements was discussed in Chapter 3. Here, the post-sphere optics will be discussed. Optics after the sphere must meet the following performance requirements (summarized below, with formal wording given in Appendix C):

6.2.1.1 WFE (R-OGSE-8630)

To enable testing of the payload spectral resolution and focusing of the telescope, the illumination module output must have 90% angular size less than 0.95 × 1.4 arcseconds in the major and minor directions of the pupil.

6.2.1.2 Field of view (R-OGSE-ILL-0150)

For near-field stray light verification, the OGSE must be able to scan the point source over a 280'' FOV[59].

To test the payload optical quality over the full instrument FOV, the WFE requirement must be met over the 120'' FOV (~the instrument channels FOV when the beam expander is present).

[58] Optical aberrations are only important if they cause throughput losses due to vignetting

[59] Angular size at the output of the illumination module

6.2.1.3 Flat field (R-OGSE-ILL-0100)

To enable flat fielding of the payload detectors, the OGSE must produce an extended source that is uniform to within 0.5%. Meeting this requirement is a driving requirement for the integrating sphere, however, the optics after the sphere can also impact the flat field[60].

6.2.1.4 Pupil imaging

The OGSE defines the pupil during ground testing using an aperture plate. The OGSE must ensure that an image of the pupil lands at the payload primary mirror, where the pupil is defined in flight. This avoids vignetting within the payload's common optics.

6.2.1.5 Pointing stability (R-OGSE-CAL-0018)

To keep the OGSE spot within the spectrometer slit during calibration measurements, the OGSE pointing must be stable to 4 arcseconds over 10 hr timescales.

6.2.2 Illumination module optical design

The optical design to meet these requirements is shown in Figure 84. The integrating sphere has two outputs. A 1.2 cm open port and a $50\,\mu m$ pinhole. The open port provides uniform (<0.5%) illumination over the payload field of view. The point source provides a star-like point source. The two outputs are viewed via a flip mirror (Figure 19). The light is then collimated and reflected by a fine steering fold mirror. An aperture plate is then used to define the pupil of the system. After the

[60] It is hoped to meet the 0.5% requirement by design. However, knowledge of the output uniformity should be sufficient for flatfielding the payload.

aperture plate, a pair of parabolic mirrors are used to expand the beam by (7.7x) to give the required ¼ aperture beam.

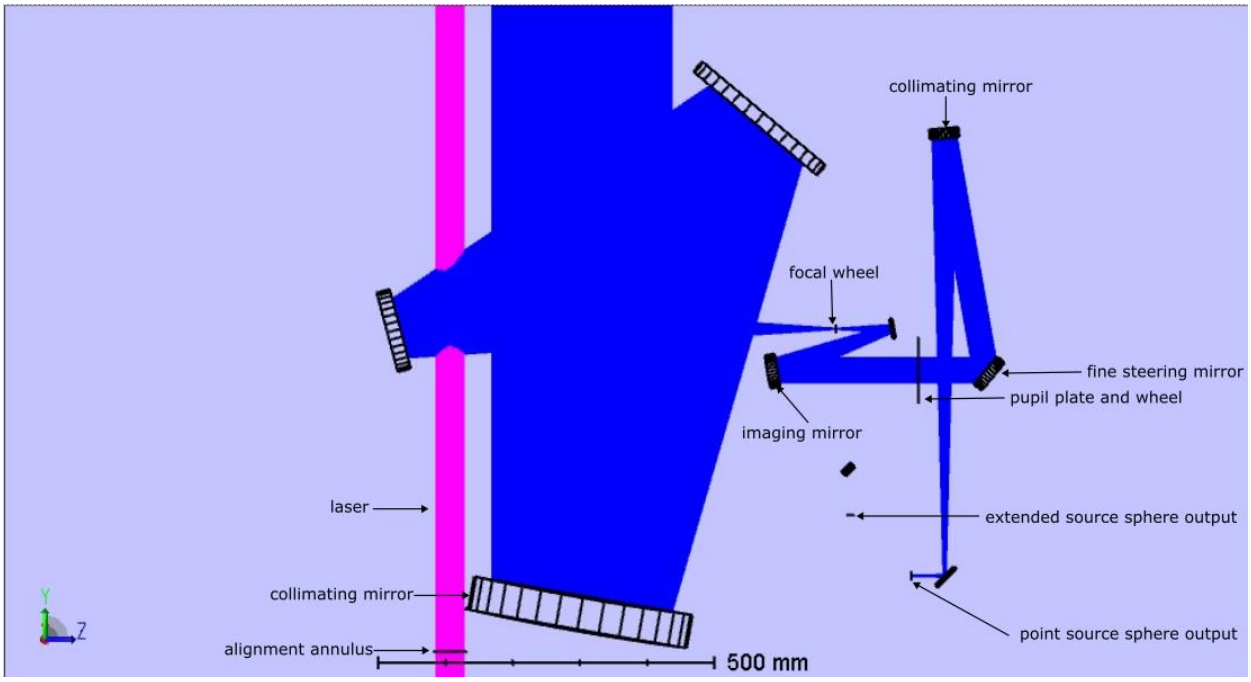

Figure 84: Illumination module cryogenic bench optical design - shown here in the point source configuration.

Multiple optical configurations were considered before the design Figure 84 was reached. To see how this design was reached, we consider how simpler designs would be inconsistent with the requirements described in 6.2.1.

The most basic function of the cryogenic optical bench is to collimate light from the sphere output. The output of the illumination module must be 27.5 cm by 18.3 cm (1/4 of the payload primary mirror). In principle, this function could be achieved by a single parabolic mirror. However, with such a design the pupil of the system would be at the parabolic mirror. This is ~6 m away from the payload primary mirror giving the incorrect pupil mapping.

The next simplest architecture would be to use an ellipsoidal mirror to view the sphere output. A parabolic mirror could then be used to collimate the image generated by the ellipsoidal mirror. With these two powered mirrors, a pupil-matching solution may exist, however, there is no way of inserting

a fine steering mirror without violating the con-focal condition of the two powered mirrors. This would lead to unacceptable aberrations when the source is steered.

To introduce a fine steering mirror, a third-powered mirror was used. This enables the fine steering mirror to be placed in the collimated beam. This motivates the three-powered mirror solution shown in Figure 84.

As well as the optical performance, a key design consideration was the size of the optical bench. This bench needs to be cooled to ~70 K and enclosed in a vacuum chamber. Therefore the size of the bench is not an insignificant complexity driver. The size of the bench is largely driven by the point at which the beams separate on P3. Shallow-angle powered mirrors were selected for their superior off-axis performance. However, a 20-degree off-axis collimating mirror has a ~750 mm separation distance. This sets the ~1 m scale of the optical bench. Accommodating the collimator next to the sphere sets a bench similar 1 m scale in the opposite direction.

The F/# of P1 is set by ensuring the correct magnification between the pinhole and the focal planes. This ensures a sufficiently small image of the pinhole at the focal planes (0.96'' at the illumination module output, approximately equal to the diffraction limit at 550 nm). The F/# of P1 is, therefore, constrained, however, the focal length of P1 is still a free parameter. By maximising the focal length of the collimating mirror (P1), the expansion of the beam between P2 and P3 can be made slower improving the off-axis performance. Therefore the focal length of P1 was maximised (695 mm) within the constraints of the bench size. After the collimating mirror, the fine steering mirror was placed. By placing this mirror before the pupil plate, the field angle can be adjusted without affecting centration, simplifying alignment.

The output of the illumination module must generate a pupil image at the payload primary mirror (where the pupil is defined in flight). The pupil is defined by an aperture plate placed just before P2. By tuning the focal lengths of P2+P3 the image of this pupil was made to match the M1 location. Achieving a pupil image ~6 m from the collimating mirror required a long (>~1.5 m) focal length for P2

+ P3. To make the focal lengths sufficiently large, >two folds were required between P2 and P3. The third fold was added to give an accessible intermediate focus. By tuning the focal lengths P2/P3 the correct (7.7 x) magnification was achieved to give a 27.5 cm by 18.3 cm output.

At the time of designing, the exact pupil distance was not known due to uncertainty in the vacuum equipment and periscope design. A key objective was therefore to have a design that could accommodate the uncertainty in the payload distance without replacing the powered mirrors. The pupil image is shifted by 0.59 m per cm motion of the pupil plate. The current plate position can be ±2 cm of the current location without vignetting the beam comfortably covering all possible optical path lengths.

The above considerations motivate the current illumination module design. The pupil matching and fine steering requirements determined the need for a three-powered mirror solution. In addition, the pinhole plate scale, output beam size and pupil matching criteria were used to tune the corresponding F-numbers and focal lengths. The imaging performance, FOV and uniformity are still to be shown. This analysis was performed in Zemax and will be discussed here.

6.2.3 Optical performance analysis

6.2.3.1 Imaging performance

This design only uses off-axis parabolic mirrors. This is because Ariel is a narrow-field (~30'') instrument optimised for single-star viewing. This choice of mirrors implies that the on-axis point source is free from design aberrations (though alignment and manufacturing aberrations will still be present).

The fine steering mirror, however, means that the light is not always on-axis when passing through the second and third-powered mirrors (P2 & P3). It is important to assess over what steering range the radius of encircled energy requirement can be met. This sets the maximum range of the fine steering mirror.

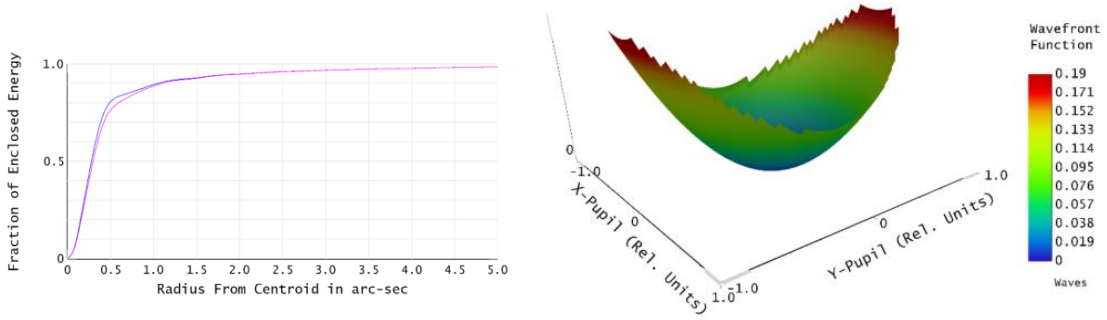

Figure 85: Imaging performance of the illumination module with a 1-degree field angle introduced by the fine steering mirror. Left compares the true encircled energy (pink) with the diffraction limit (blue). Right shows the corresponding WFE. Simulations were evaluated with 550 nm light.

With a 1-degree field angle at P2, excellent image quality is seen (Figure 85). Figure 85 shows that the beam is still almost completely diffraction-limited with 0.05 waves of WFE at 550 nm (RMS). However, by two degrees geometric distortions approximately match the diffraction limit (1'' radius). The fine steering mirror is therefore designed to introduce a ±1 degree field range (±460 arcsec at the illumination module output). Over this range, the optical quality requirements are comfortably met.

The maximum 1-degree range also starts to have a significant impact on the beam footprint size on P3 Figure 86. This is of particular importance due to the close accommodation between the test and laser optical paths (Figure 84).

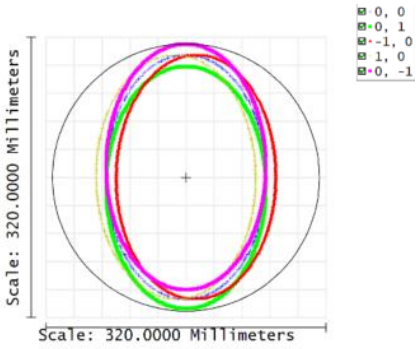

Figure 86: Footprint diagram showing off-axis beam positions on the large collimating mirror (P3). Angles shown are in units of degrees.

6.2.3.2 Baffling – driving the upper limit of the FOV

Also of importance when sizing the FOV of the system is possible vignetting on the baffle tube. Because the illumination module output is ~6m from the pupil of the system (M1), this means small angular misalignments in the payload line of sight correspond to large decenters in the illumination module position (0.1-degree offset corresponds to 1 cm offset in the illumination module output). Due to constraints imposed by the RAL chamber port and the RAL liquid nitrogen shroud, the baffle tube is only slightly (~3 cm) oversized with respect to the test beam (Figure 87). This places tight constraints on the accuracy of the payload line of sight position.

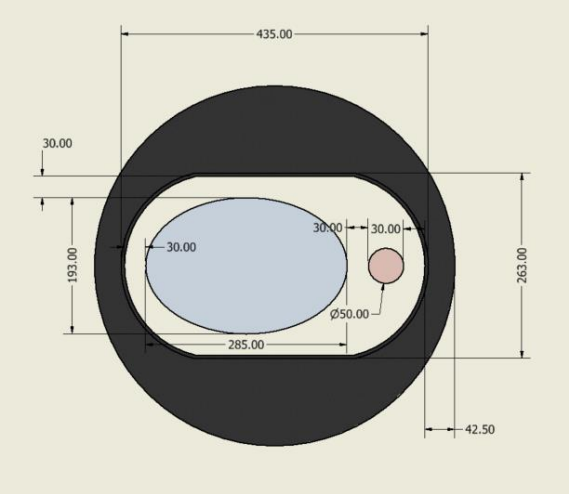

Figure 87: Illumination module output cross-section (view from periscope looking towards the illumination module). The blue shows the cross-section of the extended source. The laser output cross-section is shown in red.

Piping in the RAL liquid nitrogen shroud implies that the baffle tube can be no taller than 300 mm. This immediately rules out a configuration with the test beam and alignment beam vertically above each other. This drives the side-by-side configuration with a letterbox baffle tube shape.

The RAL chamber nipple has a 488 mm inner diameter. Allowing 1.5 cm clearance between the baffle and the chamber nipple, and 1 cm for MLI, gives a 438 mm max width for the baffle. Accounting for the beam cross sections and allowing 1cm clearance between the beams and the inner edge of the baffle, implies a maximum adjustability in the beam position of 2 cm. If we further subdivide this 2 cm

between decenter and tip-tilt, we can define the maximum adjustability of the illumination module. Assuming a 5 mm maximum centration compensation, this allows 1.5 cm for angular compensation. *This implies a maximum unvignetted angular adjustability of the illumination module of 520 arcseconds*.

This stringent angular tolerance must account for the uncertainty in the CTR trolley position when it is wheeled in as well as cooldown compensation. It is expected this should be achievable with the updated CTR wheel design that has a 1 mm slop relative to the rails.

6.2.3.2.1 Generating a light-tight seal around the gate valve

In the previous section, the maximum adjustability in the illumination module was derived based on constraints imposed by the RAL vacuum chamber. A somewhat generous 1.5 cm clearance was assumed between the baffle tube and the chamber nipple. A e.g. 5 mm reduction in this could give a significant (~200'') increase in the illumination module adjustability. However, there is an additional consideration constraining the size of the baffle tube – stray light.

As analyzed in section 5.3, thermal stray light from ambient surfaces is expected to be a significant effect at 8 microns. Because of this is likely critical to ensure no direct view factors between the ambient gate valve and the cryogenic optics. This is achieved by adding lips to the end of the baffle tube. A second baffle tube was added that mirrors the illumination tube on the other side of the gate valve (Figure 88). By making the lips significantly large relative to the baffle tube, a seal around the gate valve was generated that ensures no direct view factors between optics and the gate valve. This is illustrated by the diagonal lines in Figure 88.

If the baffle tube cross section were made larger, the lips of the baffle tube would have to become smaller. This would make generating a light-tight seal require impractically long baffling. There is therefore a tradeoff between stray light control, and FOV when sizing the baffle. The solution to this is shown in Figure 87.

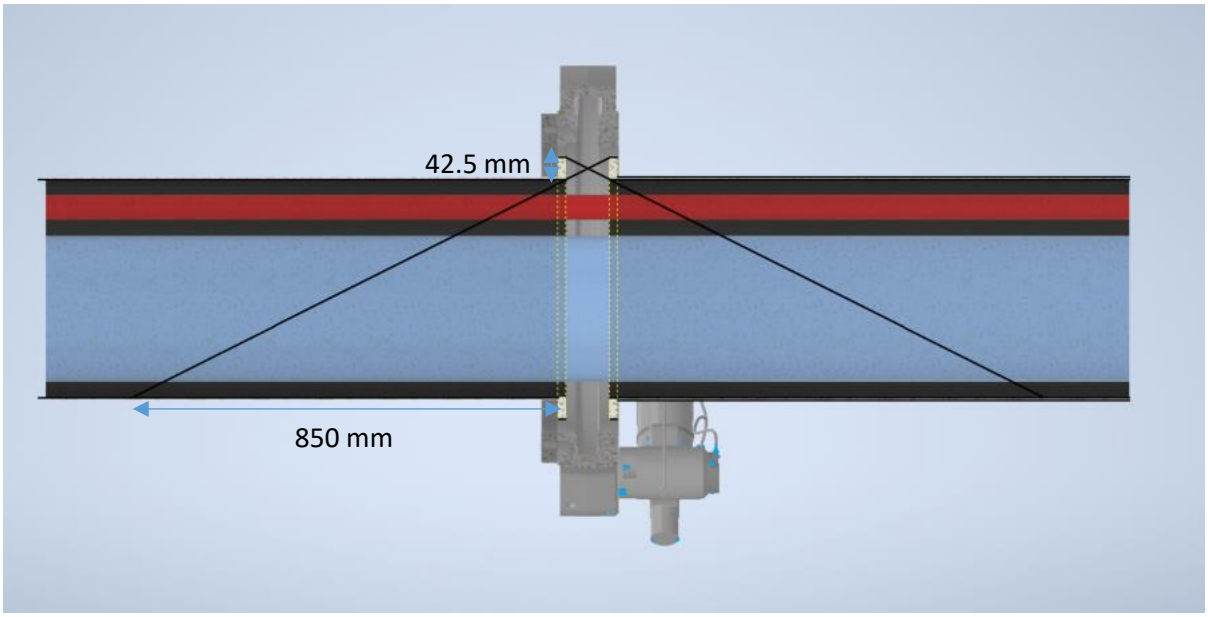

Figure 88: generating a light-tight seal around the gate valve.

6.2.3.3 Flat field

The OGSE will be used to verify the payload flat field. One method planned for doing this requires the extended source (see section 2.2.11.2). With this method, uncertainty in the uniformity of the OGSE output translates directly to uncertainty in the payload flat field. The dominant source of non-uniformity is expected to be the non-ideal behaviour of the integrating sphere. However, field-dependent vignetting or aberrations can cause mirrors to also contribute to the flat field non-uniformity.

To assess the impact of the post-sphere optics, the extended source was modelled as a Lambertian, spatially uniform object of 1.2 cm extent. The output is shown in Figure 89. In one axis, a linear gradient can be seen. The origin of this gradient is likely field distortion from the parabolic mirrors. However, over the 22 arcsecond FGS FOV (88 arcseconds with the beam expander), the variation in flux is 0.12%. Therefore, the non-uniformity contribution of the illumination module optics will not prevent flat fielding at the level of 0.5%.

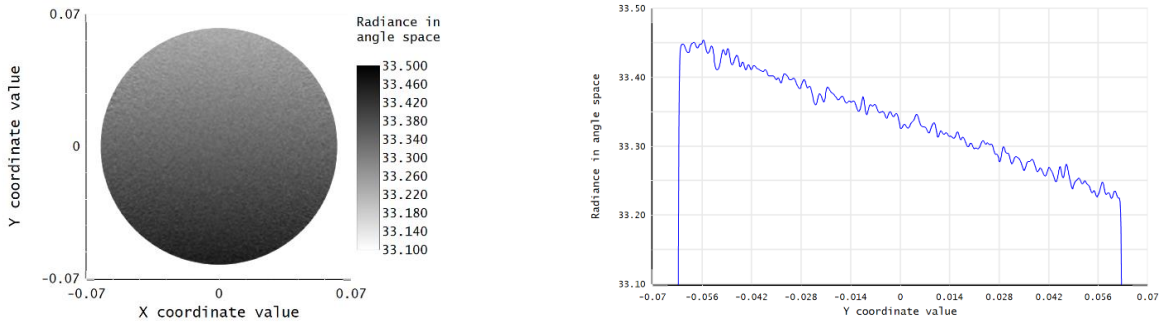

Figure 89: Extended source uniformity at the illumination module output. (angles are in units of degrees, radiance shown is in arbitrary units)

6.2.3.4 Optical performance conclusions

The illumination module design has been shown to be consistent with all of the optical performance requirements (6.2.1). It has been shown that the optical design has <0.05 waves of error (RMS at 550 nm)[61] over a ±460 FOV. This enables scanning and closed-loop pointing over this range. The maximum payload line of sight offset is only marginally larger than this fine steering range (520 arcseconds) and is limited by vignetting on the output baffle tube (and 488 mm chamber nipple). The full 520 arcseconds range is achieved by course adjustment stages outside the chamber. The design has also been shown to be consistent with flat fielding of the payload.

6.2.4 Mechanism design

The optical design has several mechanisms that facilitate the payload calibration observing modes. An overview of the required mechanisms and their designs is provided here. This includes:

1. A flip mirror to switch between the two sphere outputs and a beam dump
2. A fine steering mirror for closed loop pointing control

[61] This only includes the design aberrations. It does not include the

3. Sphere input shutters
4. A Pupil and focal wheel for applying masks to the OGSE beam during alignment

6.2.4.1 Flag flip mirror

During calibration, three key modes are: (1)the point source (2) the extended source and (3) dark. These are used for wavelength calibration, flat fielding, and dark current testing respectively. These modes are selected using the flip mirror shown in Figure 90. This was developed by the author based on a piezo-based flag concept proposed by Rory Evans. The flag contains two flat mirrors. The first mirror redirects the beam from the extended source to the collimator. The second mirror re-directs the payload line of sight to a cryogenic beam dump on the shroud wall. The third position moves the flag out of the way to allow a beam from the point source to reach the collimator.

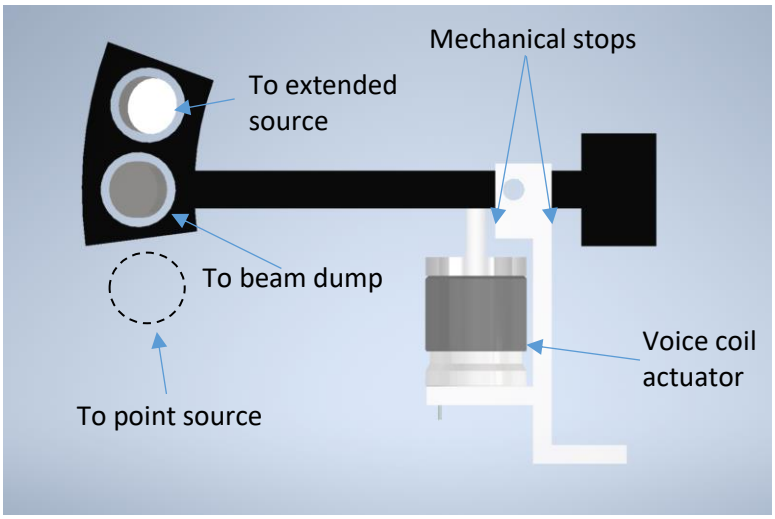

Figure 90: Flip mirror mechanism at the sphere output.

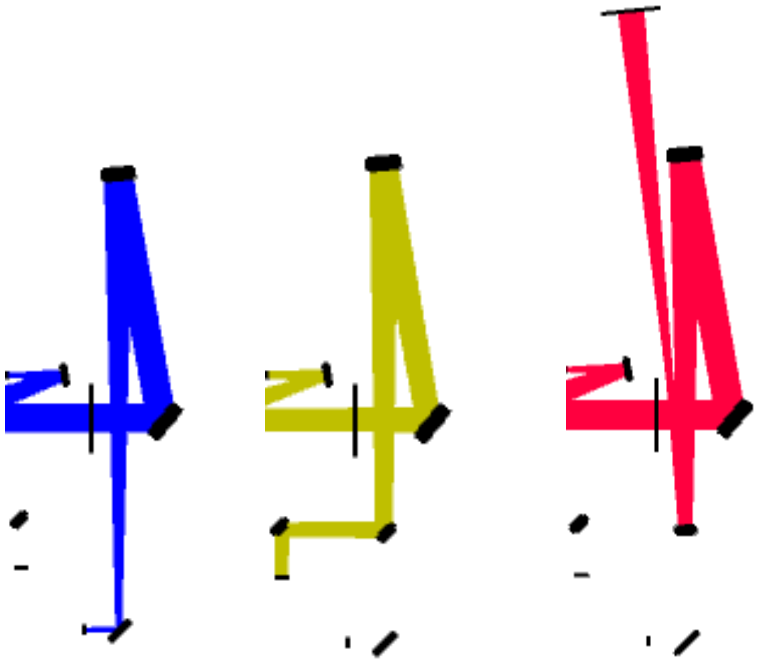

Figure 91: Point source, extended source and afocal beam dump optical configurations

To enable persistence measurements, it must be possible to shutter the source on a time scale short compared to typical focal plane integration times (<1 s). For this reason, the design was changed to a voice coil actuated system. The flag concept provides the mechanical advantage required to translate the small (+3.5 mm-2.5 mm) motion of the actuator to a large ~25 mm motion of the mirrors (driven by the beam footprint size).

To meet the diffraction-limited imaging performance requirements, there are stringent alignment requirements on the point source optical path. For this reason, the mechanism does not interact with the test beam in the point source configuration ensuring no misalignment is introduced. Alignment requirements are more relaxed for the extended source, however, reproducible alignment is still required to ensure uniformity is not impacted. For this reason, mechanical stops ensure reproducible mirror positioning. Alignment is least critical for the beam dump so the beam dump path is placed in the centre position where no mechanical stops are possible.

6.2.4.2 Fine steering mirror

To enable alignment of the OGSE output to the payload, a fine steering mirror is located on the cryogenic optical bench (Figure 84). The fine steering mirror works in conjunction with course mechanical adjustment outside the chamber to provide arcsecond alignment over a large adjustment range (0.5 degrees)[62]. This mirror also provides closed-loop pointing control (discussed further in section 6.3.1.1). The baseline tip-tilt stage is based on a commercially available stage CTTPS from JPE. This will, however, have to be customised by the supplier to accommodate the ~60 mm beam footprint. The design is based on two piezo linear actuators with flexures. Each actuator includes a relative optical encoder to aid in the pointing control calibration.

6.2.4.3 Shutters

To enable cryogenic optical shuttering of the sources, three blades are used at the entrance of the sphere (Figure 19). Their primary function is to block source and thermal radiation when a source is not in use. The design shown in Figure 92 was developed based on a concept designed by Rory Evans for PDR. The design at PDR had open and shut functionally. There was also no encoder making knowing the blade position challenging. Because of this, the shutter was re-designed around a CLD2 actuator from JPE. This actuator provides 200 nm position information via a resistive encoder (orders of magnitude better feedback than is required for this application). The enhanced travel range (52 mm) also allowed functionalities previously designed to be part of other mechanisms to be incorporated

[62] This wide range is to accommodate the angular uncertainty in the optical bench support tower. The uncertainty in the CTR trolley boresite must still be less than <<520 arcseconds (limited by the shroud, see 6.2.3.2).

into a single linear stage. The updated design features, an open aperture, a 1.5 mm hole, a black stop, and for the VIS source, a short pass filter (Figure 92).

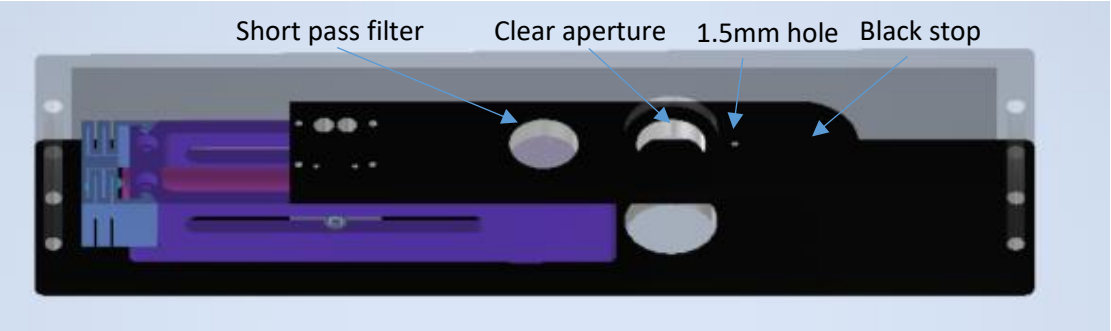

Figure 92: VIS source shutter bade.

As discussed in section 3.4.3, when the extended sphere output is used focal plane signals are ~100 times larger. If not compensated for, this would saturate the payload detectors. To compensate for this, a 1.5 mm hole was added to the shutter blade. By only exposing the 1.5 mm hole the sources are modulated by ~100 times bringing the focal plane fluxes back to usable levels. This 1.5 mm hole will be used whenever the extended source mode is selected.

The final mode added to the shutter is the FGS tracking mode. In this mode, the VIS source illuminates FGS to enable alignment monitoring whilst calibration measurements are made on other detectors. This is enabled by a short pass filter on the VIS source shutter blade (KG5 window from Shott).

The FGS tracking mode is most critical for the wavelength and co-alignment measurements as these are most sensitive to alignment changes. R-CAL-110 requires the OGSE to verify the co-alignment of instrument channels to 1/10th pix. In VISPhot, 1/10th pix corresponds to 40 mas at M1. A method that involved illuminating one channel, followed by another channel would require the OGSE test beam to remain stable to this level. This would imply positional stability on the order of a few 100 s of nanometers across the different OGSE modules – likely impossible. *Therefore, a method that provides a spot on each channel simultaneously is likely critical to achieving this level of co-alignment.*

For both the wavelength calibration and the co-alignment, the monochromator is used to produce a spot on the spectrometers. The spot position is measured relative to the spot on the FGS photometers.

By adding a shot pass filter to the shutter assembly, the VIS source and monochromator can be operated simultaneously. The simultaneous illumination enables 1/10th pix coalignment measurements. Further details on the proposed method are discussed in (2.2.13 and 2.2.14).

This linear blade, therefore, enables source shuttering, extended source attenuation, and an FGS tracking mode.

6.2.4.4 Focal/ pupil wheel

The final mechanisms on the cryogenic bench are the focal and pupil wheels. These are additional features that are not expected to be critical to the OGSE's core functionalities. These are treated as a 'goal' in the OGSE development. They may aid in the initial alignment, as well as provide the capability of changing the OGSE PSF which is beneficial for certain calibration measurements.

Being able to modify the PSF could be useful when verifying the FGS-centroiding, co-alignment and wavelength calibration. All these tests are centroiding measurements and are thus sensitive to the PSF. Given the ground test PSF will be different from the flight PSF, it may be beneficial to test the centroiding performance for a range of spot shapes.

In addition to changing the PSF, masking the pupil enables the OGSE beam to be stopped down. This provides a backup method of reducing the WFE in case above expected aberrations are seen during payload testing. This is at the cost of the diffraction-limited spot size in AIRS. However, this is a possible failure mode mitigation strategy.

The method and illumination conditions required for focusing the telescope are still to be determined. In flight, the payload team are considering the use of a dense star field. If required, the focal wheel could also be used to create a dense star field for ground testing (see Figure 93). To create a dense star field, a grid of 20 µm pinholes can be added at the intermediate focus of the illumination module (Figure 84). By back-illuminating this grid of pinholes with the extended source, a dense star field can be produced.

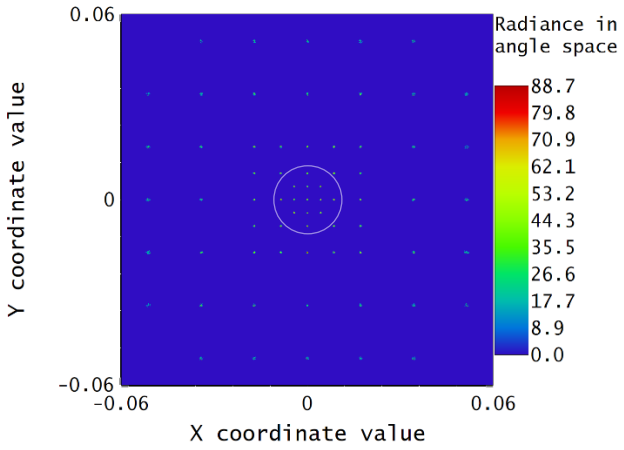

Figure 93: Dense star field observing mode. The FGS 21'' on-sky FOV is shown for scale by the central circle. Axis are shown in units of degrees.

The large (380'') FOV of the dense star field enables course (380'') steps when rastering to find the payload line of sight. For comparison, ~200'' FOV drifts are expected in the payload line of sight during cooldown [59]. In addition, the density gradient in the star field allows (see Figure 93) rapid centring on the OGSE optical axis. Finally, the dense star grouping in the centre provides 13 stars within the FGS 21'' FOV. By aligning the payload to a grid stars vs a single point source, it allows off-axis aberrations to be rapidly identified and optimized.

The planned mechanism to achieve the pupil and filter wheel is based on a CSR1-RRS cryogenic rotation stage with a resistive encoder.

6.3 ALIGNMENT MONITORING SYSTEM

In section 6.1, the challenges in maintaining alignment during cooldown were discussed. A revised optical architecture was developed to simplify the alignment monitoring system, however, alignment monitoring is still required to ensure the illumination module remains co-aligned with the payload. In this section, the system to enable the alignment monitoring will be presented. An autocollimator design will be presented that achieves angular and centration monitoring of the payload relative to the illumination module. Experimental verification of this system will also be presented.

6.3.1 The three autocollimator use cases

To motivate the autocollimator design, we will discuss the different use cases of the autocollimator, and how these drive the autocollimator design. Each places different requirements on the FOV/ resolution of the system. The three alignment phases are:

1. The initial, course, module-level alignment.
2. Alignment monitoring during cooldown.
3. Alignment maintenance during observations

The initial alignment and cooldown monitoring is to ensure the OGSE can meet its most fundamental requirement – getting a focused spot on the Ariel instrument module focal planes. Centration monitoring is also required to ensure the beam does not vignette in the payload common optics. Vignetting would cause issues for measurements such as the absolute radiometric calibration.

To ensure the OGSE output lands on the FGS detector, the alignment measurement resolution of the autocollimator must be better than ~20'' (the FGS FOV; R-PRD-8405) FOV). To prevent vignetting of the test beam within the common optics, the beam expander output beam needs to be correctly centred to within 0.1 mm (R-PRD-0610). This corresponds to a 1.4 mm centration error at the entrance of the telescope. Therefore, the autocollimator must be capable of measuring angle and centration to this level.

During the initial course alignment, misalignment between modules (Figure 16) could be considerable. The facility tolerancing is, however, still to be measured. A wide (TBD) FOV is expected to be required to measure the initial co-alignment (at least 10^2 arcseconds).

Once alignment has been established it must be monitored during cooldown. The challenges associated with maintaining alignment during cooldown were discussed at length in section 6.1, for the design of the autocollimator, the resolution and FOV requirements are similar to the initial course alignment phase.

After cooldown, a different alignment phase is entered – alignment maintenance. The alignment maintenance resolution requirements are significantly more stringent than the initial and cooldown phases and drive the resolution of the autocollimator. The motivation and required resolution will be discussed here.

6.3.1.1 Alignment maintenance – driving the autocollimator resolution

In flight, Ariel's pointing information is provided by the FGS. The information from the FGS is sent to the spacecraft which provides closed-loop pointing control. In this way, 1 arcsecond pointing stability will be achieved (SR-PER-215, [133]). During ground testing the spacecraft is not present to provide closed-loop pointing control. Therefore, an assessment must be made as to whether or not open-loop pointing control would be sufficient during ground testing.

The 1-arcsecond pointing stability to be achieved by the spacecraft in flight is derived from the spectrometer slit size (4.7'' for AIRS CH0; R-PRD-8390). This slit size must account for the PSF size as well as the misalignment of the incoming light to the slit. If the star was misaligned by more than ~1 arcsecond the outer lobes of the PSF would vignette on the slit. When coupled with a pointing drift this can result in a photometric error that is important at the level of tens of ppm potentially impacting the detection of atmospheric signals [134]. In a more extreme case where pointing drifts are a few arcseconds would cause the star to completely vignette.

During ground testing, we also require arcsecond pointing stability to prevent vignetting of the OGSE source on the spectrometer slits. Fortunately, the OGSE beam expander magnification leads to a reduction in the pointing stability tolerance by four times. This does, however, still mean that the OGSE pointing relative to the payload needs to be stable to 4 arcseconds during a calibration measurement. To enable characterization of the payload's noise on the timescales of a transit, the OGSE is designed to make measurements on up to 10-hour timescales (R-PRD-0470). This means that the OGSE needs to maintain arcsecond pointing stability on thermal timescales.

A tolerance analysis was performed to assess if the OGSE would be able to achieve arcsecond stability. This analysis was performed before the periscope tradeoff so the analysis was based on the original target projector module design. Nominally the 4 arcsecond end-to-end stability was sub-allocated in the following way:

- Illumination module drift relative to the target projector - 1''
- Target projector internal thermoelastic drift – 0.5''
- CTR interface with target projector - 1''
- CTR interface with payload – 1''
- Payload internal thermoelastic drift - 0.5''

The target projector had a 12.5 times magnification. Therefore, angular drifts between the illumination module and the target projector get contracted by 12.5x. We are therefore significantly more sensitive to tilts of the target projector compared to illumination module tilts. Efforts were therefore focused on defining the required stability at the feet of the target projector.

The feet of the target projector were separated by 0.59 m. Therefore, to achieve 1'' stability, the feet would need to be stable to $3\ \mu m$ over a ~10 hr measurement. Specifically, this refers to relative motion between the feet. This is expected to be an un-buildable stability tolerance of the interface. This tolerance would need to account for thermoelastic drifts in the target projector/trolley as well as settling effects after cooldown. The likely impossibility of this requirement was confirmed by a CTR thermoelastic analysis of the interface.

Three solutions were considered to reduce the pointing drift issue:

1. Open loop pointing control
2. Closed loop pointing control using the FGS
3. Closed loop pointing control using the OGSE autocollimator

6.3.1.1.1 Open loop pointing control

Open loop pointing control would rely on manual re-alignment if the OGSE source drifts during a measurement. This option would likely limit the maximum measurement time, though until the system is built and the optical stability is measured, we will not be able to reliably estimate the maximum measurement timescale. This is the simplest option but likely has a significant impact on the calibration of the Ariel payload due to uncontrolled pointing drifts.

6.3.1.2 Closing the loop using focal plane data

Closed loop pointing using the focal plane data would be the closest analogue to in-flight operation. Centroids of focal plane frames would be used to measure pointing drifts. The centroids would be transmitted to the OGSE and we would adjust the fine steering mirror (Figure 84) to compensate. The main drawback of this method is it will not function during all observations. When the extended source is used, centroiding is impossible meaning the system may drift. Moreover, some calibrations also only illuminate Airs and not FGS. When this is the case, Airs must be used for centroiding. In principle it should be possible to centroid on a spectrum e.g. by cross-correlation of the focal plane image, however, Airs is not designed for centroiding and this approach is still to be tested. This method does require an additional software interface between the OGSE and the payload.

6.3.1.3 Closing the loop the OGSE autocollimator

The final option involved closing the loop using the autocollimator. The autocollimator would use a laser to retroreflect a beam off a target in the illumination module and a cube mounted on the payload to track the global motion between the systems. The drifts seen by the autocollimator would then be used to actuate the illumination module fine steering mirror. The key drawback of this approach is the autocollimator does not follow the same end-to-end optical path as the source. This means the autocollimator may see different drifts compared to the test beam.

Initially, it was planned that the autocollimator ray would be injected just after the illumination module collimating mirror and would be on-axis with respect to the test beam but decentered above it. The decentered autocollimator beam would then follow the same optical path as the test beam all the way to the beam expander where it would be picked off and retroreflected back to the illumination module. In this way, the autocollimator follows most of the same optical path as the test beam providing optimal alignment monitoring. However, restrictions imposed by the baffle size made this approach significantly more complex meaning a simplified version of this method was taken. The simplified approach uses a reflective target on the illumination module optical bench and the payload alignment cube. The autocollimator then tracks the global shifts between these systems but will not see any internal deformations within the illumination module, periscope or payload.

There are three advantages to the autocollimator approach. (1) it does not require a software interface to the payload, (2) monitoring is possible during all observations and (3) the autocollimator has a significantly larger FOV than FGS (750'' compared to 84'' for FGS with the beam expander). If aliment changes are not smoothly varying (e.g. due to bolt slips after cooldown), this could push the spot outside the FGS FOV. The autocollimator, would, therefore, be more robust to large (>84'') alignment changes.

6.3.1.4 Alignment monitoring trade-off summary

	Long-timescale measurement performance	Functionality in all measurement conditions	FOV	Testability/ additional interfaces	Complexity	Total
Open loop	0	0	1	2	2	7
Closed loop with focal plane detectors	2	0	1	0	0	7
Closed loop with OGSE autocollimator	1	2	2	1	1	12
Weight	3	2	1	1	2	

Table 25: Pointing control trade-off matrix

Based on this trade-off, the decision was taken to adopt closed-loop pointing using the OGSE autocollimator. This was largely motivated by the autocollimator being usable in all test configurations – including the extended source. Additionally, the payload team were concerned about the software interface to the spacecraft. This approach, is, however, at the cost of pointing accuracy as the autocollimator due to the different paths between the test and laser beams (Figure 21).

6.3.2 Autocollimator Design

The autocollimator, therefore, has three core functions: establishing initial alignment of the system, monitoring changes during cooldown (open loop) and fine closed-loop alignment maintenance during observations. These uses drive the following performance requirements for the autocollimator:

- To keep the OGSE spot within the spectrometer slit, it must be possible to track changes in alignment to <4 arcseconds.
- To prevent vignetting in the common optics, centration must be measured to better than 1.4 mm resolution.

- The FOV of the system is driven by the initial ambient alignment of the illumination module to the CTR trolley and should be maximised, though the required FOV is TBD but definitely must be large compared to 200''[63].
- The autocollimator will be accommodated outside the illumination module chamber. It therefore must meet these FOV and resolution requirements at a ~7 m working distance.

A selection of commercial alignment telescopes/ autocollimators were considered. However, no acceptable solutions were found. The combination of the need for a large (>>200'' FOV) and a long (>7 m) working distance means the size of the entrance optic becomes critical. The custom design allows improvements in the FOV of the system as well as simultaneous tracking of decentre and angle – something that is not possible with commercial solutions.

The solution for meeting these requirements is shown below in Figure 94. A laser is first attenuated by an ND filter to prevent saturation of the detectors. The laser is then spatially filtered to produce a diffraction-limited 5mm beam. The output of the spatial filter is then expanded by 10.6x. A z-fold is then used to align and relay the autocollimator output to the illumination module cryogenic bench. On the cryogenic bench, there is a reflective annulus (Figure 84) that retroreflects the outer portion of the laser beam. The central portion of the beam propagates onwards to the payload and retroreflects off the payload alignment cube.

[63] As an example, the uncertainty in the CTR trolley position on the rails is expected to be less than 200'' and 5 mm in translation. However, the angular deviation of the rails outside the chamber is expected to considerably larger than this, though this is still to be measured.

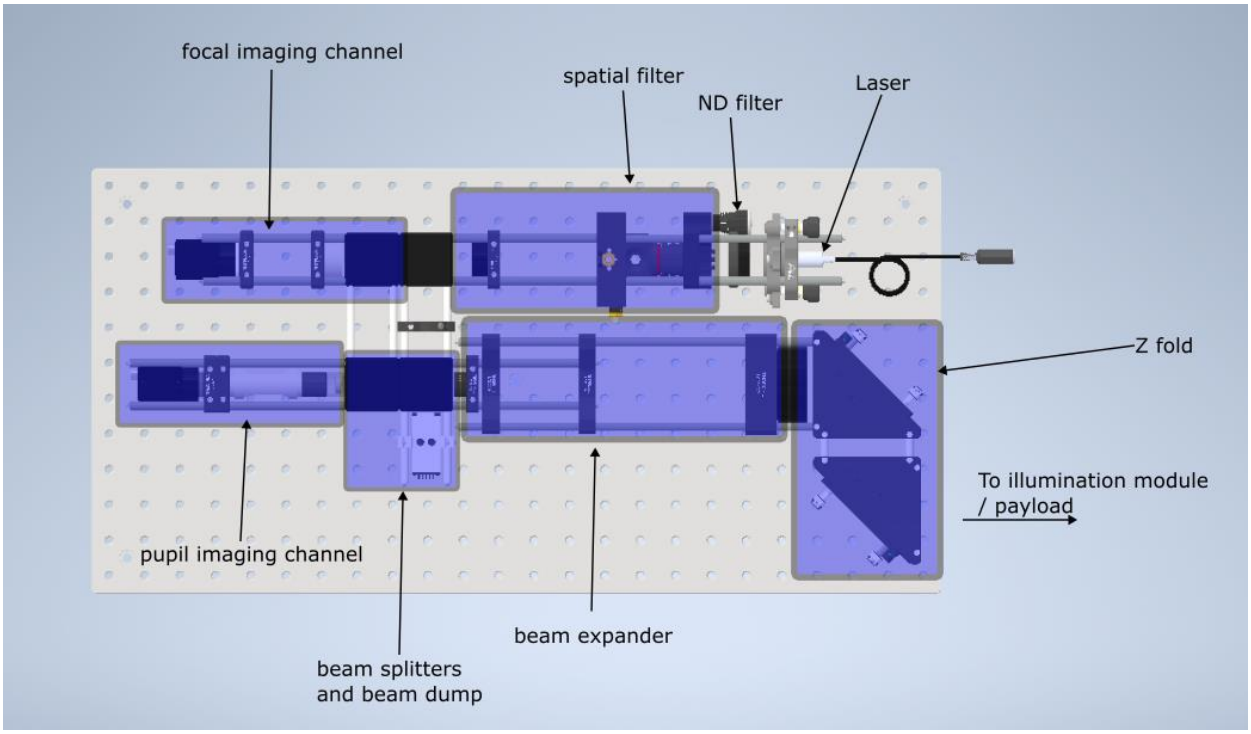

Figure 94: Autocollimator architecture

The return beam from both alignment targets passes backwards through the beam expander, contracting the beam by 10.6x. The beam then passes through a beam splitter cube directing the beam to two detector channels. A focal imaging channel for angular monitoring and a pupil imaging channel for centration monitoring.

6.3.2.1 Focal imaging channel

The focal imaging channel (Figure 94, Figure 95) is used to monitor angular variations of the illumination module relative to the payload. This channel, therefore, must meet the <4 arcsecond resolution and >200'' FOV requirements.

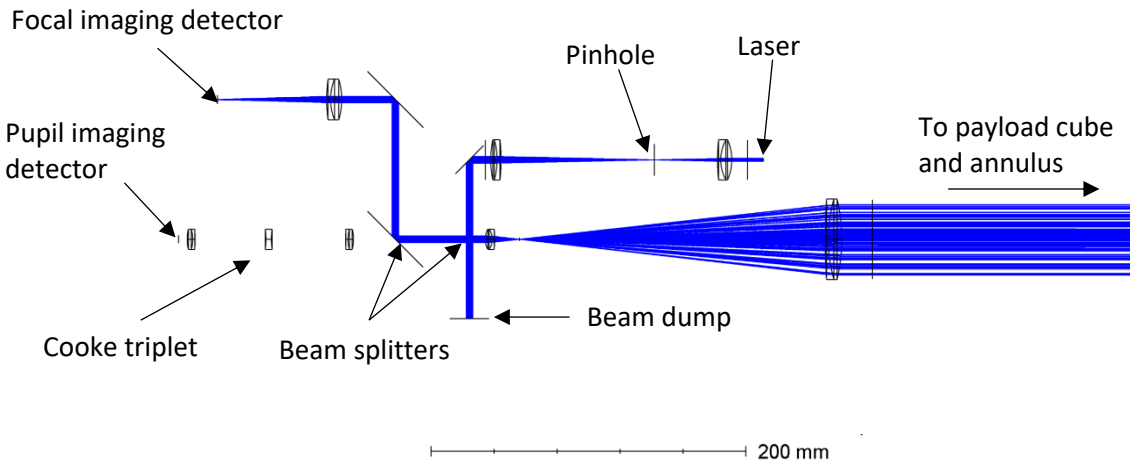

Figure 95: Autocollimator optical layout

The field of view of the autocollimator is limited by the diameter of the entrance optic. 2-inch diameter optics are the largest lenses compatible with commercially available optical cage systems. Larger optics than this would also be prohibited by the size of the RAL liquid nitrogen shroud cutout. Therefore, a 2 inch aperture was chosen.

To translate this aperture to the FOV of the system, we consider the decentre of the return beam. When the return beam is decentered by 2.5 cm, the beam will be almost completely vignetted by the autocollimator. Therefore, over a 7 m working distance, the autocollimator FOV = $\arctan(2.5\ \mathrm{cm}\ /\ 7\ \mathrm{m}) = 750''$. This 750'' FOV was then used to size the plate scale of the imaging channel.

A BFS-U3-120S4M-CS CMOS detector was chosen for its high resolution (4000 × 3000 pix) low noise (3 e-) operation at visible wavelengths. This detector has a focal plane area of 7.47 mm by 5.6 mm. To maximize the angular resolution of the system, the ±750'' FOV should fill the detector area. This implies we need an effective focal length of 0.77 m. Accommodating 0.77 m would lead to an unreasonably large system so the effective focal length should be achieved by a 10 times beam contractor followed by a 7.7 mm focal length imaging.

With this plate scale, each pixel has an angular size of 0.5''. This allows oversampling relative to the 4'' resolution required for closed loop pointing control during calibration measurements. The

anticipated imaging quality is shown in Figure 96. In this figure, the payload cube (top) is tilted by 100'' relative to the illumination module annulus (bottom).

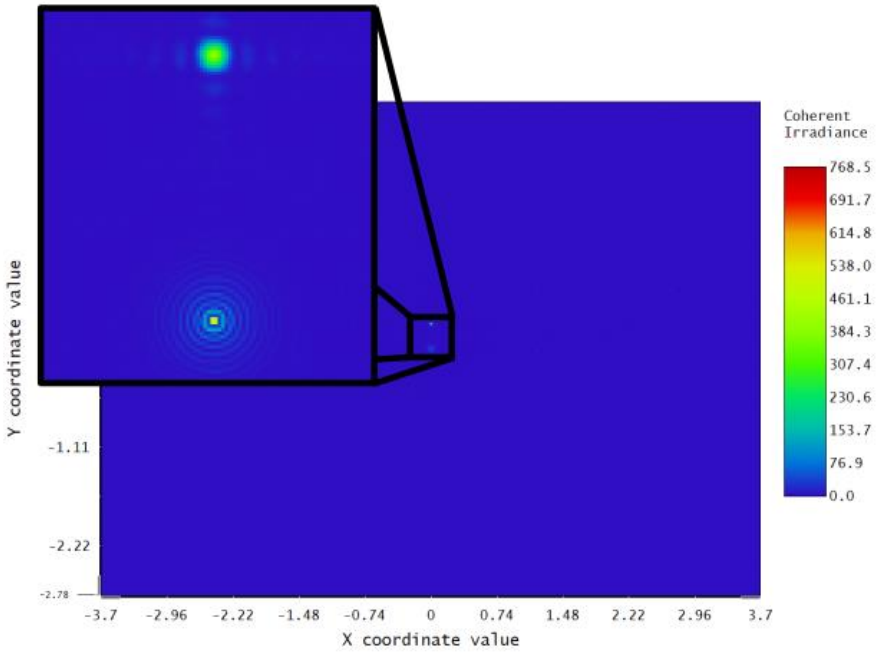

Figure 96: Simulated focal plane image for the focal imaging channel. Simulation evaluated with a 0.01 degree tilt of the payload cube. Positions shown are shown in mm.

The centroiding accuracy depends on the spot size in the detector channels. The predicted FWHM in the imaging channel is 5'' for the PLM cube and 2'' for the annulus (Figure 97). Given the size of the PSF and that the PSF is Nyquist sampled, it should be possible to find the centroid of each spot with a resolution better than 4'' with a considerable margin. This <<4'' centroiding accuracy enables the closed loop pointing control to keep the spot within the payload spectrometer slits.

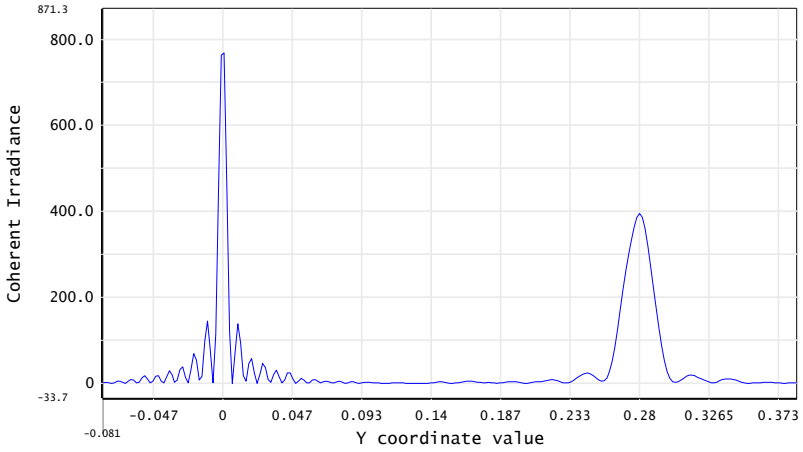

Figure 97: simulated image cross-section for the annulus (left) and the payload alignment cube (right). Positions shown are shown in mm. Irradiance is shown in arbitrary units.

6.3.2.2 Pupil imaging channel

In addition to the imaging channel, common to all alignment telescope systems, this design features a novel pupil imaging channel. This provides centration monitoring. When using a standard alignment telescope, three focuses are required to align the system (focus at target 1, focus at target 2, focus at infinity). The first two of these provide the centration measurement, the latter provides the angular misalignment. The alignment process then follows an iterative sequence of adjustment and cycling through the different focuses on the alignment telescope. The design presented here is expected to significantly simplify the alignment process by providing instantaneous, simultaneous tracking of decenter and tip-tilt.

To achieve the centration monitoring, a detector is placed within the collimated retroreflected beam (Figure 95). A simulated detector image is shown in Figure 98. The annulus seen is the retroreflection from the illumination module alignment target. The square is the retroreflection from the PLM alignment cube. The illumination module is correctly centered when the centroid of the square lies within the center of the annulus.

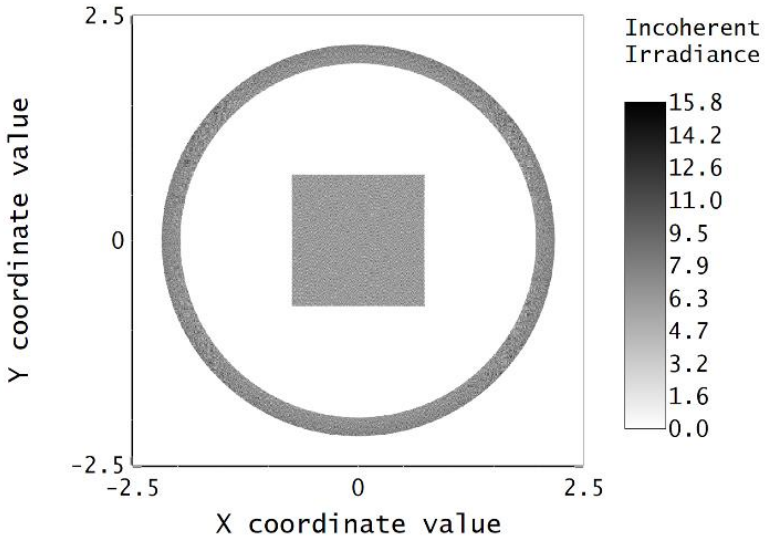

Figure 98: Simulated detector image for the pupil imaging channel. Positions shown are shown in mm. Irradiance is in arbitrary units.

The centration range viewable by the detector is also limited by the size of the 2 inch output lens. The 2 inch lens provides approximately ±2.5 cm centration error between the illumination module and payload before un-usable vignetting occurs. This is an order of magnitude larger than the expected misalignment of the CTR trolley relative to the illumination module (a few millimetres). Therefore, the pupil imaging channel is expected to provide a sufficient range.

To achieve the ±2.5 cm range of centration measurements, a magnification factor must be introduced to condense the 2 inch beam, onto the 5.6 mm detector. Fortunately, the 10 times magnification required for the imaging channel is sufficient to map the 2 inch centration range onto the detector area.

The $1.85\ \mu m$ pixels of the detector corresponds to $20\ \mu m$ resolution monitoring of the illumination relative to the payload 1.4 mm centration requirement. Therefore, the pixel scale will easily oversample the required resolution.

To ensure the centration monitoring channel measures pure centration and is not impacted by tilts, the centration monitoring channel is placed at a pupil of the system. In this way, the beam position at

the detector is independent of the tilt of the payload. The long (~7 m) distance between the autocollimator and the payload means that with just a 10.6 times beam contractor no usable pupil exists. To overcome this a Cooke triplet is added to generate an accessible pupil. The pupil position can be seen from the chief ray trace (Figure 99). The position of the detector can be adjusted relative to the Cook triplet to change the working distance of the pupil imaging channel. This design accommodates working distances from 0 to 8 m covering the full range of anticipated working distances (approx. 6-7.5 m).

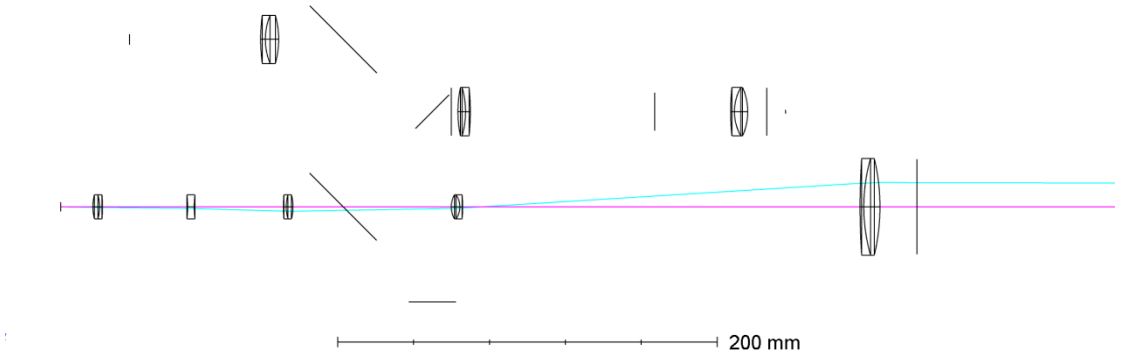

Figure 99: Chief ray trace. The optical axis is shown by the pink ray. The chief ray is shown in blue. The figure was evaluated with a 7 m payload distance and a 0.1 degree field offset in the return beam (corresponding to a 0.05 degree tilt of the payload).

6.3.3 Autocollimator testing

To demonstrate the performance, the autocollimator described in 6.3.2 was built and tested. For the autocollimator, the critical requirements to verify are the resolution and the FOV of the system. Both the FOV and resolution can be impacted by the design, but also the as-built alignment. In this section, we will therefore assess the imaging quality of the system to assess the impact of manufacturing and alignment aberrations. We will also check the FOV of the system, this is to check for vignetting internal to the autocollimator system. Finally, the resolution of the pupil imaging channel will be verified.

To test the autocollimator, a ½-inch[64] square mirror was placed in front of the autocollimator shown in Figure 94. This square mirror referred to here as the payload cube simulator, was intended to represent the optical surface of the payload cube (see Figure 98). Due to procurement delays, the annulus (Figure 84) was not present during the testing of the autocollimator.

During testing a few adjustments were made to the autocollimator design shown in (Figure 94). It was not practical to place the payload cube simulator 7 m away from the autocollimator (the nominal optical path length when the payload is in the 5 m vacuum chamber). The payload cube simulator was, therefore, positioned ~30 cm in front of the autocollimator. This, however, shifts the z position of the pupil. Because of this, the pupil imaging detector was moved back by ~6 cm.

The detector channel location was only a temporary change required in the test configuration, however, a couple of permanent optomechanical design updates were identified. The z-fold at the output of the autocollimator (Figure 94) required modification. Despite being designed for 2-inch elliptical optics, the KCB2/M mount for the z-fold at the front of the autocollimator has a limiting aperture of 42.0 mm which would vignette the beam going to the annulus. This Z-fold was, therefore, removed during testing. Subsequent iterations of the autocollimator will use two freestanding 3-inch circular flats to create the output z-fold.

It was also found that the mechanical constraints imposed by the cage system were insufficient to align the spatial filter to the beam expander (Figure 94) and to align the imaging channel to the beam expander. The fixed cage cubes (Figure 94) were, therefore, replaced with kinematic mounts to provide additional adjustability to align the modules within the autocollimator.

[64] This is the closeset commercially available flat to the 15mm payload alignment cube

Other than the position of the pupil imaging channel (due to practical testing constraints), and the described mirror mount updates, the test version of the autocollimator was as shown in Figure 94. The system was assembled using a series of cage-mounted alignment targets and a half-wave plate collimation tester. The resulting signal in the two detector channels is shown in Figure 100. The left, focal channel allowed angular changes in the PLM cube simulator to be monitored. The right figure allowed centration changes in the PLM cube simulator to be seen.

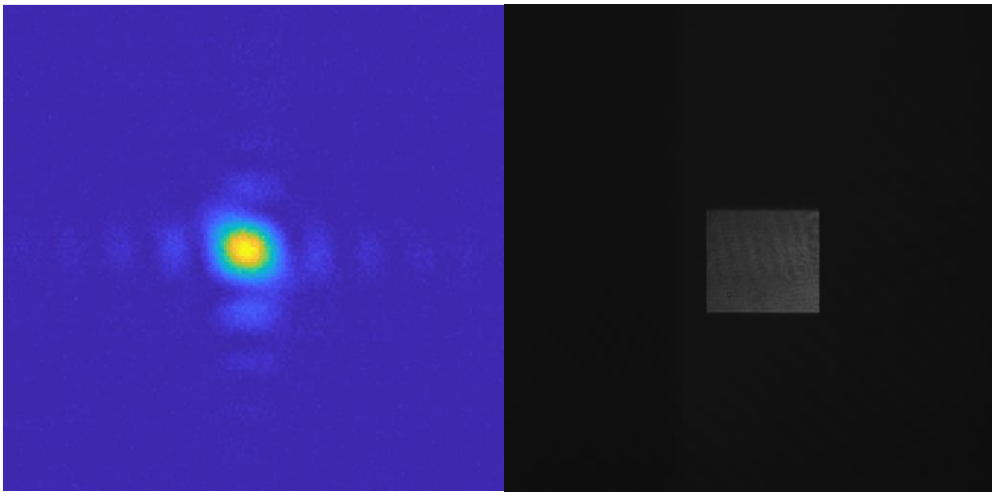

Figure 100: Sample (zoomed in) detector views. Left shows the focal imaging channel. Right shows the pupil imaging channel.

The measured signals (Figure 100) were then used to verify several key performance metrics. Of particular importance to the alignment monitoring is the PSF. To achieve < 4-arcsecond angular monitoring, the PSF must be of a similar size[65] or smaller. The PSF will be impacted by design aberrations, manufacturing errors as well as alignment-induced aberrations. The observed spot is shown in Figure 100 demonstrating diffraction-limited performance (limited by the PLM cube simulator size). Figure 101 shows a comparison between the measured and predicted focal plane

[65] It will be possible to achieve sub-spot size alignment monitoring by centeroiding.

signal, showing excellent agreement. The image has an FWHM of 29.6 microns = 8 arcseconds at the autocollimator output. By centroiding, sub-spot size tracking can be achieved (see e.g. [39]), enabling the < 4-arcsecond closed loop pointing control. This ensures we can keep the OGSE spot within the payload spectrometer slit during long calibration measurements.

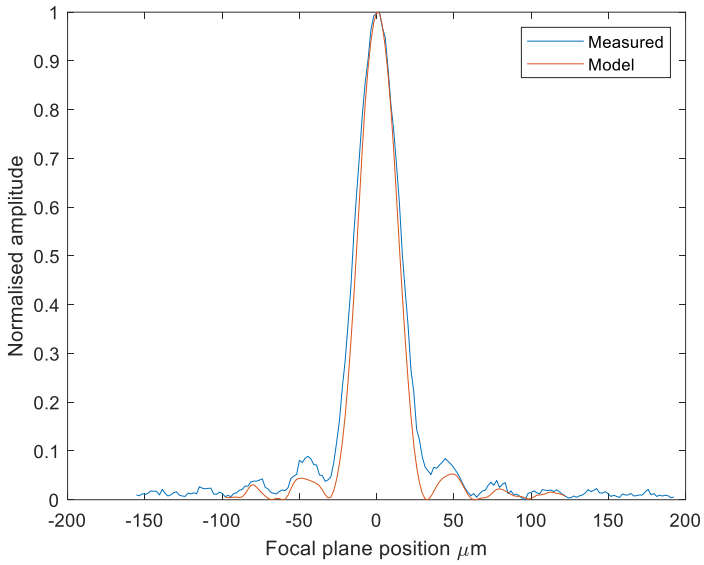

Figure 101: PSF comparison between the model and measured values.

Another key performance metric of the autocollimator is the FOV. This is particularly critical in the initial phases of alignment when the misalignment between the systems may be considerable (tolerance TBD). The goal of this test is to assess if any of the optomechanical components clip the beam and limit the FOV. To assess the FOV, the PLM cube simulator was tilted to steer the return beam over the autocollimator FOV. It was found that the full extent of the detector array could be illuminated. This is shown in Figure 102 by the images at the corners of the array (positional differences were limited by pointing jitter). This confirms that in the test configuration, the detector limits the FOV confirming no significant vignetting within the autocollimator imaging channel. It should be noted though, that the true FOV of the autocollimator depends on the working distance. This is due to the decentring of the return beam causing clipping on the 2 inch collimating lens (see 6.3.2.1).

Figure 102: FOV testing of the imaging channel. The payload cube simulator has been steered to the corners of the imaging channel FOV. This figure is shown with four images overlaid.

To assess the centration measurement resolution, the image shown in Figure 100 was horizontally integrated over the full array. The integrated image of the cube is shown in Figure 103. Stray light was noticeable in this channel, giving rise to the continuum seen. The stay light was largely caused by the monitor used during alignment teasing. In the final autocollimator setup, cage-mounted baffling will be used to reduce this effect. However, the cube can be clearly seen above the stray light and the stray light did not limit the centration measurement accuracy.

The width of the edge of the cube in the image is ~14 pix (Figure 103). This corresponds to ~ 0.27 mm uncertainty in the position of the cube. This is easily compliant relative to the 1.4 mm requirement. This shows the autocollimator will be capable of measuring the payload cube location to a level that will prevent vignetting of the OGSE test beam.

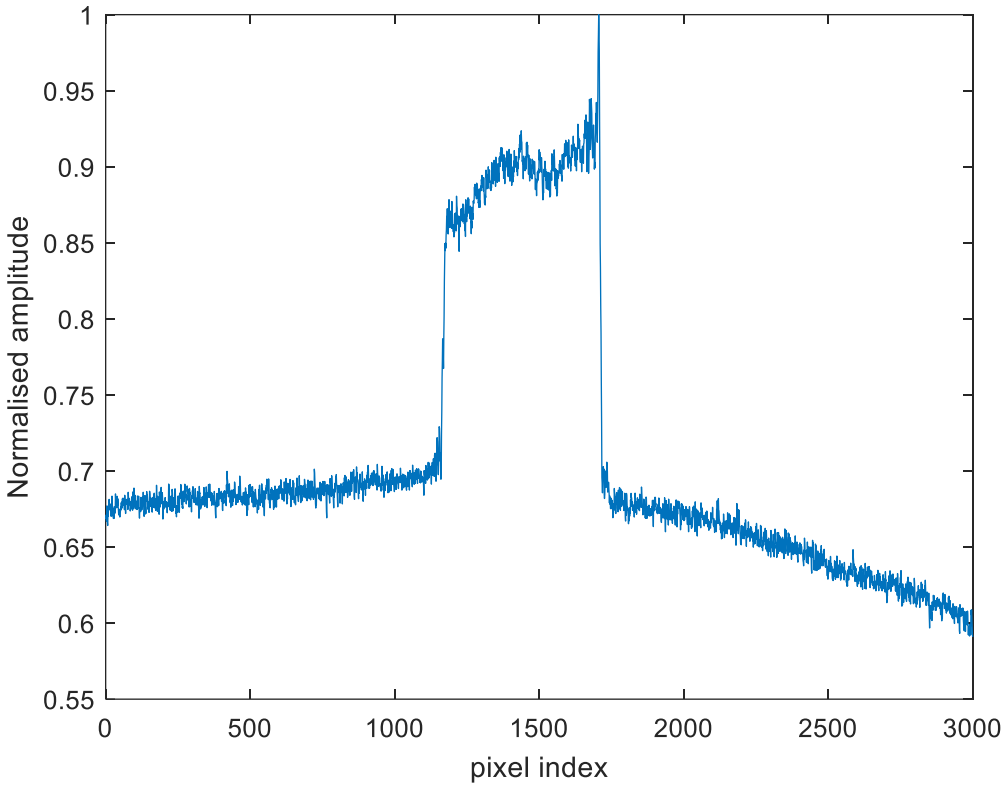

Figure 103: Horizontally integrated signal from the payload cube simulator

The remaining question to be addressed is the alignment monitoring performance of the annulus (Figure 84). This will be the subject of future work. For the angular monitoring channels, the use of the annulus will be straightforward. For the centration detector channel, there are additional subtleties. The centration detector does not lie in a pupil plane of the annulus (unlike with the payload cube). This means that the image in the centration channel will be dependent not only on the position of the annuls, but also on the angle. When designing the system, two approaches were considered to resolve this. The first approach would be to guarantee the annulus is on-axis with respect to the

autocollimator output. This can be achieved e.g. with a crosshair at the output of the autocollimator[66]. The other option would be to measure centration changes by analysis using data from both the centration and angular channels. Given the angular data from the focal channel, it should be possible to correct the angular contribution to the measured centration error.

Moreover, because the detector does not lie at a pupil, diffraction effects may prove significant. Diffraction will cause interference effects to be seen in the centration channel, potentially causing a reduction in the measured centration accuracy. An annulus has been sent out for procurement and the questions relating to centration accuracy will be assessed by test shortly.

6.4 CONCLUSIONS

In this chapter, the OGSE optical design was presented. The current design was a consequence of a trade study that assessed the feasibility of monitoring, and compensating for thermoelastic deformations. It was found that a considerable reduction in complexity could be achieved if all powered mirrors were incorporated into the illumination module leading to the design shown in Figure 84.

The tradeoff was largely a consequence of the number of degrees of freedom in the PDR design. Thermoelastic analysis was used to confirm the need for ~11 degrees of freedom in the old design. This number of degrees of freedom poses challenges for the mechanism design. The driving source of

[66] The crosshair would sit in the collimated beam at the output of the autocollimator in the collimated beam. The crosshair will therefore mask the laser in both the outbound and return directions. By ensuring the obscured parts of the beam overlap in the outbound and return directions, the mirror can be shown to be on-axis.

complexity, however, is constraining these degrees of freedom. The payload requires a collimated input to enable the focusing of the telescope. The OGSE, therefore, requires an independent means of monitoring and correcting OGSE thermoelastic deformations. To enable this monitoring, a pupil-scanning autocollimator was proposed. This enables a series of alignment targets to be viewed, and changes in angle, centration, and optical path length to be tracked. The monitoring system was, however, horrifyingly complex.

Due to this complexity, a trade-off study was conducted. The goal of the trade study was to reduce the number of degrees of freedom in the design and reduce the need for alignment monitoring. By incorporating the powered optics into the illumination module, only the illumination module to payload alignment needs to be tracked; a significant reduction compared to 5 laser references with the PDR design. The updated design also incorporated all the complex optics into the illumination module chamber enabling de-risking in Oxford.

A design was then presented which enabled the illumination module to output a ¼ aperture beam (28 cm in the major direction). It was then shown that this design would be consistent with the optical quality, FOV, and flat fielding requirements. To meet the remaining illumination module design requirements, mechanism designs were presented. These include the rapid (<1 s) stuttering required for persistence measurements, cryogenic shutter blades for low-background spectral characterisation, and filter wheels for use during alignment.

Whilst it was possible to remove most alignment monitoring, one alignment target remains: the payload alignment cube. This enables motion between the illumination module relative to the payload to be tracked. The design of this alignment monitoring system is described in section 6.3. The design used two detector channels, one to measure centration, and the other to measure angular shifts. This provides all the information required to track the global motion between the illumination module and the payload. The autocollimator was constructed and its performance was verified. It was shown that

the design was capable of meeting the centration and angular resolution requirements as well as meeting the 750'' design FOV.

7 CONCLUSIONS AND FUTURE WORK

7.1 THESIS SUMMARY

Ariel will use the transit spectroscopy method to observe the atmospheres of ~1000 exoplanets atmospheres. To detect molecular absorption features, Ariel will produce medium-resolution spectra ($R \geqslant 15$) of exoplanets using three spectroscopic channels 1.1 – 7.9 μm as well as having photometric channels covering 0.5 – 1.1 μm. The technical driver for Ariel, though, is the photometric stability. This is to enable the detection of atmospheric spectral features that are tens of ppm relative to the host star, Ariel aims to have tens of ppm stability over long (10 hr) timescales.

To enable Ariel's ambitious scientific goals, detailed calibration is also required. In Chapter 2 it was discussed how the OGSE would be used to calibrate the Ariel payload. These calibration measurements require a broad range of illumination conditions to perform these measurements. In Chapter 3, radiometric modelling was presented to simulate the focal plane signals when the payload is illuminated with the OGSE. Two particularly challenging tests are the payload photometric stability and the payload dark current testing in Chapters 4 and 5 we explored the consequences of these tests on the OGSE design. In Chapter 6 the OGSE optical architecture to achieve the planned calibration measurements was presented. Here we will summarise the key results from each section.

In Chapter 2, the payload-level ground calibration plan was presented. This was created to define the methods the OGSE will use to calibrate the payload. This work was completed for two reasons. Firstly it was to identify areas where verification is not possible at the payload level. This includes tests such as out-of-field stray light. Special emphasis must be placed on sub-system verification of tests not possible at the payload level. In cases where payload-level verification is possible, the methods planned at the payload level directly inform performance requirements for the OGSE system. This includes parameters such as the spectral resolution of the monochromator, the uniformity of the

sphere, as well as functionalities such as rapid (<1 s) cryogenic shuttering for persistence measurements.

The calibration measurements described in Chapter 2 require a diverse range of fluxes (K-magnitude of 8.8 to 3.25). In Chapter 3, radiometric modelling work was presented to demonstrate the OGSE is capable of simulating the range of stellar targets Ariel plans to view (GJ 1214 to HD 219134). Source designs were presented to meet the bright target flux (HD 219134). However, for the monochromator, achieving an output flux brighter than the faint target proved challenging. This informed several improvements to the preliminary OGSE optical design including: A variable slit to allow for special width optimisation, grating optimisation, a switch from gold to silver mirror coating to improve the throughput in the short-wave payload photometer (0.5-0.55 μm) and a reduction in the sphere size to (30 cm to 15 cm). The sphere size reduction is, however, a trade-off against the output uniformity. A feasibility study was conducted to assess the uniformity of a 15 cm sphere. A peak-to-valley uniformity of ~0.2% was predicted, consistent with the 0.5%. This enabled the reduced sphere size to be used and the output flux requirements to be met.

In Chapter 4, the feasibility of one of the most challenging calibration measurements was assessed - the verification of the payload photometric stability (see 2.2.5). An integrated OGSE-Ariel simulator was used to produce time-domain simulations of the photometric stability test. In particular, the goal was to assess how OGSE source variability would impact the photometric stability verification measurement. The analysis confirmed the expectation that reference detectors would be needed to monitor and correct source variability. It was also possible to place bounds on the maximum noise and gain stability of the OGSE reference detectors.

Literature data was then used to assess the noise/stability of different detector types, as well as determine the thermal sensitivity of the detectors. Literature data indicated the OGSE MCT detector candidates would have a QE that has a strong temperature dependence (8600 ppm K^{-1}, see 4.3.1.3.1), implying the OGSE detectors would require mK thermal stability, a challenging requirement.

A thermal control model was presented to assess the achievable level of thermal stability. It was found that temperature control parameters (PID) exist that can stabilise the expected boundary condition variability whilst being robust to temperature sensor noise. This indicated that mK thermal stability of the OGSE reference detectors may be achievable. This thermal stability enables the reference detectors to meet their gain stability requirements and enables the OGSE to verify Ariel's photometric stability.

In Chapter 5, we considered the OGSE thermal design. End-to-end simulations were presented to assess how cold OGSE optics must get. It was found that to test the payload dark current, all OGSE optics must be less than 70 K. FEA models were then presented to assess the compliance of the illumination module thermal design. It was found that with the enlarged illumination module, the ambient radiative load on the shroud would likely prevent the optical bench from reaching 70 K. Moreover, the results were extremely sensitive to the MLI emissivity, an uncertain parameter (see 5.2.2.4). To resolve this, a two-stage thermal design was proposed and is under discussion with the RAL facility team.

In addition to thermal emission from the OGSE's optical surfaces, thermal stray light may also cause issues for testing Ariel's detectors' dark current. A model was presented to assess the impact of thermal stray light from various surfaces within the test facility. The model found thermal emission from the 293 K Payload Interface Plate (PIP) would be a significant stray light source when enclosed in the CTR, causing a focal plane signal 10^3 times larger than the payload dark current. This model did, however, suffer from the limitation of using a thermal model for the ray trace. Because of this, full BRDF scattering was not possible, nor was it possible to determine the stray light path.

It has been shown that the current illumination module thermal design produces marginal performance relative to the 70K requirement, however, with a two-stage design this risk will be removed. With the updated design, thermal emission from OGSE optical surfaces can be made to be

small compared to the payload dark current. The main risk to dark testing of the payload remains stray light which will be assessed during payload EM testing.

In Chapter 6 we considered the OGSE optical architecture. In particular, we considered the feasibility of maintaining alignment of the PDR design over the vast (~210 K) range of operating temperatures. It was found that to maintain alignment over this temperature range, ~11 degrees of freedom are required in the OGSE system. This presents challenges with the number of cryogenic mechanisms, but more significantly, constraining all these degrees of freedom was found to be horrifyingly complex. A pupil-splitting autocollimator was proposed to monitor the deformations, however, this was a challenging system requiring 5 reference surfaces to be monitored.

A trade-off study was presented to simplify the alignment monitoring systems. This led to a major re-design in the illumination module and target projector designs. The optical design for the new illumination module was presented, as well as an analysis to demonstrate the design is capable of the various calibration functions.

Whilst it was possible to greatly simplify the alignment monitoring requirements, four degrees of freedom remained – the motion of the illumination module relative to the payload. To achieve this monitoring, an autocollimator system was designed (section 6.3). This system monitors an annulus on the illumination module optical bench and the payload alignment cube to ensure alignment between the illumination module and the payload. Experimental testing was then conducted to verify the angular and centration measuring performance of the system. In all cases, the design was found to be able to monitor alignment changes to a level consistent with the testing of Ariel.

7.2 FUTURE WORK

The work completed in this thesis focused on performance simulation, requirement derivation and design; all to enable the calibration of the Ariel space telescope. The OGSE has now completed the System Requirement Review (SRR) and Preliminary Design Review (PDR) for all its sub-systems. The

performance analysis and requirements derivation are now well-defined. Future developments of the OGSE will focus on developing the design maturity for Critical Design Review (CDR), as well as experimental verification of the performance of the system as we enter the build phase. Here we will describe key areas of development relevant to each of the thesis chapters.

In section 2, the plan for payload-level testing using the OGSE was described. The methods described provide a comprehensive set of methods to perform all the tests currently required by the payload. The payload calibration requirements are still expected to change, with new products such as the super-bias expected to be required. Moreover, there is a drive to standardize calibration methods between the sub-systems, payload level testing and flight. There is also uncertainty regarding how the OGSE will be used to focus the payload (see e.g. 6.2.4.4). Defining and agreeing on the remaining tests/ methods remains key for the OGSE development pre-CDR. In particular, we must demonstrate the OGSE design is capable of all illumination conditions required for testing of the payload.

In Chapter 3 radiometric modelling results were presented. This was to predict the focal plane signal when the payload is being illuminated by the OGSE. This analysis has remained stable for a while now, with the key design parameters for throughput frozen. Testing is, however, required to validate the end-to-end throughput of the system. These OGSE throughput measurements will also be used as a part of the radiometric calibration of the payload (section 2.2.1.1).

In Chapter 4, a particularly challenging calibration measurement was considered – photometric stability verification of the payload. To test the payload's photometric stability, the OGSE must meet several stringent performance requirements. The analysis presented in Chapter 4 showed the required noise/ stability in the OGSE reference detectors (Table 9, Table 10) as well as the need for mK thermal stability. To demonstrate the feasibility of verifying Ariel's stability, efforts should be focused on characterising the OGSE reference detectors and readout electronics. In particular, the long-timescale (~10 hr) noise and stability are expected to be particularly challenging relative to the tens of ppm required to test the payload.

The thermal stability of the OGSE reference detectors remains critical to testing the photometric stability of Ariel. A commercially available solution has been found that can monitor and control an ideal thermal system with 1 mK stability implying achieving mK stability should be possible. Moreover, section 4.4 showed PID parameters exist that can stabilise the expected thermal boundary condition variability. The thermal control model was, however, a nodal model that assumed an isothermal optical bench. There is still a risk that the thermal control system could drive time-varying thermal gradients preventing mK stability of our reference detectors. Minimising this effect may require optimisation of the heater/ temperature sensor locations.

In addition to thermal control, the steady-state temperatures are also challenging. Cryogenic operation of the OGSE optics (<70 K) is required to enable testing of the dark current payload detectors (driven by Airs CH1). The FEA analysis presented in Chapter 5, showed <70 K optics would likely not be possible with a single-stage illumination module thermal design. A liquid nitrogen cooled shroud concept was proposed to resolve these challenges. An alternative approach using a 2-stage thermal design with two cold heads would likely also be sufficient. The thermal trade-off between these options will be the subject of immediate future work. However, it seems likely that the decision will be driven by RAL test facility constraints.

The optical design of the system was discussed in Chapter 6. The optical design is stable and has been shown to meet all the optical performance requirements. The immediate priorities for the development of the optics are related to the illumination module optomechanics. Cryogenic operation of the optics poses several challenges to optical mounting. Firstly, stress-free mounts are required to ensure thermal stresses do not cause WFE on the mirrors' surfaces. Moreover, the detailed design of the cryogenic adjustment stages and mechanisms requires finalising. With the detailed design of the mounts and adjusters, a tolerancing analysis will be conducted on the OGSE mirrors' positions. The positional tolerancing analysis results can then be combined with thermoelastic analysis and predicted manufacturing aberrations to predict the expected aberrations in the OGSE output beam. The predicted aberrations will then be compared to the WFE required to test the payload.

The combination of this future work will put the OGSE in an excellent position be begin the build and test of the OGSE.

In this thesis, the payload-level testing of the Ariel payload has been explored. It has been shown that calibrating the Ariel payload places many stringent performance requirements on the OGSE system. Designs to meet these stringent requirements have been presented. As the OGSE progresses from the design to the build phase we hope to test and show the performance of the OGSE system. This system will then be capable of calibrating the Ariel payload, enabling Ariel's ambitious scientific goals of characterising the atmospheres of 1000 exoplanet atmospheres.

8 REFERENCES

[1] M. Mayor and D. Queloz, "A Jupiter-mass companion to a solar-type star," *Nature,* vol. 378, no. 6555, pp. 355-359, 1995/11/01 1995, doi: 10.1038/378355a0.

[2] Exoplanet Team. "The Extrasolar Planets Encyclopaedia." http://exoplanet.eu/catalog/ (accessed 14/9/23, 2020).

[3] N. Madhusudhan, "Exoplanetary Atmospheres: Key Insights, Challenges, and Prospects," *Annual Review of Astronomy and Astrophysics,* vol. 57, pp. 617-663, 2019.

[4] C. Hellier *et al.*, "WASP-43b: the closest-orbiting hot Jupiter," *A&A,* vol. 535, p. L7, 2011. [Online]. Available: https://doi.org/10.1051/0004-6361/201117081.

[5] K. B. Stevenson *et al.*, "Thermal structure of an exoplanet atmosphere from phase-resolved emission spectroscopy," *Science,* vol. 346, no. 6211, pp. 838-841, 2014, doi: 10.1126/science.1256758.

[6] D. A. Fischer *et al.*, "Exoplanet detection techniques," *arXiv preprint arXiv:1505.06869,* 2015.

[7] G. Ricker *et al.*, "Transiting Exoplanet Survey Satellite," *Journal of Astronomical Telescopes, Instruments, and Systems,* vol. 1, no. 1, p. 014003, 2014. [Online]. Available: https://doi.org/10.1117/1.JATIS.1.1.014003.

[8] G. Tinetti *et al.*, "ARIEL Definition Study Report (Red Book)," 2020.

[9] W. J. Borucki *et al.*, "Kepler's Optical Phase Curve of the Exoplanet HAT-P-7b," *Science,* vol. 325, no. 5941, pp. 709-709, 2009, doi: 10.1126/science.1178312.

[10] J. L. Birkby, "Exoplanet Atmospheres at High Spectral Resolution," *arXiv preprint arXiv:1806.04617,* 2018.

[11] B. Edwards *et al.*, "ARES I: WASP-76 b, A Tale of Two HST Spectra*," *The Astronomical Journal,* vol. 160, no. 1, p. 8, 2020/06/09 2020, doi: 10.3847/1538-3881/ab9225.

[12] G. Tinetti *et al.*, "A chemical survey of exoplanets with ARIEL," *Experimental Astronomy,* vol. 46, no. 1, pp. 135-209, 2018/11/01 2018, doi: 10.1007/s10686-018-9598-x.

[13] A. F. Al-Refaie, Q. Changeat, I. P. Waldmann, and G. Tinetti, "TauREx 3: A Fast, Dynamic, and Extendable Framework for Retrievals," *The Astrophysical Journal,* vol. 917, no. 1, p. 37, 2021/08/12 2021, doi: 10.3847/1538-4357/ac0252.

[14] P. G. J. Irwin *et al.*, "The NEMESIS planetary atmosphere radiative transfer and retrieval tool," *Journal of Quantitative Spectroscopy and Radiative Transfer,* vol. 109, no. 6, pp. 1136-1150, 2008/04/01/ 2008, doi: https://doi.org/10.1016/j.jqsrt.2007.11.006.

[15] C. Visscher, J. I. Moses, and S. A. Saslow, "The deep water abundance on Jupiter: New constraints from thermochemical kinetics and diffusion modeling," *Icarus,* vol. 209, no. 2, pp. 602-615, 2010.
[16] B. Edwards, L. Mugnai, G. Tinetti, E. Pascale, and S. Sarkar, "An Updated Study of Potential Targets for Ariel," *The Astronomical Journal,* vol. 157, no. 6, p. 242, 2019/05/30 2019, doi: 10.3847/1538-3881/ab1cb9.
[17] B. J. Fulton *et al.*, "The California-Kepler survey. III. A gap in the radius distribution of small planets," *The Astronomical Journal,* vol. 154, no. 3, p. 109, 2017.
[18] E. D. Lopez and K. Rice, "How formation time-scales affect the period dependence of the transition between rocky super-Earths and gaseous sub-Neptunesand implications for $\eta \oplus$," *Monthly Notices of the Royal Astronomical Society,* vol. 479, no. 4, pp. 5303-5311, 2018.
[19] K. I. Öberg, R. Murray-Clay, and E. A. Bergin, "The effects of snowlines on C/O in planetary atmospheres," *The Astrophysical Journal,* vol. 743, no. 1, p. L16, 2011/11/21 2011, doi: 10.1088/2041-8205/743/1/l16.
[20] P. G. Irwin *et al.*, "2.5 D retrieval of atmospheric properties from exoplanet phase curves: application to WASP-43b observations," *Monthly Notices of the Royal Astronomical Society,* vol. 493, no. 1, pp. 106-125, 2020.
[21] V. Parmentier *et al.*, "From thermal dissociation to condensation in the atmospheres of ultra hot Jupiters: WASP-121b in context," *A&A,* vol. 617, p. A110, 2018. [Online]. Available: https://doi.org/10.1051/0004-6361/201833059.
[22] L. Kreidberg *et al.*, "Absence of a thick atmosphere on the terrestrial exoplanet LHS 3844b," *Nature,* vol. 573, no. 7772, pp. 87-90, 2019/09/01 2019, doi: 10.1038/s41586-019-1497-4.
[23] G. Tinetti *et al.*, "ARIEL Assessment Study Report (Yellow Book) " ESA, 2017.
[24] L. Dressel. "Wide Field Camera 3 Instrument Handbook, Version 12.0." (accessed.
[25] E. Sedaghati *et al.*, "Detection of titanium oxide in the atmosphere of a hot Jupiter," *Nature,* vol. 549, no. 7671, pp. 238-241, 2017/09/01 2017, doi: 10.1038/nature23651.
[26] C. A. Beichman and T. P. Greene, "Observing Exoplanets with the James Webb Space Telescope," 2017.
[27] T. P. Greene, M. R. Line, C. Montero, J. J. Fortney, J. Lustig-Yaeger, and K. Luther, "Characterizing transiting exoplanet atmospheres with JWST," *The Astrophysical Journal,* vol. 817, no. 1, p. 17, 2016.
[28] J. K. Barstow and K. Heng, "Outstanding Challenges of Exoplanet Atmospheric Retrievals," *arXiv preprint arXiv:2003.14311,* 2020.
[29] K. Gordon, "Science Operations Design Reference Mission (JWST-STScI-CI-000045)," no. Revision C, 2012.

[30] N. Cowan *et al.*, "Characterizing transiting planet atmospheres through 2025," *Publications of the Astronomical Society of the Pacific,* vol. 127, no. 949, p. 311, 2015.
[31] J. K. Barstow, S. Aigrain, P. G. J. Irwin, S. Kendrew, and L. N. Fletcher, "Transit spectroscopy with James Webb Space Telescope: systematics, starspots and stitching," *Monthly Notices of the Royal Astronomical Society,* vol. 448, no. 3, pp. 2546-2561, 2015, doi: 10.1093/mnras/stv186.
[32] ARIEL SST, "ARIEL Science Requirement Document (ESA-ARIEL-EST-SCI-RS-001)," 2019.
[33] A. Rosich *et al.*, "Correcting for chromatic stellar activity effects in transits with multiband photometric monitoring: Application to WASP-52," *arXiv preprint arXiv:2007.00573,* 2020.
[34] J. Martignac *et al.*, *AIRS: ARIEL IR spectrometer status* (SPIE Astronomical Telescopes + Instrumentation). SPIE, 2022.
[35] ARIEL team, "ARIEL Telescope Requirements Document (ARIEL-CSL-PL-RS-001)," no. 3.0.
[36] A. Caldwell, P. Eccleston, and G. Tinetti, "ARIEL Payload Design Description (ARIEL-RAL-PL-DD-001)," 2020, 4.0.
[37] G. Morgante, "PLM Thermal Analysis Report GTMM Description and Results (ARIEL-INAF-PL-TN-003)," 2022.
[38] A. Philippon, J. Fontignie, J. Martignac, and M. Berthé, "AIRS Optical Design Description (ARIEL-IAS-INST-DD-002)," 2021, issue 3.1.
[39] M. Rataj *et al.*, "ARIEL FGS Design Description Document (ARIEL-CBK-INST-DD-001)," 2023, issue 4.4.
[40] R. S. Konrad *et al.*, "ARIEL fine guidance system: design, challenges, and opportunities," in *Proc.SPIE*, 2022, vol. 12180, p. 1218013, doi: 10.1117/12.2629862. [Online]. Available: https://doi.org/10.1117/12.2629862
[41] R. Kimble *et al.*, *The integration and test program of the James Webb Space Telescope* (SPIE Astronomical Telescopes + Instrumentation). SPIE, 2012.
[42] J. Sullivan *et al.*, *Manufacturing and integration status of the JWST OSIM optical simulator* (SPIE Astronomical Telescopes + Instrumentation). SPIE, 2010.
[43] C. Atkinson *et al.*, *Architecting a revised optical test approach for JWST* (SPIE Astronomical Telescopes + Instrumentation). SPIE, 2008.
[44] L. Feinberg, J. Hagopian, and C. Diaz, *New approach to cryogenic optical testing the James Webb Space Telescope* (SPIE Astronomical Telescopes + Instrumentation). SPIE, 2006.
[45] R. Kimble *et al.*, *James Webb Space Telescope (JWST) optical telescope element and integrated science instrument module (OTIS) cryogenic test program and results* (SPIE Astronomical Telescopes + Instrumentation). SPIE, 2018.

[46] L. Gaspar Venancio *et al.*, *An account of the Euclid payload module test results* (International Conference on Space Optics — ICSO 2022). SPIE, 2023.
[47] S. Liébecq, "EUCLID Payload Module: Thermal Balance and Thermal Vacuum Test at CSL Premises," in *ECSSMET 2023*, 2023: CNES, Toulouse, France.
[48] O. Pirnay *et al.*, *EUCLID: design, analysis, fabrication, and test of a 1.3 m collimator for the on-ground characterization of the EUCLID payload module* (SPIE Astronomical Telescopes + Instrumentation). SPIE, 2018.
[49] L. F. Rolo, M. H. Paquay, R. J. Daddato, J. A. Parian, D. Doyle, and P. d. Maagt, "Terahertz Antenna Technology and Verification: Herschel and Planck - A Review," *IEEE Transactions on Microwave Theory and Techniques,* vol. 58, no. 7, pp. 2046-2063, 2010, doi: 10.1109/TMTT.2010.2050179.
[50] N. E. Bowles, K. Nowicki, M. Abreu, M. Tecza, and R. Spry, "OGSE Trade Off Discussion (ARIEL-OXF-PL-TN-026)," 2022, issue 1.3.
[51] N. Bowles *et al.*, "OGSE Design Description (ARIEL-OXF-PL-DD-003)," 2020.
[52] L. Desjonqueres, C. Simpson, C. Duff, and T. Rawlings, "Ariel Cryogenic Test Rig Design Description," 2023, issue 6.0.
[53] L. Desjonqueres, C. Simpson, and C. Duff, "Ariel Cryogenic Test Rig Requirements Document," 2023, issue 4.0.
[54] T. Rawlings, C. Duff, and L. Desjonqueres, "Ariel CTR CAD Model (ARIEL-RAL-PL-ML-018)," 2023, issue 3.0.
[55] C. Pearson, M. Krijger, E. Pascale, S. Sarkar, P. Eccleston, and G. Tinetti, "ARIEL Calibration Requirements," 2021, issue 2.0.
[56] T. van Kempen, C. Pearson, E. Pascale, A. Caldwell, P. Eccleston, and A. Davidson, "Ariel Instrument Ground Testing and Calibration Plan," 2022, issue 3.0.
[57] K. Nowicki, N. E. Bowles, and M. Rashman, "ARIEL OGSE Periscope Design Description (ARIEL-OXF-PL-DD-010)," 2023, issue 1.0.
[58] J. Guy, J. Schmoll, C. Bourgenot, and C. Davison, "Beam expander design description," 2023.
[59] A. Caldwell, A. Davidson, and E. Paul, "Ariel Payload STOP Analysis Overview (ARIEL-RAL-PL-RP-045)," 2022, issue 1.0.
[60] G. Bishop, A. Davidson, A. Caldwell, and P. Eccleston, "ARIEL Payload Requirements Document," 2022, issue 7.0.
[61] T. van Kempen and C. Pearson, "Payload ground calibration plan (ARIEL-RAL-PL-PL-005)," 2022, issue 3.0.
[62] R. Spry, N. Bowles, M. Tecza, M. Abreu, P. Machado, and E. Pascale, "OGSE payload test plan (ARIEL-OXF-PL-TN-032)," 2021.
[63] G. Malaguti and C. Pearson, "ARIEL Science Data Product Levels Description Document (ARIEL-INAF-GS-DD-001)," 2020, issue 2.5.

[64] C. Pearson *et al.*, "The Ariel ground segment and instrument operations science data centre," *Experimental Astronomy,* vol. 53, no. 2, pp. 773-806, 2022/04/01 2022, doi: 10.1007/s10686-020-09691-8.
[65] D. Charbonneau *et al.*, "Detection of Thermal Emission from an Extrasolar Planet," *The Astrophysical Journal,* vol. 626, no. 1, p. 523, 2005/06/10 2005, doi: 10.1086/429991.
[66] G. P. Eppeldauer, J. Zeng, H. W. Yoon, B. Wilthan, T. C. Larason, and L. M. Hanssen, "Extension of the NIST spectral responsivity scale to the infrared using improved-NEP pyroelectric detectors," *Metrologia,* vol. 46, no. 4, p. S155, 2009/06/02 2009, doi: 10.1088/0026-1394/46/4/S04.
[67] E. Pascale, "ARIEL PSF Size requirements (ARIEL-SAP-PL-RS-001)," 2020, issue 2.2.
[68] E. Pascale, "ARIEL Noise Model (ARIEL-SAP-PL-TN-004)," 2020, issue 1.5.
[69] M. B. Stephan *et al.*, "Noise performance of the JWST/NIRSpec detector system," in *Proc.SPIE*, 2018, vol. 10709, p. 1070930, doi: 10.1117/12.2313524. [Online]. Available: https://doi.org/10.1117/12.2313524
[70] S. Sarkar, "Pipeline Design Description Document (ARIEL-CDRF-GS-DD-001)," no. 4.1, 2020.
[71] M. B. Candice, W. M. Craig, L. P. Judith, J. F. William, and D. G. James, "Burst noise in the HAWAII-1RG multiplexer," in *Proc.SPIE*, 2005, vol. 5902, p. 59020K, doi: 10.1117/12.624191. [Online]. Available: https://doi.org/10.1117/12.624191
[72] B. J. Rauscher *et al.*, "Detectors for the James Webb Space Telescope Near‐Infrared Spectrograph. I. Readout Mode, Noise Model, and Calibration Considerations," *Publications of the Astronomical Society of the Pacific,* vol. 119, no. 857, p. 768, 2007/07/31 2007, doi: 10.1086/520887.
[73] S. Tulloch, E. George, and E. D. Systems Group, "Predictive model of persistence in H2RG detectors," *Journal of Astronomical Telescopes, Instruments, and Systems,* vol. 5, no. 3, p. 036004, 2019. [Online]. Available: https://doi.org/10.1117/1.JATIS.5.3.036004.
[74] G. Isopi, E. Pascale, and L. Mugnai, "Flat field calibrations for Ariel," in *Ariel consortium meeting*, 2021.
[75] V. Lapeyrère, T. Pichon, A. Philippon, and B. Horeau, "AIRS Calibration Plan Document (ARIEL-LES-INST-PL-001)," no. 2.0, 2022.
[76] B. Hilbert, "Non-Linearity Correction Algorithm for the WFC3 IR Channel," *Instrument Science Report WFC3 ISR WFC3-2004-06, Space Telescope Science Institute,* 2004.
[77] A. Tsiaras and J. Ozden, "Testing known and unknown systematics in HST/WFC3 spatial scans with the Wayne simulator," *arXiv preprint arXiv:1908.01692,* 2019.

[78] B. Hilbert, "Updated non-linearity calibration method for WFC3/IR," *Baltimore, Maryland,* 2014.
[79] W. D. Vacca, M. C. Cushing, and J. T. Rayner, "Nonlinearity Corrections and Statistical Uncertainties Associated with Near‐Infrared Arrays," *Publications of the Astronomical Society of the Pacific,* vol. 116, no. 818, p. 352, 2004/04/05 2004, doi: 10.1086/382906.
[80] G. Bishop, A. Caldwell, and P. Eccleston, "ARIEL Payload Requirements Document (ARIEL-RAL-PL-RS-001)," no. 3, 2020.
[81] L. Desjonqueres, C. Simpson, and C. Duff, "Ariel Cryogenic Test Rig Requirements Document (ARIEL-RAL-PL-RS-004)," 2023, issue 4.0.
[82] A. Moore, Z. Ninkov, and W. Forrest, "Quantum efficiency overestimation and deterministic cross talk resulting from interpixel capacitance," *Optical Engineering,* vol. 45, no. 7, p. 076402, 2006. [Online]. Available: https://doi.org/10.1117/1.2219103.
[83] S. Calcutt, N. Bowles, and et al., "PLM OGSE Requirements (ARIEL-OXF-PL-RS-002)," 2020, issue 2.1.
[84] R. Spry, "OGSE integrating sphere radius trade off (ARIEL-OXF-PL-TN-039)," 2022, issue 0.1.
[85] R. Spry, "OGSE monochromator radiometric model (ARIEL-OXF-PL-TN-054). In preperation.," 2023.
[86] Labsphere, "Technical Guide: Integrating Sphere Theory and Applications," ed: Labsphere North Sutton, NH, 2013.
[87] J. Barnett *et al.*, *Prelaunch calibration of the HIRDLS instrument* (SPIE's International Symposium on Optical Science, Engineering, and Instrumentation). SPIE, 1998.
[88] Y. S. Touloukian and D. P. DeWitt, *Thermal radiative properties. Non-metallic solids* (Thermophysical Properties of Matter). New York: IFI/Plenum Press, 1971.
[89] Crystran. "Calcium Fluoride CaF2 " https://www.crystran.co.uk/optical-materials/calcium-fluoride-caf2 (accessed 2024).
[90] C. Palmer, *Diffraction Gratings Ruled and Holographic Handbook*, 8 ed. New York: MKS Instruments, 2020.
[91] L. V. Mugnai, E. Pascale, B. Edwards, A. Papageorgiou, and S. Sarkar, "ArielRad: the Ariel radiometric model," *Experimental Astronomy,* vol. 50, no. 2, pp. 303-328, 2020.
[92] S. Sarkar, E. Pascale, A. Papageorgiou, L. J. Johnson, and I. Waldmann, "ExoSim: the Exoplanet Observation Simulator," *arXiv preprint arXiv:2002.03739,* 2020.
[93] R. Spry, S. Sarkar, and C. Pereira, "The OGSE Gain Noise Budget (ARIEL-OXF-PL-TN-004)," 2022, issue 0.2.
[94] R. Spry, "OGSE IR detector selection and thermal implications (ARIEL-OXF-PL-TN-036)," no. 0.1, 2022.

[95] R. Spry, "OGSE Thermal Control (ARIEL-OXF-TN-047)," 2022, issue 0.1.
[96] C. Clanton, C. Beichman, G. Vasisht, R. Smith, and B. S. Gaudi, "Precision Near-Infrared Photometry for Exoplanet Transit Observations. I. Ensemble Spot Photometry for an All-Sky Survey," *Publications of the Astronomical Society of the Pacific,* vol. 124, no. 917, p. 700, 2012/06/25 2012, doi: 10.1086/666901.
[97] F. Wildi, A. Deline, and B. Chazelas, *A white super-stable source for the metrology of astronomical photometers* (SPIE Optical Engineering + Applications). SPIE, 2015.
[98] F. Wildi, B. Chazelas, A. Deline, M. Sarajlic, and M. Sordet, *The CHEOPS calibration bench* (International Conference on Space Optics — ICSO 2016). SPIE, 2017.
[99] C. Pedroso, M. Abreu, and A. Cabral, "ARIEL OGSE VISNIR reference Detectors (ARIEL-UOL-PL-TN-023)," no. 0.1, 2021.
[100] E. Pascale and L. Mugnai, "Ariel gain noise ", 2021, issue 2.
[101] L. Mugnai, E. Pascale, G. Savini, and P. Eccleston, "Science Performance Analysis (ARIEL-SAP-PL-TN-003)," 2020, issue 2.2.
[102] O. Boulade *et al.*, *Development and characterisation of MCT detectors for space astrophysics at CEA* (International Conference on Space Optics — ICSO 2014). SPIE, 2017.
[103] A. Bounab *et al.*, *LWIR quantum efficiency measurements using a calibrated MCT photodiode read by a cryo-HEMT-based amplifier* (SPIE Astronomical Telescopes + Instrumentation). SPIE, 2020.
[104] C. W. McMurtry, J. L. Pipher, and W. J. Forrest, "Spitzer space telescope: dark current and total noise prediction for InSb detector arrays in the infrared array camera (IRAC) for the post-cryogen era," in *Space Telescopes and Instrumentation I: Optical, Infrared, and Millimeter*, 2006, vol. 6265: International Society for Optics and Photonics, p. 626508.
[105] J. Martignac and M. Berthé, "AIRS Budget Justification Document (ARIEL-CEA-INST-DD-010)," 2022, issue 2.0.
[106] D. Figer *et al.*, *Independent testing of JWST detector prototypes* (Optical Science and Technology, SPIE's 48th Annual Meeting). SPIE, 2004.
[107] O. Gravrand *et al.*, "Latest achievements on MCT IR detectors for space and science imaging," in *Infrared Technology and Applications Xlii*, 2016, vol. 9819: International Society for Optics and Photonics, p. 98191W.
[108] Lake Shore Cryotronics. "Typical Sensor Performance." https://www.lakeshore.com/products/product-detail/model-336/typical-sensor-performance (accessed 01/09/2023, 2023).
[109] A. Caldwell and P. Eccleston, "Payload AIT Plan (ARIEL-RAL-PL-PL-007)," no. 4.1, 2020.

[110] R. Spry, N. E. Bowles, and S. Sarkar, "The impact of the OGSE thermal background on dark current verification (ARIEL-OXF-PL-TN-006)," no. 0.1, 2021.
[111] R. Spry, "OGSE Thermal Stray Light Analysis (ARIEL-OXF-PL-TN-053)," 2022, issue 0.3.
[112] R. Laureijs *et al.*, *The Euclid Mission* (SPIE Astronomical Telescopes + Instrumentation). SPIE, 2010.
[113] SHI Cryogenics Group. "SRDK-500B Cold Head Capacity Map." https://www.shicryogenics.com/wp-content/uploads/2020/09/RDK-500B_Capacity_Map.pdf (accessed 2024).
[114] P. E. Bradley and R. Radebaugh, "Properties of selected materials at cryogenic temperatures," *NIST Publ,* vol. 680, pp. 1-14, 2013.
[115] "NIST Material Measurement Laboratory, Applied Chemicals and Materials Division " https://trc.nist.gov/cryogenics/materials/materialproperties.htm (accessed.
[116] J. Ekin, *Experimental Techniques for Low-Temperature Measurements: Cryostat Design, Material Properties and Superconductor Critical-Current Testing*. Oxford University Press (in eng), 2006.
[117] E. Eldridge and H. Deem, "Physical Properties of Metals and Alloys from Cryogenic to Elevated Temperatures," in *Report on Physical Properties of Metals and Alloys from Cryogenic to Elevated Temperatures*: ASTM International, 1960.
[118] TAI. *CuTS Catalog*. (2022).
[119] G. Jones and S. Calcutt, "Thermal analysis and testing of a spaceborne passive cooler," University of Oxford, 1994.
[120] E. D. F. da Silva and E. C. Garcia, "Experimental Determination of the Effective Thermal Properties of a Multi-Layer Insulation Blanket," in *22nd International Congress of Mechanical Engineering (COBEM 2013) Ribeirão Preto, SP, Brazil*, 2013.
[121] L. Kauder, "Spacecraft thermal control coatings references," *NASA, Goddard space flight center,* 2005.
[122] A. L. Woodcraft, "Predicting the thermal conductivity of aluminium alloys in the cryogenic to room temperature range," *Cryogenics,* vol. 45, no. 6, pp. 421-431, 2005/06/01/ 2005, doi: https://doi.org/10.1016/j.cryogenics.2005.02.003.
[123] K. Liles and R. Amundsen, "NASA Passive Thermal Control Engineering Guidebook," 2022.
[124] E. Fest, *Stray light analysis and control*. 2013.
[125] R. Evans, "OGSE Stray Light Analysis (ARIEL-OXF-PL-TN-041)," 2022, issue 0.1.
[126] C. Simpson, A. Davidson, G. Bishop, and P. Eccleston, "Cleanliness Requirement Specification (ARIEL-RAL-PL-RS-007)," 2022, issue 4.0.

[127] C. Simpson, A. Davidson, G. Bishop, and P. Eccleston, "Payload Cleanliness and Contamination Control Plan (ARIEL-RAL-PL-PL-013)," 2022, issue 3.0.
[128] M. Farina, D. Elia, M. Krijger, and E. Pascale, "Stellar light scattering from particulate contamination (ARIEL-INAF-PL-TN-009)," 2021, issue 2.2.
[129] E. Tunarli, T. Samuel, L. Desjonqueres, and R. Drummond, "CTR Thermal Design and Analysis Report (ARIEL-RAL-PL-AN-003)," 2021, issue 2.0.
[130] R. B. Roberts, R. J. Tainsh, and G. K. White, "Thermal properties of Zerodur at low temperatures," *Cryogenics,* vol. 22, no. 11, pp. 566-568, 1982/11/01/ 1982, doi: https://doi.org/10.1016/0011-2275(82)90002-9.
[131] Ariel Project Team, "Ariel Spacecraft System Requirements Document (SSRD) (ESA-ARIEL-SC-RS-001)," no. 2, 2020.
[132] M. Viada, "ARIEL M2MD Design Description (ARIEL-SEN-PL-DD-004)," no. 3.0, 2023.
[133] A. P. Team", "S/C systems requirements SSRD," 2021, issue 1.0.
[134] E. Pascale and S. Sarhar, "Pointing Jitter Analysis (ARIEL-SAP-PL-TN-001)," 2019, issue 0.7.
[135] Bentham. "Monochromator Selection Guide." https://www.bentham.co.uk/knowledge/tools-resources/technical-notes/monochromator-selection-guide-1109/ (accessed 2024).
[136] Crystran, *The Crystran handbook of infra-red and ultra-violet optical materials*.
[137] Bentham. "Monochromator Configurations." https://www.bentham.co.uk/products/components/monochromators/configurable-monochromators/tmc300-single-monochromator-38/configuration (accessed.
[138] Thorlabs. "A Comparisons of Thorlabs' Thin Film Gold Mirror Coatings." https://www.thorlabs.com/newgrouppage9.cfm?objectgroup_id=744&pn=PFSQ10-03-M01 (accessed 2024).

9 APPENDICES

Appendix A: Monochromator radiometric model data

Model	Line density (g/mm)	Blaze wavelength	Quoted wavelength range
GA-T312R0U75	1200	Plane ruled, 750nm blaze	300-1,200
GA-T304R1U6	400	Plane ruled, 1.6µm blaze	1,000-3,000
GA-T3015R4U0-AU	150	Plane ruled, 4µm blaze. Gold coated.	3,000-10,000

Table 26: Grating configuration for operation within Ariel's wavelength range

Model	Line density (g/mm)	Blaze wavelength	Quoted wavelength range
GA-T318R0U4	1800	Plane ruled, 400nm blaze	250-900
GA-T301R9U0-AU	100	Plane ruled, 9µm blaze. Gold coated.	4,500-16,000

Table 27: Grating configuration for out-of-band radiation testing

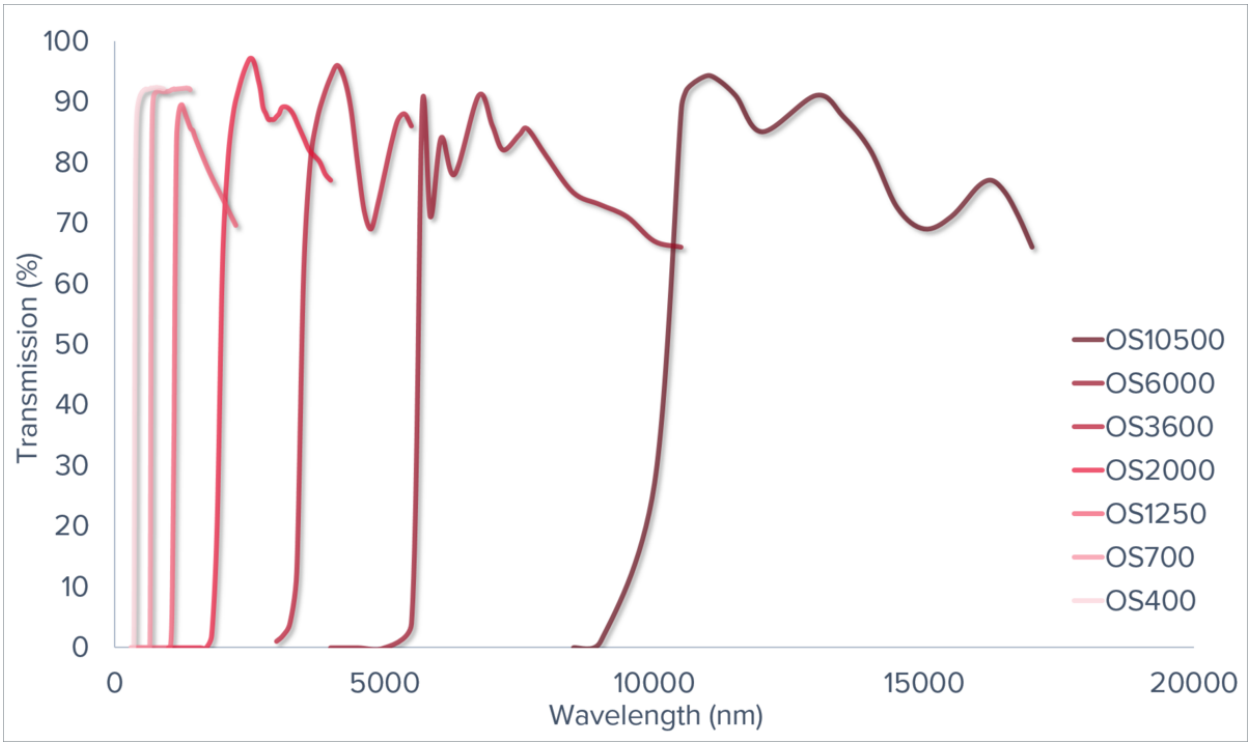

Figure 104: Transmittance of order sorting filters [135]

Configuration (wheel number-position number)	Part	Wavelength range	Supplier
1-1	OS400	400-700nm	Bentham
1-2	OS700	700-1250nm	Bentham
1-3	OS1250	1250-2000nm	Bentham/NOC
1-4	OS2000	2000-3600nm	Bentham/NOC
1-5	OS3600	3.6-6 µm	Bentham/NOC
2-1	OS6000	6-10.5 µm	Bentham/NOC
2-2	OS10500	10.5-21 µm	Bentham/NOC
1-6 & 2-3	Clear	-	-
2-4	Shuttered	-	Bentham
2-5	ND	-	Thorlabs

Table 28: Planned monochromator filters

Parameter	Value	Comments

Mono Vis source temperature	3360K	Bentham IL1
VIS filament dimensions	4.7mm*2.7mm	(h*w) 64623 HLX
VIS source F#	1	
Vis source emissivity	0.8	
VIS source throughput	0.9	Reflective relay to monochromator
Mono IR source temperature	1250K	Bentham IL8
IR filament dimensions	3.5mm (D) x 12mm (L)	(h*w) IR-SiX Series Hawkeye
IR source F#	1	
IR source emissivity	0.8	IR-SiX Series Hawkeye
IR source throughput	0.9	Reflective relay to monochromator
Short grating line spacing	1200 lines per mm	
Mid grating line spacing	400 lines per mm	
Long grating line spacing	150 lines per mm	
Grating efficiency	0.5	(see Figure 106 for short grating)
Short grating coverage	0.5-1.2µm	
Mid grating coverage	1.2µm-3µm	
Long grating coverage	3µm-7.8µm	
Slight Height	2cm	TMc300 data sheet
Monochromator F/#	4.1	TMc300 data sheet
Monochromator focal length	300mm	TMc300 data sheet
Monochromator internal angle	2*0.2333	Angle between entrance and exit collimators
Pre sphere optics throughput	0.5	(also accounts for order sorting filter throughput + throughput of mirrors within the monochromator)
Window throughout	0.7if $0.375 < \lambda < 13\mu m$ $else\ 0.01$	(ZnS, see Figure 105) Out of band is an upper bound.
Sphere reflectivity	0.35if $\lambda < 0.55\mu m$ 0.94 if $\lambda > 0.55\mu m$	Infragold see figures below
Port fraction	5%	
Pinhole diameter	50µm	
Sphere output F/#	24	(geometric average of major and mirror directions)

Post sphere optics throughput	0.5	(also accounts for order sorting filter throughput + throughput of mirrors within the monochromator)

Table 29: Assumed parameters in the monochromator radiometric model

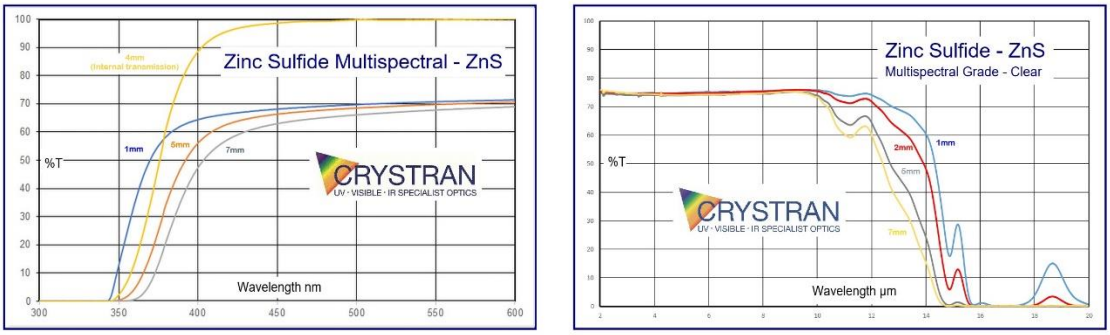

Figure 105: Chamber window transmission spectrum [136].

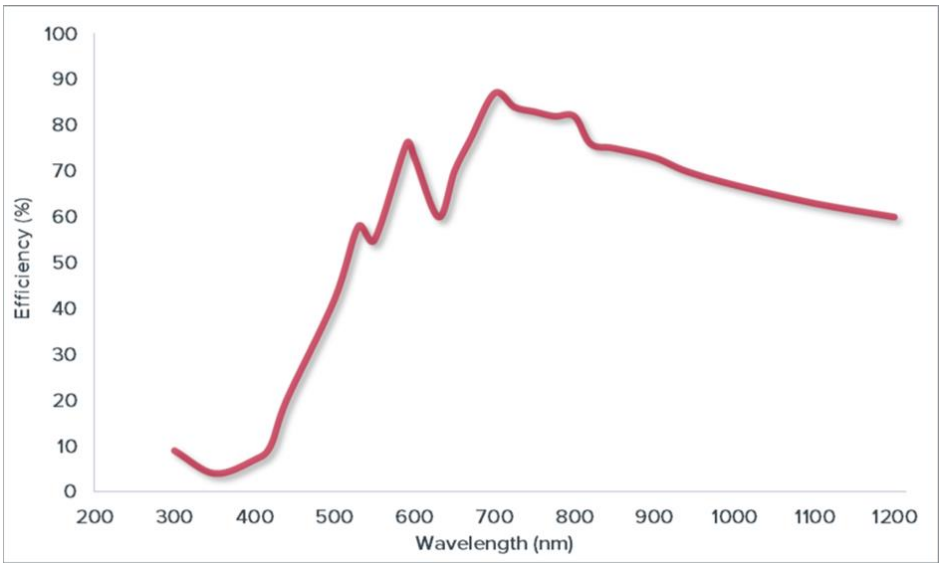

Figure 106: GA-T312R0U75 grating efficiency curve [137]

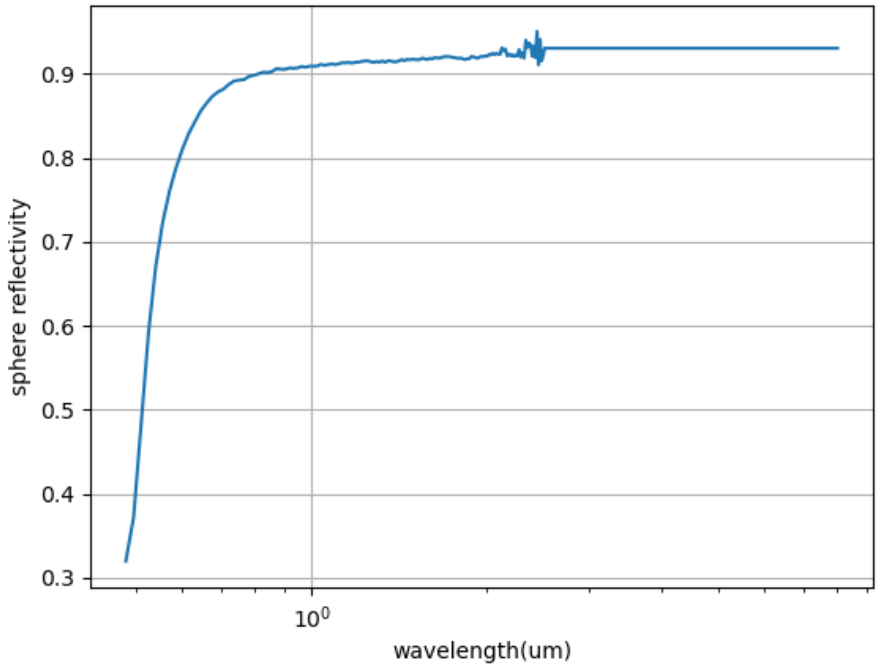

Figure 107: Infragold reflectance used in the model. Up to 2 microns, Thorlabs [138] data was used. At longer wavelengths, a constant value was assumed based on data from Labsphere. To account for the difference in reflectivity between specular gold and Infragold, the Thorlabs data was scaled to match the Labspehre data.

Appendix B:Spectral irradiance derivation

In section 5.3.1.1 a brief derivation of the mirror's irradiance was provided. Here, a more detailed justification is provided. In the first part of this derivation, the goal is to evaluate the spectral power absorbed at a mirrors surface. This thermal power originates from ambient (or close to ambient surfaces) within the CTR. The absorbed spectral power can be calculated using the radiative transfer coefficients from ESATAN (G_R) and the emitting surface temperature. Finally, given the absorbed spectral power and the emissivity of the mirror, the spectral irradiance at the mirrors surface can be calculated. Given also the BSDF, the stray light radiance can be calculated.

Use of the ESATAN thermal model to predict the radiative coupling between stray light sources and mirrors

A non-cryogenic surface (e.g. the PIP plate) emits black body radiation with a radiance equal to $\epsilon_{pip} BB(T_{pip}, \lambda)$. A fraction of this radiance will be absorbed by a mirror's surface.

The distribution factor $D_{pip\rightarrow mirror}$ is defined to be the fraction of the total power emitted from the pip plate that gets absorbed by the mirror:

$$D_{pip\rightarrow mirror} \equiv \frac{P_{AbsMirr}}{\epsilon_{pip} BB\left(T_{pip}, \lambda\right) A_{pip} \pi} \tag{A1}$$

Therefore, the total bolometric power absorbed by the mirror from the pip plate is:

$$\Phi_{AbsMirr} \equiv \int_0^\infty P_{AbsMirr} d\lambda = \int_0^\infty D_{pip\rightarrow mirror} \epsilon_{pip} BB\left(T_{pip}, \lambda\right) A_{pip} \pi d\lambda \tag{A2}$$

Assuming a wavelength-independent PIP MLI emissivity and distribution factor:

$$\Phi_{AbsMirr} = D_{pip\rightarrow mirror} \epsilon_{pip} A_{pip} \pi \int_0^\infty BB\left(T_{pip}, \lambda\right) d\lambda \tag{A3}$$

$$= D_{pip\rightarrow mirror} \epsilon_{pip} A_{pip} \sigma T_{pip}^4 \tag{A4}$$

Similarly, we can consider the (albeit small) flux emitted by the mirror that gets absorbed by the pip plate. The fraction of flux emitted by the mirror that gets absorbed by pip plate is given by:

$$D_{mirror\rightarrow pip} \equiv \frac{P_{AbsPip}}{\epsilon_{mirror} BB(T_{mirror}, \lambda) A_{mirror} \pi} \tag{A5}$$

As before,

$$\Phi_{AbsPip} = D_{mirror\rightarrow pip} \epsilon_{mirror} A_{mirror} \pi \int_0^\infty BB(T_{mirror}, \lambda) d\lambda \tag{A6}$$

$$= D_{mirror\rightarrow pip} \epsilon_{mirror} A_{mirror} \sigma T_{mirror}^4$$

Therefore, the net flux, Φ_{net} from the pip plate to the mirror is given by the power absorbed by the mirror from the pip plate, less the power absorbed by the pip plate from the mirror.

$$\Phi_{net} = \Phi_{AbsMirr} - \Phi_{AbsPip} \tag{A7}$$

$$= D_{pip\rightarrow mirror} \epsilon_{pip} A_{pip} \sigma T_{pip}^4 - D_{mirror\rightarrow pip} \epsilon_{mirror} A_{mirror} \sigma T_{mirror}^4 \tag{A8}$$

From the second law of thermodynamics, the distribution factors obey the following property[67] :

$$D_{1\to2}\epsilon_1 A_1 = D_{2\to1}\epsilon_2 A_2 \qquad (A9)$$

Therefore, the net heat flux is given by:

$$\Phi_{net} = D_{pip\to mirror}\epsilon_{pip}A_{pip}\sigma\left(T_{pip}^4 - T_{mirror}^4\right) \qquad (A10)$$

The net heat flux can also be computed from ESATAN. And is reported in the following form:

$$\Phi_{net} = G_R\sigma\left(T_{pip}^4 - T_{mirror}^4\right) \qquad (A11)$$

By comparing equations A10 and A11:

$$D_{pip\to mirror}\epsilon_{pip}A_{pip} = G_R \qquad (A12)$$

We have therefore obtained the distribution factor $D_{pip\to mirror}$ in terms of the radiative transfer coefficient G_R, a quantity that can be estimated from ESATAN.

Substituting this value of $D_{pip\to mirror}$ (equation A12) into equation A1:

$$\frac{G_R}{\epsilon_{pip}A_{pip}} = \frac{P_{AbsMirr}}{\epsilon_{pip}BB\left(T_{pip},\lambda\right)A_{pip}\pi} \qquad (A13)$$

Therefore, the spectral power absorbed by the mirror $P_{AbsMirr}$ is given by:

$$P_{AbsMirr} = G_R\pi BB\left(T_{pip},\lambda\right) \qquad (A14)$$

Converting the absorbed thermal emission to a stray light radiance

To calculate the stray light we need to know the incident irradiance at a mirror's surface. The thermal model, however, provides the power absorbed by the mirror. The two can be related given knowledge of the emissivity of the mirror. If there is an irradiance I_{in} incident at the mirror's surface, a fraction

[67] See e.g. Maria Sánchez, thesis CH2

ϵ_{mirror} would be absorbed, and the remainder would be reflected. Therefore, the absorbed power that results from an irradiance I_{in} is given by:

$$P_{AbsMirr} = I_{in}\epsilon_{mirror}A_{mirror} \quad (A15)$$

Therefore, from equations A15 and A14, the irradiance at the mirror's surface caused by PIP plate thermal emission is given by:

$$I_{in} = \frac{G_R \pi BB(T_{pip}, \lambda)}{\epsilon_{mirror}A_{mirror}} \quad (A16)$$

To calculate the stray light radiance, the mirrors BSDF can be used. The BSDF is defined to be the ratio of the scattered radiance to the incident irradiance. Therefore, the stray light radiance is given by:

$$dL_{stray} = BSDF(\theta_{in}, \theta_s)dI_{in} \quad (A17)$$

Without knowledge of the angular irradiance distribution, this is only solvable in two limits. (1) isotropic irradiance and (2) point source irradiance, which if located at the BRDF minimum gives a best-case limit of the stray light rejection (further details in section 5.3.1.2).

Appendix C: Selected applicable requirements

Appendix redacted from ORA version

Appendix D: Assumed CDS sampling cadence

Integration time (s)	Number of ramps	Time required (hr)
1.0E-01	401	0.01
1.6E-01	330	0.01
2.6E-01	272	0.02
4.3E-01	224	0.03
7.0E-01	184	0.04
1.1E+00	152	0.05
1.8E+00	125	0.06
3.0E+00	103	0.09
4.8E+00	85	0.11
7.8E+00	70	0.15
1.3E+01	57	0.20
2.1E+01	47	0.27
3.4E+01	39	0.36
5.5E+01	32	0.49
8.9E+01	26	0.65
1.4E+02	22	0.87
2.3E+02	18	1.16
3.8E+02	15	1.55
6.2E+02	12	2.08
1.0E+03	10	2.78
		10.99 hr

Table 30: Planned sampling for the measurement of the CDS noise.